The Effect of Height Scaling on the Flexural Crack Width Controlling Behavior of Hybrid R/SHCC Beams

A Numerical and Experimental Study

H.J. Bezemer

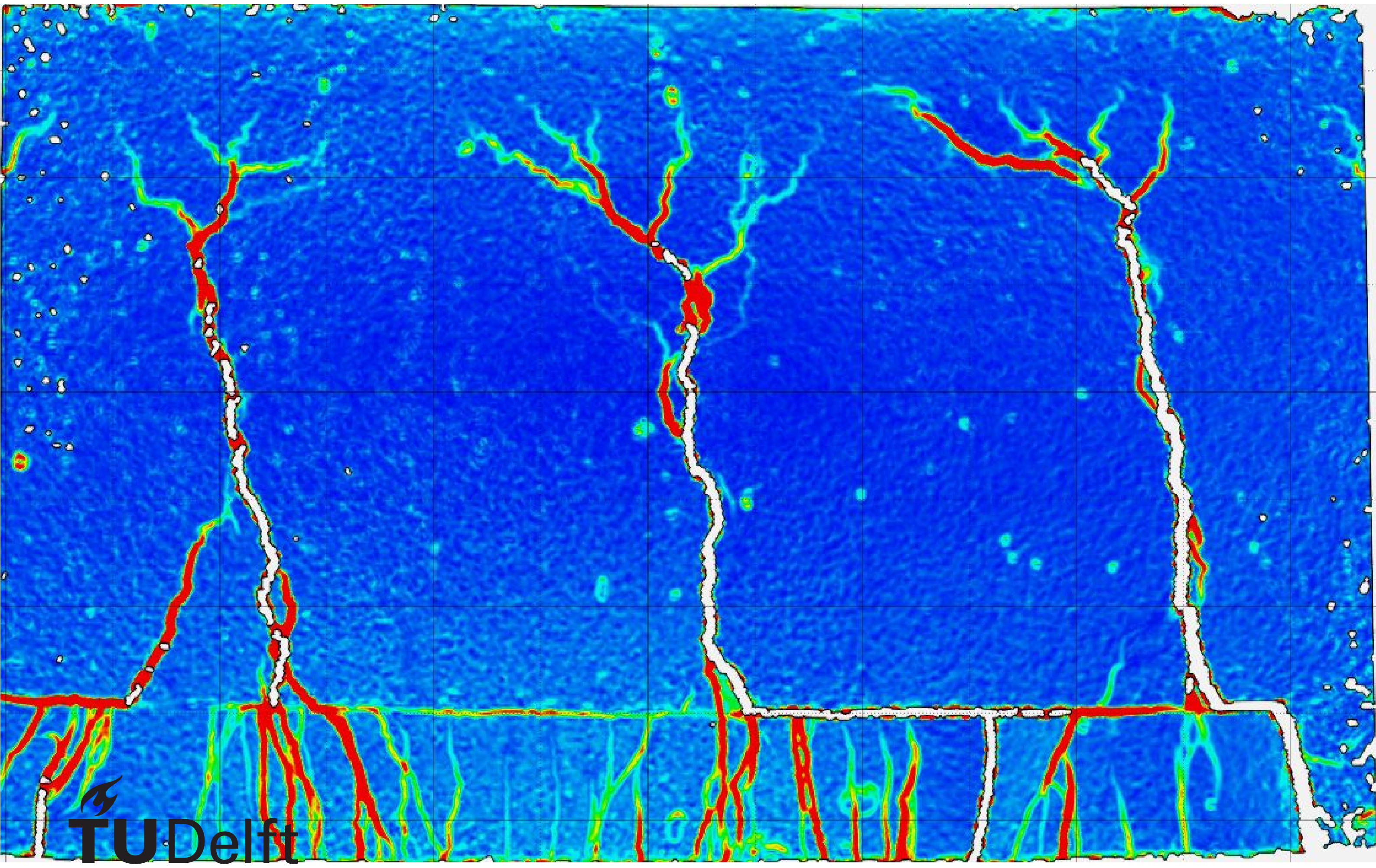

The Effect of Height Scaling on the Flexural Crack Width Controlling Behavior of Hybrid R/SHCC Beams

A Numerical and Experimental Study

by

H.J. Bezemer

To obtain the degree of Master of Science
at the Delft University of Technology,
to be defended publicly on Friday September 30, 2022 at 02:00 PM.

Student number:	4687760	
Project duration:	November 1, 2021 – September 30, 2022	
Thesis committee:	Mrs. dr. ir. M. Luković (chair),	TU Delft - Concrete Structures
	Ir. S. Mustafa (daily supervisor),	TU Delft - Concrete Structures
	Dr. ir. B. Šavija,	TU Delft - Materials and Environment

TU Delft

Preface

Like Mladena said: ”If you had till December, you will keep on finding things to work on”. I think she is right. As one part of me feels sorry that this project ends, another part is really glad I made it. It has been a great journey, which I could have never taken alone.

I want to thank Mladena for suggesting this topic. Even more, thank you Mladena for all the support during the project. Whenever I freaked out of a delay or setback, you reassured me. You motivated me to push for the best outcome. Even when you should be on maternity leave, you were involved. I also want to thank Shozab. Shozab, thank you for being there every morning (especially the early ones), afternoon and evening. You were of great help both inside and outside the lab. You have taught me so much about how to conduct a good experiment. I admire how you remain calm during all the delays and setbacks and never wanted to sacrifice even the smallest bit on the quality of the experiment. Due to all the help you provided, your own work got delayed. I hope you are able to proceed with your own work now. Branko, thank you for thinking outside the box and providing me with feedback. Thank you for your patience and time. In addition to my committee, I want to thank the lab staff for all their support. Many staff got involved, too many to mention all of them. However, I do want to mention Jakub. Thank you for your hard work and your problem solving mind. I also want to mention Albert. Thank you for your experience and your confidence in the project. Thank you Louis. When everyone was busy, you always found the time to help me out. It was not even your job to be in the concrete section of the lab and still you supported me so much in adjusting the setup and scanning the samples. Thank you for your time, patience and faith in me. Lastly, I need to mention Kees. Kees's involvement started, once I started analysing the test setup. He made so many suggestions of what I had to check. However, in the end the new cylinder needed to be connected. My schedule was really tight and Kees stayed till late in the evening to connect all the electronics. Thank you Kees.

After the first testing series, new reinforcement cages were needed. The delivery time of 5 weeks would cause serious delays in the project. However, J. van Vliet Vlechtwerken, was willing to help me out and made the cages over the weekend. Thank you so much for prioritizing me, and squeezing my cages into your tight schedules.

Lastly, I want to thank my family. Thank you all for your unconditional loving support. Thank you dad for all the discussions we had. Thank you for your involvement and problem-solving ideas. Thank you mother, for always taking care of me. Thank you parents-in-law for supporting me, housekeeping and finding me a silent place to work. And last but not least, thank you Ankie for your loving support. Because of you it feels like we did this together.

H.J. Bezemer
Delft, August 2022

Abstract

Limiting maximum crack widths is a serviceability limit state, which ensures the durability of reinforced structures. In current practice, maximum crack widths are limited by using additional reinforcement, on top of the amount of reinforcement required for the designed ultimate bearing capacity. Reducing the amount of reinforcing steel used, could make the construction industry more sustainable. Recent studies showed that, hybrid reinforced beams with a 70 mm thick bottom layer of strain hardening cementitious composite (SHCC), so-called hybrid R/SHCC beams, are promising in controlling crack widths under pure bending, without using additional reinforcement (Huang, 2017; Singh, 2019). SHCC is made from a binder, fine particles and PVA fibers, which leads to ductile material properties and crack bridging. The beams studied in these previous studies were limited to a height of 200 mm. In practice larger heights are demanded. Increasing the height of a hybrid R/SHCC beam, by keeping the thickness of the SHCC layer constant, reduces the relative contribution of SHCC. In addition, cementitious materials exhibit strong size effects. Therefore, the effect of height scaling on the flexural crack width controlling behavior of hybrid R/SHCC beam is studied in this thesis. In addition, the optimization potential of the crack controlling behavior of the hybrid R/SHCC beams is studied, by the delamination of the SHCC-rebar interface.

The effect of height scaling on the flexural crack width controlling behavior of the hybrid R/SHCC beams is studied both experimentally and numerically, by 200 mm, 300 mm and 400 mm high hybrid R/SHCC beams, with a constant 70 mm thick bottom layer of SHCC. Reinforced concrete beams of the same heights are used as reference. The length of the higher beams are increased, to prevent direct force transfer. The experimental results of the 200 mm high beams are used from a previous study by (Singh, 2019). To study the effect of delamination of the SHCC-rebar interface, a 300 mm high hybrid R/SHCC beam with smooth and Vaseline treated longitudinal reinforcement bars is used. The beams are tested in a four-point bending configuration, with a 500 mm constant bending moment region. All the beams have the same amount of longitudinal reinforcement. The numerical study is performed with the Delft Lattice Model. As lattice models are only recently used for the modelling of structural behavior, the use of the Delft Lattice model in this study is a contribution to the development of lattice models. Analytical calculations, with use of the multi-layer model (Yassiri, 2020), are used in the comparison of the numerical and experimental results.

From the performed experiments, it is found that, the load, at which the 0.3 mm crack width limit is reached, decreases from 109% to 97% and 91% of the yielding load, upon increasing the height from 200 mm to 300 mm and 400 mm, respectively. Whereas, the beam with smooth and Vaseline treated longitudinal reinforcement bars, reached the crack width limit already at 59% of the yielding load. Increasing the height of the reinforced concrete beams does not lead to a reduction in the crack width limit load, relative to the yielding load (76%-78%). From the cracking patterns, it is found that, upon increasing the height, the number of propagated concrete cracks decrease, both in the reinforced concrete beams and in the hybrid R/SHCC beams, whereas the hybrid beam with smooth and Vaseline treated reinforcement bars showed a single propagated crack in the concrete layer. An effective tensile area is developed for the 300 mm and 400 mm high beams, which was not observed in the 200 mm high beams. Uniform cracking distributions are found in all the SHCC layers of the hybrid beams, except for the hybrid beam with smooth and Vaseline treated reinforcement bars. The delamination of the concrete-SHCC interface increases, upon increasing the height, whereas the ultimate bearing capacity is similar for the 300 mm and 400 mm high hybrid R/SHCC beams. On the contrary, the hybrid beam with smooth and Vaseline treated reinforcement bars shows very limited delamination. From the out of plane measurements, it is found that, hybrid R/SHCC beams show out of plane displacements, which are highly correlated to the applied vertical forces. This is not observed for the reinforced concrete beams.

The numerical models are able to simulate the trends in the cracking patterns, as observed in the experiments. In addition, the numerical models are able to simulate the trends in delamination. Increasing the concrete-SHCC bond strength, in the 400 mm high hybrid R/SHCC numerical model, leads to the formation of an additional propagated crack in the concrete layer. In addition, the deformation capacity

and the delamination of the concrete-SHCC layer reduces, for the beam with the stronger concrete-SHCC interface bond strength. Using a coarser 25 mm voxel size in the numerical models, instead of the 10 mm voxel size used in previous studies (Mustafa et al., 2022), leads to similar simulated structural behavior of the beams. The voxel size limits the crack spacing, which is of larger importance for the SHCC, compared to conventional concrete. For the reinforced concrete beams, the numerical models are able to predict the yielding load, whereas for the hybrid beams, the yielding deformation is underestimated, due to the overestimation of the ductility of the modelled SHCC. The analytical calculations show good comparison with the numerical models, both for the hybrid beams and for the reinforced concrete beams. The hybrid beam with smooth and Vaseline treated reinforcement leads to an unreinforced hybrid beam, which is different from the experimental results. This difference is attributed to the numerical model simulating a weak bond over the full length of the beam, whereas in the experiments Vaseline is only applied over the 700 mm central span.

To conclude, upon increasing the height of the hybrid R/SHCC beams, the effectiveness of the crack controlling behavior decreases. This is both found in the numerical and in the experimental results and holds both for a 0.2 mm and 0.3 mm crack width limit. However, the hybrid beams scaled in height still lead to a significant increase in the crack controlling behavior, compared to reinforced concrete beams of the same heights. Full delamination of the rebar-SHCC interface leads to worse crack controlling behavior for the hybrid R/SHCC beams. Even more, if the full delamination occurs over the full length of the beam, the beam could be considered unreinforced. The Delft Lattice model shows large potential in the simulation of the structural behavior of both the reinforced concrete beams and the hybrid R/SHCC beams. The coarser 25 mm voxel size is found to be a time efficient and suitable modelling solution to gain insight in trends in the structural behavior of reinforced structures.

The numerical model with a stronger concrete-SHCC interface showed potential in improving the crack width controlling behavior of the hybrid R/SHCC beams in height. Therefore, it is recommended to study the effect of interface roughness for hybrid R/SHCC beams scaled in height. Additionally, determining the material input for SHCC remains a challenge in numerical simulations with the Delft Lattice Model. In order to improve the simulations of the numerical models, it is recommended to study the material input possibilities for SHCC. Even more, before the beams are applied in practise, it is recommended to gain deeper understanding of the increased out of plane sensitivity of the hybrid R/SHCC beams. Studying the fiber dispersion would be logical start for this.

Contents

1
Introduction

1.1. Background and Motivation

Concrete is a widely used construction material. Concrete behaves strong in compression, but weak in tension. Therefore, concrete structures expected to experience tensile stresses are usually reinforced with steel bars. Upon loading of a reinforced concrete structure, concrete cracks, once the tensile strength of concrete is exceeded. Cracking of concrete is allowed, as long as the crack widths are limited. Crack widths should be limited as, cracks increase the penetration of substances, such as water, carbon dioxide and chloride. The ingress of such substances leads to enhanced deterioration processes of the reinforced concrete element, such as corrosion of steel reinforcement. If the steel corrodes, it loses cross sectional area over time, which is unwanted as this reduces the load bearing capacity of the reinforced element over time. Whereas, reinforced concrete structures should be durable. Therefore, the limiting of crack widths is a Serviceability Limit State (SLS). A general limit for crack width is 0.3 mm, which can be more strict if the element is exposed to environments with a larger presence of deteriorating substances (*Eurocode 2: Design of concrete structures*, 2004). In current practice, crack widths are limited by using additional reinforcement, on top of the required reinforcement for the designed bearing capacity (Ultimate Limit State, ULS). Therefore, reinforced structures are over-reinforced, with respect to ULS. With the current rise in climate awareness, the construction industry could become more sustainable by searching for other ways to limit crack widths. Another way of limiting the crack widths, without adding additional reinforcement, is the use of strain hardening cementitious composite (SHCC) in the tension zone, instead of ordinary concrete (Figure 1.1). SHCC is usually made from a binder, fine particles and fibers. Usually PVA fibers are used. The fibers in the mix allow for crack bridging, which leads to improved crack width controlling behavior (Singh, 2019). It was found that, a reinforced concrete beam with a 70 mm thick SHCC in the tension zone, is promising in dealing with the crack width criteria, when loaded in pure bending (Huang, 2017 & Singh, 2019). These beams, called hybrid reinforced SHCC beams (hybrid R/SHCC beams), have only the amount of reinforcement applied, as required for ULS.

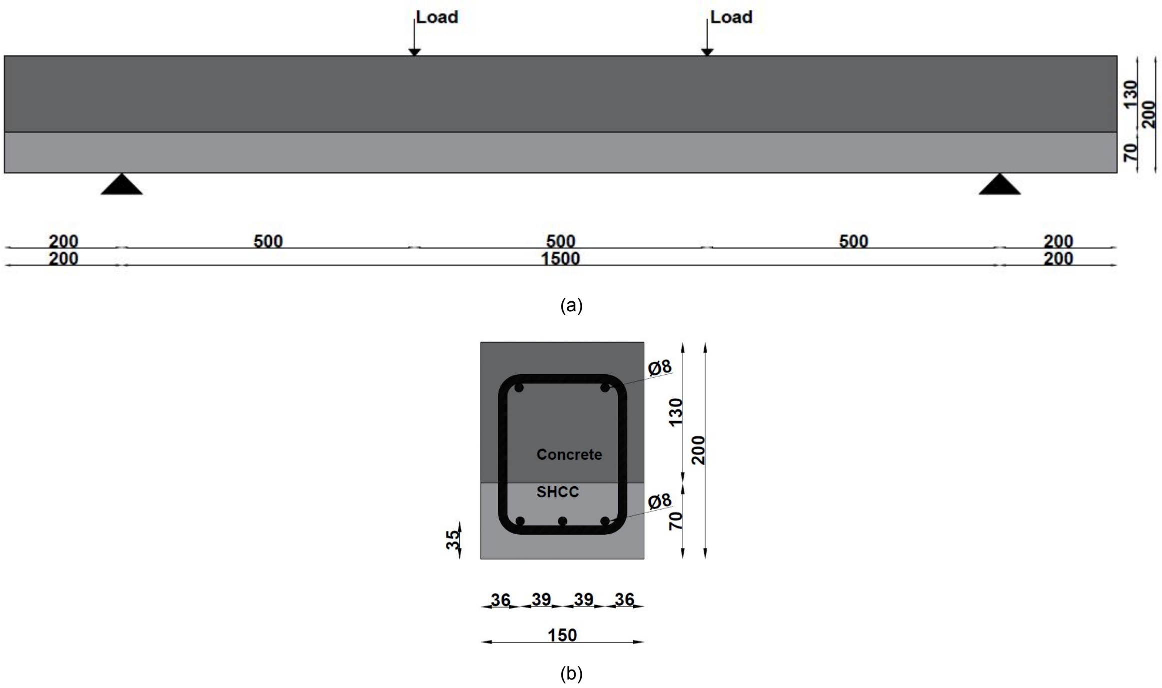

Figure 1.1: 200 mm high R/SHCC hybrid beam with (a) geometry of beam and (b) cross section of beam as studied by (Huang, 2017 & Singh, 2019).

In addition, PVA fibers and a smooth interface layer between conventional concrete and SHCC are found to be effective in controlling crack widths for 200 mm high hybrid R/SHCC beams (Huang, 2017 & Singh, 2019). These studies showed promising results, but only results of 200 mm high beams were obtained. In practice larger sizes are demanded. Increasing the height of the hybrid beams from the previous studies, while keeping the thickness of the SHCC constant, leads to a relative reduction in the contribution of SHCC in the cross section. In addition, cementitious materials exhibit strong size effects. Therefore, the effect of height scaling on the flexural crack width controlling behavior of hybrid R/SHCC beams is studied in this thesis.

1.2. Scope of the Research

This thesis is part of a research line, aiming at upscaling of innovative concretes. Within this research line, multiple studies (experimental, numerical and analytical) are performed, among which are the master thesis studies from (Huang, 2017) & (Singh, 2019). They studied the crack controlling behavior of 200 mm high R/SHCC beams. This master thesis is limited to the investigation of the effects of height scaling on the flexural crack controlling behavior of hybrid R/SHCC beams. This study combines experimental and numerical work. In addition, this study investigates the possibilities of optimizing the hybrid R/SHCC beams, by studying the effect of delamination of the rebar-SHCC interface. This optimization is both addressed in the experiments and in the numerical part.

1.3. Research Hypothesis

The decrease in relative contribution of SHCC in a hybrid R/SHCC beams scaled in height, and the presence of strong size effects in cementititous materials, are expected to reduce the effectiveness of the crack controlling behavior of the hybrid R/SHCC beams. Therefore, the hypothesis is formulated as:

”The effectiveness of the crack controlling behavior of the SHCC layer decreases, upon increasing the height of hybrid R/SHCC beams.”

1.4. Research Objectives and Methodology

The main objective of this research is to study the effect of height scaling on the flexural crack width controlling behavior of hybrid R/SHCC beams. In order to reach this objective, the following research question is posed:

1. To what extent is the flexural crack controlling behavior of hybrid R/SHCC beams sensitive to height scaling?
    - The literature is used, to study the cracking behavior of reinforced concrete. In addition, the material properties of SHCC and the hybrid R/SHCC system are studied, based on previously performed experiments. The experimental results of the 200 mm high beams (S-PVA and CC) of (Singh, 2019) are used.
    - Experiments, including 300 mm and 400 mm high hybrid R/SHCC beams, are performed. Reinforced concrete beams are used as reference. In the experiments, crack widths are measured from two sides and the out of plane displacement of the beams are determined, to gain better insight in the fracturing behavior of hybrid R/SHCC beams.
    - Numerical models of 200, 300 and 400 mm high hybrid R/SHCC beams and reinforced concrete beams are made, to simulate the structural behavior. In order to develop these models, the literature is used to gain insight in the Delft Lattice Model. In addition, prism models are made to study the effect of mesh size, number of segments used as material input and material input used for SHCC. The experimental results are compared with the numerical results and analytical calculations, to determine the ability of the Delft Lattice Model, to simulate the structural behavior of the studied beams

In addition to this main objective, a second objective of this thesis is to study the effect of delamination of the longitudinal reinforcement bars in hybrid beams. In order to reach this objective, the following research question is posed:

2. To what extent is the delamination of longitudinal reinforcement bars affecting the flexural crack controlling behavior of hybrid R/SHCC beams?
    - The literature is used to study the effect of roughness of the reinforcement bars. In addition, the concrete-SHCC delamination is studied.
    - Experiments are performed on a 300 mm high hybrid R/SHCC beam with plain and Vaseline treated longitudinal reinforcement bars. A 300 mm high hybrid beam with ribbed reinforcement bars is used as reference.
    - Numerical models are made of a 300 mm high hybrid R/SHCC beam, with the delaminated reinforcement bars. A 300 mm high hybrid beam with ordinary longitudinal reinforcement bars is used as reference. To determine the best modelling possibility of the delaminated reinforcement bar, numerical models are made of a 200 mm high reinforced concrete beam. The numerically simulated structural behavior is compared with the experimental results, to determine the modelling potential of the Delft Lattice Model.

1.5. Outline of the Thesis

The outline of this thesis is shown in Figure 1.2. After the introduction, the study starts with performing a literature study. The literature study builds up gradually from cracking of reinforced concrete, up to the material properties of SHCC and finally the cracking behavior of hybrid R/SHCC beams. From the literature study, the effect of roughness of the reinforcement bars and the delamination of the concrete-SHCC are studied. After the literature study is performed, the beams to be investigated are designed. Design constraints are present to allow for comparison with previous studies. With the beams designed, the numerical study is performed, which starts by explaining the background of the Delft Lattice Model. After the background of the modelling method is provided, the models are defined. Defining the models starts by calibration of material properties and is followed by the modelling of the rebar-concrete interface. Different model parameters are addressed in the calibration part to investigate their effect on the response of the model. After calibration, the designed beams are modelled and tested numerically. After the numerical part, the experimental study is performed. This study starts with series 1 of experiments, followed by an analysis of the performed tests and used testing setup. A tool is designed that allows to measure the out of plane displacements, based on 2D in plane displacement data. After analysing the setup, series 2 of experiments is performed. With the experiments performed, the results of the numerical part and experimental part are compared and differences are addressed and discussed. Lastly, the research objectives are reviewed in the conclusions part and recommendations are made for future research.

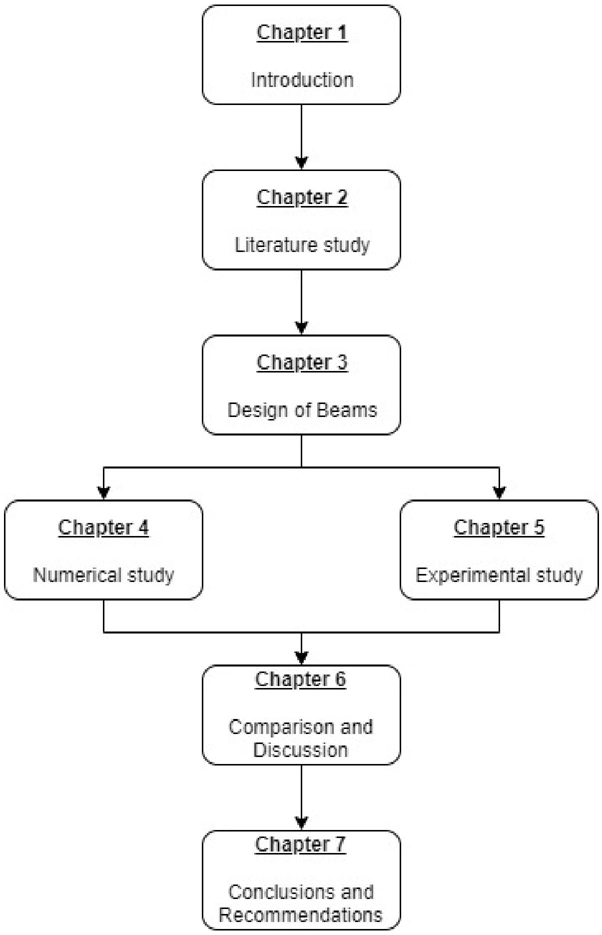

Figure 1.2: Outline of thesis.

2

Literature Study

2.1. Conventional Reinforced Concrete

In this section, the cracking behavior of conventional reinforced concrete is studied. First, the heterogeneity of concrete is discussed, followed by the formation of cracks and the crack spacing in reinforced concrete. In addition, the moment-curvature is discussed for a reinforced beam subject to bending, followed by the effect of the concrete cover on the crack width, the effective tensile area and the effect of tension stiffening.

2.1.1. Natural Variability of concrete

Concrete is a heterogeneous material, which means that the material properties vary at different cross sections and even within these cross sections (Gibb and Harrison, 2010). This heterogeneity of concrete is present due to the nature of concrete. Concrete is a multi-phase composite material, due to the mixture of cement paste and different types and sizes of aggregates, which needs to be bounded by the cement paste. Therefore, the strength of concrete is dependent on the strength of the paste, the paste to aggregate interface bond and the aggregate strength. As all these properties also have a natural variability, the mixing of these materials to obtain concrete results in a high variability in material properties for the concrete. Therefore, characteristic (95th percentile) or average values of the concrete properties are used in practise (Figure 2.1).

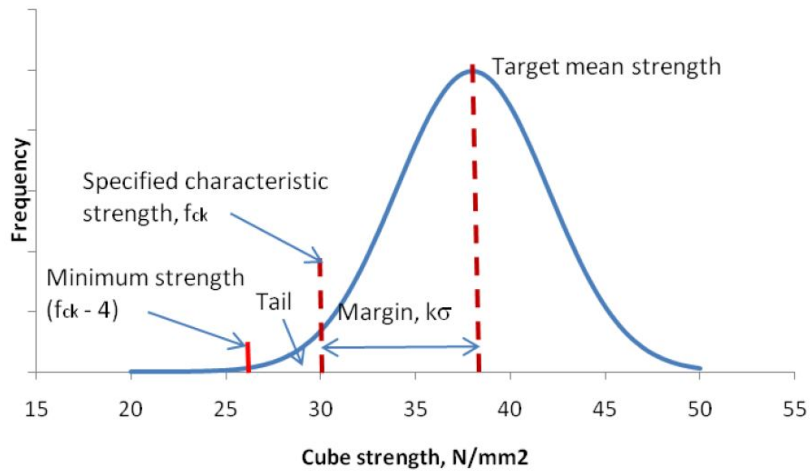

Figure 2.1: Normal distribution of concrete compressive cube strength for C30/37 (Gibb and Harrison, 2010).

The use of characteristic values is called the probabilistic approach. This approach models the heterogeneous material into a homogeneous material, which allows for design in practice (Gibb and Harrison, 2010). Based on the probabilistic approach, concrete classes are created. By classification of concrete, the material properties of concrete are empirically related to each other. Therefore, it is possible to estimate the properties of the concrete based on tested compressive strength only (Braam and Lagendijk, 2008). Increasing the concrete strength class results not only in a higher compressive strength, but also in a higher tensile strength. However, beyond concrete class C50/60, concrete is regarded high-strength and the ultimate compressive strain reduces (Figure 2.2). Therefore, high-strength concrete is more brittle compared to normal strength concrete (Pendyala, Mendis, et al., 1996).

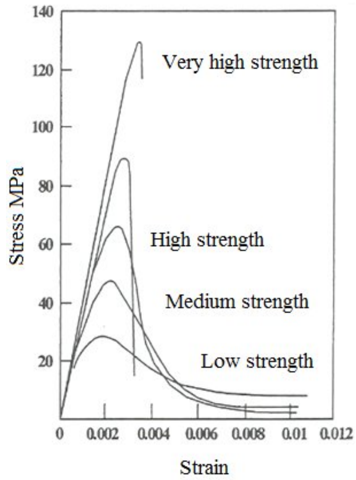

Figure 2.2: Stress-strain curves for different concrete strength classes (Pendyala, Mendis, et al., 1996).

2.1.2. Crack formation of reinforced concrete

The cracking of concrete occurs when at a certain point the tensile strength is exceeded. This can have multiple causes such as: temperature loading, autogenous shrinkage, application of loads and imposed deformations. The focus of this study is on the cracking of reinforced concrete beams subjected to a bending moment. Therefore, other sources of cracks are not be considered. A crack is often formed at the aggregate-cement interface, as this is generally the weakest link in the concrete matrix (Van Mier, 2012). The stress that was present before cracking cannot be transferred anymore through concrete and is redistributed to the reinforcing steel, which acts as a bridge. The steel takes over the stresses locally at a crack, but at a certain distance from the crack the stresses are again shared by concrete and reinforcement (Figure 2.3). This means that, a stress transfer from steel to concrete occurs. The transferring of stresses from concrete to steel and from steel back to concrete occurs via shear (Tepfers, 1973).

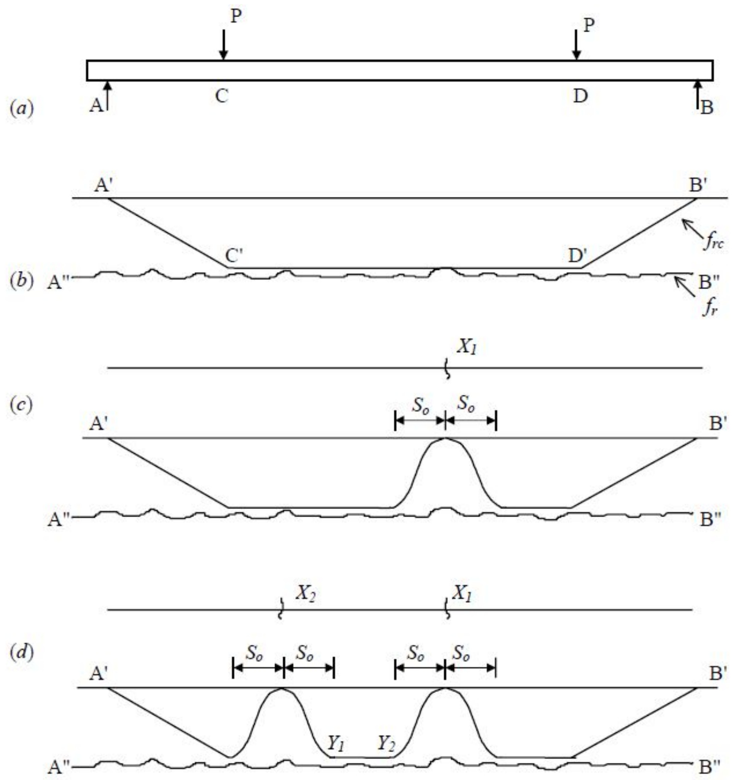

Figure 2.3: Cracking of concrete over the length of beam with (a) schematization of load configuration, (b) concrete stresses in the elastic stage, (c) concrete stresses with first crack formed and (d) concrete stresses with second crack formed (Piyasena, 2002). f_{rc} = calculated concrete stress. f_r = flexural strength.

These shear stresses are developed by slipping of the reinforcement relative to concrete, and thereby activating a restraining concrete hoop around the reinforcement (Figure 2.4). Abrupt introduction of the steel stresses is not possible, as this would result in large slipping of the reinforcement. Therefore, a bonding length of reinforcement is needed to transfer the stress (Tepfers, 1973). This means that, the stress in concrete is increasing away from the crack. Until at a certain point the tensile strength is exceeded again, leading to the formation of another crack.

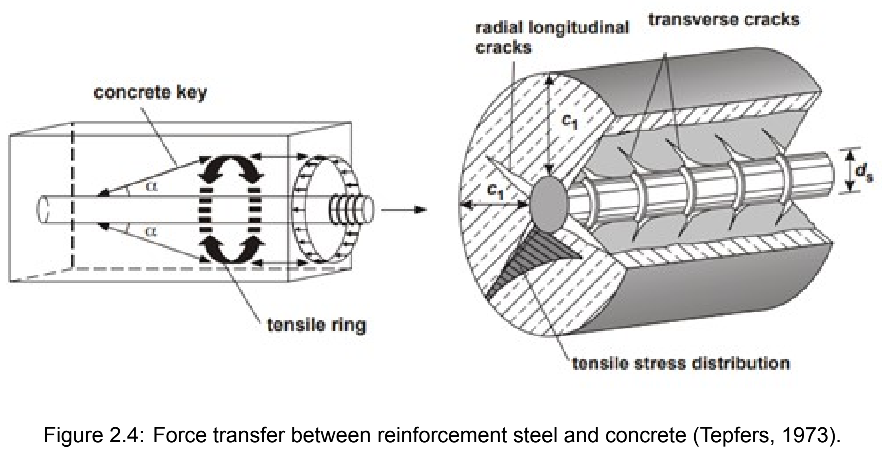

Figure 2.4: Force transfer between reinforcement steel and concrete (Tepfers, 1973).

2.1.3. Crack spacing

The distance at which the next crack occurs is dependent on the bond strength of the steel-concrete interface, the concrete strength, the diameter of the reinforcement, amount of tensile reinforcement present in the cross section, but also on the ability of concrete to spread stresses (Chan, 2012). A lower bond strength results in a longer transfer length and thus a larger crack spacing, as the same stress needs to be spread over a larger area of concrete. The bond of the reinforcement bar (rebar) with the paste is dependent on adhesion, friction and mechanical interlocking (Tepfers, 1973). A higher tensile strength of concrete results in a larger crack spacing as it takes a larger distance from the crack before the tensile strength is reached again to form a new crack. A smaller rebar diameter, for the same area of reinforcement, results in a larger contact area with concrete. This results in a shorter required transfer length and thus a smaller crack spacing. More tensile reinforcement in the cross section, results in a lower reinforcement stress as the applied force is spread over a larger area. Therefore, a smaller transfer length is obtained and thus a smaller spacing of cracks if the reinforcement area is increased. Lastly, the ability of concrete to spread stresses depends on the angle over which the concrete is able to spread stresses (Figure 2.4). A narrow spreading angle results in a long transfer length and therefore large crack spacing (Tepfers, 1973). The spreading is not only dependent on the concrete, but also on the orientation of the ribs of the rebar (Tepfers, 1973).

Due to the natural variability in concrete properties as mentioned before, the exact crack spacing cannot be found a priori. However, the range of this spacing is known by using upper and lower limits of the influencing factors on crack spacing. Therefore, the maximum crack spacing and minimum crack spacing are defined. The maximum crack spacing is based on the probability that, at a certain distance from the adjacent crack, the concrete stress is constant again and a new weak point is found. The minimum crack spacing is reached when no constant stress regions in the concrete are present anymore (Figure 2.3). New cracks cannot be formed and the cracking pattern is fully developed. This means that, in the regions in between the cracks, the concrete is not reaching the tensile strength (Piyasena, 2002). Upon increasing the load existing cracks increase in width. The rate at which crack widths increase is dependent on the crack spacing. As a smaller crack spacing, means that the increase in elongation is spread over more cracks. Therefore, the crack widths are smaller compared to a situation with larger crack spacing.

2.1.4. Moment-curvature

When a reinforced concrete beam is loaded in bending, the beam is compressed on the top part and elongated on the bottom part. The beam is uncracked and acts linear elastic upon loading in bending, until at one point in the tension zone the tensile strength is locally exceeded. Reaching the tensile strength occurs at a weak spot in the material (Braam and Lagendijk, 2008). The moment applied at which this first crack occurs, is called the cracking moment (M_{cr}). At the location of the crack, the reinforcing steel bridges the crack and takes over the concrete stresses. The formation of cracks lowers the bending stiffness (Figure 2.5). A further increase in the load leads to the formation of new cracks. Once the cracking pattern is fully developed, the formed cracks will widen and propagate. This leads to increased bridging stresses for the steel and a reduction of the available height for the compression zone. At a certain load the steel reaches yielding stress. This is called the yielding moment (M_{yield}). The bending stiffness of the beam reduces, due to the stiffness reduction of the rebar (Figure 2.5). Further load increments are possible until either the height of the compression zone becomes too low, leading to compression zone failure or the yielded steel reached the ultimate strain leading to rupture of the reinforcement (Braam and Lagendijk, 2008). The highest applied moment on the beam is called the ultimate bending moment ($M_{ultimate}$) (Figure 2.5).

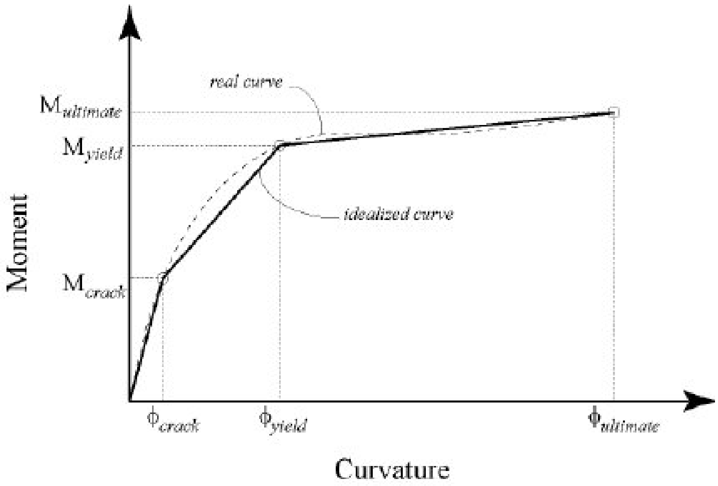

Figure 2.5: Moment curvature graph for a reinforced concrete beam subjected to bending (Baji and Ronagh, 2011).

2.1.5. Concrete cover

The concrete cover also influences the crack width and crack spacing. The concrete cover is a design parameter, which makes it an important factor in controlling crack widths (Beeby, 2005). The concrete cover (c) is the thickness of the concrete layer from the outer of the beam to the outer of the reinforcement (Figure 2.6). If stirrups are used, the concrete cover is from outer of beam to the outer of the stirrup. The concrete cover is needed in order to protect the reinforcement from ingress of deteriorating substances. Concrete is porous and therefore some ingress of substances will always occur. In addition, the concrete cover is needed to allow for sufficient transfer of stresses between concrete and reinforcement (Tepfers, 1973). Sufficient cover is present if the tensile ring can be fully developed (Figure 2.4). If the cover is too small, the tensile ring cannot be fully developed, resulting in failure of the embedded reinforcement (Tepfers, 1973). This is called splitting failure. However, it is desired to limit the concrete cover, as when reinforced concrete is used in bending the cover is decreasing the internal lever arm. The internal lever arm (z) is the lever arm over which the bending moment resistance of a cross section is determined (Figure 2.6). This is the distance between the point of application of the compression force (N_c) and the point of application of the tension force (N_s) of a cross section. The compression force is determined by the compression strength, width of the cross section (b), and height of the compression zone (x_u). The height of the compression zone of a cross section subjected to bending is the distance from the top of the beam to the neutral line (n.l.). The tension force is determined by the steel strength and the area of the reinforcement (A_s). The application point of the tension force is at distance (d) from the top of the cross section. This distance is called the effective depth (d).

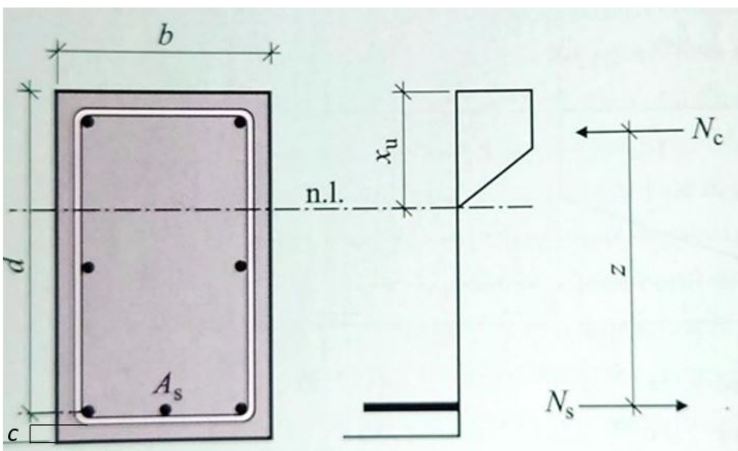

Figure 2.6: Cross section of a reinforced concrete beam with internal lever arm (z) (Braam and Lagendijk, 2008).

The increase of the internal lever arm lowers the force in the reinforcement, for the same bending moment applied on the beam. This results in a similar effect as the increase of reinforcement ratio. The reinforcement ratio is the ratio of reinforcement area relative to the concrete area of a cross section. Lower steel stress results in smaller crack spacing and therefore in smaller crack widths.

2.1.6. Effective tensile area

In the previous paragraphs it was already briefly mentioned that around the reinforcement a tensile ring is formed (Figure 2.4). The stress distribution is generally considered to be uniform if the height of the beam, and therefore height of the tensioned zone, is not too big (Braam, 2019). However, if the height of the tensioned zone is larger than the height of the tensile ring, the stresses will not be uniform over the height of the tensile area anymore (Figure 2.7). This results in a crack, which will not propagate over the full height of the tension zone. Around the reinforcement, a fully developed crack pattern can be formed, but away from the reinforcement this will not be the case (Figure 2.7). The area over which the fully developed crack pattern can be formed is called the effective tensile area ($A_{c,eff}$). The cracks from the fully developed crack pattern join into a wider crack outside the effective tensile area. This wider crack is considered uncontrolled and the cracks in the effective tensile area are considered to be controlled by the reinforcement (Braam, 2019).

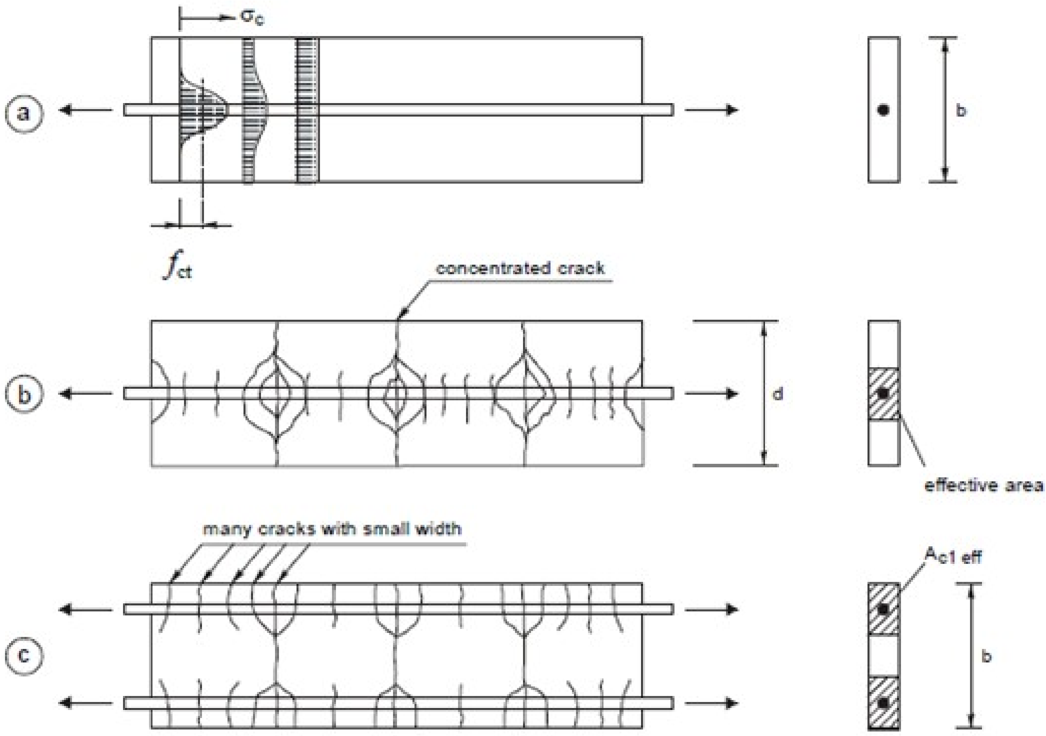

Figure 2.7: Principle of effective tensile area explained with (a) stress distributions for a high beam with reinforcement concentrated in the middle of the beam, (b) crack pattern for a high beam with concentrated reinforcement in the middle and (c) crack pattern for a high beam with reinforcement on the outsides (Braam, 2019).

Only empirical models are available to determine the height of the effective tensile area. This effective tensile area is used to determine the steel stresses and the crack widths at a certain load. The Eurocode considers the effect of the tensile member by use of the effective reinforcement ratio (*Eurocode 2: Design of concrete structures*, 2004). The effective reinforcement ratio ($\rho_{l,eff}$) is the ratio of reinforcement area in the tension zone over the effective tensile area of concrete. The effective tensile area ($A_{c,eff}$) of concrete for a beam is determined by the width (b), and the effective height of concrete (Figure 2.8). This leads to the following formula's for a beam:

$$h_{c,eff} = \min\begin{pmatrix} \frac{h}{2} \\ 2,5(h-d) \\ \frac{(h-x)}{3} \end{pmatrix} \tag{2.1}$$

$$A_{c,eff} = h_{c,eff}b \tag{2.2}$$

$$\rho_{l,eff} = \frac{A_{s,l}}{A_{c,eff}} \tag{2.3}$$

With $h_{c,eff}$ the effective height of concrete around the reinforcement, h the height of the cross section, d the effective height of the reinforcement, x the height of the compression zone, $A_{c,eff}$ the effective concrete area around the reinforcement, b the width of the cross section, $A_{s,l}$ the area of the longitudinal reinforcement, and $\rho_{l,eff}$ the effective reinforcement ratio.

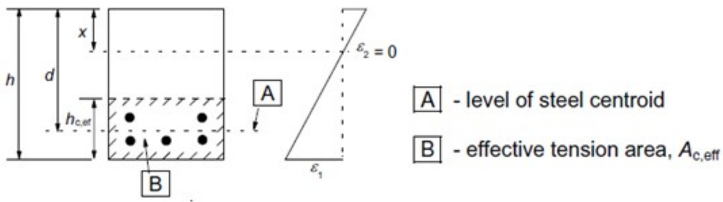

Figure 2.8: Cross section of a reinforced concrete beam with the effective tension area (*Eurocode 2: Design of concrete structures*, 2004).

2.1.7. Tension stiffening

As discussed in subsection 2.1.2, concrete between the cracks is stressed by the transfer of stresses from the steel. Therefore, concrete between cracks contributes to carrying the load. The contribution of tensioned concrete is called tension stiffening, as in design formulas this contribution is not included (Verschuur, 2018). This assumption in the design formulas is a safe approach for determining the ultimate capacity. However, the tensioned concrete is significantly contributing to the stiffness of the cross section, even when cracked (Castel et al., 2006). The flexural stiffness of the beam limits the deflection when subjected to a bending moment (Figure 2.9). A lower deflection, due to a higher stiffness, results in lower stresses and strains in the material and therefore it results in smaller cracks widths. Therefore, the tensioned and cracked concrete, that allows for the tension stiffening, is important to consider when studying crack widths.

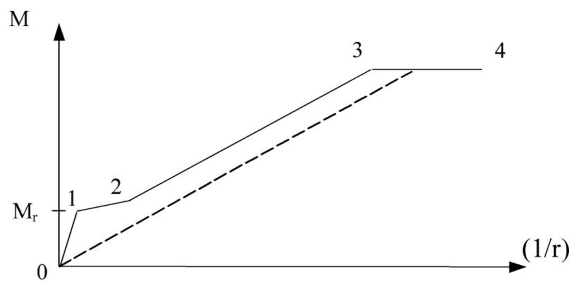

Figure 2.9: Moment-curvature graph with (solid) and without (dashed) accounting for tension-stiffening (Castel et al., 2006).

The effect of tension stiffening is dependent on the slipping of the reinforcement, as this determines the development of stresses in the concrete transferred from the reinforcement. The slipping is determined by the difference in strain of concrete and steel. This makes the tension stiffening effect dependent on the stress in the reinforcement, the Young's modulus of reinforcement, the Young's modulus of concrete, the tensile strength of concrete and the effective reinforcement ratio (Verschuur, 2018). A higher stress in the reinforcement results in a larger strain in the steel and therefore a larger difference with the concrete strain. The Young's modulus of steel and concrete are both affecting the slip, as the Young's modulus is related to the strain. This relation is not easily quantified beyond the elastic limit (Braam and Lagendijk, 2008). The effect of the tensile strength is also complicated as an increase in tensile strength is generally obtained by increasing the concrete class. Increasing the concrete class also increases in general the Young's modulus of concrete. An increase of the effective reinforcement ratio results in smaller crack spacing (see subsection 2.1.3), which thus lowers the length over which slip occurs.

2.1.8. Prediction of crack widths

From the previous subsections it becomes clear that numerous factors are of influence on the cracking behavior of reinforced concrete. Mainly the heterogeneous nature of concrete affects the cracking behavior. This makes the prediction of crack widths complex. As crack widths should not be too large, it is needed to predict crack widths when designing with concrete. Therefore, simplified models are developed to predict crack widths. These models have the following starting points in common (Goszczyńska et al., 2021):

1. The cracking moment, from which cracks will exist in the material as the tensile strength is reached.
2. The crack width, which is a function of the bending moment applied
3. The crack spacing, which is a function of the bending moment applied

Eurocode approach

One of the models to predict crack widths is the Eurocode approach. In Eurocode, crack widths are determined based on the maximum crack spacing and the mean strain difference in the reinforcing steel (ε_{sm}) and the concrete in tension (ε_{cm}). Mean strains are used as at a crack, concrete releases stored strain and reinforcing steel is additionally strained by bridging the crack (*Eurocode 2: Design of concrete structures*, 2004). This local difference of strains, between tensioned concrete and the reinforcing steel, at a crack is called slip. The difference in this mean strain is determined based on: the steel stress (σ_s), the concrete tensile strength ($f_{ct,eff}$), the effective reinforcement ratio of the tensile member ($\rho_{p,eff}$), the steel Young's modulus (E_s), the Modulus ratio of steel and concrete (α_e), and a load duration factor (k_t). The maximum crack spacing ($s_{r,\max}$) is dependent on the concrete cover (c), the bond of the reinforcement (k_1), the distribution of strains (k_2), the bar diameter (∅), and the effective reinforcement ratio ($\rho_{p,eff}$) (*Eurocode 2: Design of concrete structures*, 2004). The crack width (w_k) can be determined with:

$$w_k = s_{r,\max}\left(\varepsilon_{sm} - \varepsilon_{cm}\right) \tag{2.4}$$

$$\left(\varepsilon_{sm} - \varepsilon_{cm}\right) = \frac{\sigma_s - k_t \frac{f_{ct,eff}}{\rho_{p,eff}}\left(1 + \alpha_e \rho_{p,eff}\right)}{E_s} > 0.6\frac{\sigma_s}{E_s} \tag{2.5}$$

$$s_{r,\max} = 3.4c + 0.425 k_1 k_2 \frac{\emptyset}{\rho_{p,eff}} \tag{2.6}$$

If the spacing of the reinforcement exceeds $5(c+0.5\emptyset)$, the crack width should be limited, by applying an upper bound limit for the maximum crack spacing (*Eurocode 2: Design of concrete structures*, 2004).

Multi-layer model

The crack width relations of Eurocode can be used in the multi-layer model. The multi-layer model divides the cross section of the beam into a number of layers. Each layer is schematized as a spring (Figure 2.10). When the beam is loaded by a bending force, horizontal equilibrium should always be satisfied and therefore the sum of the forces from the springs should equal zero (Hordijk, 1991). Initially, the model assumes the neutral axis to be at central height of the beam. A strain is imposed, from which it is known that the linear elastic limit is not reached yet. This keeps the neutral axis at central height of the beam. From the stress-strain curve of the material and the strain at the middle of every layer the stress for every layer can be determined (Hordijk, 1991). With the thickness and width of the layer the force of the modelled spring can be found. If the horizontal equilibrium is satisfied, the strain is slightly increased with a small increment and once more the forces are generated and checked for horizontal equilibrium. If the equilibrium is not satisfied, the neutral axis is shifted upwards with an increment until horizontal equilibrium is found again (Figure 2.10).

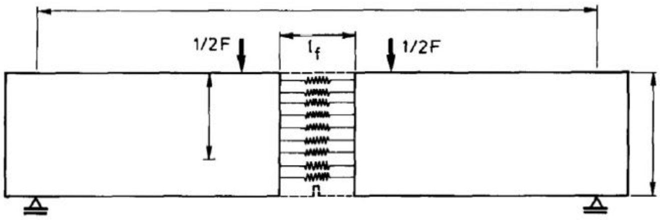

(a)

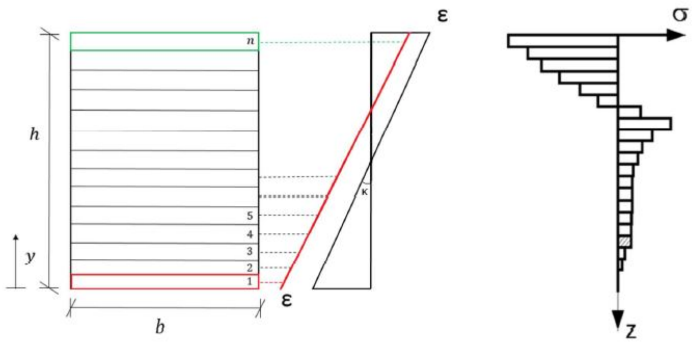

(b)

Figure 2.10: Multi-layer model with (a) layers of springs in the center of the beam and (b) shifting of the neutral axis (Hordijk, 1991; Yassiri, 2020).

This approach allows for the implementation of more complex stress-strain curves for the materials and thus also for the inclusion of the tensile softening behavior of concrete. This approach also allows to account for different material properties over the height, for example in the case of hybrid beams (Hordijk, 1991). In order to find the crack width at each applied load, different formulations can be used as the model provides the stresses and strains at specified layers. One of the formulations that can be used are the relations as provided by the Eurocode. The benefit of this multi-layer model is that at every load step the crack width can be determined (Yassiri, 2020). This is not possible with conventional approaches.

2.2. Strain Hardening Cementitious Composites (SHCC)

This section starts with explaining the material properties of SHCC. In addition, the effect of different binders, the effect of aggregates in SHCC, the effect of fiber type, the effect of fiber content, and the effect of fiber shape and orientation is discussed. Lastly, the interaction between SHCC and reinforcement is studied.

2.2.1. Material properties of Strain Hardening Cementitious Composite

Strain Hardening Cementitious Composite (SHCC), also known as Engineered Cementitious Composite (ECC), is a cementitious material with strain hardening properties. SHCC is made from a binder, fine particles, water and around 2% fibers (by volume). Usually PVA or HDPE fibers are used. These fibers help to control the crack width as they are able to bridge the cracks similar to reinforcement bars (Huang, 2017). This bridging of cracks leads to a stress transfer between fibers and the uncracked SHCC. This leads to the ductile behavior of SHCC (Figure 2.11). SHCC can have a strain capacity of 2-5% (van Zijl, 2011). Compared to conventional concrete, this is significant as conventional concrete has a strain capacity around 0.0087%. Steel can have an ultimate strain of 9-20%. Therefore, the ductility of SHCC is more comparable with steel than with conventional concrete.

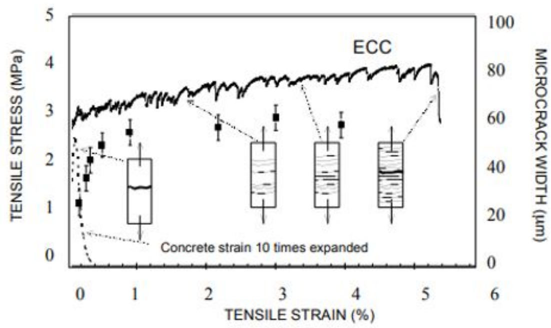

Figure 2.11: Stress-strain curve of EEC compared to conventional concrete (Li, 2008).

Upon bridging a crack with fibers of SHCC, the fracture localization in SHCC is postponed by formation of new cracks (van Zijl, 2011). New cracks are formed until the fibers, bridging a crack, fail (Fischer et al., 2007). Failure of a fiber would require the fiber to break, yield (if the fiber is ductile), or be pulled out. Due to the presence of the fibers, the crack spacing is smaller compared to conventional concrete. The crack spacing in SHCC is determined by fiber and matrix properties and the interface interaction of the fiber with the matrix. Therefore, the crack spacing of SHCC is considered to be a material property of SHCC instead of a structural property (Li and Stang, 2004).

2.2.2. Effect of binder composition

The binder used in the SHCC mix design influences the material properties. A common variation among binders is the inclusion of blast furnace slag or fly ash. The inclusion of blast furnace slag in the mix design, makes the SHCC more homogeneous and results in a smaller pore distribution in the cement. This makes the SHCC stronger in tension, but also more vulnerable to autogenous shrinkage (Lukovic, 2016). It is therefore advised to apply sufficient curing. In addition, the crack pattern changes. The inclusion of blast furnace slag resulted in larger crack spacing and larger crack widths compared to SHCC with inclusion of fly ash (van Zijl, 2011). Therefore, a lower ductility is obtained for the inclusion of blast furnace slag in SHCC, compared to the inclusion of fly ash in SHCC (Figure 2.12).

If fly ash is used, the matrix strength decreases. The presence of fly ash improves the slip of the fibers from the matrix. This postpones breaking of a fiber (van Zijl, 2011). The increased slip of fibers occurs due to a lower chemical bond between the fibers and the matrix. The overall effect is an increase in ductility of the SHCC, but a lower tensile strength (Figure 2.12).

If both fly ash and blast furnace slag are included in the mix, the ductility and the tensile strength increase. The increase in ductility is smaller compared to the inclusion of only fly ash. Additionally, the crack widths are found to increase significantly compared to the inclusion of only fly ash in the mix (van Zijl, 2011).

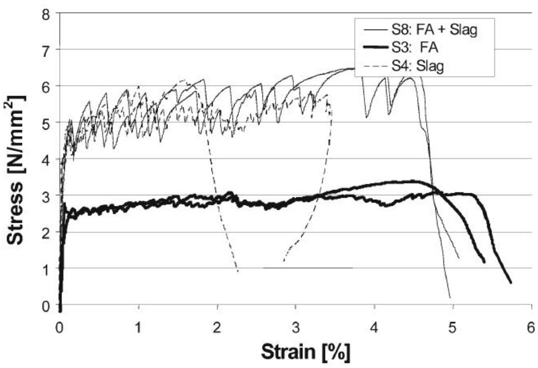

Figure 2.12: Effect of addition of fly ash or blast furnace slag to the SHCC mix (van Zijl, 2011).

2.2.3. Aggregates in SHCC

Conventional concrete includes aggregates. The main reason for this is to lower the amount of cement needed. Cement is expensive and therefore inclusion of aggregates in concrete is economically feasible (Neville and Brooks, 2010). The inclusion of the aggregates does result in a more heterogeneous material, as it includes additional material phases to the mix. Another benefit of the inclusion of aggregates in concrete is, the reduction of drying shrinkage of the concrete (Neville and Brooks, 2010). Nevertheless, aggregates are only limited used in SHCC. A study has been conducted to the use of geopolymer fine aggregates (Xu et al., 2022). Geopolymer aggregates (GPA) are artificial aggregates from industrial byproducts. Generally, GPA are weaker than natural aggregates. However, GPA allow for a stronger interface with the cement-paste, due to a larger interfacial transition zone and stronger chemical bond (Xu et al., 2022). The low strength and Young's modulus of GPA compared to natural aggregates are used to lower the cracking strength and modify fracture toughness (Xu et al., 2022). Therefore, GPA can be considered as additional flaws in the matrix. This can be beneficial in crack controlling, as a finer cracking pattern is formed. Different from natural aggregates, the cracks in SHCC with GPA can run through the GPA (Xu et al., 2022). Additionally, the inclusion of GPA results in bridging of cracks by GPA (Figure 2.13). This bridging of cracks by GPA leads to a higher tensile strength and a larger ductility of SHCC with inclusion of GPA, compared to ordinary SHCC (Xu et al., 2022).

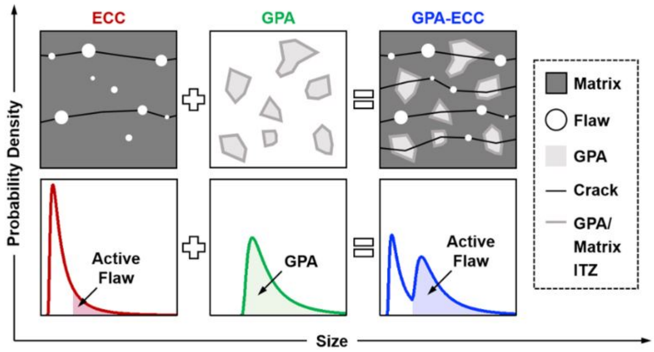

Figure 2.13: Crack bridging effect with GPA (Xu et al., 2022).

Besides GPA, small aggregates (for example sand or limestone powder) can be included in the mix. Inclusion of fine sand is found to increase the first cracking strength and toughness of SHCC (van Zijl, 2011). In addition, a decrease in ductility is found. However, the average crack width is less sensitive to this, as an increase of aggregate to cement portion (by mass) from 1.0 to 1.2 does not result in a significant change in the average crack width (van Zijl, 2011). The effect on the maximum crack widths have not been reported. The effect of the inclusion of small aggregates on the maximum crack widths is of importance, as this is determining the susceptibility to penetration of aggressive substance. By inclusion of small aggregates the crack spacing is almost doubled (van Zijl, 2011). Upon inclusion of coarse aggregates in SHCC is found that, the number of cracks decrease by an increase in content of coarse aggregates (Ueda and Kawamoto, 2017). This means that larger cracks are formed and there is less strain-hardening behavior in the SHCC. This also means that, the ductility of the material is decreased compared to SHCC with only inclusion of fine aggregates (Magalhães et al., 2010). Lastly, it was found that both coarse and fine aggregates in the SHCC mix, show a similar crack formation stage (Magalhães et al., 2010). The difference in cracking behavior occurs when SHCC with coarse aggregates localizes cracks at a lower deflection and stress, compared to SHCC with fine aggregates (Figure 2.14).

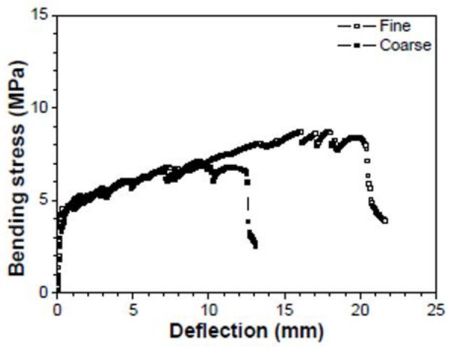

Figure 2.14: Stress-deflection curve for SHCC with fine or coarse aggregates in the mix (Xu et al., 2022).

2.2.4. Fiber type

SHCC contains fibers. The properties of SHCC, such as ductility, Young's modulus and tensile strength dependent partly on the fiber type, amount of fibers and fiber size (Bentur and Mindness, 2007). Different fiber types result in different behavior of the engineered cementitious composites (Figure 2.15).

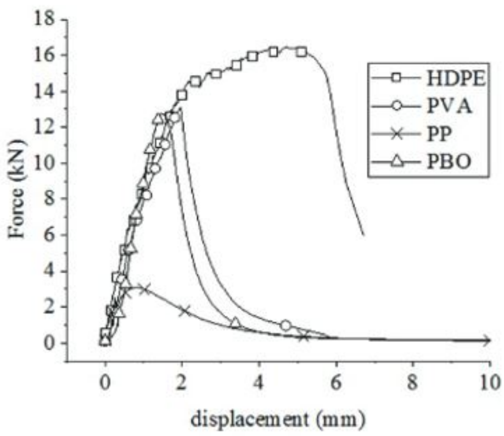

Figure 2.15: Force-displacement curve of $160x40x40mm^3$ SHCC samples with different fiber types in three-point bending test (Al Ghazali et al., 2017).

The bridging of cracks by fibers can only occur if the tensile strength of the fiber is larger than the tensile strength of paste (Bentur and Mindness, 2007). In order to increase the strength of the composite, the Young's modulus of the fibers should be equal or higher compared to the matrix. In addition, a higher Young's modulus of fibers enhances the crack width controlling behavior of the composite, as the elongation difference between fiber and paste is controlled (Bentur and Mindness, 2007). Lastly, the fiber-matrix bond is important, as the fibers should not be pulled out when bridging a crack. The pulling out resistance is dependent on the size and shape of the fiber (van Zijl, 2011). The bonding strength of the interface between fiber and paste is dependent on mechanical interlocking, adhesion and friction (Bentur and Mindness, 2007). Based on the found effects of fiber properties on the composite, multiple fiber types have been used in mix designs (Table 2.1).

Table 2.1: Properties of different fibers used in SHCC (Al Ghazali et al., 2017).

Fibre type	Diameter (μm)	Specific gravity	Tensile strength (GPa)	Elastic modulus (GPa)	Ultimate elongation (%)
Acrylic	20–350	1.16–1.18	0.2–1.0	14–19	10–50
Aramid (Kevlar)	10–12	1.44	2.3–3.5	63–120	2–4.5
Carbon (PAN)	8–9	1.6–1.7	2.5–4.0	230–380	0.5–1.5
Carbon (Pich)	9–18	1.6–1.21	0.5–3.1	30–480	0.5–2.4
Nylon	23–400	1.14	0.75–1.0	4.1–5.2	16–20
polyester	10–200	1.34–1.39	0.23–1.2	10–18	10–50
Polyethylene	25–1000	0.92–0.96	0.08–0.60	5	3–100
Polyolefin	150–635	0.91	275	2.7	15
Polypropylene	20–400	0.9–0.95	0.45–076	3.5–10	15–25
PVA	14–650	1.3	0.8–1.5	29–36	5.7
Steel (for comparison)	100–1000	7.84	0.5–2.6	210	0.5–3.5
Cement matrix	—	1.5–2.5	0.003–0.007	10–45	0.02

Note
a The values in the table are for fibres that are commercially available. They may vary considerably from manufacturer to manufacturer.

Currently, most SHCC mixes use PVA fibers, as they have a high tensile strength and good bonding properties. The good bonding properties are obtained from the hydrophilic behavior of the PVA fibers in SHCC (Bentur and Mindness, 2007). A downside of the PVA fibers is the rough surface. This rough surface leads to stress concentrations and damages the matrix when pulled out. Therefore, PVA fibers are oil coated. Oil coating the PVA fibers increases the complementary energy (Figure 2.16). Increasing the complementary energy results in a lower frictional and chemical bond with the cement paste (van Zijl, 2011).

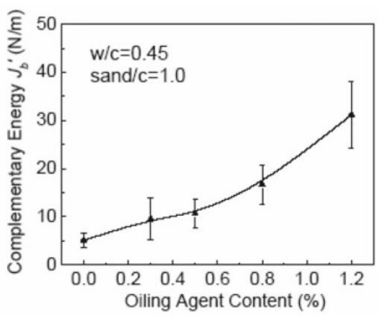

Figure 2.16: Complementary energy with respect to different oiling agent contents for a water to cement ratio (w/c) of 0.45 and sand to cement ratio (sand/c) of 1.0 (van Zijl, 2011).

The complementary energy is the area on the left side of the stress-displacement graph (hatched area in figure 2.17). The stored energy, also known as crack tip toughness, is the area under the curve (white area under curve in figure 2.17). As long as the complementary energy is higher than the crack tip toughness, the crack grows in length instead of width (Li et al., 2002). Coating the PVA fibers with oil reduces the bond and thereby reduces the crack spacing, compared to SHCC with PVA fibers without coated in oil. The reduction in crack spacing results in smaller crack widths. Oil coating the PVA fibers works up to an oiling agent content of 1.2%. A higher oiling agent content reduces the tensile capacity of SHCC (van Zijl, 2011).

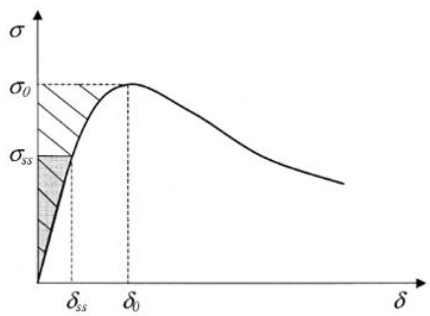

Figure 2.17: Stress-displacement curve with the stored and complementary energy(Li et al., 2002).

2.2.5. Fiber content

The amount of fibers is of influence on the crack controlling behavior of SHCC. The amount of fibers in a material is called the fiber content, which is the volume of fibers relative to the total volume of SHCC. The presence of fibers enhances the crack width controlling behavior of the composite by bridging the initial cracks. Increasing the amount of fibers results in more fibers that can bridge a crack (Bentur and Mindness, 2007). This enhances the crack width controlling behavior of the composite. In addition, increasing the fiber content results in a higher tensile strength and a larger ductility of SHCC (Bentur and Mindness, 2007). The effect of increasing the fiber content on the average crack width decreases at a higher fiber content (Figure 2.18). This is independent of the fiber type (Al Ghazali et al., 2017). Later, it was found that a too high fiber content leads to the interaction of fibers. The fiber interaction theory implies that there are so much fibers present that they start touching each other in the mix (van Zijl, 2011). This results in the higher probability of large flaws in the matrix. Therefore, if the fiber content is increased from 2% to 2.5% the crack widths do not significantly change anymore (van Zijl, 2011).

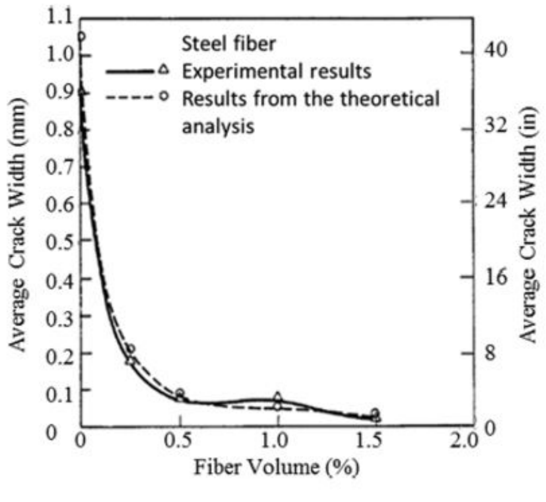

Figure 2.18: Effect of fiber volume on average crack width (Grzybowski and Shah, 1990).

2.2.6. Fiber shape and orientation

The fiber length and orientation in the cement paste are both of influence on the behavior of SHCC (Bentur and Mindness, 2007). If nanometer scaled fibers are used in SHCC, this leads to an increase in tensile strength, compared to conventional concrete. This increase in tensile strength is attributed to the bridging of micro cracks. Therefore, the stress at which macro cracks are formed is increased (Mechtcherine et al., 2018). However, nanometer scaled fibers are unable to bridge macro cracks, leading to a low ductility. If larger fibers (in the order of millimeters) are used, the cracking strength is not affected. Millimeter scaled fibers lead to increased toughness due to the fiber bridging effect, compared to SHCC with nanometer scaled fibers (Mechtcherine et al., 2018). In addition, for the millimeter scaled fibers it is found that, longer fibers have a better bridging effect. This is attributed to the longer embedment length of a longer fiber. Therefore, the longer fiber can spread the stress over a longer embedded length (Bentur and Mindness, 2007). This leads to a higher pull-out resistance of the fiber in the matrix. A downside of longer fibers is the lower workability of the mix (Tai, 2015). The improved bridging effect of longer fibers is not solely due to the increased embedment length. The orientation of a fiber in the composite is also of influence. The orientation of the fiber is dependent on the size of the fiber. Longer fibers, up to 12 mm, tend to align better with the axis of the beam (Bentur and Mindness, 2007). Fibers tend to orientate 3D (the 3D effect) if all three dimensions of the element exceed the length of the fiber (Bentur and Mindness, 2007). The 3D effect is the possibility of the fiber to be inclined on a 3D plane (Figure 2.19). The 3D effect results in a lower bending strength and reduced deformation capacity (Toshiyuki et al., 2013). Additionally, the 3D effect results in an increase in crack spacing and crack width compared to specimens 2D orientated fibers (Toshiyuki et al., 2013).

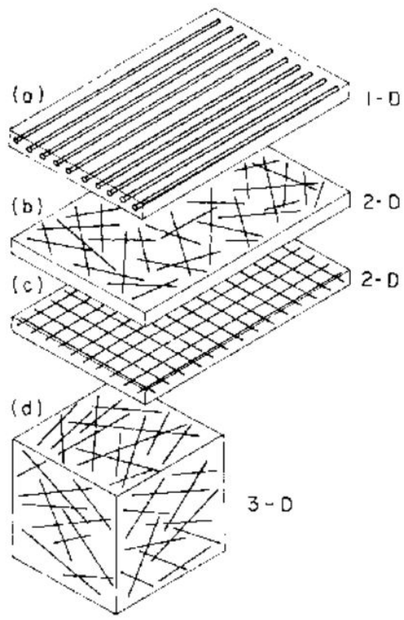

Figure 2.19: Fiber orientation in (a) 1-D, (b) random 2-D, (c) organized 2-D and (d) random 3-D space (Bentur and Mindness, 2007).

Determining the orientation of PVA fibers is difficult, as there is no non-destructive practical applicable method to quantify the alignment (Visser and Van Zijl, 2007). One of the reasons for this, is the low color contrast of PVA fibers with the matrix. However, with complicated equipment it is possible to assess the dispersion of PVA fibers (Visser and Van Zijl, 2007). The orientation of fibers affects the Young's modulus of the composite as the fibers are less effective under an angle (Visser and Van Zijl, 2007). Computational studies have been performed to study the effect of fiber orientation (Yao and Leung, 2017). From this study it is found that, the bridging stress of a fiber is increased with increasing the fiber inclination (Figure 2.20). This increase in bridging stress occurs as the inclined fiber is not pulled in axial direction, but under an angle when a crack is opening. This is called the fiber orientation effect (Wu and Li, 1992). Up to 60 degrees of fiber inclination, the fibers act quite similar. Beyond 60 degrees of inclination, spalling becomes governing. Spalling of the fiber results in a lower bridging stress (Yao and Leung, 2017).

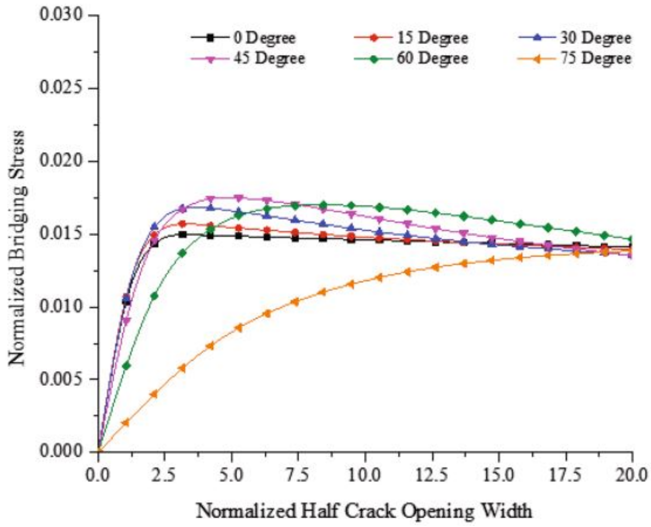

Figure 2.20: Computed bridging stress related to crack width for different fiber orientations subjected to small imposed deformation of the fiber (Yao and Leung, 2017).

The increase in bridging stress for inclinations up to 60 degrees cannot solely be attributed to the fiber orientation effect. The snubbing effect also plays a major role in the increase of the bridging stress for inclined fibers (Yao and Leung, 2017). Due to inclination, the fiber is loaded in tension and bending (Figure 2.21). Bending of the fiber results in deformation of the fiber, which increases the pull-out resistance. The higher pull-out resistance, allows for higher bridging stresses to occur. The deformation of the fiber in the cement paste is called the snubbing effect.

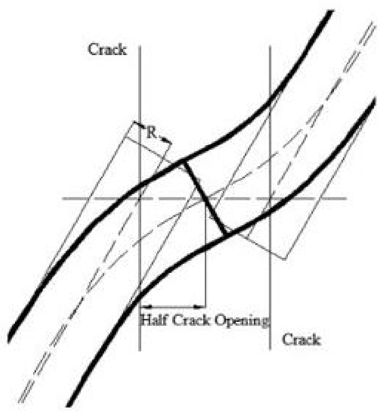

Figure 2.21: Deformation of a fiber due to bending and tension forces (Yao and Leung, 2017).

This snubbing effect is more pronounced for larger deformations. Therefore, fibers behave differently for larger crack widths compared to smaller crack widths (Yao and Leung, 2017). It has also been found that, if fibers are stiffer than cement-paste, the snubbing effect increases (Yao and Leung, 2017). The bigger the difference in stiffness with the paste, the larger the snubbing effect (Figure 2.22). This increase in snubbing effect for relatively stiffer fibers can be attributed to a higher bending component, compared to fibers with less difference in stiffness with the cement paste. A similar effect is found for shorter fibers, which are stiffer in bending, compared to longer fibers. Even more, the snubbing effect reduces with an increasing embedment length as the axial component increases relatively to the bending component (Yao and Leung, 2017). Additionally, it was found that smaller crack spacing is obtained when a large snubbing effect is present (Wu and Li, 1992). For a high snubbing effect, the snubbing effect is dominant over the fiber orientation effect (Wu and Li, 1992).

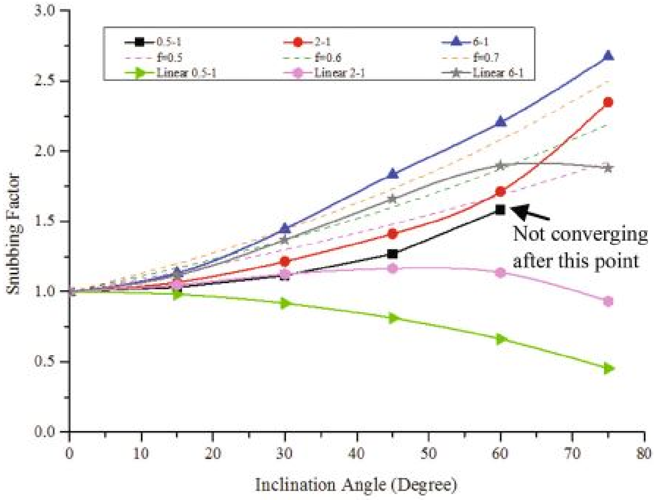

Figure 2.22: Effect of increasing the fiber stiffness relative to the cement-paste stiffness on the snubbing effect for different fiber inclination angles (Yao and Leung, 2017).

2.2.7. SHCC and Reinforcement interaction

Even with the strain-hardening capacity of SHCC, the tensile strength is similar to conventional concrete and much lower than the strength of reinforcement steel. Therefore, steel reinforcement is used to improve the tension bearing capacity. In addition, the reinforcement contributes to the crack width control (Sunaga et al., 2020). Fibers and reinforcement both bridge cracks. Therefore, the bridging stresses are shared among fibers and reinforcement. The effect of fibers on the reinforcement stress is dependent on the fiber content. A higher fiber content results in smaller crack widths at the same steel strain. Or vice versa, due to the presence of 1%-2% fibers, the steel strain is lower at the same crack width compared to a situation without fibers (Figure 2.23). It should be noted that, the average crack widths are used to make these conclusions, whereas the maximum crack width is determining the susceptibility to penetration of aggressive substances.

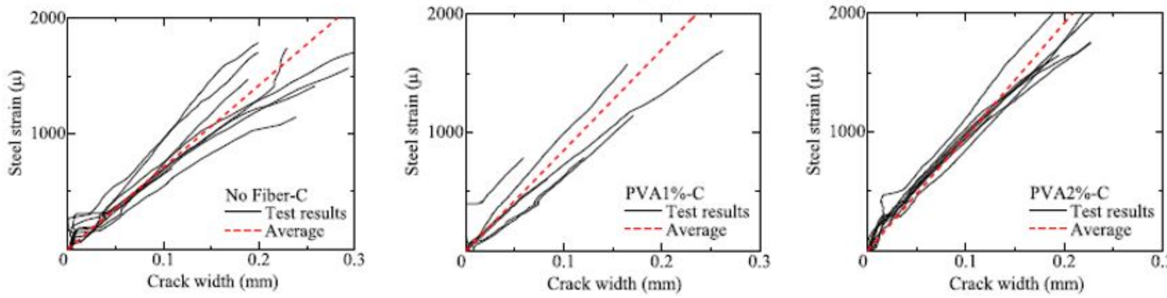

(a) (b) (c)

Figure 2.23: Steel strain with respect to crack width for (a) no fibers, (b) 1% PVA fibers and (c) 2% PVA fibers (Sunaga et al., 2020).

The effects of fibers and reinforcement on the crack width are dependent on their bridging stresses (Sunaga et al., 2020). In a tensile member with one reinforcement bar, the maximum crack width can be predicted based on the difference between the average strain of the reinforcement and the cement-paste (*Eurocode 2: Design of concrete structures*, 2004). This average strain difference between reinforcement and SHCC is smaller, due to the increased strain capacity of SHCC, compared to the average strain difference between reinforcement and conventional concrete. However, the crack width prediction based on a tensile member requires the distribution of stresses between the activated fibers and the reinforcement. A uniform fiber dispersion is assumed in this distribution of stresses (Sunaga et al., 2020). Additionally, the combination of reinforcement and SHCC results in increased bonding strength of the reinforcement (Chen et al., 2020). This effect can be attributed to the crack controlling behavior of the SHCC with fibers and the ability of the matrix to fully embed the reinforcement, without flaws from aggregates (Chen et al., 2020). Due to the crack controlling behavior of the SHCC, cracks that are created by slipping of the reinforcement are directly bridged by fibers in the cement paste (Li, 2008).

2.3. Hybrid Beams with SHCC layer in the Tension Zone

Concrete beams with a bottom layer of SHCC is called a hybrid beam. Besides the different material properties as already described in earlier sections, interaction between the two materials is present. Therefore, their interface is also of interest. Additionally, the difference in drying shrinkage is discussed, followed by a discussion of hybrid reinforced beams from previous studies. After this, general size effects will be addressed, followed by a discussion of the effect the roughness of reinforcement.

2.3.1. Interface layer

Different from an ordinary reinforced concrete beam, a hybrid R/SHCC beam has a concrete-SHCC interface. If the interface is very strong, a rigid connection is formed between the two stacked beams (Hartsuijker, 2016). If the interface is weak, no connection is present and the stacked beams deform independent of each other resulting in difference in elongations (Figure 2.24). These differences in elongations are restrained in case of a strong interface, which means that shear stresses are formed at the interface (Hartsuijker, 2016). The stiffness for two rigidly connected beams (I_{rigid}) can be determined with:

$$I_{\text{rigid}} = \frac{1}{12}b(2h)^3 = \frac{4}{6}bh^3 \tag{2.7}$$

With the width (b) and height ($2h$) of the beam. The stiffness between two weakly connected beams (I_{weak}) can be determined with:

$$I_{\text{weak}} = 2\frac{1}{12}b(h)^3 = \frac{1}{6}bh^3 \tag{2.8}$$

The rigid connection between the stacked beams results in a four times higher bending stiffness, compared to a weak interface. In addition, the strength of the rigidly connected beam is two times higher, compared to the weakly connected beams, as the applied forces are divided over the larger stiffness (Hartsuijker, 2016).

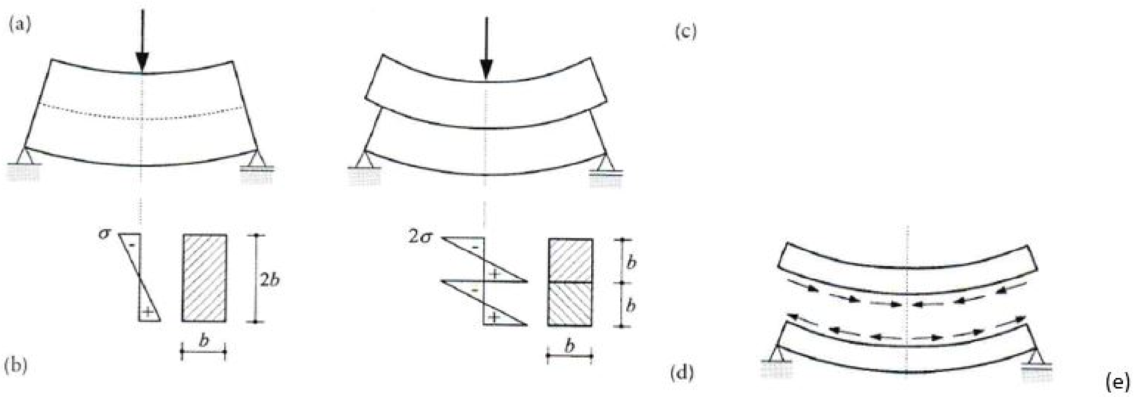

Figure 2.24: Two beams (a) rigidly connected, with (b) corresponding bending stresses (σ) over cross sectional height (2b). Two beams (c) without connection stacked, with (d) corresponding bending stresses over cross sectional height and (e) shear interaction stresses between two stacked beams to compensate for elongation differences (Hartsuijker, 2016).

Therefore, the bonding strength of the interface is of importance for the structural behavior of the beam. The bonding of two surfaces depends on three aspects: chemical adhesion of the materials, friction and if protruding elements are present on dowel action (Mohamad and Ibrahim, 2015). These aspects interact with each other and this also affects the bond strength. The chemical adhesion is dependent on the matrices (presence of pores) and chemical composition of the materials (Mohamad and Ibrahim, 2015). The bonds are established by Van der Waals forces. This bond allows for the transfer of shear forces, even if the surface is smooth (Randl, 2013). The main parameter determining this bond is the contact surface area (Randl, 2013). This area is dependent on the presence of pores and the roughness of the surface. A more porous or rougher surface leads to a larger contact surface area. For concrete to concrete bonding the chemical adhesion is found to be the major factor for interface bonding (Mohamad and Ibrahim, 2015). However, the chemical bond only allows for small slip up to 0.05 mm (Randl, 1997). Beyond this slip, the bond fails. The friction of the interface is dependent on the surface roughness and the presence of a normal pressure. A rougher surface enhances mechanical interlocking (Randl, 2013). The bonding surface can be classified based on its roughness in the following categories (*Eurocode 2: Design of concrete structures*, 2004:

- Very smooth (cast against steel formwork)
- Smooth (untreated, $R_a < 1.5mm$)
- Rough (treated, $R_a > 1.5mm$)
- Very Rough ($R_a > 3mm$)

R_a is the average deviation of the surface compared to the mean line of the surface (Figure 2.25). If the roughness increases, a higher shear strength is obtained due to mechanical interlocking (Lukovic, 2016). However, normal pressure is needed in order to establish friction. It was found that, an increase of the normal pressure from 0 to 0.5 N/mm^2 leads to an increase in the shear strength from 1.89 N/mm^2 to 4.69 N/mm^2 for conventional concrete (Mohamad and Ibrahim, 2015). If the normal pressure is increased to 1.5 N/mm^2, the shear strength increases up to 6.42 N/mm^2 for a steel brushed roughened surface (Mohamad and Ibrahim, 2015).

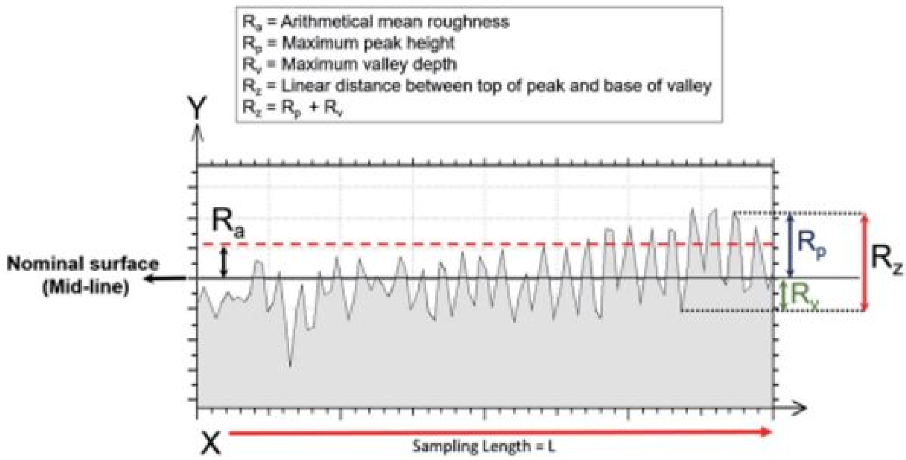

Figure 2.25: Surface roughness expressed using the mean R_a (Tekçe et al., 2018).

The dowel action is dependent on the presence of protruding elements at the bonding surface, such as steel dowels or steel stirrup reinforcement. A transfer of shear stresses at the interface, leads to slip of the interface and opening of the joints (Randl, 2013). This results in differential lateral displacement of the reinforcement end protruding the interface. This difference in lateral displacement of the steel ends, results in bending stresses in the reinforcement. The bending resistance of the steel limits the deformation of the steel. This is called dowel action. Besides bending of the steel, the steel is also subject to shearing and kinking. Kinking is of relevance when the lateral displacement is big (Randl, 2013). However, it is not common that kinking or shearing becomes governing in design, as a big lateral displacement results in crushing of the concrete. If multiple protruding elements are present, cooperation occurs after slip activation of the protruding reinforcement (Randl, 2013). However, the spacing of the reinforcement should not be too small, as bending of the steel is preferred (Randl, 2013). Bending of the steel leads to a large lateral displacement, which allows the structure to warn before the interface fails. On top of the dowel action, the friction of the interface is increased due to the protruding steel. This can be attributed to clamping forces (Mohamad and Ibrahim, 2015). The opening of the joint results in tensile stresses in the protruding reinforcement, which results in compressive stresses on the interface in order to restore vertical force equilibrium (Figure 2.26). Lastly, steel protruding prevents the interface from sudden failure, which is the case without protruding steel.

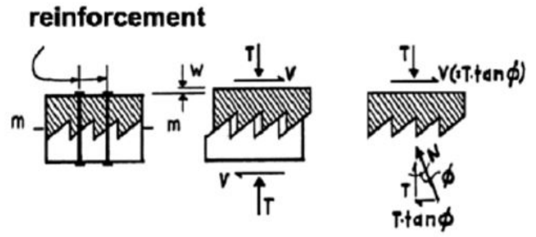

Figure 2.26: Shear friction with protruding reinforcement, indication of the joint opening (w), indication of mean roughness level (m), shear forces (v) and normal force (T) (Randl, 2013).

The chemical adhesion, friction and dowel action also interact with each other. Upon increasing the roughness of the interface, the chemical bond can be weakened (Randl, 2013). Therefore, roughness treatment can decrease the chemical adhesion. It is therefore not evident that a rougher surface results in an increase in bond strength (Zhou, 2011). Additionally, protruding elements are not beneficial in all cases. The slip activation of the dowels result in crushing of concrete and therefore also in (micro)cracking of the interface. This decreases the chemical bond (Randl, 2013). This means that, when one of the bonding strength parameters reaches its maximum, the others might not. Based on the slip of the interface, different bonding parameters are dominant for the bonding strength (Randl, 2013). In case of a small slip (smaller than 0.05 mm) a brittle bond is obtained. The bond strength is a combination of adhesion and friction and allows for a high bond strength. This brittle bond is thus without consideration of possible protruding reinforcement. The following formula can be used for the brittle bond (*Eurocode 2: Design of concrete structures*, 2004):

$$\tau_{Rd} = c_a f_{ctd} + \mu \sigma_n < 0.5 \nu f_{cd} \tag{2.9}$$

$$\nu = 0.6 \left(1 - \frac{f_{ck}}{250}\right) \tag{2.10}$$

c_a and μ are factors depending on the surface roughness. This formula also includes the shear strength of the interface (τ_{Rd}), the tensile design strength of concrete (f_{ctd}), the external compressive pressure (σ_n), the design strength of concrete in compression (f_{cd}), and the characteristic compression strength of concrete (f_{ck}). ν is a strength reduction factor for concrete in a diagonal strut. If protruding steel is present, a ductile bond, which allows for larger slip, is obtained. This is the combination of mechanical interlocking, friction and dowel action. The following formula can be used for this ductile bond (*Eurocode 2: Design of concrete structures*, 2004):

$$\tau_{Rd} = c_r f_{ck}^{1/3} + \mu \left(\sigma_n + \rho k_1 f_{yd}\right) + k_2 \rho \sqrt{f_{yd} f_{cd}} < \beta_c \nu f_{cd} \tag{2.11}$$

$$\nu = 0.55 \left(\frac{30}{f_{ck}}\right)^{1/3} < 0.55 \tag{2.12}$$

This formula includes the roughness of surface (c_r), the coefficient of friction (μ), the joint reinforcement ratio ($\rho = A_s / A_{c,shearplane}$), the efficiency for tensile force activation (k_1), the external compressive pressure (σ_n), the flexural resistance factor of reinforcement (k_2), the design yielding strength of steel (f_{yd}), the correction factor for the angle of the diagonal strut in concrete (β_c), and a reduction factor for concrete strength in a diagonal strut (ν).

A stronger bond does not necessarily mean that crack widths are better controlled. Similar cracking patterns are found for a grooved and a smooth profiled interface for a 200 mm high hybrid R/SHCC beams (Figure 2.27). Based on these cracking patterns, it is concluded that, a grooved surface in a hybrid R/SHCC beam does not improve the crack distribution (Singh, 2019). Earlier it was stated that a grooved interface does improve friction, but that it also shortens the bonding length, resulting in larger stress concentrations (Lukovic, 2016). A smooth interface layer allows for partial delamination in SHCC repair patches. Partial delamination of the interface is beneficial in SHCC repair patches, as it releases stress, which allows for better crack width control (Lukovic, 2016). However, too large delamination leads to a reduced bearing capacity of the 200 mm high hybrid R/SHCC beams (Singh, 2019).

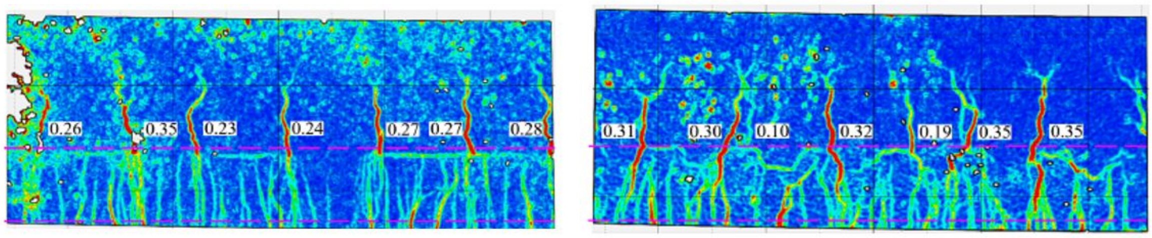

(a) (b)

Figure 2.27: Contour plot of strains showing crack widths (in mm) in a R/SHCC beam with (a) a smooth interface and (b) a profiled interface (Singh, 2019).

The bond is also affected by the execution. Contamination of the concrete surface prior to casting and bad climate conditions (for example low humidity) decrease the bond strength (Randl, 2013). Additionally, bad roughening methods can lead to surface cracks, which decreases the bond strength (Randl, 2013). Lastly, attention should be paid to the quality of the concrete mix and the edge zones of the specimen to prevent constraining stresses (Randl, 2013).

2.3.2. Drying shrinkage

Cementitious materials are fluid when casted, but harden over time. By hardening, the material develops strength. Hardening occurs due to hydration of the cement (Neville and Brooks, 2010). During the hardening process, the stored water in the capillary pores is used for hydration of the cement. By emptying of the capillary pores, suction occurs. This suction leads to narrowing of the pores, which leads to shrinkage (Neville and Brooks, 2010). The emptying of the pores is not only due to the hydration process, but can also come from evaporation to the environment or suction from a dry porous material that is present (Neville and Brooks, 2010). The extent of shrinkage of the cementitious material is dependent on the mixture and presence of aggregates, as aggregates restrain the shrinkage locally (Neville and Brooks, 2010). The mixture is of influence on the pace of the hydration. A faster hydration process results in faster emptying of the capillary pores, and therefore in larger shrinkage (Neville and Brooks, 2010). SHCC has a high binder content, and therefore a fast hardening process. Additionally, SHCC is often made without coarse aggregates. Both the high binder content and the lack of aggregates result in high shrinkage of SHCC (Jang et al., 2019). For conventional concrete the amount of shrinkage is smaller, due to the presence of aggregates and a lower binder content. The effect of the high shrinkage for SHCC results in the danger of cracking before the element is even loaded (Jang et al., 2019). The cracking occurs as the strength is still low at an early age and the shrinkage is restrained by already hardened paste (Neville and Brooks, 2010). Especially when the surface of SHCC cracks, it can affect the concrete-SHCC interface in a hybrid beam (Jang et al., 2019). The conventional concrete can penetrate the cracks, but the shrinkage rate of the partly hardened SHCC and yet to harden conventional concrete differs (Figure 2.28). This can result in delamination of the interface (Jang et al., 2019). Therefore, it is important to cure the SHCC after casting and to use a proper mix design for SHCC. In addition, experiments have been conducted, in order to investigate the effect of replacing ordinary cement by calcium sulfoaluminate expansion admixture (CSA-based EXA) on the shrinkage of SHCC (Jang et al., 2019). It is found that, the shrinkage reduces by replacing ordinary cement by CSA-based EXA. However, at early age, expansion occurs in the SHCC with CSA-based EXA (Figure 2.28). This expansion needs to be controlled, to prevent compressive failure (Jang et al., 2019). In order to limit the expansion, 10% replacement of cement by CSA-based EXA is used. A different study showed that the compressive strength of SHCC increases with CSA-based EXA replacement due to smaller pores in the matrix (Choi and Yun, 2013). However, another study showed that the compressive strength reduces, due to the presence of microcracks and a weak interfacial zone in the matrix (Meddah et al., 2011). Therefore, the effect of CSA-based EXA replacement on the compressive strength of SHCC is inconclusive. The tensile strength and early crack width controlling behavior show more promising results when CSA-based EXA is used in SHCC (Jang et al., 2019). However, this is only tested on small scaled samples. Therefore, additional study to the material behavior of SHCC with CSA-based EXA is needed.

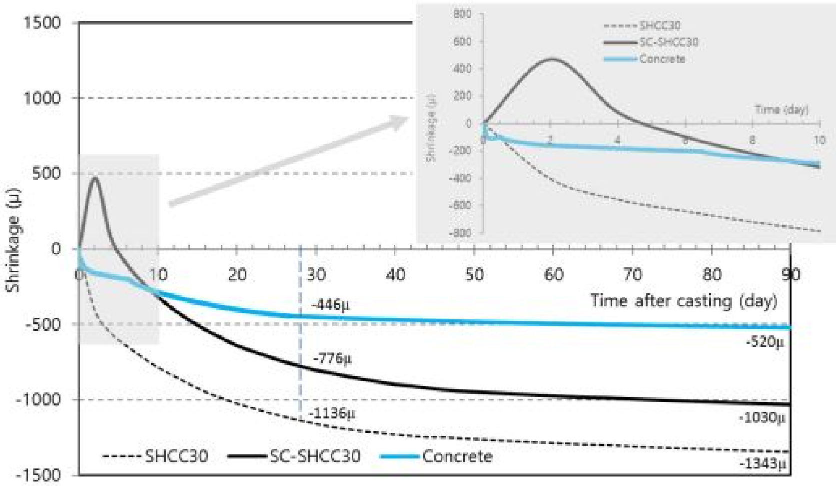

Figure 2.28: Shrinkage over time for SHCC, concrete and SHCC with CSA-based EXA replacement (Jang et al., 2019).

2.3.3. Hybrid reinforced beams

Hybrid beams with a height of 200 mm have been studied by (Huang, 2017) & (Singh, 2019). These beams have a 70 mm bottom layer of SHCC, in which the longitudinal reinforcement is embedded. On top of the SHCC layer, regular concrete is cast. These beams are called hybrid reinforced SHCC beams (hybrid R/SHCC beams). Reinforced concrete beams (RC beam) of the same height are used as reference (Figure 2.29).

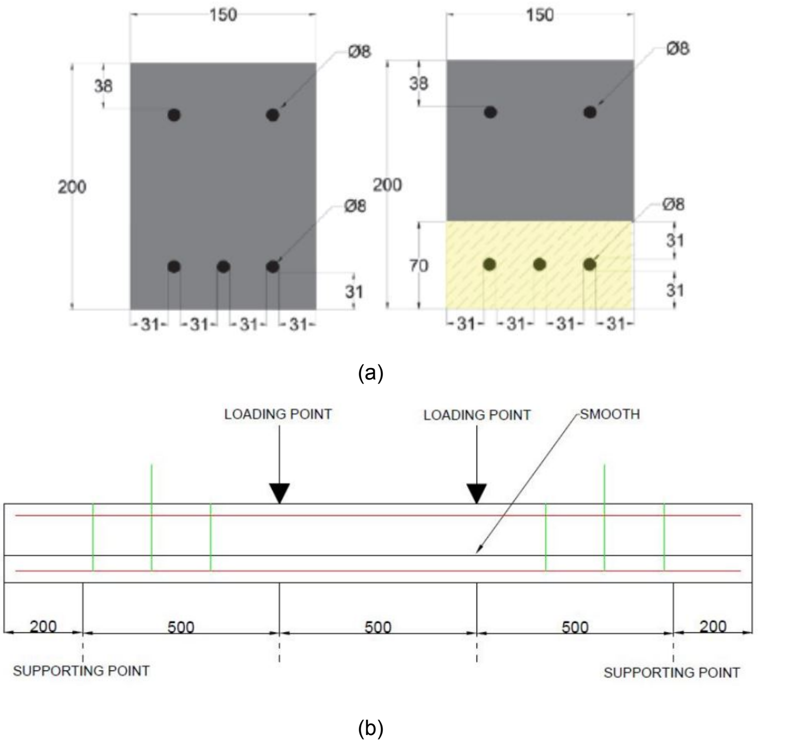

Figure 2.29: Schematic presentation of (a) cross sections of (left) 200 mm high reinforced concrete beam, (right) 200 mm high hybrid R/SHCC beam and (b) experiment design (Singh, 2019).

It was found that, the use of a hybrid R/SHCC beam of 200 mm height, with a smooth concrete-SHCC interface, improved the control of crack widths when loaded in bending, compared to an ordinary 200 mm high reinforced concrete beam (RC200) (Huang, 2017; Singh, 2019). In addition, the load bearing capacity of the hybrid beam increased to 77 kN, compared to the 62 kN of the reinforced concrete beam (Figure 2.30). The load at which the 0.3 mm crack width criteria is reached, increased from 39 kN (RC200) to 71 kN (H200) (Singh, 2019). Thereby, the hybrid beam is able to control the maximum crack width, for a 0.3 mm crack width limit, up to 109% of the yielding load, whereas the reinforced concrete beam is able to control the maximum crack width up to 76% of its yielding load. The deformation capacity of the hybrid R/SHCC beam is similar to the reinforced concrete beam.

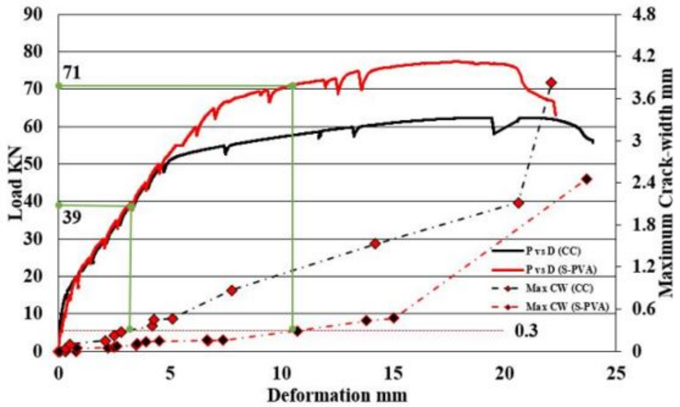

Figure 2.30: Load-deformation and deformation-crack width plots of RC200 and R/SHCC 200 mm high beam (Singh, 2019).

Additionally, the cracking pattern for the hybrid R/SHCC beam differed from the RC beam (Figure 2.31). The first crack is formed at 10kN load for the hybrid beam, whereas this is at 15kN load for the reinforced concrete beam. After the first crack is formed, the SHCC layer showed a dense cracking pattern, whereas the reinforced concrete beam developed less cracks (Figure 2.31). In addition, the hybrid R/SHCC beam developed 7 propagated cracks in the concrete layer, whereas this were only 4 cracks in the reinforced concrete beam. Both the hybrid beam and the reinforced concrete beam are reported to fail in the compression zone. Lastly, delamination of the concrete-SHCC interface of the hybrid beam is reported (Singh, 2019).

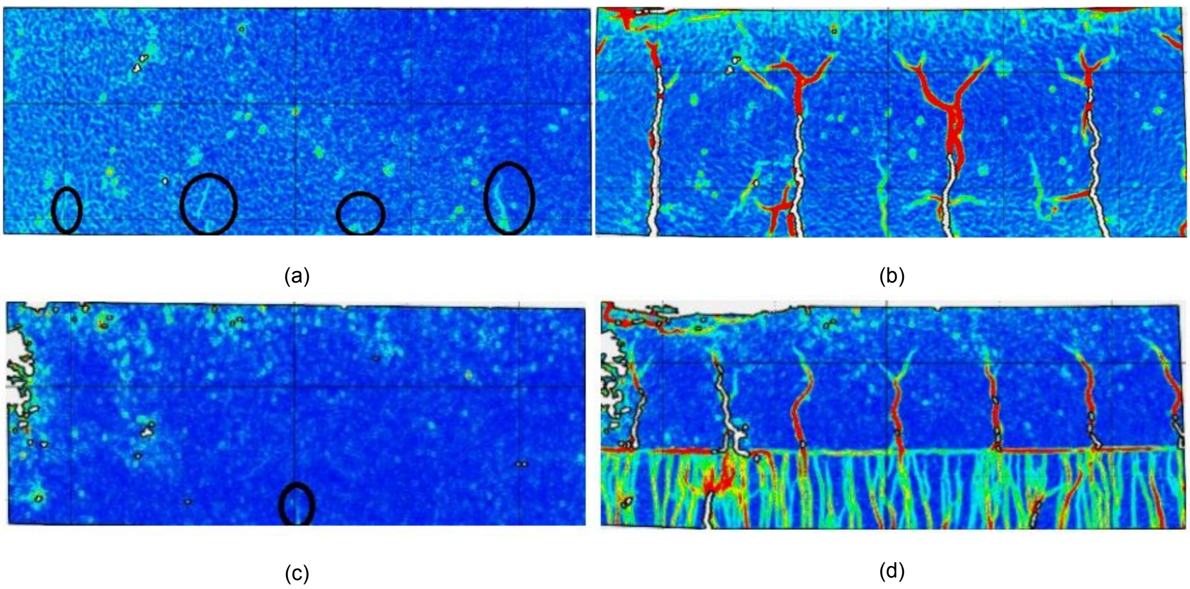

Figure 2.31: Contour plots of: (a) first crack in reinforced concrete beam, (b) final cracking pattern of the reinforced concrete beam, (c) first crack in SHCC for the hybrid beam and (d) final cracking pattern for the hybrid beam (Singh, 2019).

2.3.4. General size effect

The aim of this study is to increase the height of the hybrid beams, by keeping the SHCC layer constant in thickness. In general, cementitious elements exhibit strong size effects (Van Mier, 2012). Multiple models for describing size effects are present, such as Weibull's weakest link theory and a deterministic approach, which makes use of the Linear Elastic Fracture Mechanics theory (Van Mier, 2012). Weibull's weakest link theory is a statistical approach of determining the size effect. The theory states that, the strength of a chain is as strong as the weakest link in the chain. Therefore, ideally brittle material behavior is assumed (Bazant, 2000). A longer the chain leads to more links, and thus a higher probability of a weaker link in the chain. Therefore, a longer chain leads to a lower strength of the chain. The probability of failure according to the Weibull theory can be predicted with (Van Mier, 2012):

$$p_f(\sigma, V) = 1 - e^{\left(-\frac{V}{V_0}\left(\frac{\sigma}{\sigma_0}\right)^m\right)} \tag{2.13}$$

Where the formula includes the applied external stress (σ), the structure's volume (V), the normalized volume on which characteristic strength was determined (V_0), characteristic strength (σ_0) and the Weibull modulus (m). The Weibull modulus is considered a material property (Van Mier, 2012). The representative volume element for concrete is the smallest volume of a material, such that the element can be considered as a continuum (Van Mier, 2012). This means that for concrete, the sample size should be big enough to include aggregates, instead of only cement-paste. In order to allow for multiple aggregates in the element, the representative volume for concrete is assumed to be three to five times the maximum aggregate size, and is therefore usually chosen as 100-150 mm cubes for normal concrete (Van Mier, 2012).

However, the Weibull theory is applicable for ideally brittle materials. Concrete is not an ideally brittle material, as concrete exhibit some softening (Van Mier, 2012). Even more, reinforced concrete and SHCC are far from brittle. Therefore, an energy approach is used to describe the size effect (Bazant, 2000). This is also called the energetic size effect. Upon loading of the element, strain energy is stored in the material. If a crack is formed, due to exceeding the strength of the material, the strain is locally released (Bazant, 2000). The formation of a crack does not lead to the release of all the stored strain energy. Part of the stored energy is absorbed by the fracture process zone (Bazant, 2000). It is found that, for large sized structures, the energy absorption rate by the fracture process zone is small, compared to the energy release rate by creating fracture zones (Bazant, 2000). It was also found that, by increasing the size of the element, the energy release rate increases with the second power, whereas the energy absorption rate increases proportional to the increasing size (Bazant, 2000). In order to match the energy release rate with the energy absorption rate, the nominal strength must decrease. Decreasing the nominal strength, reduces the energy release rate as less strain energy will be stored before fracturing occurs (Bazant, 2000).

Size effects affect the crack widths and crack spacings of reinforced concrete beams (Alam et al., 2010). The Eurocode design formulas do not include these size effects. The deviation of crack widths and crack spacings between experimental results and the Eurocode design formulas is larger for larger beam sizes and larger applied strains (Figure 2.32).

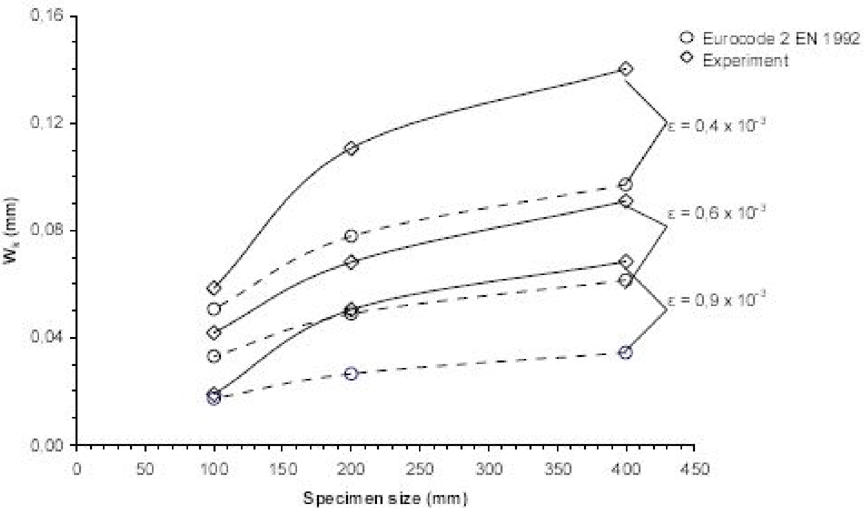

Figure 2.32: Crack widths for different specimen sizes compared between experiment and Eurocode design formulas (Alam et al., 2010).

2.3.5. Roughness of reinforcement

The bond between reinforcement and cement-paste is influencing the crack spacing (Subsection 2.1.3). The bond of the rebar with the paste is dependent on adhesion, friction and mechanical interlocking (Tepfers, 1973). For SHCC, the adhesion is increased (Subsection 2.2.7). The friction component is only activated once slip of the rebar occurs (Tepfers, 1973). The friction is dependent on the microscale roughness of the rebar, microscale roughness of the cementitious material interface, and the confinement of the cementitious material (Chan, 2012). The mechanical interlocking is mainly dependent on the roughness of the rebar, and is the main contributing factor to rebar-concrete bond in cracked concrete (Tepfers, 1973). The ribs of the rebar are anchored in the cement-paste, and thereby increase the pull-out resistance. Pulling the rebar results in stresses on the tips of these ribs, which results in cracking and crushing of the concrete, if concrete's strength is exceeded. Therefore, the presence of ribs results in the formation of so called secondary cracks at the rebar-SHCC interface. For reinforced concrete, these secondary cracks are generally not governing for the maximum crack width. Therefore, ribbed rebars are often used in reinforced concrete. For SHCC the cracking behavior is different from conventional concrete. The crack bridging of the SHCC fibers does lead to increased adhesion of the SHCC-rebar interface. In addition, the cracking pattern for SHCC is different from conventional reinforced concrete (Cai et al., 2020). The cracking pattern of SHCC is characterized by multiple small cracks (Figure 2.33).

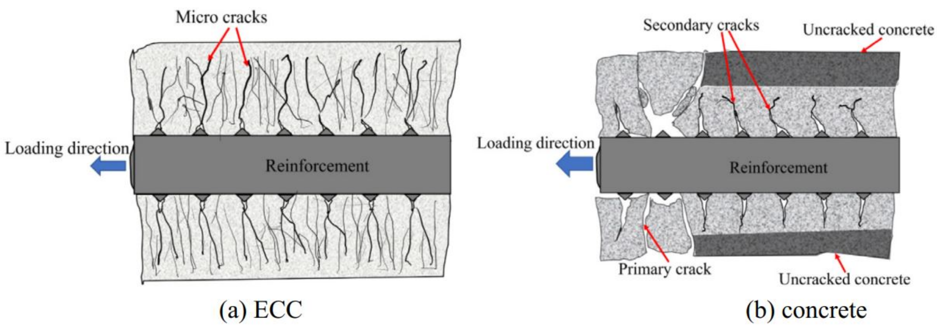

Figure 2.33: Schematization of cracks at the interface of reinforcement rebar and concrete for (a) Engineered Cementitious Composite (ECC) and (b) conventional concrete (Cai et al., 2020).

This cracking pattern leads to a shorter debonding length of the reinforcement at a crack, compared to reinforced concrete (Deng et al., 2018). The mechanical interlocking of ribbed bars in SHCC is stronger, due to the better deformability of SHCC, compared to conventional concrete (Deng et al., 2018). This leads to the development of large plastic areas in SHCC (Cai et al., 2020). Therefore, the rebar-SHCC bond is stronger than the rebar-concrete bond. If plain bars embedded in SHCC are tested under pull-out, an 71% higher bond strength is found, compared to a plain bar in conventional concrete (Deng et al., 2018). After initiation of the pull-out of the plain bar in SHCC, the residual bond remained more than half of the ultimate bond strength (Figure 2.34). This residual bond is found to be much lower for the plain bar in conventional concrete (Deng et al., 2018). Even more, the ductility of the rebar-SHCC bond for the plain bar in SHCC showed a significant larger ductility, compared to the plain bar in conventional concrete.

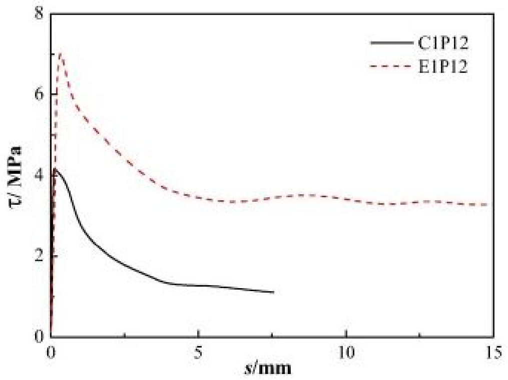

(a)

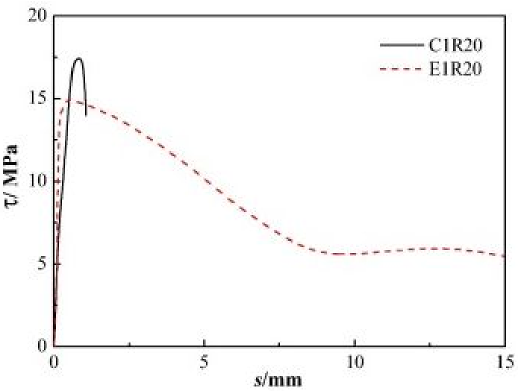

(b)

Figure 2.34: Bond strength slip behavior from a pull-out test with ECC (dashed) and conventional concrete (solid) with (a) a 12 mm plain rebar and (b) a 20 mm ribbed rebar (Deng et al., 2018).

2.4. Conclusions

Based on the performed literature study the following can be concluded:

- Strain hardening cementitious materials (SHCC) are able to reach a ductility of 2% strain. This ductility can be attributed to the crack bridging of fibers in SHCC. Due to this crack bridging, SHCC is a promising material to use for the control of crack widths.
- The inclusion of blast furnace slag in the binder of SHCC leads to a smaller pore distribution. Therefore, the SHCC becomes stronger in tension. However, the inclusion of blast furnace slag in the binder of SHCC leads to larger autogeneous shrinkage. Therefore, curing of the cast SHCC is important.
- Small aggregates, like sand, in the SHCC mix does decrease the crack spacing. In addition, the first cracking strength is increased. The ductility is however found to decrease. Including sand in SHCC mixtures could be beneficial from both an economical viewpoint. It is recommended to investigate the effect of (small) aggregates in SHCC on the crack width controlling behavior in a future study.
- A 200 mm high hybrid R/SHCC beam, with a 70 mm thick SHCC layer at the bottom, showed promising crack width controlling behavior. It was found that, the load at which the 0.3 mm crack width limit is increased to 71 kN, whereas this load was 39 kN for a 200 mm high reinforced concrete beam. The cracking pattern of the hybrid R/SHCC beam showed a uniform cracking pattern in the SHCC layer and 7 cracks in the concrete layer propagating towards the compression zone. Whereas, the cracking pattern of the reinforced concrete beam showed 4 concrete cracks propagating towards the compression zone.
- A plain reinforcement bar embedded in SHCC is found to decrease the formation of (secondary) cracks at the rebar-SHCC interface. In addition, a plain bar embedded in SHCC leads to a significant stronger rebar-SHCC bond, compared to a plain bar in conventional concrete. The ductility

of the rebar-SHCC bond of a plain bar embedded in SHCC is significantly larger, compared to a plain bar in conventional concrete.

- The concrete-SHCC interface affects the structural behavior of the hybrid R/SHCC beam. However, for a 200 mm high R/SHCC beam, the roughness of the interface did not affect the cracking behavior. For SHCC repair patches it was found that, delamination of the concrete-SHCC interface improved the crack controlling behavior. This improved crack controlling behavior can be attributed to the release of strain energy by the interface. Delamination of the longitudinal reinforcement could be another source to release additional strain energy in the hybrid beams, which could improve the crack controlling behavior. Therefore, the delamination of the longitudinal reinforcement is studied.

- Height scaling of a beam being subject to bending increases the internal lever arm. Therefore, the steel stress is lower for the same applied bending moment in reinforced concrete beams. Upon increasing the height of a beam, the bearing moment capacity increases, by keeping the length of the beam constant.

- Increasing the height of the beam might lead to the development of an effective tensile area. This is caused by the development of a more or less uniform stress distribution in the tensile area. The development of an effective tensile area, leads to a branched cracking pattern in the tensile area. The cracks from the tensile area coalescence outside the tensile area.

- Upon height scaling of the hybrid beams, by keeping the thickness of the SHCC bottom layer constant, the interface roughness could affect the crack controlling behavior. It was found that, too large delamination of the concrete-SHCC interface leads to a reduced bearing capacity of the 200 mm high hybrid R/SHCC beam. The effect of a stronger concrete-SHCC bond is numerically studied (chapter 4). A rougher interface surface does not only lead to a stronger bond, but also results in mechanical interlocking and a different stress distribution at the interface. Therefore, it is recommended to study the effect of interface roughness on the crack controlling behavior of height scaled hybrid R/SHCC beams in the future.

- Cementitious materials exhibit strong size effects. Therefore, the effect of height scaling on the crack controlling behavior of hybrid R/SHCC beams is studied numerically (chapter 4) and by experiments (chapter 5).

3

Design of Beams

The main objective of this thesis is the investigation of the effect of height scaling on the crack width controlling behavior of hybrid R/SHCC beams. Therefore, beams of different heights are designed. These designs are subject to design constraints, which will be addressed first. After this, the beam dimensions are determined. Lastly, design checks are made.

3.1. Design Constraints

In order to compare the results of this study with results from (Singh, 2019), the beams needs to have a similar design. Therefore, the following constraints are present:

- The test configuration is a four point bending test, with a 500 mm constant bending moment region (Figure 3.1)
- All hybrid beams have a 70 mm layer of SHCC at the bottom (Figure 3.1)
- All beams have 3Ø8 longitudinal reinforcement bars at the bottom
- All beams have 2Ø8 longitudinal reinforcement bars at the top
- All beams have shear reinforcement in the shear spans, but not in the constant bending moment section
- Concrete quality C30/37 with concrete mixture used by (Singh, 2019)
- SHCC properties with SHCC mixture used by (Singh, 2019)

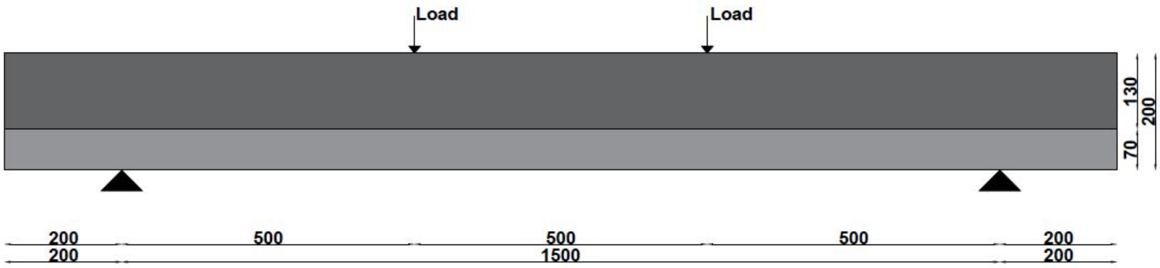

(a)

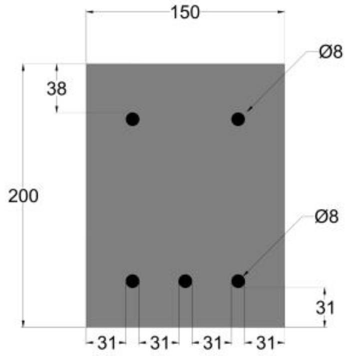

(a)

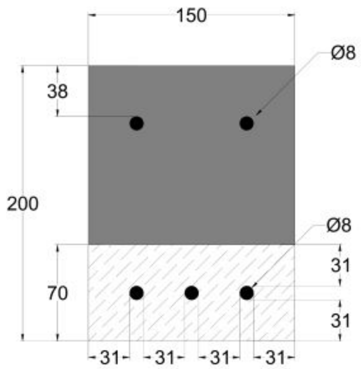

(b)

Figure 3.1: Experimental design with (a) test configuration, (b) cross section of reinforced concrete beam and (c) cross section of hybrid R/SHCC beam designed and used by (Huang, 2017 & Singh, 2019).

3.2. Beam Dimensions

3.2.1. Cross section

With these design constraints, 5 beams are designed, in addition to the 200 mm high beams of (Singh, 2019). The effect of height scaling on the crack controlling behavior of hybrid R/SHCC beams is studied by the comparison of the structural behavior of beams of three different heights. The heights studied are: 200 mm, 300 mm and 400 mm (Table 3.1). Reinforced concrete beams of the same height are used as a reference of the hybrid beams. In the literature study it was found that, a plain bar embedded in SHCC was found to delay the formation of cracks at the rebar-SHCC interface. The (partial) delamination of the concrete-SHCC interface of 200 mm high hybrid R/SHCC beams, was found to decrease the flexural crack controlling behavior. However, the delamination of the concrete-SHCC layer in SHCC repair patches led to increased release of strain energy, which improved the crack controlling behavior of SHCC. In order to study the effect of increased strain release due to delamination, fully delaminated longitudinal reinforcement bars in the 700 mm central region are studied. This is studied by a 300 mm high hybrid beam with plain and Vaseline treated rebars. The Vaseline is applied over the 700 mm central span (Figure 5.3). The ordinary 300 mm high hybrid R/SHCC beam is used as a reference.

Table 3.1: Beam designs.

Label	Type	Height	Span	Longitudinal reinforcement
RC200	Reinforced concrete	200 mm	1500 mm	Ribbed
H200	Hybrid R/SHCC	200 mm	1500 mm	Ribbed
RC300	Reinforced concrete	300 mm	1825 mm	Ribbed
H300	Hybrid R/SHCC	300 mm	1825 mm	Ribbed
H300s	Hybrid R/SHCC	300 mm	1825 mm	Plain and Vaseline treated
RC400	Reinforced concrete	400 mm	2325 mm	Ribbed
H400	Hybrid R/SHCC	400 mm	2325 mm	Ribbed

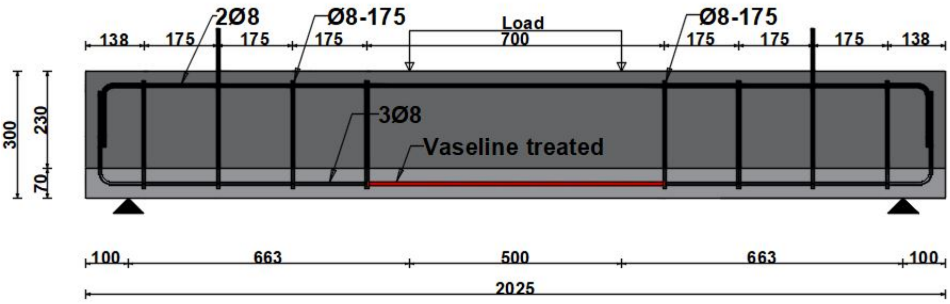

Figure 3.2: Schematic side view of 300 mm high hybrid beam with plain longitudinal rebars and Vaseline treated central section.

With the constraint of the 70 mm high bottom SHCC layer and the configuration of the longitudinal reinforcement, 4 cross sections can be distinguished, in addition to the 200 mm high cross sections (Figure 3.3).

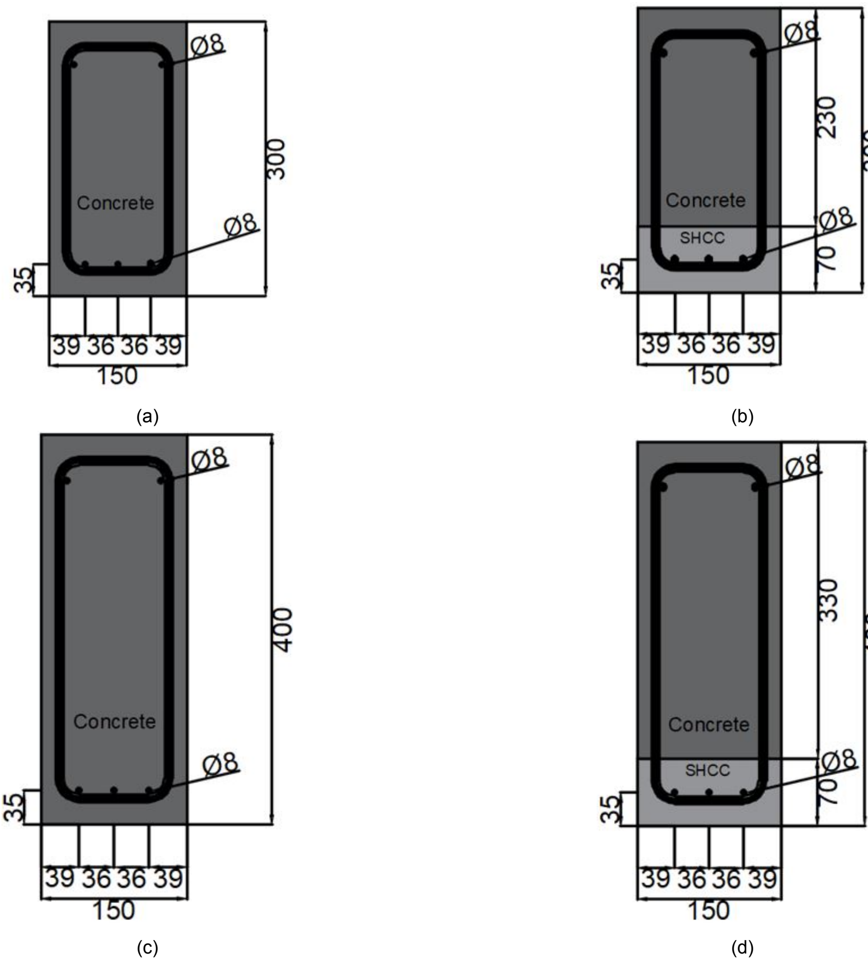

Figure 3.3: Cross section of (a) 300 mm high reinforced concrete beam, (b) 300 mm high hybrid R/SHCC beam, (c) 400 mm high reinforced concrete beam and (d) 400 mm high hybrid R/SHCC beam.

As no significant difference in cracking behavior was found between a rough or smooth concrete-SHCC interface in a 200 mm high hybrid R/SHCC beam, all hybrid beams are designed with a smooth concrete-SHCC interface. Additionally, the width is kept constant at 150 mm, which is similar to the previous performed study by (Singh, 2019). Increasing the width of the beams would increase the bearing capacity of the beams. However, it is expected that increasing the width of the beam has no influence on the cracking behavior.

3.2.2. Length of beam

The length of the beams varies for different heights (Figure 3.4). The distance between the load application points, thus the constant bending moment region, is 500 mm. The length for the beams scaled in height are scaled in length as well, in order to prevent stocky beam behavior. Stocky beam behavior results in direct transfer of the load to the supports. Therefore, the length of the shear spans of the beams should be at least $2.5D$, where D is the effective height of the beam (*Eurocode 2: Design of concrete structures*, 2004). This result in a designed length for the 300 mm high beams of:

$$\begin{aligned} L_{300\ \mathrm{mm}} &= L_{\text{support}} + 2.5D + L_{\text{constant moment}} + 2.5D + L_{\text{support}} \\ &= 100 + 2.5 * (300 - 35) + 500 + 2.5 * (300 - 35) + 100 = 2025\ \mathrm{mm} \end{aligned}$$

The length of the 400 mm high beams is designed as:

$$\begin{aligned} L_{400\ \mathrm{mm}} &= L_{\text{support}} + 2.5D + L_{\text{constant moment}} + 2.5D + L_{\text{support}} \\ &= 100 + 2.5 * (400 - 35) + 500 + 2.5 * (400 - 35) + 100 = 2525\ \mathrm{mm} \end{aligned}$$

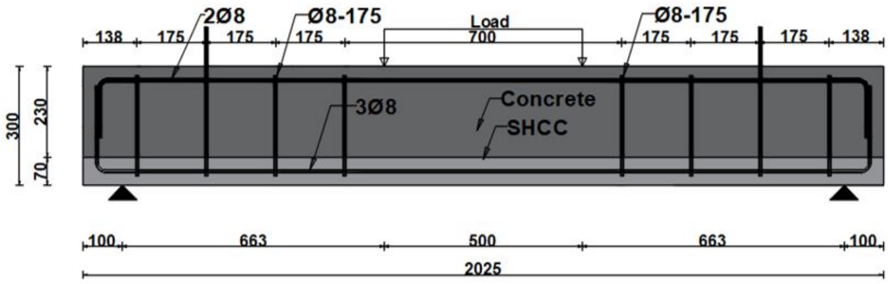

(a)

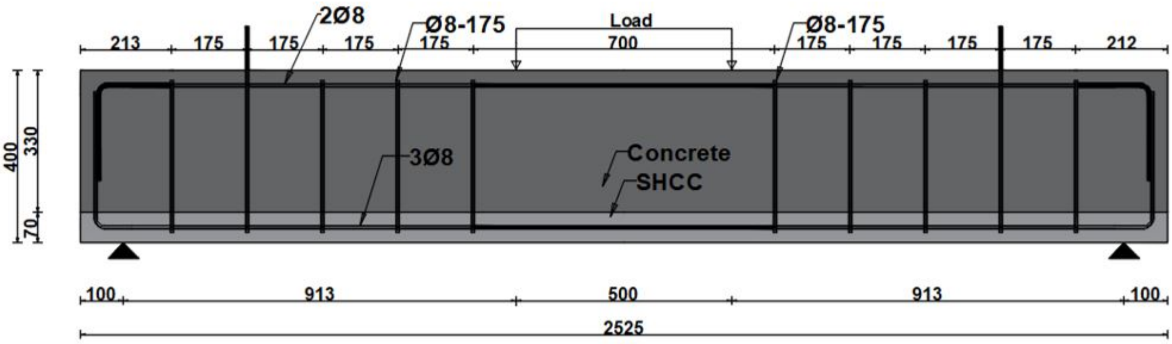

(b)

Figure 3.4: Schematized side view of (a) 300 mm high hybrid beams and (b) 400 mm high hybrid beams.

3.3. Design Checks

3.3.1. Concrete cover

Sufficient concrete cover is needed to ensure full load transfer between steel and concrete, as discussed in subsection 2.1.5. The minimum required cover according to Eurocode is (*Eurocode 2: Design of concrete structures*, 2004):

$$c_{nom} = c_{\min} + \Delta dev = 8 + 5 = 13\ \mathrm{mm} \tag{3.1}$$

In the design the following covers are present:

$$c_{\text{bottom,midspan}} = 35 - \frac{\varnothing}{2} = 35 - 4 = 31 \text{ mm}$$
$$c_{\text{bottom,shearspan}} = 35 - \varnothing_{\text{stirrup}} - \frac{\varnothing_{\text{longitudinal}}}{2} = 35 - 8 - 4 = 23 \text{ mm}$$
$$c_{\text{side,midspan}} = 39 - \frac{\varnothing_{\text{longitudinal}}}{2} = 35 \text{ mm}$$
$$c_{\text{side,shearspan}} = 39 - 16 - 8 = 15 \text{ mm}$$

As the designed covers are larger than the minimum required covers, sufficient force transfer between reinforcement and concrete/SHCC can be expected.

3.3.2. Bending moment design

Sufficient reinforcement in the beams is needed, to prevent failure of the steel before cracking occurs. Failure of the steel before cracks are formed, leads to brittle failure. Therefore, the reinforcement applied should be above the minimum required ($A_{s,\min}$). The code prescribes the criteria as (*Eurocode 2: Design of concrete structures*, 2004):

$$A_{s,\min} = \max\left(\frac{0.26 f_{ctm}}{f_{yk}} bd; 0.0013bd\right) \tag{3.2}$$

Determined by the width of the beam (b), effective depth of the beam (d), mean tensile strength of concrete (f_{ctm}), and the characteristic yielding strength of steel (f_{yk}). For the 300 mm high beams this results in the minimum reinforcement needed:

$$A_{s,\min} = \max\left(\frac{0.26 f_{ctm}}{f_{yk}} bd; 0.0013bd\right)$$
$$= \max\left(\frac{0.26 * 3}{500} * 150 * (300 - 35); 0.0013 * 150 * (300 - 35)\right) = 61.39 \text{ mm}^2$$

In the 300 mm beams, three longitudinal reinforcement bars of 8 mm diameter are used. This gives a steel area of:

$$A_{s,\text{applied}} = 3 * \frac{1}{4} * \pi * 8^2 = 150.80 \text{ mm}^2 > A_{\text{s,min}}$$

For the 400 mm beams the minimum reinforcement needed is:

$$A_{s,\min} = \max\left(\frac{0.26 f_{ctm}}{f_{yk}} bd; 0.0013bd\right)$$
$$= \max\left(\frac{0.26 * 3}{500} * 200 * (400 - 35); 0.0013 * 200 * (400 - 35)\right) = 112.74 \text{ mm}^2$$

In the 400 mm beams, three longitudinal reinforcement bars of 8 mm diameter are used. This gives a steel area of:

$$A_{s,\text{applied}} = 3 * \frac{1}{4} * \pi * 8^2 = 150.80 \text{ mm}^2 > A_{\text{s,min}}$$

In addition, the steel should yield, before the compressive zone fails, and therefore the amount of reinforcement that should be applied, is limited. The maximum allowable reinforcement can be determined by:

$$N_s = A_{s,\max} f_{yd} \tag{3.3}$$

$$N_c = \frac{3}{4} b x_{u,\max} f_{cd} \tag{3.4}$$

$$N_s = N_c \text{ (horizontal equilibrium)} \tag{3.5}$$

$$A_{s,\max} = \frac{\frac{3}{4} b x_{u,\max} f_{cd}}{f_{yd}} \tag{3.6}$$

$$f_{cd} = \frac{f_{ck}}{y_c} \tag{3.7}$$

$$, f_{yd} = \frac{f_{yk}}{y_s} \tag{3.8}$$

$$x_{u,\max} = 0.448d \tag{3.9}$$

With N_s the steel force determined by the area of reinforcement ($A_{s,\max}$) and the design yield strength of steel (f_{yd}). With N_c the compression force of concrete determined by the width of the beam (b), height of the compression zone ($x_{u,max}$) and compression design strength of concrete (f_{cd}). For the 300 mm high beam, the maximum applicable reinforcement is:

$$A_{s,\max} = \frac{\frac{3}{4} * 150 * 0.448 * (300 - 35) * \frac{30}{1.5}}{\frac{500}{1.15}} = 614.07 \text{ mm}^2 > A_{s,\text{applied}}$$

For the 400 mm high beam, the maximum applicable reinforcement is:

$$A_{s,\max} = \frac{\frac{3}{4} * 200 * 0.448 * (400 - 35) * \frac{30}{1.5}}{\frac{500}{1.15}} = 1127.72 \text{ mm}^2 > A_{s,\text{applied}}$$

As both the minimum reinforcement requirement and the maximum reinforcement requirement is met for both beam heights, the applied reinforcement is sufficient. All longitudinal reinforcement are of quality B500. All reinforcement bars are ribbed, except for the plain longitudinal reinforcement bars in the H300s beam.

3.3.3. Shear design

Stirrups are needed in the design, as shear forces are present in the side spans. In order to design the shear reinforcements, it is first needed to determine the maximum present shear force. This will be determined based on the beams with a SHCC layer. This layer is assumed to have a uniform tensile capacity, when the ultimate moment capacity is reached.

For the 300 mm high beam, it holds:

$$x_u = \frac{A_{s,applied} f_{yk} + f_{ctm,SHCC} b_{SHCC} h_{SHCC}}{\frac{3}{4} b f_{cm}} = \frac{150.80 * 500 + 3 * 150 * 70}{0.75 * 150 * 39.2} = 24.24 \text{ mm}$$

$$M_{ult} = \left(A_{s,applied} f_{yk} + f_{ctm,SHCC} b_{SHCC} h_{SHCC}\right)\left(d - \frac{7}{18} x_u\right)$$

$$= (150.80 * 500 + 3 * 150 * 70) * \left(300 - 35 - \frac{7}{18} * 24.24\right) = 27,320,337 \text{Nmm}$$

$$V_{Ed} = \frac{M_{ult}}{663} = 41.24 \text{kN}$$

$$v_{Ed} = \frac{V_{Ed}}{bd} = \frac{41238}{150 * (300 - 35)} = 1.04 \text{ N/mm}^2$$

$$k = \min\left(\sqrt{\frac{200}{d}}; 2\right) = 1.87$$

$$v_{rdc} = 0.18k\,(100\rho_l f_{ck})^{1/3} = 0.18 * 1.87 * \left(100 * \frac{150.80}{150 * (300 - 35)} * 30\right)^{1/3} = 0.74 \text{ N/mm}^2$$

$v_{rdc} < v_{Ed}$ thus stirrups needed.

$\theta = 45°$

$$\frac{A_{sw}}{s} = \frac{V_{Ed}}{f_{ywd} z \cot\theta} = \frac{41238}{500 * \left(300 - 35 - \frac{7}{18} * 24.24\right) * 1} = 0.34 \text{ mm/mm}$$

$s = 175$ mm

$A_{\text{sw,required}} = 0.34 * 175 = 59.95 \text{ mm}^2$

$A_{\text{sw,applied}} = 8\pi \frac{1}{4} \emptyset_{sw}{}^2 = 8 * \pi * 0.25 * 8^2 = 402.12 \text{ mm}^2$

Max distance from support $= z \cot\theta = 256$ mm

Ø8-175 are applied in the shear spans. This means that, 4 stirrups in each shear span are applied. The stirrups have the ribbed B500 steel quality. This design is used for all 300 mm high beams.

For the 400 mm high beam, it holds:

$$x_u = \frac{A_{s,applied} f_{yk} + f_{ctm,SHCC} b_{SHCc} h_{SHCC}}{\frac{3}{4} b f_{cm}} = \frac{150.80 * 500 + 3 * 150 * 70}{0.75 * 150 * 39.2} = 24.24 \text{ mm}$$

$$M_{ult} = \left(A_{s,applied} f_{yk} + f_{ctm,SHCC} b_{SHCC} h_{SHCC}\right)\left(d - \frac{7}{18} x_u\right)$$

$$= (150.80 * 500 + 3 * 150 * 70) * \left(400 - 35 - \frac{7}{18} * 70.25\right) = 38{,}010{,}159 \text{Nmm}$$

$$V_{Ed} = \frac{M_{ult}}{913} = 41.66 \text{kN}$$

$$v_{Ed} = \frac{V_{Ed}}{bd} = \frac{41655}{150 * (400 - 35)} = 0.76 \text{ N/mm}^2$$

$$k = \min\left(\sqrt{\frac{200}{d}}; 2\right) = 1.74$$

$$v_{rdc} = 0.18k \left(100 \rho_l f_{ck}\right)^{1/3} = 0.18 * 1.87 * \left(100 * \frac{150.80}{150 * 365} * 30\right)^{1/3} = 0.61 \text{ N/mm}^2$$

$v_{rdc} < v_{Ed}$ thus stirrups needed.

$\theta = 45°$

$$\frac{A_{sw}}{s} = \frac{V_{Ed}}{f_{ywd} z cot\theta} = \frac{41655}{500 * \left(365 - \frac{7}{18} * 24.24\right) * 1} = 0.24 \text{ mm}^2/\text{mm}$$

$s = 175$ mm

$A_{\text{sw,required}} = 0.24 * 175 = 42.78 \text{ mm}^2$

$A_{\text{sw,applied}} = 10\pi \frac{1}{4} \emptyset_{sw}{}^2 = 10 * \pi * 0.25 * 8^2 = 502.65 \text{ mm}^2$

Max distance from support $= z \cot\theta = 356$ mm

Ø8-175 are applied in the shear spans. This means that, 5 stirrups in each shear span are applied. The stirrups have steel quality ribbed B500. This design is used for all 400 mm high beams.

3.3.4. Compression reinforcement

In addition, longitudinal reinforcement in the compressive zone is applied. 2Ø8 reinforcement of ribbed steel B500 is used in all beams (Figure 3.4). This reinforcement is used, to provide stiffness to the reinforcement cage, which makes casting and transport of the cages easier. The effect of longitudinal reinforcement in the compression zone is expected to be minor. Theoretically, the reinforcement increases the flexural stiffness of the beam, but due to the low section area of this reinforcement the contribution is limited. Additionally, the reinforcement strengthens the compressive zone and delays a compressive failure. However, it is not expected to impact the cracking behavior.

4

Numerical Study

In this numerical study, the designed beams from chapter 3 are modelled, in order to study the effect of height scaling of the beams. The numerical study is performed with the Delft Lattice Model. Lattice modelling is chosen for the numerical study, as it is known to be a representative model for the modelling of fracture of a heterogeneous material (Van Mier, 2012). However, macro scale lattice models have only recently gained attention for the modelling of structural behavior of reinforced concrete and new types of concrete. It was found that, the macro scale Delft Lattice Model is able to predict the structural behavior, such as the cracking pattern, of reinforced concrete (Lukovic et al., 2018). The benefit of a lattice model is the simple material input as linear elastic computations are performed in each analysis step.

4.1. Introduction

In this section an introduction to lattice modelling is made. This is done by explaining the basics of lattice modelling, the fracture modelling approach, the possibilities for accounting for heterogeneity, the mesh generation, and the selection of the material properties. Finally, the Delft Lattice model is explained.

4.1.1. Mechanics of lattice modelling

A lattice model is a discrete element model, that discretizes a continuum into a lattice of beam elements (H. Schlangen, 1993). Each element represents a certain volume and mass of material. The beams have a starting point and an endpoint and are connected at these points with other beams, creating a network of beams (Figure 4.1). The points of connection are called nodes. 2D beam elements have three degrees of freedom in every node (Figure 4.1). This results in the displacement vector for a beam (Van Mier, 2012):

$$\bar{\mathbf{v}}^{\mathbf{T}} = \begin{bmatrix} \bar{\mathrm{u}}_{\mathrm{i}} & \bar{\mathrm{v}}_{\mathrm{i}} & \bar{\varphi}_{\mathrm{i}} & \bar{\mathrm{u}}_{\mathrm{j}} & \bar{\mathrm{v}}_{\mathrm{j}} & \bar{\varphi}_{\mathrm{j}} \end{bmatrix} \tag{4.1}$$

The subscripts i and j indicate the two nodes of a beam. From the displacement vector it is found that, a 2D beam element has 6 degrees of freedom. Each node has two displacements degrees of freedom and one rotational degree of freedom.

Each beam element has stiffness and strength properties assigned. A lattice model uses kinematic, constitutive and equilibrium equations (Simone, 2011). The kinematic equations relate the displacement with the strain. The constitutive equations relate the stress with the strain. The equilibrium equations relate the external forces with internal stresses. This leads to the following kinematic equations for a beam element (Van Mier, 2012):

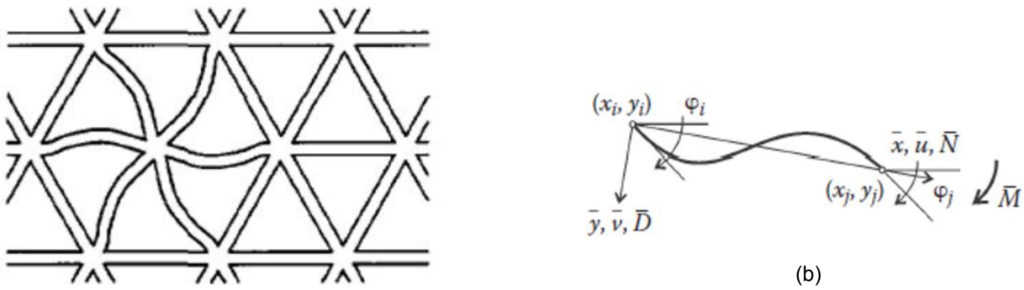

(b)

(a)

Figure 4.1: Part of lattice model with (a) triangular mesh of beam elements (H. Schlangen, 1993) and (b) the degrees of freedom of a beam element (Van Mier, 2012).

$$\boldsymbol{\varepsilon} = \begin{bmatrix} \varepsilon_1 = -\mathrm{u_i} + \mathrm{u_j} \\ \varepsilon_2 = \frac{\mathrm{v_i}}{\mathrm{l}} + \varphi_\mathrm{i} - \frac{\mathrm{v_j}}{\mathrm{l}} \\ \varepsilon_3 = \frac{\mathrm{v_i}}{\mathrm{l}} - \frac{\mathrm{v_j}}{\mathrm{l}} + \varphi_\mathrm{j} \end{bmatrix} = \begin{bmatrix} -1 & 0 & 0 & 1 & 0 & 0 \\ 0 & 1/\mathrm{l} & 1 & 0 & -1/\mathrm{l} & 0 \\ 0 & 1/\mathrm{l} & 0 & 0 & -1/\mathrm{l} & 1 \end{bmatrix} \begin{bmatrix} \overline{\mathrm{u}}_\mathrm{i} \\ \overline{\mathrm{v}}_\mathrm{i} \\ \overline{\varphi}_\mathrm{i} \\ \overline{\mathrm{u}}_\mathrm{j} \\ \overline{\mathrm{v}}_\mathrm{j} \\ \overline{\varphi}_\mathrm{j} \end{bmatrix} = \mathbf{C}\overline{\mathbf{v}} \tag{4.2}$$

This equation contains the C-matrix, which is called the combination matrix. With the strains related to the degrees of freedom, the strains can be related to stresses with the constitutive equations (Van Mier, 2012):

$$\boldsymbol{\sigma} = \begin{bmatrix} \sigma_1 = \frac{\mathrm{EA}}{\mathrm{l}}\varepsilon_1 \\ \sigma_2 = \frac{4\mathrm{EI}}{\mathrm{l}}\varepsilon_2 + \frac{2\mathrm{EI}}{\mathrm{l}}\varepsilon_3 \\ \sigma_3 = \frac{2\mathrm{EI}}{\mathrm{l}}\varepsilon_2 + \frac{4\mathrm{EI}}{\mathrm{l}}\varepsilon_3 \end{bmatrix} = \begin{bmatrix} \mathrm{EA/l} & 0 & 0 \\ 0 & 4\mathrm{EI/l} & 2\mathrm{EI/l} \\ 0 & 2\mathrm{EI/l} & 4\mathrm{EI/l} \end{bmatrix} \begin{bmatrix} \varepsilon_1 \\ \varepsilon_2 \\ \varepsilon_3 \end{bmatrix} = \overline{\mathbf{S}}_{\boldsymbol{\varepsilon}} \tag{4.3}$$

In this relation, the Young's modulus (E), the cross sectional area (A), the length (l), and the moment of inertia (I) of an element is required. With use of the combination matrix and the stresses, the equilibrium equation can be made:

$$\overline{\mathbf{k}} = \begin{bmatrix} \mathrm{N_i} & \mathrm{D_i} & \mathrm{M_i} & \mathrm{N_j} & \mathrm{D_j} & \mathrm{M_j} \end{bmatrix}^\mathrm{T} = \mathbf{C^T}\boldsymbol{\sigma} \tag{4.4}$$

With the three set of equations known, it is now possible to go directly from nodal displacements to nodal forces (Simone, 2011):

$$\overline{\mathbf{k}} = \mathbf{C^T}\boldsymbol{\sigma} = \mathbf{C^T}\mathbf{S}\boldsymbol{\varepsilon} = \mathbf{C^T}\overline{\mathbf{S}}\mathbf{C}\overline{\mathbf{v}}$$
$$= \begin{bmatrix} \frac{\mathrm{EA}}{\mathrm{l}} & 0 & 0 & -\frac{\mathrm{EA}}{\mathrm{l}} & 0 & 0 \\ 0 & \frac{12\mathrm{EI}}{\mathrm{l}^3} & \frac{6\mathrm{EI}}{\mathrm{l}^2} & 0 & -\frac{12\mathrm{EI}}{\mathrm{l}^3} & \frac{6\mathrm{EI}}{\mathrm{l}^2} \\ 0 & \frac{6\mathrm{EI}}{\mathrm{l}^2} & \frac{4\mathrm{EI}}{\mathrm{l}} & 0 & -\frac{6\mathrm{EI}}{\mathrm{l}^2} & \frac{2\mathrm{EI}}{\mathrm{l}} \\ \frac{\mathrm{EA}}{\mathrm{l}} & 0 & 0 & \frac{\mathrm{EA}}{\mathrm{l}} & 0 & 0 \\ 0 & -\frac{12\mathrm{EI}}{\mathrm{l}^3} & -\frac{6\mathrm{EI}}{\mathrm{l}^2} & 0 & \frac{12\mathrm{EI}}{\mathrm{l}^3} & -\frac{6\mathrm{EI}}{\mathrm{l}^2} \\ 0 & \frac{6\mathrm{EI}}{\mathrm{l}^2} & \frac{2\mathrm{EI}}{\mathrm{l}} & 0 & -\frac{6\mathrm{EI}}{\mathrm{l}^2} & \frac{4\mathrm{EI}}{\mathrm{l}} \end{bmatrix} \begin{bmatrix} \overline{\mathrm{u}}_\mathrm{i} \\ \overline{\mathrm{v}}_\mathrm{i} \\ \overline{\varphi}_\mathrm{i} \\ \overline{\mathrm{u}}_\mathrm{j} \\ \overline{\mathrm{v}}_\mathrm{j} \\ \overline{\varphi}_\mathrm{j} \end{bmatrix} \tag{4.5}$$

Above equations are derived for the local orientation of a beam element. In order to derive the system matrices, transformation to the global orienation is needed. This is done with the transformation matrix (Simone, 2011):

$$\mathbf{T} = \begin{bmatrix} \cos\alpha & \sin\alpha & 0 & 0 & 0 & 0 \\ -\sin\alpha & \cos\alpha & 0 & 0 & 0 & 0 \\ 0 & 0 & 1 & 0 & 0 & 0 \\ 0 & 0 & 0 & \cos\alpha & \sin\alpha & 0 \\ 0 & 0 & 0 & -\sin\alpha & \cos\alpha & 0 \\ 0 & 0 & 0 & 0 & 0 & 1 \end{bmatrix} \tag{4.6}$$

In this relation, α is the angle between the local axis orientation of an element and the global axis orientation of the model. The local displacements and forces need to be transformed, such that they align with the global orientation of the model. This is done by (Van Mier, 2012):

$$\mathbf{k} = \mathbf{T^T}\overline{\mathbf{k}} \tag{4.7}$$

$$\overline{\mathbf{v}} = \mathbf{Tv} \tag{4.8}$$

This results in the relation between displacements and external forces with global orientation (Van Mier, 2012):

$$\mathbf{k} = \mathbf{T^T C^T \overline{S} C T v} = \mathbf{Sv} \tag{4.9}$$

In this relation, $\mathbf{S}$ is the local stiffness matrix of a beam element. The total stiffness matrix is obtained by adding the stiffness contributions of other beam elements, sharing the same node. This leads to, additional components are added linearly to the respective degree of freedom, in the stiffness matrix (Simone, 2011). Upon applying a load to the model, all the degrees of freedom are solved for, with help of the stiffness matrix. It should be noted that the above derived equations only hold for 2D beam elements. If 3D beam elements are used, this results in 6 degrees of freedom per node and thus 12 degrees of freedom per beam element. The 3D beam elements are an extension of the above derived 2D beam elements. The additional degrees of freedom of a 3D beam element are two additional rotational ones and one additional translation.

4.1.2. Fracture modelling

Besides using beam elements also spring or truss elements can be used. The benefit of spring elements is the decoupled bending, torsion and shear components of the elements, which allow for faster computation (van Vliet, 2018). The benefit of truss elements is the simplicity of the element, as it does not include shear, bending or torsion at all. 2D truss elements have two degrees of freedom, which are solely translations. However, concrete fractures by localization of cracks. Upon crack formation, the crack face bridges bend and rotate, allowing for a crack tip to propagate (Figure 4.2). This means that, cracks rotate while propagating, and therefore rotational degrees of freedom are needed to simulate a realistic cracking pattern (H. Schlangen, 1993). Beam elements do have these rotational degrees of freedom. In addition, beam elements couple these rotational degrees of freedom with transverse displacements. However, the use of beam elements result in larger computational costs, as the stiffness matrix is no longer diagonal (Van Mier, 2012).

A lattice model simulates fracture by removal of elements that exceeds a certain threshold. Often this threshold is set at stress level, meaning that an element is removed from the lattice if the stress exceeds the strength (H. Schlangen, 1993). In order to simulate ongoing fracture, the model only removes one element every load step. Only the element with the highest stress/strength ratio is removed (H. Schlangen, 1993). The stress of an beam element can be determined with:

$$\sigma = \alpha\left(\frac{F}{A}\right) + \beta\left(\frac{Q}{A}\right) + \gamma\left(\frac{M}{W}\right) \tag{4.10}$$

In this relation, F is the axial force on an element, A is the cross sectional area of an beam element, Q is the shear force on an element, M is the bending moment on an element, and W is the section modulus of the element. α, β and γ are factors for determining the fracture mechanism. For example, γ indicates if bending is dominant or not. Altering γ affects the tail of the stress-deformation curve (H. Schlangen, 1993). Therefore, these factors are dependent on the material type and test setup. If an element is removed from the mesh, the model is unloaded and loaded once more without the removed element. The removal of the element from the lattice mesh, alters the force distribution of the elements. Again, the element with the highest stress/strength ratio is removed. This process continues until the

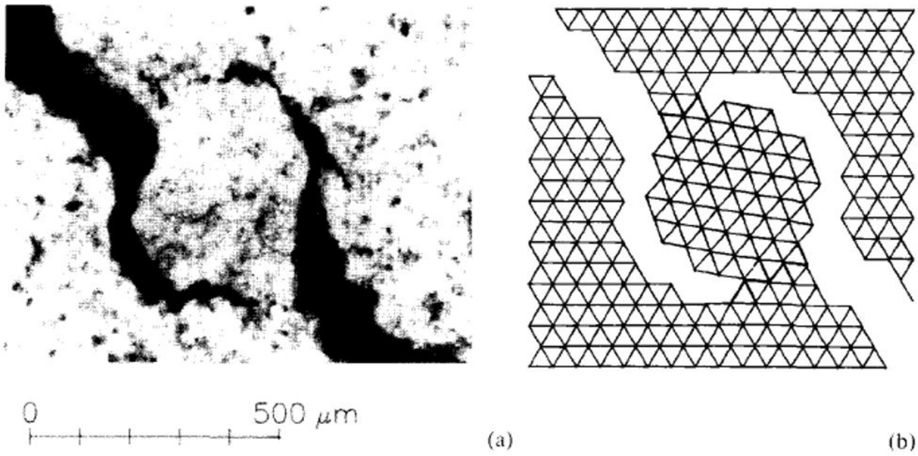

Figure 4.2: Rotation of a crack face bridge in (a) experiment and (b) modelled in lattice (H. Schlangen, 1993).

model fails, which means that it becomes unstable or a certain predefined threshold is reached such as a maximum applied load or displacement. Each element removed resembles a small crack. Fractured parts are not able to carry load. As a stiffness matrix with a zero entry on its diagonal results in an unstable matrix to solve for, element removal is an effective way of modelling fracture (Van Mier, 2012). This also shows the difference with a continuum model, which would cause stress singularities at the crack tip, if zero entries are encountered. If a continuum model is used with removal of elements, it requires re-meshing every load step, which is time consuming.

4.1.3. Heterogeneity

In order to develop a representative fracture model for concrete, the lattice model should include heterogeneity. Multiple possibilities exist for introducing heterogeneity into the model. Commonly referred to in literature are:

1. **Asymmetrical meshing**
   The first possibility is to generate a mesh that has no symmetry axis. As a mesh with symmetry axis could lead to a preferential fracture path. This preferential fracture path could develop in a symmetric mesh, as the beam elements are also symmetrical (Van Mier, 2012). In order to overcome this mesh dependency, a triangular meshing geometry could be used, with randomly varying element lengths. The variability in beam lengths eliminates mesh dependency in the fracture patterns. The benefit of this approach is that, only the length of the element need to be assigned randomly. However, limits should be set for the beam lengths as a too short element results in a too stiff matrix entry.

2. **Statistical distribution of elastic properties**
   Another possibility is to vary the elastic properties or strength threshold over the elements. This eliminates the before-mentioned preferential fracture path and introduces heterogeneity at the same time. A possible way for assigning different elastic properties is with use of a statistical distribution, such as the Weibull distribution (Van Mier, 2012). The Weibull probability density function is:

   $$f(x) = \frac{\beta}{\delta}\left(\frac{x}{\delta}\right)^{\beta-1} e^{-(x/\delta)^{\beta}} \text{ for } x > 0 \tag{4.11}$$

   In this function, β is the shape parameter and δ is the scale parameter. The Weibull distribution shows an asymmetric curve, where lower strengths are more likely to occur than higher strength values (Figure 4.3).

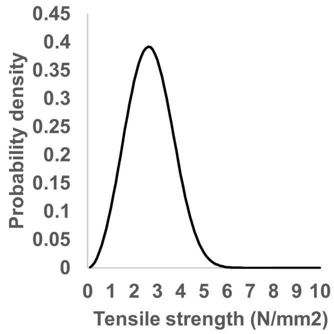

Figure 4.3: Weibull distribution for β=3 and δ = 3.

The challenge with incorporating a statistical distribution in the lattice model is the random distribution that is simulated. When using a statistical distribution, it is important that there is a match in the global response of the model and the real global response. Therefore, fitting of the distribution function is required (Van Mier, 2012).

4.1.4. Mesh generation

The geometry of the mesh can influence the response of the model (Van Mier, 2012). Besides triangular meshes, other shapes are possible as well. Both regular meshes and random meshes are possible. Generating a regular mesh is straightforward, as the regularity allows for placement of nodes on the regular grid. When making a regular mesh, the main choice to be made is the size of the mesh. Generating a random mesh is more challenging. For smaller scale models it is possible to use a predefined random structure, such as a particle distribution model. However, for macro scale models this is time consuming (Van Mier, 2012). In order to make a random mesh for a macro scale model, the model is divided into a regular cubical grid, where in each cube one node is randomly placed. This leaves a 3D body with a set of randomly placed nodes. If a triangular mesh is desired, as discussed in subsection 4.1.3, the three nodes closest to each other are connected with each other with beam elements, such that they form a triangle. Multiple ways exist for generating these triangles. One way is with use of Delaunay triangulation based on Voronoi polygons (Lee and Schachter, 1980). Voronoi polygons are created to find the nodes closest to each other. Voronoi polygons are polygons, which are centralized around a node and increase in size until one of the borders make contact with a neighboring border (Lee and Schachter, 1980). As both neighboring polygons grow at the same rate, the distance from the node to the border is similar for both polygons. The growth of the polygon continues for all sides of the polygon that did not make contact with neighboring polygons. The growth of the polygon continues, until all sides of the polygons make contact with neighboring polygons (Figure 4.4). At this stage, certain points of a polygon are neighboring two other polygons. These points, called Voronoi points, have an equal distance to the nodes (centers) of each of the polygons. Therefore, the Voronoi point is the circumcenter of the to be created triangle. The nodes of the Voronoi polygons of a Voronoi can form the triangle (Figure 4.4). This is called Delaunay triangulation, as triangles are created with the nodes closest to each other. The benefit of Delaunay triangulation is that narrow angles in the triangle are prevented (Lee and Schachter, 1980). With help of triangulation, a random triangular mesh is created.

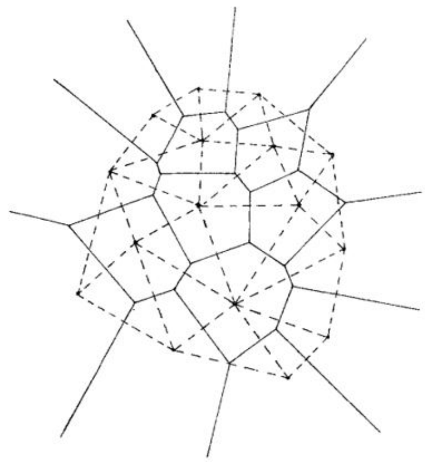

Figure 4.4: Construction of Delaunay triangulation (dashed) of random nodes with help of Voronoi polygons (solid) (Lee and Schachter, 1980).

The mesh size influences the number of nodes in the model, the computation time, but also the models accuracy to some point. As a finer mesh increases the number of nodes, and thereby the number of elements to be modelled. This increases the computation time. However, a finer mesh influences the number of cracks that can be formed during fracturing, as removal of one element resembles one crack. Therefore, a finer mesh leads to an improvement of the modelling ability of cracks. In addition, the brittleness of the material increases for a finer mesh, as upon removal of an element a smaller crack is simulated, which releases less strain energy, compared to a coarse mesh (E. Schlangen and Garboczi, 1997). However, making the mesh finer does not always lead to an improvement in the accuracy of the model, as in order to include lower scale phenomena, such as micro cracks, shrinkage and aggregate-cement interface, the additional material properties and fracture laws also need to be incorporated (Van Mier, 2012). Therefore, increasing the accuracy of the lattice model is not solely depending on the mesh size.

4.2. Delft Lattice Model

The model used in this study is the Delft Lattice model. The aspects of this model are treated in this section. The Delft Lattice model can be applied from micro scale up to macro scale models. The aim of this study is to model macro scale beams. Therefore, the focus is on macro scale models.

4.2.1. Reinforced Concrete

The macro model is created by dividing the 3D geometry into a regular cubical grid. The cube formed in this grid is called a voxel and represents the mesh size of the model. Within a voxel, a sub-voxel is created. A sub-voxel is a regular cube sharing the center with the voxel (Figure 4.5). The size of the sub-voxel relative to the voxel is called the randomness. A randomness of 0.5 means that the sub-voxel has half the size of the voxel. Within the sub-voxel, a random point, called a node, is created. With use of Delaunay Triangulation, the nodes are connected with beam elements. This creates a random mesh of beam elements, where the beam elements have varying elemental lengths. This random mesh leads to heterogeneity in the model. In case of a reinforced concrete beam, reinforcement is modelled, by manually specifying the location of the rebars in the model. Rebar nodes are created at the boundary of a voxel (Figure 4.5). Interface elements are created between concrete nodes and reinforcement nodes, in order to include slipping and stress transfer, between the reinforcement elements and concrete elements. Interface elements are created by connecting a reinforcement node with the concrete node closest by (Figure 4.5).

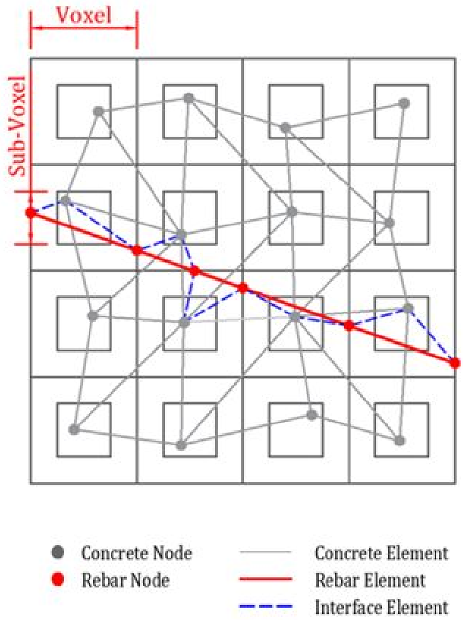

Figure 4.5: 2D schematization of mesh generation with the Delft Lattice model for reinforced concrete (Mustafa et al., 2022).

With the elements generated, material properties are assigned. All elements sharing the same type of node have the same material properties assigned. All elements with a concrete node and a reinforcement node (interface elements) have the same interface properties assigned. All elements get a circular shape assigned. The elemental radius can be either uniform for all elements of the same type, or depending on the length of the beam element. If the elemental radius depends on the elemental length, it can be determined by the area of the Voronoi polygons. Assigning uniform dimensions of the elemental shape to all elements of the same type, simplifies the computation of the mesh. With the shape and dimensions of the elements determined, only a limited amount of material properties need to be assigned. The material properties are assigned with segments (Figure 4.6).

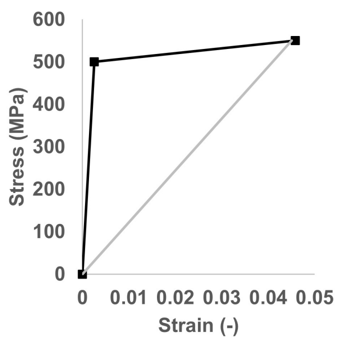

Figure 4.6: Stress-strain curve of reinforcement steel modelled as a 2 segmented material.

For each segment, it is needed to assign: the Young's modulus, the shear modulus, the tensile strength and the compressive strength. The bearing capacities of the elements can be determined with the material properties and the size of the element. For example, the axial bearing capacity of an element in compression is determined by the cross sectional area and compressive strength of the element. The stress (σ) in the elements is determined by the axial force (F) only, by:

$$\sigma = \alpha \left(\frac{F}{A} \right) \tag{4.12}$$

With $\alpha = 1$

The first calculation is performed with all elements in the first segment of their material input. After calculating the stresses, the element with the highest stress/strength ratio is assigned with the material properties of the second segment, if this segment is present. If there is no second segment for this element, the element is removed from the mesh. All the stresses due to the first load step are removed. The load is applied again, and a second linear elastic calculation is performed. The element with the highest stress/strength ratio gets material properties assigned of the next segment. This means that a second element is having material properties assigned of the second segment. If this element does not have a second segment, it is removed from the mesh. If the element that had the highest stress/strength ratio in the first calculation, is again the element with the highest stress/strength ratio, it is having properties assigned of the third segment, if this is segment is present. This procedure is repeated, until a predefined stop criteria is reached. As stop criteria a certain deflection or load of the model can be chosen. The elements that are removed from the mesh are stored in a data file and labelled as damaged elements. By post processing of the data of the simulation, the deformed elemental lengths are calculated and compared with the initial elemental lengths with:

$$L_{initial} = \sqrt{(x_{1,i} - x_{2,i})^2 + (y_{1,i} - y_{2,i})^2 + (z_{1,i} - z_{2,i})^2} \tag{4.13}$$

$$L_{deformed} = \sqrt{(x_{1,d} - x_{2,d})^2 + (y_{1,d} - y_{2,d})^2 + (z_{1,d} - z_{2,d})^2} \tag{4.14}$$

$$Crackwidth_{potential} = L_{deformed} - L_{initial} > 0 \tag{4.15}$$

In these formulas, $x_{1,i}$, $y_{1,i}$, $z_{1,i}$, $x_{2,i}$, $y_{2,i}$, and $z_{2,i}$ are the initial coordinates of the nodes of an element and $x_{1,d}$, $y_{1,d}$, $z_{1,d}$, $x_{2,d}$, $y_{2,d}$, and $z_{2,d}$ are the coordinates of the nodes of the deformed element. If the deformed length ($L_{deformed}$) is larger than the initial elemental length ($L_{initial}$), there is a potential crack, where the potential crack width the difference between the deformed length and the initial length is. If the element with a potential crack is also a damaged element, it is a real crack.

4.2.2. Hybrid Concrete Beams

In case a hybrid beam is modelled, part of the concrete elements are assigned a different material type, and therefore these elements are different material properties assigned (Figure 4.7). The mesh is not altered for this. Elements that have on one end a concrete node and on the other end a SHCC node, are labelled as interface elements. Therefore, these interface elements are assigned to a different element type and different material properties.

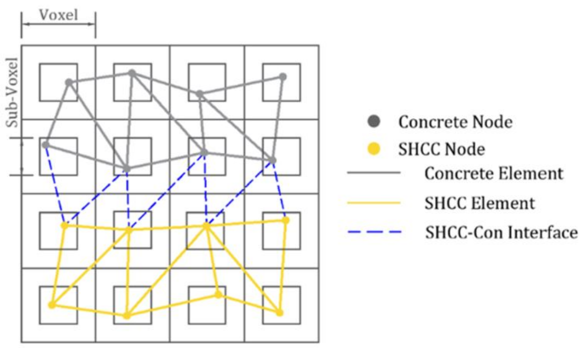

Figure 4.7: 2D schematization of mesh generation of the Delft Lattice model for a hybrid material (Mustafa et al., 2022).

4.3. Model Setup

The material properties of the lattice elements need to be determined. There are multiple possibilities for determining these material properties. One way is output modelling, where the material input of the elements are iterative altered, to find a desired structural response of the model. Another way is input modelling, where the material input of the elements are determined with a theoretical model. As only recently macro scale lattice models are used for the simulation of the structural behavior of reinforced concrete, this section investigates the effect of different modelling parameters on the structural behavior of lattice models. The effects of these different modelling parameters are used to develop a representative macro scale lattice model for the beams investigated in this study.

4.3.1. Concrete

Firstly, the concrete material properties are calibrated on a 25 mm voxel (mesh) sized 250 x 250 x 500 mm concrete prism model (Figure 4.8). A 25 mm mesh size is used, in order to reduce the computational time. The model uses cylindrical beam elements, which is used in all lattice models in this study. The prism is loaded axially from the top by imposing a displacement to the top surface. The bottom part of the prism is fixed. The elements directly connected to the top and bottom surfaces cannot fail, as no fracture law is prescribed for these elements. Concrete is modelled as a 1-segmented material. This means that, concrete beam elements are considered elastic-brittle.

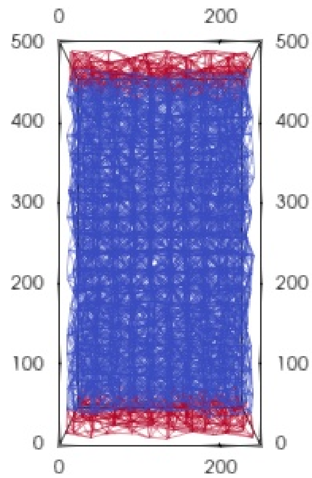

Figure 4.8: Lattice prism model with a sample size of 250 x 250 x 500 mm and a mesh size of 25 mm. Red = constrained elements. Blue = unconstrained concrete elements.

Concrete is calibrated for theoretically found stiffness and strength properties for concrete class C30/37 (Table 4.1). The calibration starts by adjusting the elemental radius, such that the average Young's modulus of the model is similar to the Young's modulus (E) used as material property for the elements. During the process of calibration, a higher Young's modulus, compared to the theoretically Young's modulus, has been adopted as material input. As their difference is small, it is expected to have insignificant influence on the simulations of the numerical models. The average Young's modulus of the model is referred to as the global model response, whereas the material properties of the individual elements are referred to as model input. With the Young's modulus of the model calibrated, the tensile strength (f_t) and compressive strength (f_c) are calibrated, such that the average failure stress of the model response equals the theoretically found material properties (Table 4.1). The shear modulus (G) can be determined by the Young's modulus, with a 0.2 Poisson ratio (ν) of concrete, with:

$$G = \frac{E}{2(1+\nu)} \tag{4.16}$$

The average failure stress of the model is found by:

$$\sigma = \frac{F_{total}}{A} \tag{4.17}$$

In this formula, F_{total} is the sum of the reaction forces at a certain load step and A is the cross sectional area of the prism.

Table 4.1: Concrete material properties inputted for the concrete elements (model input), found upon simulation of the model (global model response) and belonging to concrete class C30/37 (theoretical).

Property	Model input	Global Model response	Theoretical
Radius (mm)	10.50	-	-
E (MPa)	33119	32320	32837
G (MPa)	13800	13466	13678
f_c (MPa)	-70.00	-39.83	-38.00
f_t (MPa)	3.90	3.00	2.90

The calibrated prism shows the formation of a single crack at the center of the height (Figure 4.9). After cracking, a steep softening branch is found.

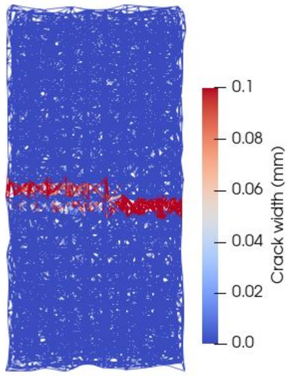

Figure 4.9: Cracking pattern of 25 mm mesh sized concrete prism when loaded in tension

Effect of changing mesh size
In a previous study by (Mustafa et al., 2022), where the 200 mm high hybrid R/SHCC beams of (Singh, 2019) were modelled, a 10 mm mesh sized 100 x 100 x 200 mm prism was used, to calibrate the material properties. As this current study is using a 25 mm mesh size, the effect of the increase of mesh size is investigated. This effect is investigated by comparison of three prism models (Figure 4.10):

- Prism 1: 100 x 100 x 200 mm prism with a mesh size of 10 mm
- Prism 2: 100 x 100 x 200 mm prism with a mesh size of 25 mm
- Prism 3: 250 x 250 x 250 mm prism with a mesh size of 25 mm

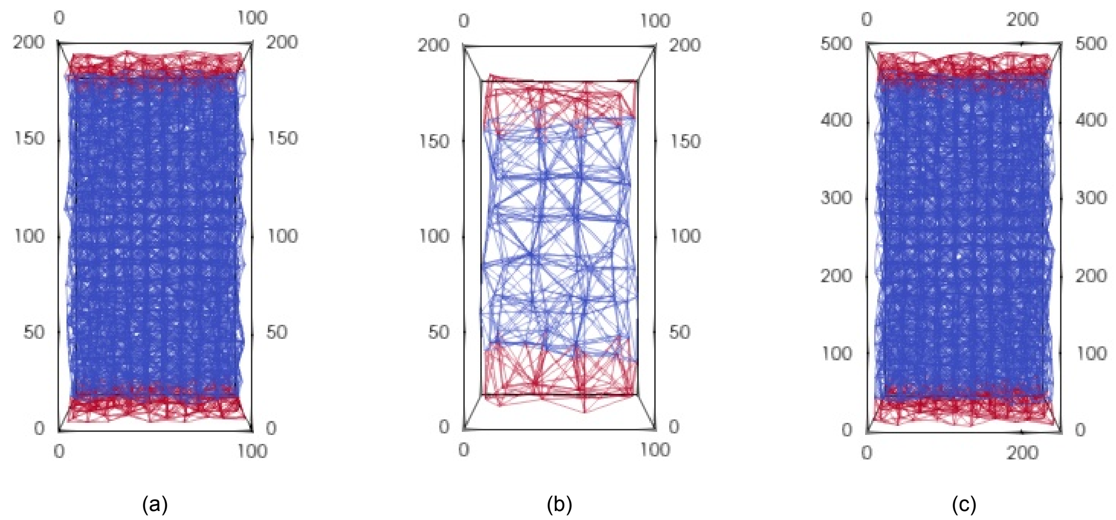

Figure 4.10: Prisms sampled in the lattice model with (a) a sample size of 100 x 100 x 200 mm and a mesh size of 10 mm (prism 1), (b) a sample size of 100 x 100 x 200 mm and a mesh size of 25 mm (prism 2) and (c) a sample size of 250 x 250 x 500 mm and a mesh size of 25 mm (prism 3). Red = constrained elements. Blue = unconstrained concrete elements.

All the prisms are modelled in the same way, with the same elemental material input as specified before (Table 4.1). The 10 mm mesh sized model is modelled with an elemental radius of 4.2 mm, which is the similar ratio between elemental radius and mesh size as for the 25 mm meshed prisms. The stress-strain curves of the global model responses are compared of these prisms (Figure 4.11). The strain (ε) is determined by dividing the imposed deformation ($u_{imposed}$) over the height ($h_{sample} - meshsize$) of the sample by:

$$\varepsilon = \frac{u_{imposed}}{h_{sample} - meshsize} \tag{4.18}$$

Upon formation of cracks, the strain remains to be determined over the full height of the sample. Thereby, the strain as defined in this study, is not solely including the material strain, but also the deformation of a crack (crack width).

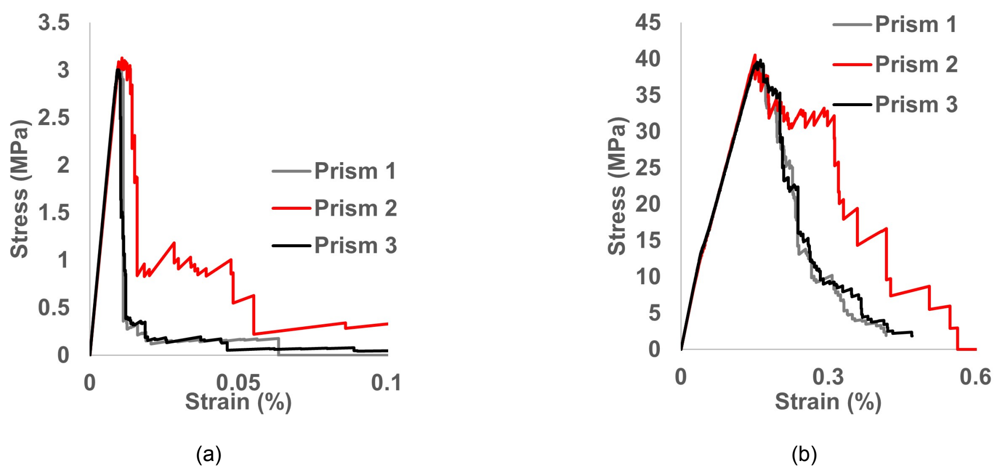

Figure 4.11: Stress-strain curves for prism models of a sample size of 100 x 100 x 200 mm and a mesh size of 10 mm (prism 1), a sample size of 100 x 100 x 200 mm and a mesh size of 25 mm (prism 2) and a sample size of 250 x 250 x 500 mm and a mesh size of 25 mm (prism 3) in (a) tension and (b) compression.

Upon comparison of the stress-strain curves of the different prisms, it is found that, the 100 x 100 x 200 mm prism with 25 mm mesh size (prism 2) has a less steep softening branch, compared to the global model responses of the 100 x 100 x 200 mm prism with 10 mm mesh size (prism 1) and the 250 x 250 x 500 mm prism with 25 mm mesh size (prism 3). In addition, the softening branch is found to be smoother for prism 1 and 3 compared to prism 2. The softening branch is the post peak behavior of the stress-strain curve. These differences in the softening branches of prism 2 are found both in compression and tension. The peak stresses are insignificantly affected. The explanation for this behavior can be found in the limited number of elements representing the prisms volume. Therefore, if an element fails a large portion of the volume of the model is removed. This results in a relative large fracture length, releasing a large portion of the stored strain in the model. In the other prisms the elements represent a relative smaller part of the total volume of the prism. In prism 1 this is obtained by a smaller mesh size, leading to more elements to represent the same volume. In prism 3 the sample size is increased such that an element, made from a 25 mm mesh size, represents the same portion of the total volume compared to prism 2. Therefore, the amount of elements relative to the sample size affect the global model response. Upon increasing the mesh size, without increasing the sample size, the ductility of the model increases. Therefore, it is recommended to pay attention to the relation between mesh size and sample size when increasing the mesh size. As the softening branch of prism 3 is smoother and the brittle nature of concrete is resembled well, the study is continued with the results of prism 3.

4.3.2. SHCC

SHCC is calibrated for the material properties found in literature, with use of a prism sample size of 250 x 250 x 500 mm and a mesh size of 25 mm. The same relation between Young's modulus and Shear modulus as for concrete is used. The strain hardening behavior of SHCC is modelled by modelling the material with 7 segments in order to obtain at least 2% strain with the simulated prism (Table 4.2). In compression SHCC behaves brittle, and therefore only the first segment has compressive strength (Table 4.2). The remaining six compressive segments have a low strength assigned in order to prevent zero entries in the stiffness matrix and divisions by zero in the computations of the model.

Table 4.2: SHCC material properties modelled with (a) initial segment showing input properties for an element (material input), output of the model (global model response) and literature found properties and (b) full material input of SHCC. *Properties found in numerical study of (Mustafa et al., 2022).

Property	Model input	Global model response	Literature*
Radius (mm)	10.50	-	-
E (MPa)	18500	18332	18500
G (MPa)	7708	7638	7708
f_c (MPa)	-70.00	-44.58	-49.30
f_t (MPa)	3.50	2.95	2.99

(a)

Property/Segment	1	2	3	4	5	6	7
E (MPa)	18500	13875	2000	1000	750	500	150
G (MPa)	7708	5781	833	417	313	208	62
f_c (MPa)	-70.00	-0.10	-0.10	-0.10	-0.10	-0.10	-0.10
f_t (MPa)	3.50	2.50	2.50	2.50	3.00	4.00	5.50

(b)

The 7 segmented material input results in a strain hardening response of the model with a ductility of 2.36%. In compression the model response is showing a steep softening branch (Figure 4.12). The cracking pattern is found to show multiple localized cracks, spread over the height of the sample. The sample is able to form cracks, without significant strength loss. In comparison with the concrete compressive strength, it is found that, the ductility of the SHCC is larger.

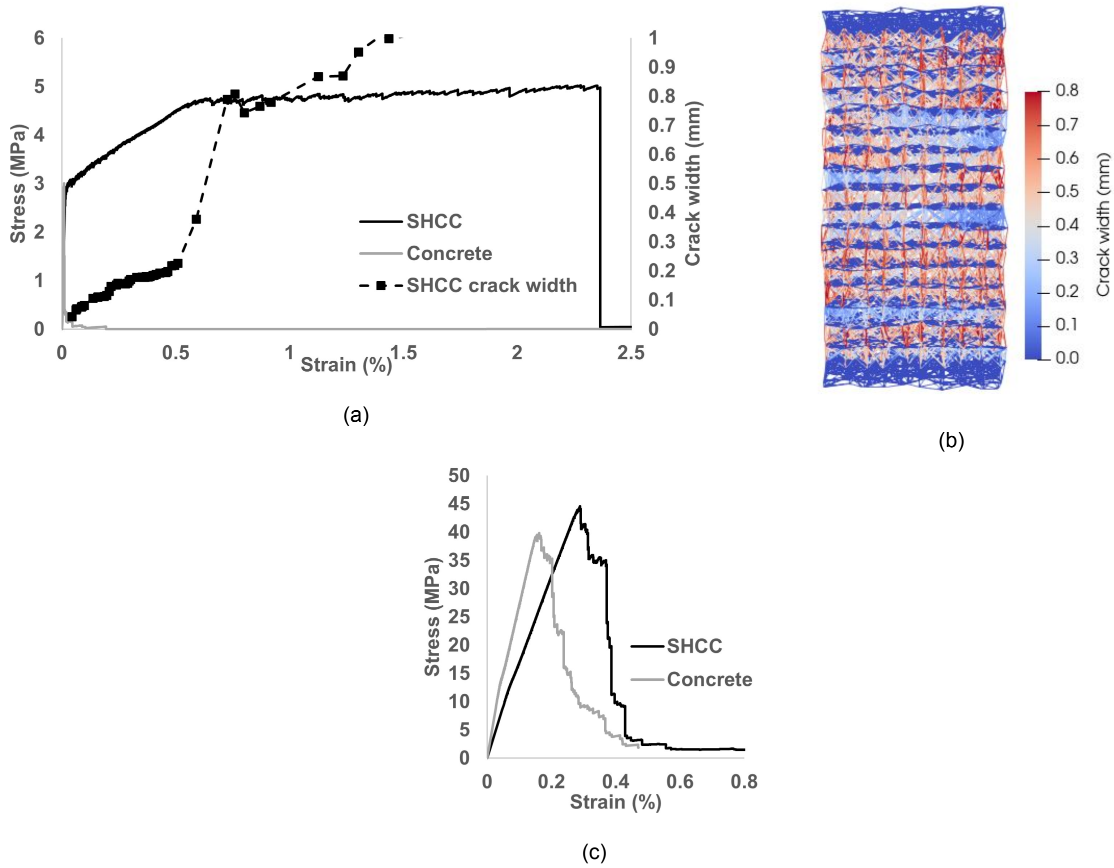

Figure 4.12: Global model response of SHCC prism model in (a) tension, (b) cracking pattern at 2.36% tensile strain and (c) stress-strain curve in compression.

The effect of the number of segments in the material input

In a previous study by (Mustafa et al., 2022), SHCC has been modelled with use of 3 segments instead of 7 segments material input in tension (Table4.3). 3 segments were used in order to be able to use a 10 mm mesh size and limit the computation time. As this study uses a 25 mm mesh size, it is possible to use 7 segments as material input for SHCC and still limit the computation time. The effect of implementing a 7 segmented material input relative to a 3 segmented material input for SHCC in tension is investigated (Figure 4.13).

Table 4.3: 3 segmented SHCC material input as used in a previous study by (Mustafa et al., 2022).

Property/Segment	1	2	3
E (MPa)	18500	9250	1125
G (MPa)	7708	3854	469
f_c (MPa)	-60	-60	-60
f_t (MPa)	3.00	3.75	4.5

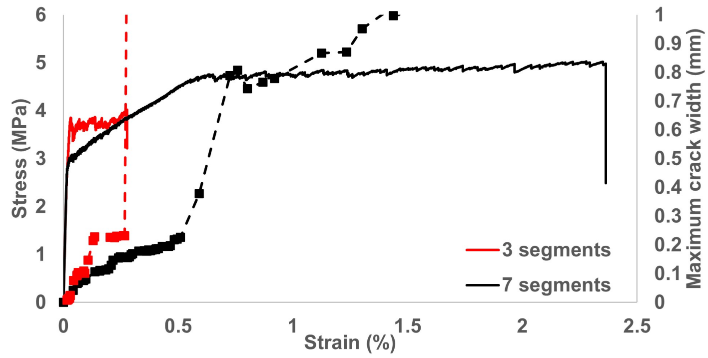

Figure 4.13: Global model response of the SHCC prism in tension for 7 segmented material input compared to 3 segmented material input. Solid = stress-strain. Dashed = crack width - strain.

It is found that, the 7 segmented material input leads to a higher ductility. The ductility for the 7 segmented material input is 2.36%, whereas the ductility for the 3 segmented material input is 0.28%. The limited ductility for the 3 segmented material input has also been reported by (Mustafa et al., 2022). If the maximum crack widths are compared, it is found that these are similar in size for both material inputs. Additionally, the 3 segmented material input shows the first crack to be formed at a stress of 2.21 MPa, whereas the first crack in the 7 segmented material input is formed at a stress of 2.43 MPa. The peak stress found in the 3 segmented material input is 4.02 MPa, whereas the 7 segmented material input is found to have a peak stress of 5.02 MPa. The difference in first cracking stress and peak stress can be explained by the difference in tensile strength of the segments used, as the 7 segmented material used a higher strength for the first segment and the final segment compared to the 3 segmented material input. The increase in ductility can however be explained by the number of segments used, as the 3 segmented material input was only able to provide a global model response, without too large local instabilities, if the last segment was provided a Young's modulus of at least 1125 MPa. The maximum allowed material strain for the last segment of a beam element in the 3 segmented material is:

$$\varepsilon = \frac{f_{t,finalsegment}}{E_{finalsegment}} = \frac{4.5}{1125} = 0.4\%$$

A local instability occurs when after removing a failed element and reloading the mesh, other elements fail at a lower load compared to the previously failed element (Van Mier, 2012). Local instabilities can be observed as a rough, saw-tooth like, part of the load-deflection curve. The 7 segmented material input was able to provide a global model response, with only small local instabilities, with the last segment having a Young's modulus of 150 MPa. The maximum allowed material strain for the last segment of a beam element is therefore:

$$\varepsilon = \frac{f_{t,finalsegment}}{E_{finalsegment}} = \frac{5.5}{150} = 3.67\%$$

The local instabilities, which are found to be larger in the 3 segmented material, can be explained by the large jumps in stiffness, upon assigning a beam element to the next material segment. The difference in local instabilities can be seen from the stress-strain curves of the global model response as, the 7 segmented stress-strain curve is smoother compared to the 3 segmented stress-strain curve. As the 7 segmented material input allows for a more realistic strain-hardening curve for SHCC, it is recommended to use the 7 segmented material input.

Constant elemental radius vs. varying elemental radius

Up to now the beam elements of the lattice models are assigned a constant elemental radius. The lattice nodes are randomly generated in sub-voxels, leading to a semi-randomly lattice of beam elements, as explained in section 4.2. Therefore, each beam represents a different volume of the sample. With use of a constant elemental radius, the amount of volume a beam element represent is solely dependent on the length of the element. A possible way to overcome this simplification of the model is by varying the elemental radius among the elements. This can be done with help of Voronoi polygons of the elemental nodes. From these Voronoi polygons the area facet is determined. This area (A) can be translated into an elemental radius (r) with:

$$r = \sqrt{\frac{A}{\pi}} \tag{4.19}$$

As each element has a different area facet, a different radius is assigned to the element. By varying the radius of the elements the stiffness of each element is different introducing an additional heterogeneity source besides the varying elemental length. The effect of the varying elemental radius on (Voronoi radius) the global model response is investigated by comparing with constant elemental radius input (see figure 4.14).

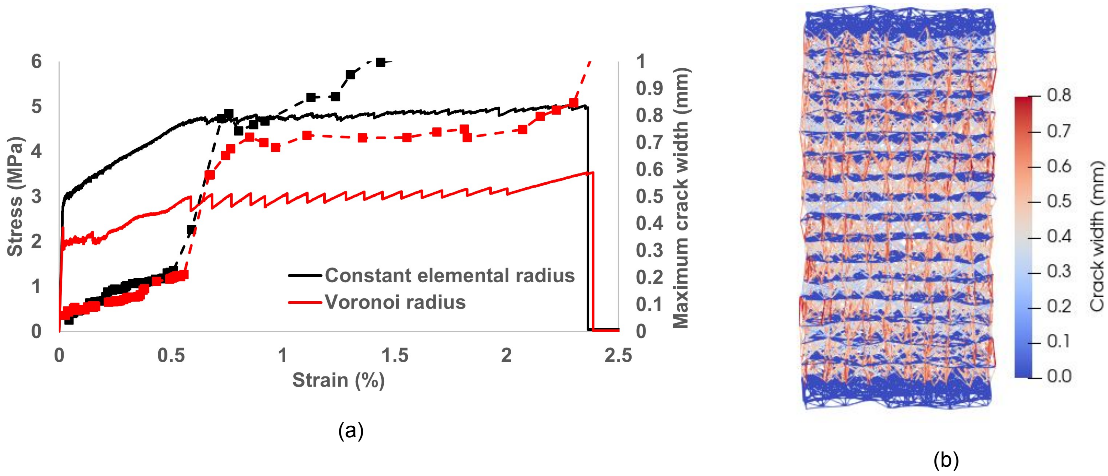

Figure 4.14: Global model response of SHCC prism model for (a) comparison of constant elemental radius and varying radius determined by Voronoi polygons and (b) cracking pattern at 2.30% tensile strain for the varying radius model. Solid = stress-strain. Dashed = crack width - strain.

The result is a lower strength of the model, as the constant elemental radius model has a peak strength of 5.02 MPa, whereas the Voronoi radius model has a peak strength of 3.53 MPa. Initially, little differences are found in the maximum crack width, however after 0.85% strain the Voronoi radius model shows little increase in maximum crack width. A similar ductility of 2.39% is found for the Voronoi radius model compared to the 2.36% ductility of the constant elemental radius model. The stability of the Voronoi radius model is lower, which can be seen by the smoothness of the stress-strain curve (Figure 4.14). The maximum crack widths are initially similar with the constant elemental radius model, but hardly any increase in maximum crack width is found after 0.72% for the Voronoi radius model. This means that other cracks are formed or smaller existing cracks increase in width. The cracking pattern for this Voronoi radius model shows crack localization over the full height of the prism, whereas the constant elemental radius model showed multiple localized cracks (Figure 4.14). The lower strength found in the Voronoi radius model can be explained by the presence of really weak elements due to the varying of the radius. The radius of the element is controlling the cross sectional area and therefore the axial strength of the element. In the constant elemental radius model all elements have the same radius, leading to the same cross sectional strength. This effect is also reflected upon the stiffness of the global response of the model as the Young's modulus for the Voronoi radius model is 14168 MPa compared to the 18333 MPa of the constant radius model. The increased instability of the global output of the model with Voronoi radius can also be found in the presence of really weak elements, as upon redistributing the load after removing an element, the next element can fail at a lower strength. The difference in maximum crack widths after reaching 0.85% strain is also linked to this, as more elements fail instead of the widening of existing cracks. As the constant elemental radius model shows a more realistic cracking pattern, it is decided to continue with constant elemental radius models.

Output modelling versus Input modelling
The SHCC material is calibrated by changing the elemental input in order to find a satisfying global model response (output modelling). This output modelling results in lowering the material input strength properties in segment 2 to 5 (Table 4.2). Such a material input seems contradicting, if strain hardening behavior should be modelled. In order to see the effect of this output modelling approach, another material input is made, which shows no variation in tensile strength among the segments (Table 4.4). The material input with constant strength over the segments is input driven (input modelling). The global model responses of the output modelling approach is compared with the global model response of the input modelling approach (see figure 4.15).

Table 4.4: 7 segmented SHCC material input with constant strength over the segments used for the input modelling approach.

Property/Segment	1	2	3	4	5	6	7
E (MPa)	18500	13875	2000	1000	750	500	150
G (MPa)	7708	5781	833	417	313	208	63
f_c (MPa)	-70	-0.1	-0.1	-0.1	-0.1	-0.1	-0.1
f_t (MPa)	3.00	3.00	3.00	3.00	3.00	3.00	3.00

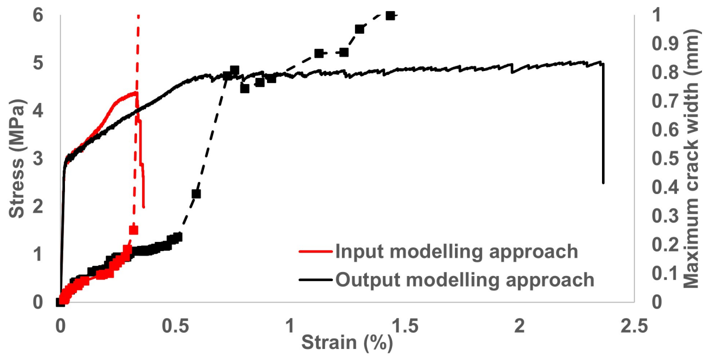

Figure 4.15: Global model response comparison the output modelling approach and the input modelling approach of the prism model in tension. Solid = stress-strain. Dashed = crack width - strain.

Upon comparison of the global model responses, the elastic branches are found to be very similar for both the modelling approaches. Differences occur in the strain hardening section, where the input modelling approach shows a steeper hardening branch. Additionally, it is found that the ductility of the input modelling approach is limited to 0.34%, whereas the ductility of the output modelling approach is 2.36%. The maximum crack widths are found to be similar until the input modelling approach model fails. The strain-hardening observed in the input modelling approach can be explained by the semi-randomly created lattice mesh. All the lattice elements have the same elemental strength, independent of the material segment. Therefore, the load distribution over the elements is dependent on the stiffness and orientation of the beam elements in the lattice. Both the stiffness and orientation vary among the elements, due to the semi-randomly created lattice mesh. As the weakest element is the first element to be placed in the next segment, the stiffness of this element decreases due to a reduction in Young's modulus. Upon reloading the lattice, other elements become relative stiffer and are therefore carrying more load. As these elements had lower stress/strength ratios in the first load step, the lattice is able to withstand a higher load. The ductility of the input modelling approach is low, because at a certain point a region of elements are in the last segment and upon removing of the weakest element the model starts uncontrollable cracking. As the ductility of the output modelling approach is more realistic, compared to the input modelling approach, it is decided to continue with the output modelling approach.

4.3.3. Reinforcement

Reinforcement is modelled by creating beam elements between predefined node locations, as described in subsection 4.2.1. The beam elements are cylindrical and have a radius of 4 mm assigned, which corresponds to the designed 8 mm diameter bars (Chapter 3). A two-segmented material input is provided, to obtain a bi-linear stress-strain curve (Figure 4.6). Steel is modelled to yield at 500 MPa and fail at an ultimate strain of 4.5% (Table 4.5). For steel, a Poisson ratio of 0.3 is used in order to relate the Young's modulus with the shear modulus.

Table 4.5: Material input for steel reinforcement.

Property/Segment	1	2
Radius (mm)	4.00	4.00
E (MPa)	200000	12000
G (MPa)	76923	5000
f_c (MPa)	-500.00	-550.00
f_t (MPa)	500.00	550.00

4.3.4. Rebar-concrete interface

The effective span of the 200 mm reinforced concrete beam (RC200) is modelled (Figure 4.16). A 25 mm mesh is used. The beam model is loaded in four point bending, with a constant bending moment section of 500 mm. The simulation is load controlled. The beam is simply supported. The RC200 beam model is used to investigate the effect of multiple modelling possibilities for the rebar-concrete interface on the force-displacement and crack width pattern. The aim is to find a modelling approach that leads to similar structural behavior, as was found in the experiments conducted by (Singh, 2019).

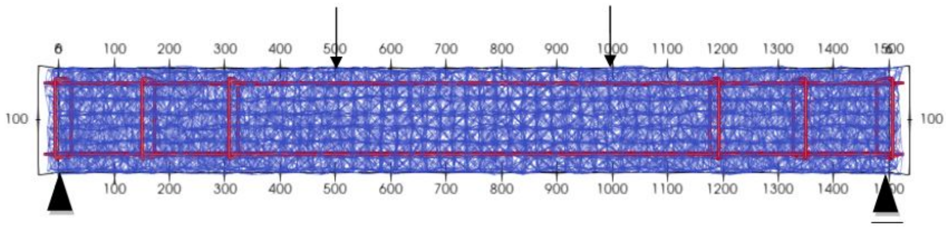

Figure 4.16: 200 mm high reinforced concrete beam model. Red = reinforcement. Blue = concrete elements. Arrow = load application point. Triangle = support point.

A good modelling approach is found for a 15 segmented input of the rebar-concrete interface (Table 4.6). The input is determined by the pull-out envelope (Figure 4.17). Three slip criteria are used (Harajli, 2009):

$$s_1 = 0.15c_0 \tag{4.20}$$

$$s_2 = 0.35c_0 \tag{4.21}$$

$$s_3 = c_0 \tag{4.22}$$

c_0 is the clear distance between the ribs of the reinforcement bar. A clear rib distance of 8 mm is used for ribbed bars. The elemental radius is determined by the maximum bonding stress (u_m) with (Harajli, 2009):

$$u_m = 2.57\sqrt{f_c} \tag{4.23}$$

$$r = m\sqrt{\frac{0.1u_m D}{4E_c s_1 0.1^{\frac{10}{3}}}} \tag{4.24}$$

D is the bar diameter of the reinforcement, E_c is the Young's modulus of concrete, f_c is the compression strength of concrete and m is the mesh size of the lattice model. The elemental radius for interface elements is 10.68 mm.

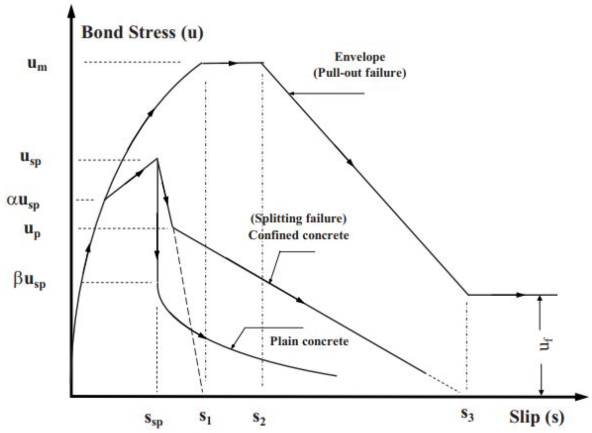

Figure 4.17: Pull-out envelope used for input as rebar-concrete interface (Harajli, 2009).

Table 4.6: Rebar-concrete interface material input based on the pull-out envelope.

Property/Segment	1	2	3	4	5	6	7	8	9	10
E (MPa)	52570	10431	4050	2070	1230	804	560	411	312	244
G (MPa)	21904	4346	1687	862	512	335	234	171	130	102
f_c (MPa)	-1.97	-3.94	-5.90	-7.87	-9.84	-11.81	-13.77	-15.74	-17.71	-19.68
f_t (MPa)	1.97	3.94	5.90	7.87	9.84	11.81	13.77	15.74	17.71	19.68

Property/Segment	11	12	13	14	15
E (MPa)	105	60	37	22	13
G (MPa)	44	25	15	9	5
f_c (MPa)	-19.68	-16.48	-13.28	-10.08	-6.89
f_t (MPa)	19.68	16.48	13.28	10.08	6.89

The experiment showed a bearing capacity of 62.4 kN (Singh, 2019), where the lattice model simulates an ultimate capacity of 66.4 kN (Figure 4.18). The deformation capacity of the lattice model (27.97 mm) is found to be higher, compared to the experimental results (23.98 mm). The 0.3 mm crack width limit is reached at a deflection of 3.80 mm for the numerical model, whereas a deflection of 3.22 mm was found in the experiments. The cracking pattern simulated, when the 0.3 mm crack width limit is reached, is similar to the experimentally found cracking pattern. The cracking pattern of the lattice model shows 5 localized cracks, whereas the experiment showed only 4. The difference in the number of cracks is found by the development of additional cracks closely to earlier formed cracks in the numerical model. This is not observed in the experiments. The numerical results of (Mustafa et al., 2022) are used as comparison (Num10mm). Their numerical models were designed with a 10 mm voxel size. Upon comparison of the numerical results of this previous study (Num10mm) with this current study (Num25mm), it is found that, similar structural behavior is found both in the load-deflection curve as in the cracking pattern. It should be noted that, Mustafa et al., 2022 used a different rebar-concrete material input. With these differences in mind, it is found that, the coarser voxel size, as used in this current study, is not affecting the ability of the lattice model to simulate the structural behavior of the reinforced concrete beam.

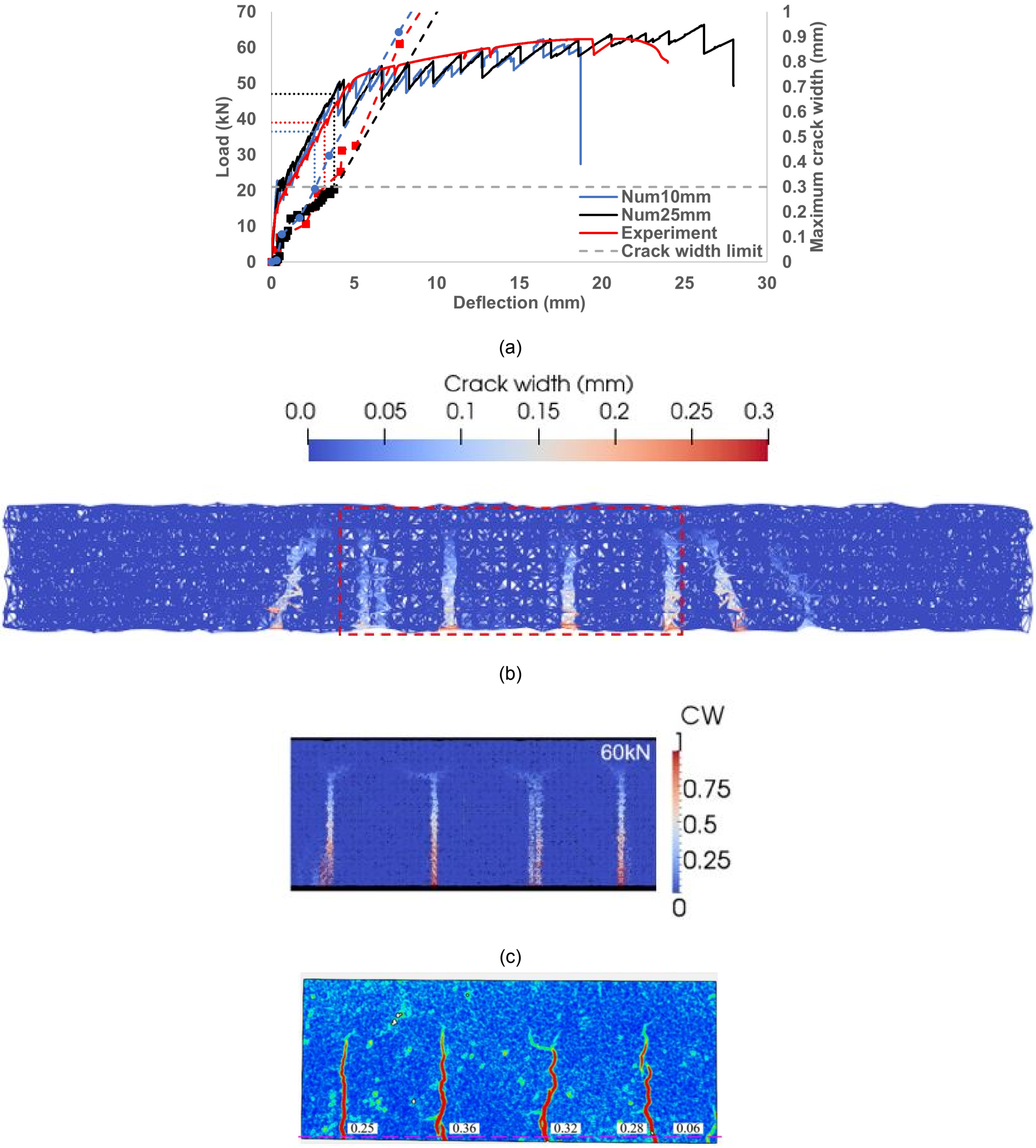

(a) (b) (c) (d)

Figure 4.18: Comparison of experimental results and numerical results of RC200 for (a) load-deflection curve vs. crack width - deflection curve, (b) cracking pattern at a deflection of 3.80 mm from Num25mm, (c) cracking pattern at a deflection of 17.67 mm from Num10mm, and (d) experimentally cracking pattern at a deflection of 3.22 mm. Solid = load-deflection. Dashed = crack width - deflection. Experimental results obtained from (Singh, 2019). Num25mm = numerical results of RC200 beam with 25 mm voxel size. Num10mm = numerical results of RC200 beam with 10 mm voxel size. Num10mm results are obtained from (Mustafa et al., 2022).

Effect of the clear rib distance in the pull-out envelop approach

The pull-out envelope approach, as used in the previous simulation, leads to good comparison with the experimental results. Therefore, the pull-out envelop is desired to be used for the numerical models. However, one of the beams studied in this thesis has smooth and Vaseline treated reinforcement bars. In order to model the rebar-SHCC bond for this beam, the clear rib distance and the strength is changed with use of the same pull-out envelop. The effect of the clear rib distance (c_0) on the load-deflection curve and the crack widths-deflection curves are investigated for different clear rib distances (Figure 4.19).

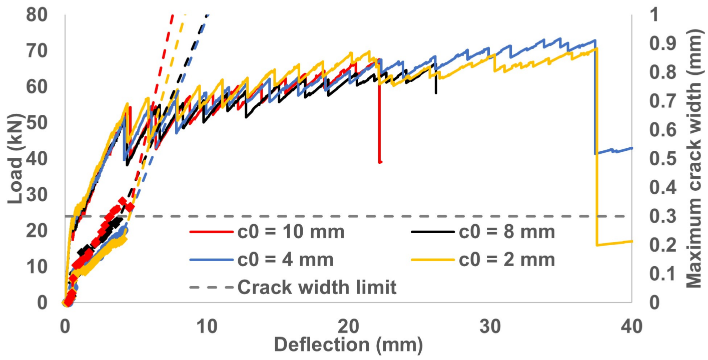

Figure 4.19: Comparison of load-deflection vs crack width - deflection curve of the reinforced concrete beam model for different clear rib distances (c_0).

It is found that, the clear rib distance is mainly affecting the deformation capacity, as a larger clear rib distance decreases the deformation capacity, and a smaller clear rib distance increases the deformation capacity of the beam (Figure 4.19). No significant differences are found in the ultimate load upon changing the clear rib distance. This can be explained by the ultimate bond strength being solely dependent on the compressive strength of the concrete. Therefore, the bond strength is not altered upon changing the clear rib distance. As the ultimate bond strength is not changed, the maximum crack widths do also not change significantly. The increase in deformation capacity for a smaller clear rib distance can be explained by the slip criteria of the pull-out envelop. A smaller clear rib distance, allows for smaller bond slip to occur for the slip criteria. Therefore, the bond is more brittle for a smaller clear rib distance. The increase in brittleness of the bond leads to earlier failure of the interface elements. This results in more release of stored strain energy, allowing for a higher deformation capacity. This supports the idea of applying smooth reinforcement bars in the beam to improve the crack controlling behavior, similar as a smooth concrete-SHCC interface was found to improve the crack controlling behavior (Chapter 2).

Effect of elemental radius of interface elements

Upon decreasing the clear rib distance, the elemental radius of the interface elements increases. The effect of changing the elemental radius of the interface elements on the structural behavior of the reinforced concrete beam is studied. Therefore, a 7 segmented rebar-concrete interface input is used (Table 4.7). This material input is manually determined, without the use of the pull-out envelop. This allows to vary the elemental radius, without affecting other interface properties. The load-deflection curves and the crack width-deflection curves are compared (Figure 4.20).

Table 4.7: 7 segmented material input for interface elements used for studying effect of radius of interface elements.

Property/Segment	1	2	3	4	5	6	7
E (MPa)	33119	2000	1500	1000	750	500	400
G (MPa)	13800	833	625	417	313	208	167
f_c (MPa)	-32.5	-32.5	-32.5	-32.5	-32.5	-32.5	-32.5
f_t (MPa)	3.25	3.25	3.25	3.25	3.25	3.25	3.25

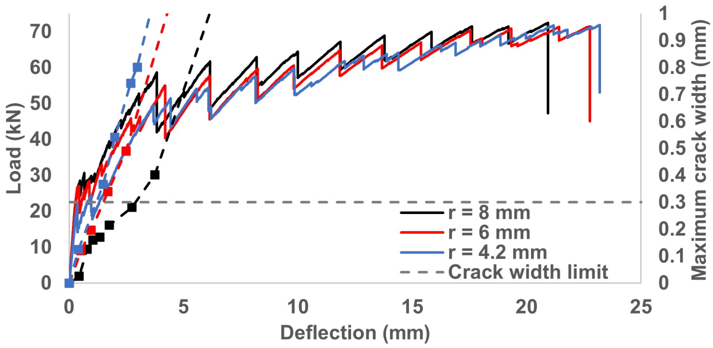

Figure 4.20: Comparison of load-deflection (solid) vs crack width - deflection curve (dashed) of the reinforced concrete beam model for different radius of interface elements.

It is found that, upon increasing the radius of the interface elements, the deformation capacity of the beam decreases, the stiffness of the model increases and the load at which the first cracks are formed increases. In addition, the maximum crack widths decrease. The decrease in maximum crack width, by an increasing elemental radius of the interface elements, can be explained by the stronger bond. A stronger bond leads to a shorter bonding length of the reinforcement. Therefore, more cracks can be formed, which reduces the maximum crack width. The increase in strength for an increasing radius is caused by the increase in cross sectional area of the interface elements. The increase in stiffness of the model for an increasing radius is caused by the increase in stiffness of the interface elements. Therefore, the interface elements transfer a larger portion of the load from the concrete to the steel. This attributes to the delay in the formation of cracks, which leads to a larger cracking load. Upon crack formation, the rebar-concrete bond is broken and a relative large redistribution of the load is needed, compared to a less stiff bond. This larger redistribution of load leads to larger local instabilities of the simulation. Therefore, the increase in stiffness of the rebar-concrete interface elements, due the increase in radius, is undesired. Lastly, the increase in deformation capacity of the simulation with a smaller radius of the rebar-concrete interface elements could be explained by the lower bond strength, as a lower bond strength leads to earlier delamination of the bond, compared to a simulation with larger elemental radius of the rebar-concrete interface elements. Therefore, more strain energy is released at the rebar-concrete interface.

Effect of strength input of interface elements

Increasing the radius of the interface elements leads to a stronger and stiffer rebar-concrete bond. The effect of the bond strength is studied, by comparison of 2 different 7 segmented bond strength material inputs (Table 4.8). The load-deflection curves versus crack width-deflection curves, of the 2 different interface strengths used in the reinforced concrete beam model, are compared (Figure 4.21).

Table 4.8: 7 segmented material input for interface elements used for studying effect of strength of interface elements for (a) constant tensile strength of 9.5 MPa and (b) constant tensile strength of 12.5 MPa.

Property/Segment	1	2	3	4	5	6	7
E (MPa)	33119	2000	1500	1000	750	500	400
G (MPa)	13800	833	625	417	313	208	167
f_c (MPa)	-95	-95	-95	-95	-95	-95	-95
f_t (MPa)	9.50	9.50	9.50	9.50	9.50	9.50	9.50

(a)

Property/Segment	1	2	3	4	5	6	7
E (MPa)	33119	2000	1500	1000	750	500	400
G (MPa)	13800	833	625	417	313	208	167
f_c (MPa)	-125	-125	-125	-125	-125	-125	-125
f_t (MPa)	12.50	12.50	12.50	12.50	12.50	12.50	12.50

(b)

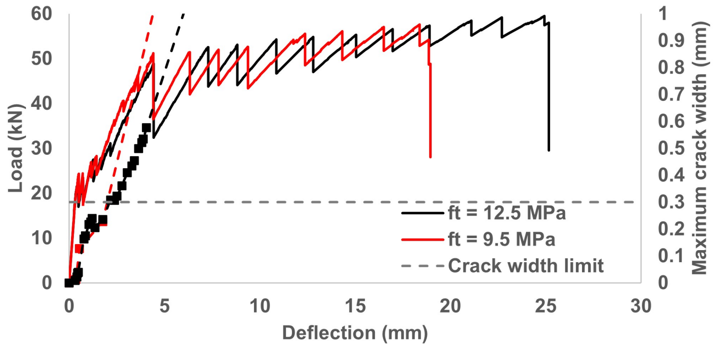

Figure 4.21: Comparison of load-deflection curve (solid) vs. crack width - deflection curve (dashed) for varying strengths of interface elements in the 200 mm high reinforced concrete beam model.

It is found that, an increased strength of the rebar-concrete interface elements leads to an increased deformation capacity and a reduced maximum crack width. This is caused by the stronger bond being able to form more cracks, due to a smaller bonding length. As more cracks are formed, the maximum crack width reduces. The deformation capacity increases due to more release of strain energy and a delayed failure of bond elements. This is similar as was found for the increase in cross sectional area due to an increase in elemental radius of the interface elements. Therefore, the reduction in maximum crack widths upon increasing the elemental radius of the interface elements, can be attributed to the increase in strength of the interface elements. In addition, there is no difference in first cracking strength for the different bond strengths. Therefore, the difference in first cracking strength, as observed in the comparison of the structural behavior of models with different elemental radius of the interface elements, can be attributed to the change in stiffness of the rebar-concrete interface elements.

Rebar-concrete interface of smooth reinforcement bars

Determining the material input for the rebar-concrete interface elements, based on the pull-out envelop, led to a good comparison of the structural behavior of the lattice model and the conducted experiments by (Singh, 2019). Therefore, this material input is used in the simulations of the beams studied in this thesis. However, one of the beams studied in this thesis has smooth and Vaseline treated reinforcement bars. In order to use the same pull-out envelope, as used for the ribbed rebar-concrete interface, for the rebar-concrete interface elements of plain and Vaseline treated reinforcement bars, the effect of the clear rib distance and the bond strength was studied. Upon comparison of different clear rib distances, it was found that, a decrease in the clear rib distance leads to a more brittle bond between rebar and concrete. In addition, a decrease in the bond strength, led to larger crack widths and a lower deformation capacity. In the literature study it was found that, the bond of smooth reinforcement is mainly depending on the chemical adhesion, which is a brittle bond. A bond is called brittle, if the slip is smaller than 0.05 mm (Randl, 2013). Therefore, it is decided to reduce the clear rib distance in the pull-out envelop approach for the smooth reinforcement bar to 0.05 mm. In addition, the bond strength is reduced, as the bars are Vaseline treated, such that the same initial stiffness of the ribbed bond is obtained (Table 4.9). This leads to an elemental radius of the interface elements of 10.68 mm, which is similar to the elemental radius of the interface elements of ribbed rebars.

Table 4.9: Rebar-concrete interface material input for smooth and Vaseline treated longitudinal reinforcement bars.

Property	1	2	3	4	5	6	7	8	9	10
E (MPa)	52570	10431	4050	2070	1230	804	561	411	312	244
G (MPa)	21904	4346	1688	863	513	335	234	171	130	102
f_c (MPa)	-0.012	-0.025	-0.037	-0.049	-0.061	-0.074	-0.086	-0.098	-0.11	-0.12
f_t (MPa)	0.012	0.025	0.037	0.049	0.061	0.074	0.086	0.098	0.11	0.12

Property	11	12	13	14	15
E (MPa)	105	60	37	22	13
G (MPa)	44	25	15	9	5
f_c (MPa)	-0.12	-0.10	-0.083	-0.063	-0.043
f_t (MPa)	0.12	0.10	0.083	0.063	0.043

4.3.5. Concrete-SHCC interface

The interface between concrete and SHCC in the hybrid beam models are modelled with a one segmented material input (Table 4.10). The interface strength is 50% of the concrete strength.

Table 4.10: Concrete-SHCC interface model input.

Property/Segment	1
Radius (mm)	10.50
E (MPa)	33119
G (MPa)	13800
f_c (MPa)	-35.00
f_t (MPa)	2.00

4.4. Numerical results

In this section, the modelling results from both the reinforced concrete beams and the hybrid R/SHCC beams are shown. In the first three subsections the results of the reinforced concrete beams are presented, starting with the 200 mm high beam (RC200). In subsection 4.4.4 - 4.4.7, the results of the hybrid beam models are shown, starting with the 200 mm high hybrid R/SHCC beam (H200). Lastly, in subsection 4.4.8 the results of the beam models are compared.

4.4.1. Reinforced concrete beam of 200 mm height

The 200 mm high reinforced concrete beam is modelled with an effective span of 1500 mm modelled (Figure 4.22). The beam is loaded with two point loads which are each 250 mm from the center line of the beam as described in chapter 3. At one end of the beam the beam is constrained for displacements in all directions. At the other end only the vertical displacement is constrained.

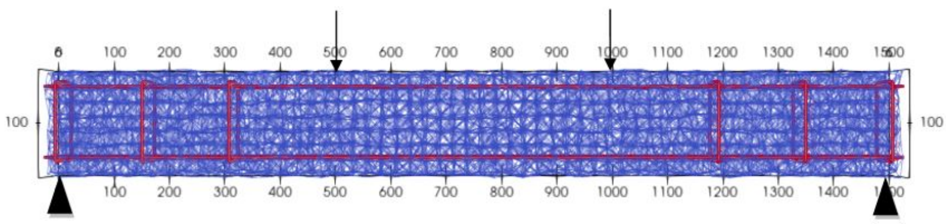

Figure 4.22: Model of 200 mm high reinforced concrete beam. Red = reinforcement. Blue = concrete elements. Arrow = load application point. Triangle = support point.

A maximum load of 66.36 kN is found with a deformation capacity of 27.97 mm (Figure 4.23). The crack width limit of 0.3 mm is reached at a load of 47.01 kN (Table 4.11).

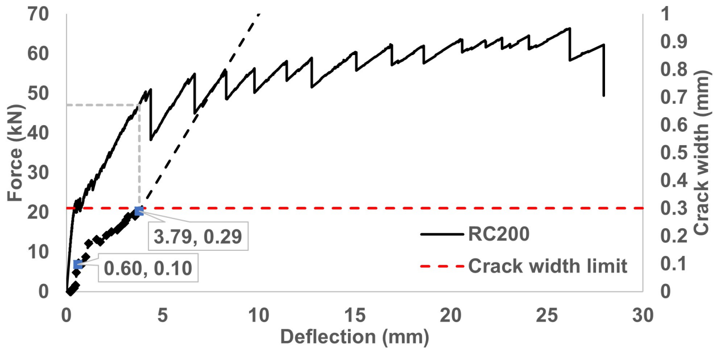

Figure 4.23: Numerical results of RC200 beam with load - deflection curve (solid) and maximum crack width - deflection curve (dashed). The maximum crack widths, of the cracking patterns presented in figure 4.24, are labelled.

Table 4.11: Overview of results of the RC200 beam model.

Key performance indicators	
Ultimate load	66.36 kN
Maximum deflection	27.97 mm
Number of cracks	8
Average crack spacing	63 mm
Load at 0.3 mm crack width	47.01 kN

The final cracking pattern shows 8 localized cracks at the bottom of the beam in the central 500 mm constant bending region (Figure 4.24). Whereas, at a deflection of 3.79 mm, when 0.3 mm crack width is reached, 5 localized cracks are found.

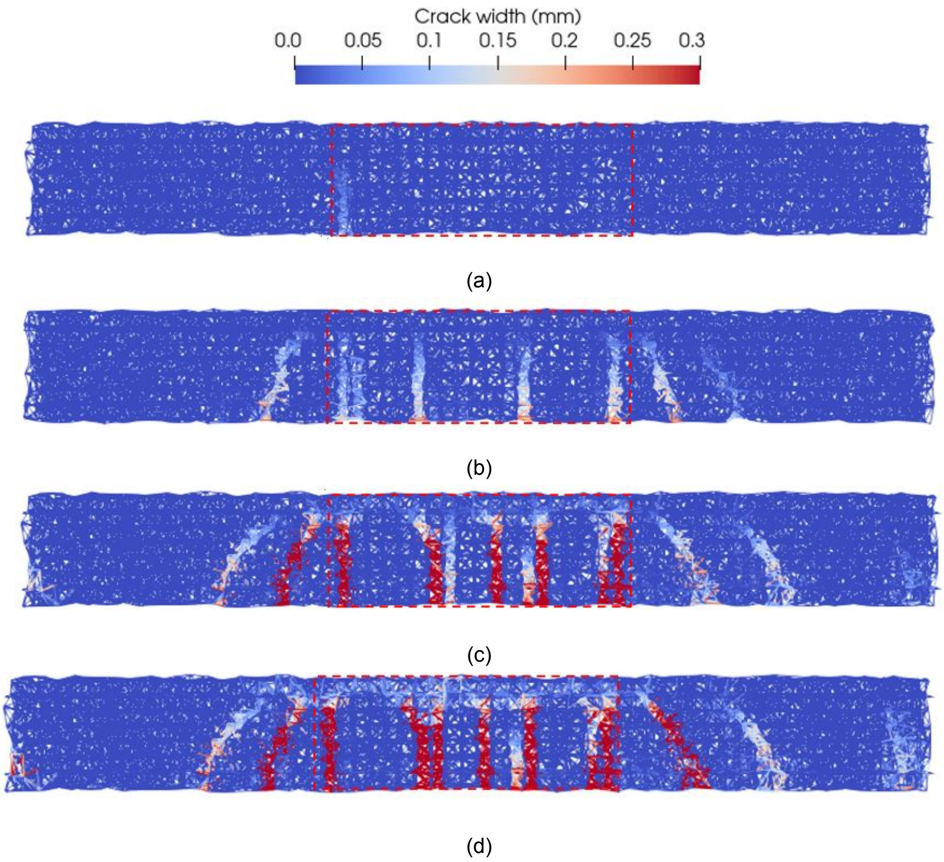

Figure 4.24: Cracking pattern of RC200 beam model at a deflection of (a) 0.60 mm (22.32 kN), (b) 3.79 mm (46.95 kN), (c) 16.77 mm (61.68 kN) and (d) 26.19 mm (66.36 kN).

The model reaches yielding strength of the steel at a load of 50.45 kN. A maximum steel stress of 500 MPa is found at a deflection of 26.19 mm deflection (Figure 4.25). The beam failed by failure of the compression zone, as the last element to fail is a concrete element of the compression zone. A maximum steel stress of 456 MPa is found at a deflection of 3.79 mm, which is when the 0.3 mm crack width limit is almost reached.

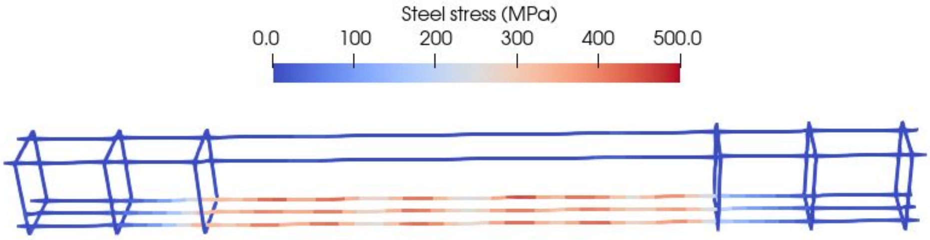

(a)

(b)

Figure 4.25: Steel stress of RC200 beam model at (a) 3.79 mm deflection (46.95 kN) and (b) 26.19 mm deflection (66.36 kN).

4.4.2. Reinforced concrete beam of 300 mm height

The 300 mm high reinforced concrete beam is modelled with an effective span of 1825 mm (Figure 4.26). The supporting conditions are similar to the RC200 beam.

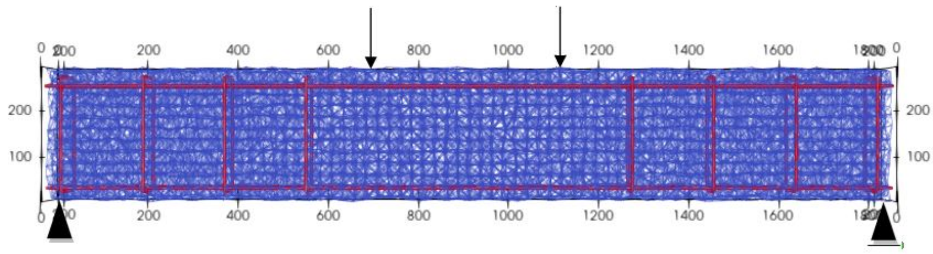

Figure 4.26: Model of 300 mm high reinforced concrete beam. Red = reinforcement. Blue = concrete elements. Arrow = load application point. Triangle = support point.

A maximum load of 79.88 kN is found with a deformation capacity of 36.75 mm (Figure 4.27). The crack width limit of 0.3 mm is reached at a load of 58.45 kN (Table 4.12).

Table 4.12: Overview of results of the RC300 beam model.

Key performance indicators	
Ultimate load	79.88 kN
Maximum deflection	36.75 mm
Number of cracks	8
Average crack spacing	63 mm
Load at 0.3 mm crack width	58.45 kN

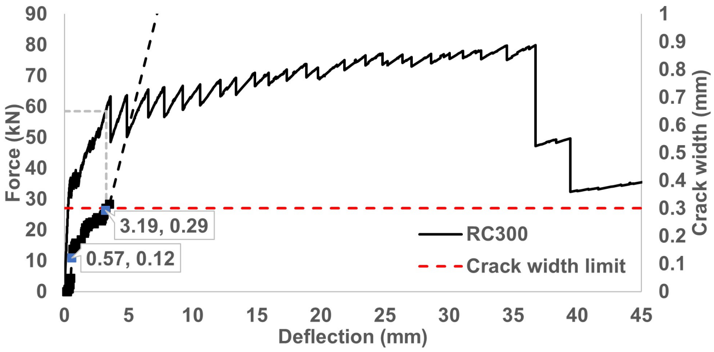

Figure 4.27: Numerical results of RC300 beam with load - deflection curve (solid) and maximum crack width - deflection curve (dashed). The maximum crack widths, of the cracking patterns presented in figure 4.28, are labelled.

The final cracking pattern shows 8 localized cracks at the bottom of the beam in the central 500 mm constant bending region. Whereas, at a displacement of 3.19 mm, when 0.3 mm crack widths are reached, 5 localized cracks are found (Figure 4.28).

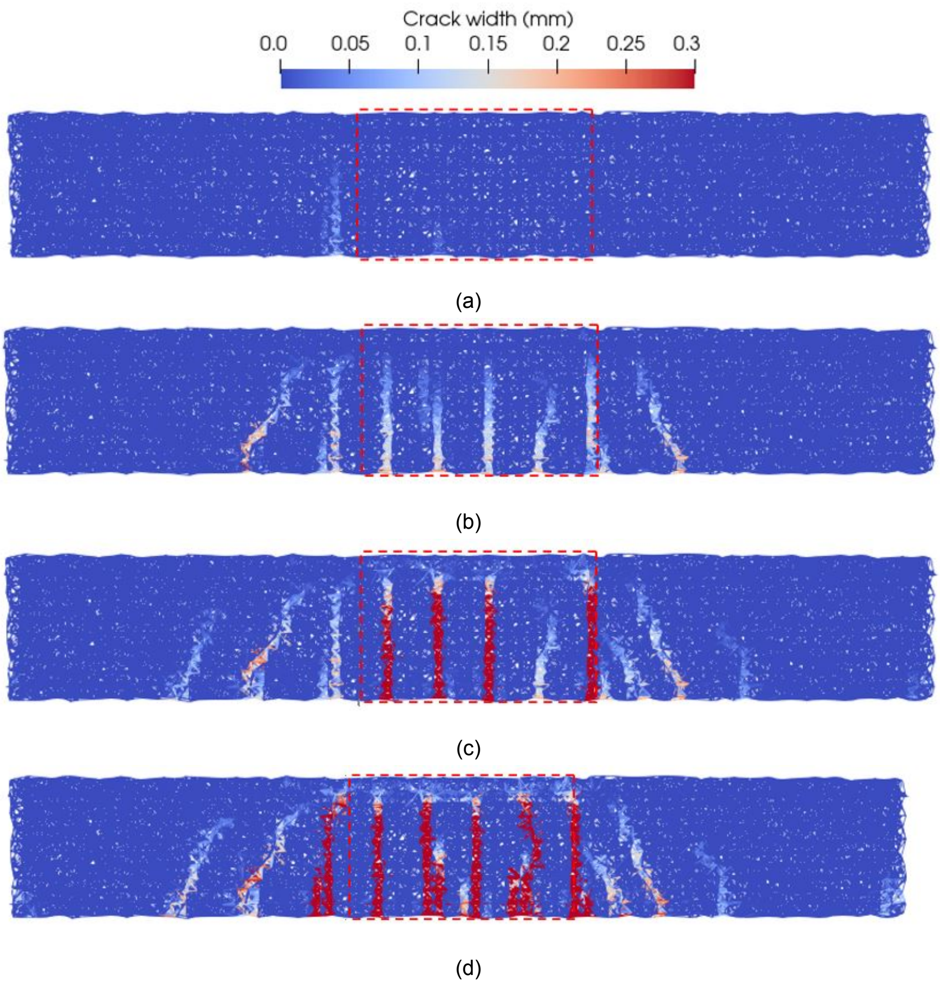

Figure 4.28: Cracking pattern of RC300 beam model at a deflection of (a) 0.57 mm (32.76 kN), (b) 3.19 mm (58.11 kN), (c) 12.24 mm (63.69 kN) and (d) 34.23 mm (79.23 kN).

The model reaches the yielding strength of the steel at a load of 63.36 kN. A maximum steel stress of 524 MPa is found at a deflection of 34.23 mm (Figure 4.29). The beam failed upon rupture of the reinforcement, as the last element to fail is found to be a steel element. A maximum steel stress of 452

MPa is found at a deflection of 3.19 mm, which is when the 0.3 mm crack width limit is almost reached.

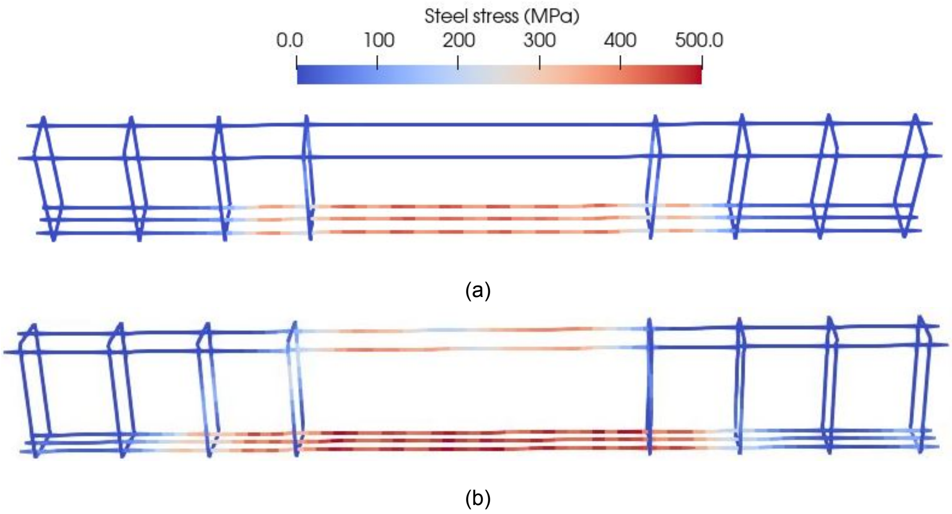

Figure 4.29: Steel stress of RC300 beam model at (a) 3.19 mm deflection (58.11 kN) and (b) 34.23 mm deflection (79.23 kN).

4.4.3. Reinforced concrete beam of 400 mm height

The 400 mm high reinforced concrete beam is modelled with an effective span of 2325 mm (Figure 4.30). A similar testing configuration as for the RC200 beam is used.

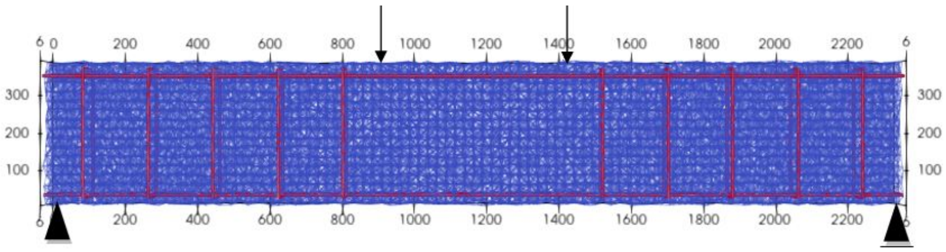

Figure 4.30: Model of 400 mm high reinforced concrete beam. Red = reinforcement. Blue = concrete elements. Arrow = load application point. Triangle = support point.

A maximum load of 80.78 kN is found with a deformation capacity of 38.18 mm (Figure 4.31). The crack width limit of 0.3 mm is reached at a load of 57.59 kN (Table 4.13).

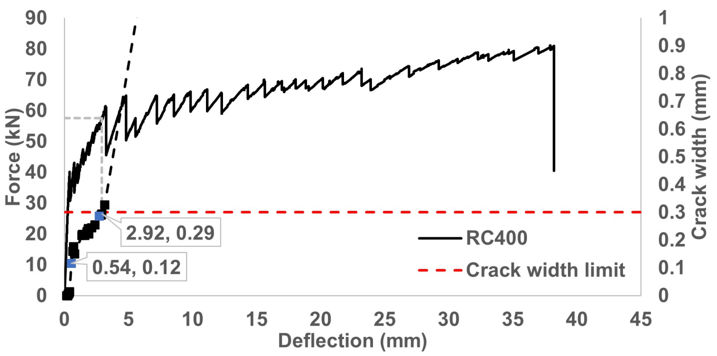

Figure 4.31: Numerical results of RC400 beam with load - deflection curve (solid) and maximum crack width - deflection curve (dashed). The maximum crack widths, of the cracking patterns presented in figure 4.32, are labelled.

The final cracking pattern shows 12 localized cracks at the bottom of the beam in the central 500 mm constant bending region. Whereas, at a displacement of 2.92 mm, when 0.3 mm crack widths are

Table 4.13: Overview of results of the RC400 beam model.

Key performance indicators	
Ultimate load	80.78 kN
Maximum deflection	38.18 mm
Number of cracks	12
Average crack spacing	42 mm
Load at 0.3 mm crack width	57.59 kN

reached, 4 localized cracks are found (Figure 4.32).

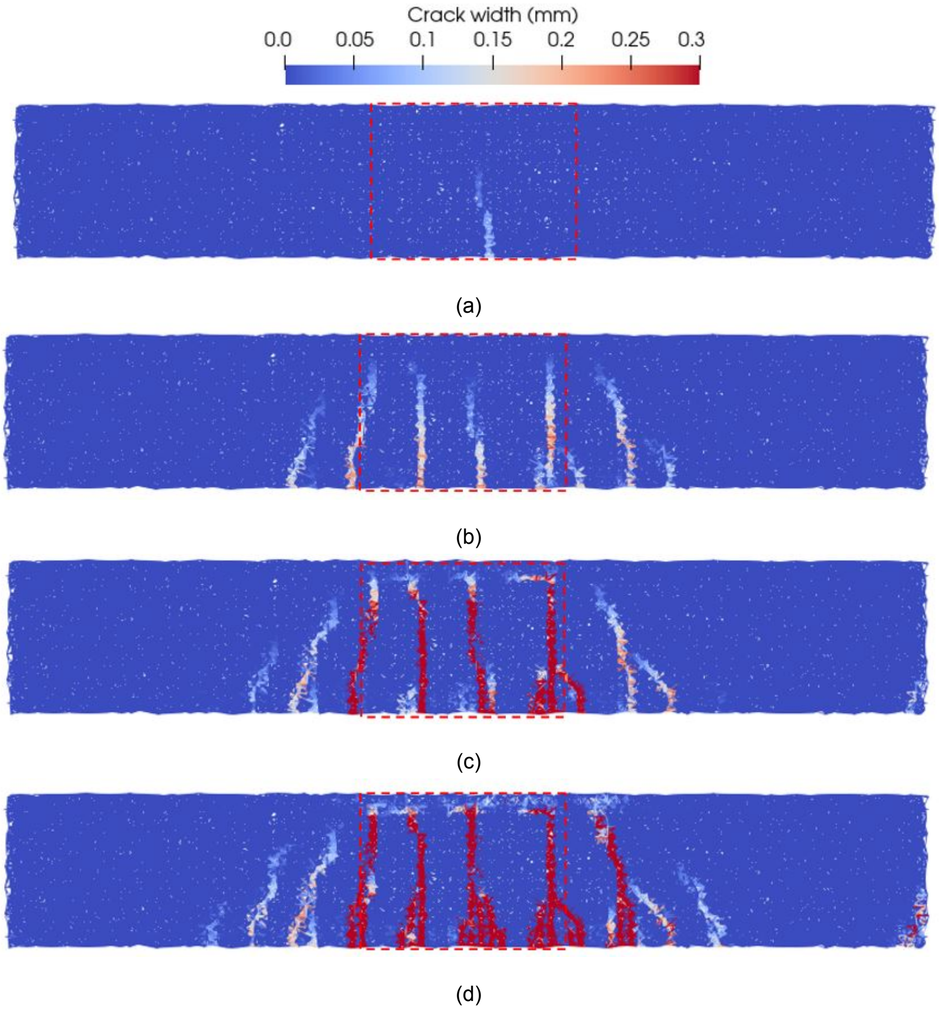

Figure 4.32: Cracking pattern of RC400 beam model at a deflection of (a) 0.54 mm (34.04 kN), (b) 2.92 mm (57.59 kN), (c) 15.08 mm (66.61 kN) and (d) 38.10 mm (80.61 kN).

The model reaches yielding strength of the steel at a load of 61.19 kN. A maximum steel stress of 541 MPa is found at a deflection of 38.10 mm (Figure 4.33). The beam failed by rupture of the reinforcement, as the last element to fail is found to be a steel element. A maximum steel stress of 449 MPa is found at a deflection of 3.19 mm, which is when the 0.3 mm crack width limit is almost reached.

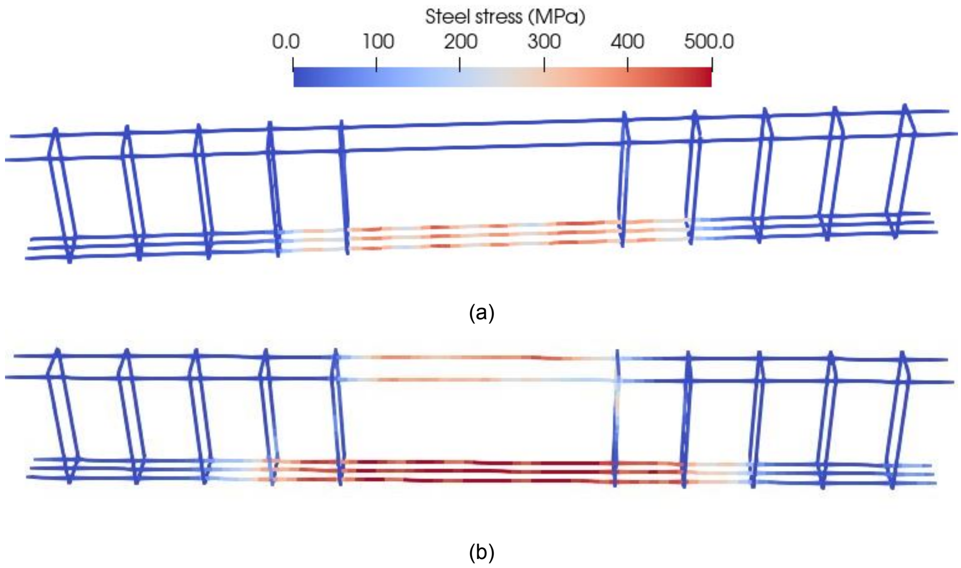

Figure 4.33: Steel stress of RC400 beam model at (a) 2.92 mm (57.59 kN) and (b) 38.10 mm deflection (80.61 kN).

4.4.4. Hybrid R/SHCC beam of 200 mm height

The 200 mm high hybrid reinforced beam is modelled with an effective span of 1500 mm (Figure 4.34). As the mesh size is 25 mm the SHCC layer is modelled as a 75 mm high layer, instead of 70 mm as determined in chapter 3. Similar loading and supporting conditions are used as for the RC200 beam.

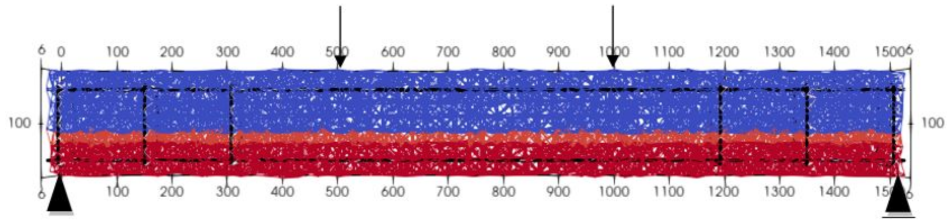

Figure 4.34: Model of 200 mm high hybrid reinforced beam. Red = SHCC elements. Orange = concrete-SHCC interface elements. Black = reinforcement. Blue = concrete elements. Arrow = load application point. Triangle = support point.

A maximum load of 80.61 kN is found with a deformation capacity of 20.77 mm (Figure 4.35). The crack widths are determined for the SHCC layer. The crack width limit of 0.3 mm is reached at a load of 73.19 kN (Table 4.14).

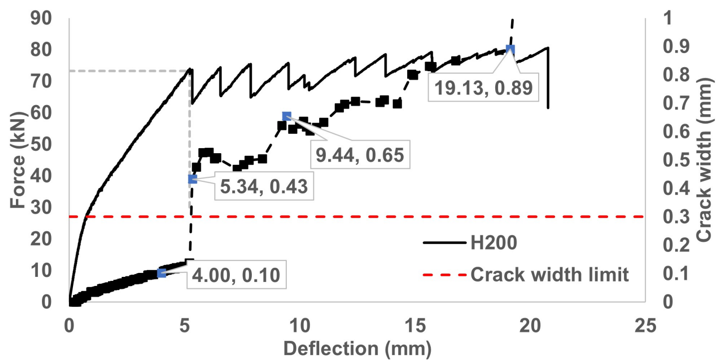

Figure 4.35: Numerical results of H200 beam with load - deflection curve (solid) and maximum crack width - deflection curve (dashed). The maximum crack widths, of the cracking patterns presented in figure 4.36, are labelled.

Table 4.14: Overview of results of the H200 beam model.

Key performance indicators	
Ultimate load	80.61 kN
Maximum deflection	20.77 mm
Number of cracks	20
Average crack spacing	25 mm
Load at 0.3 mm crack width	73.19 kN

The final cracking pattern shows 20 localized cracks, in the central 500 mm constant bending region at the bottom of the beam. 8 cracks are formed in the concrete layer, directly above the interface. The cracking pattern develops upon load increments (Figure 4.36). At a deflection of 5.34 mm, the maximum crack width increases suddenly from 0.14 mm to 0.43 mm. At this deflection, a longitudinal steel element fails, meaning that the steel is yielding.

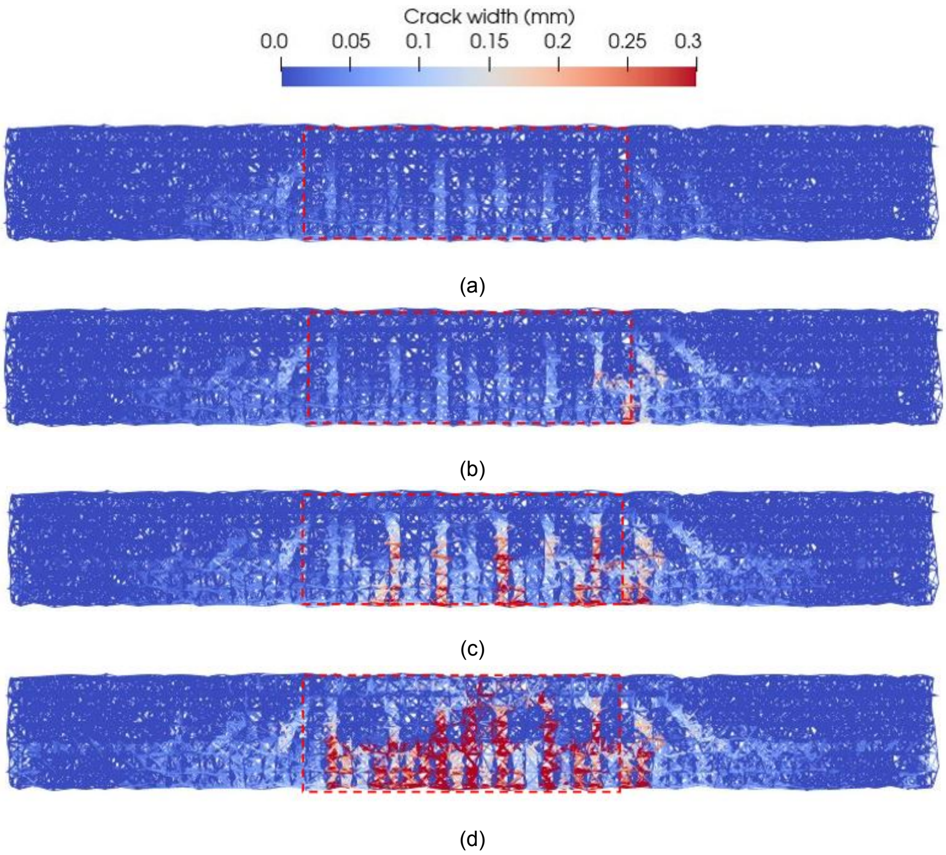

Figure 4.36: Cracking pattern of H200 beam model at a deflection of (a) 4.00 mm (62.08 kN), (b) 5.34 mm (63.29 kN), (c) 9.44 mm (75.24 kN) and (d) 19.13 mm (80.30 kN).

Yielding of the reinforcement steel is reached at a load of 73.39 kN. The steel stress is found to be 470 MPa, at a deflection of 19.13 mm (Figure 4.37). The beam failed by failure of the compression zone as the last element to fail is a concrete element from the compression zone. A maximum steel stress of 494 MPa is found at a deflection of 5.22 mm, which is when the 0.3 mm crack width limit is almost reached.

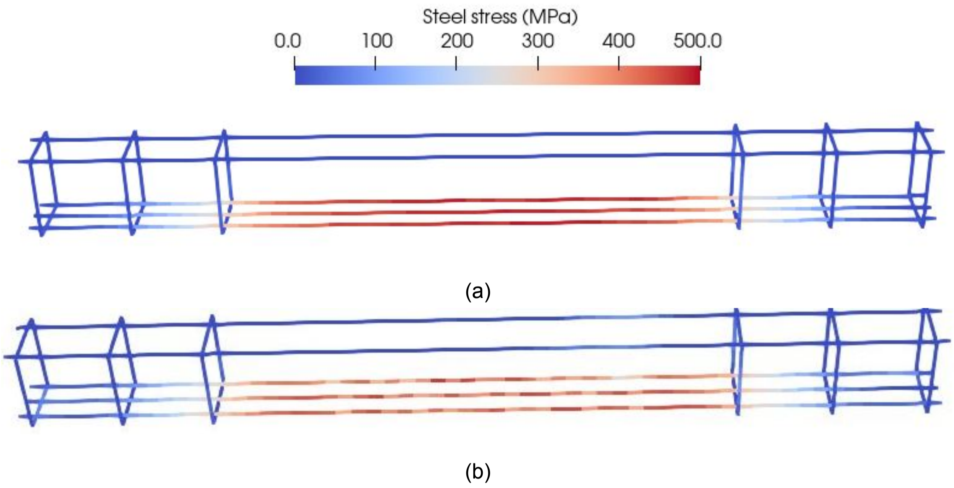

Figure 4.37: Steel stress of H200 beam model at a deflection of (a) 5.22 mm (73.91 kN) and (b) 19.13 mm (80.39 kN).

The delamination of the concrete-SHCC interface is determined by cracking of concrete-SHCC interface elements (Figure 4.38). At a deflection of 5.22 mm (73.91 kN), a maximum delamination of 0.22 mm is found. The delamination increases to 0.62 mm, at a deflection of 19.13 mm (80.39 kN).

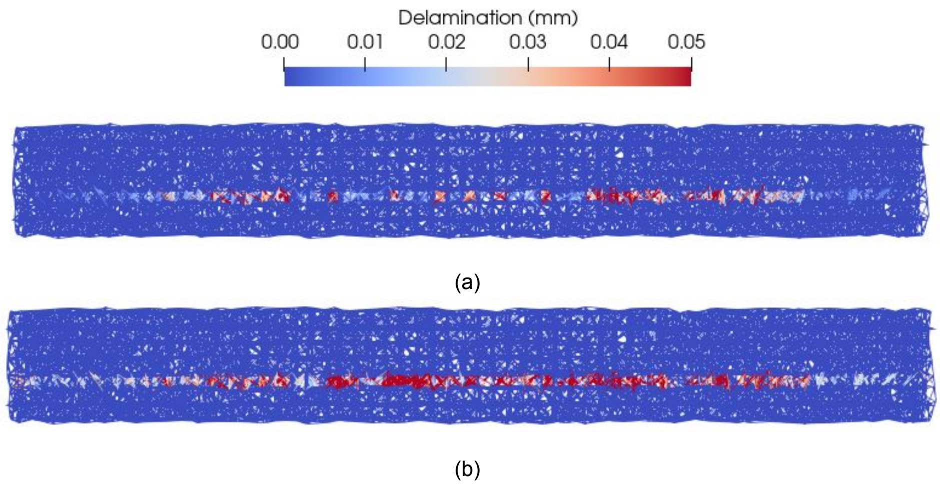

Figure 4.38: Delamination of the concrete-SHCC interface at a deflection of (a) 5.22 mm (73.91 kN) and (b) 19.13 mm (80.39 kN).

4.4.5. Hybrid R/SHCC beam of 300 mm height

The 300 mm high hybrid reinforced beam is modelled with an effective span of 1825 mm (Figure 4.39). As the mesh size is 25 mm, the SHCC layer is modelled as a 75 mm high layer, instead of the 70 mm as determined in chapter 3. Similar loading and supporting conditions are used as for the RC200 beam.

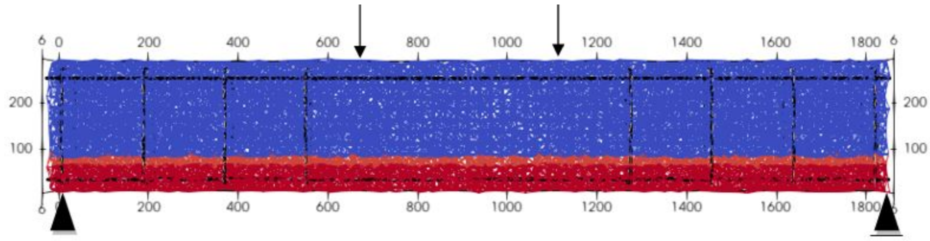

Figure 4.39: Model of 300 mm high hybrid reinforced beam. Red = SHCC elements. Orange = concrete-SHCC interface elements. Black = reinforcement. Blue = concrete elements. Arrow = load application point. Triangle = support point.

A maximum load of 99.12 kN is found with a deformation capacity of 19.47 mm (Figure 4.40). The crack widths are determined for the SHCC layer. The crack width limit of 0.3 mm is reached at a load of 87.82 kN (Table 4.15). At a deflection of 4.21 mm, the maximum crack width increases suddenly from 0.15 mm to 0.38 mm. At this deflection, a longitudinal steel element fails, meaning that the steel is yielding.

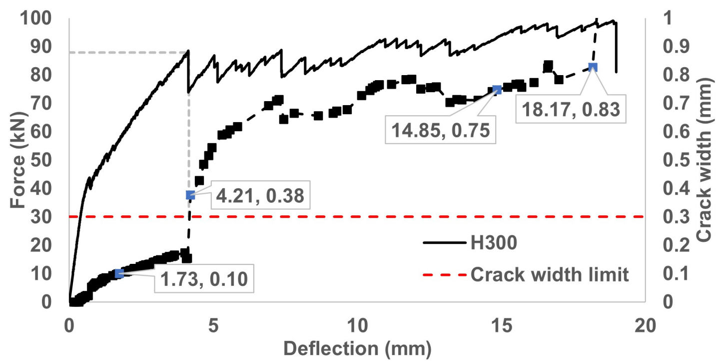

Figure 4.40: Numerical results of H300 beam with load - deflection curve (solid) and maximum crack width - deflection curve (dashed). The maximum crack widths, of the cracking patterns presented in figure 4.41, are labelled.

Table 4.15: Overview of results of the H300 beam model.

Key performance indicators	
Ultimate load	99.12 kN
Maximum deflection	19.47 mm
Number of cracks	20
Average crack spacing	25 mm
Load at 0.3 mm crack width	87.82 kN

The final cracking pattern shows 20 localized cracks in the central 500 mm constant bending region. 4 cracks are formed in the concrete layer, directly above the concrete-SHCC interface. The cracking pattern develops upon load increments (Figure 4.41). From the development of the cracking pattern it is found that, cracks in concrete are localizing before cracks in SHCC are localizing.

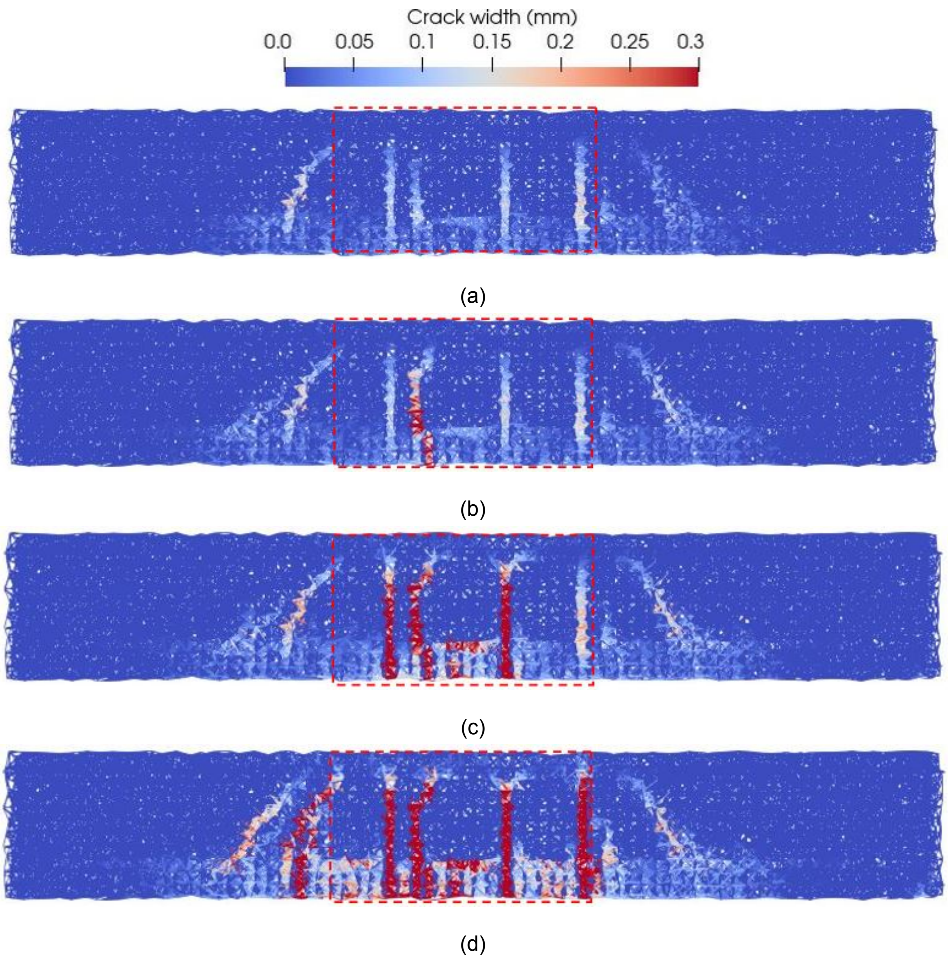

Figure 4.41: Cracking pattern of H300 beam model at a deflection of (a) 1.73 mm (57.27 kN), (b) 4.21 mm (75.21 kN), (c) 14.85 mm (93.15 kN) and (d) 18.17 mm (97.81 kN).

Yielding of the reinforcement is reached at a load of 88.52 kN. The steel stress is found to be 489 MPa, at a deflection of 18.38 mm (Figure 4.42). The beam fails by rupture of the reinforcement, as the last element to fail is a steel element. A maximum steel stress of 481 MPa is found at a deflection of 4.02 mm, which is when the 0.3 mm crack width limit is almost reached.

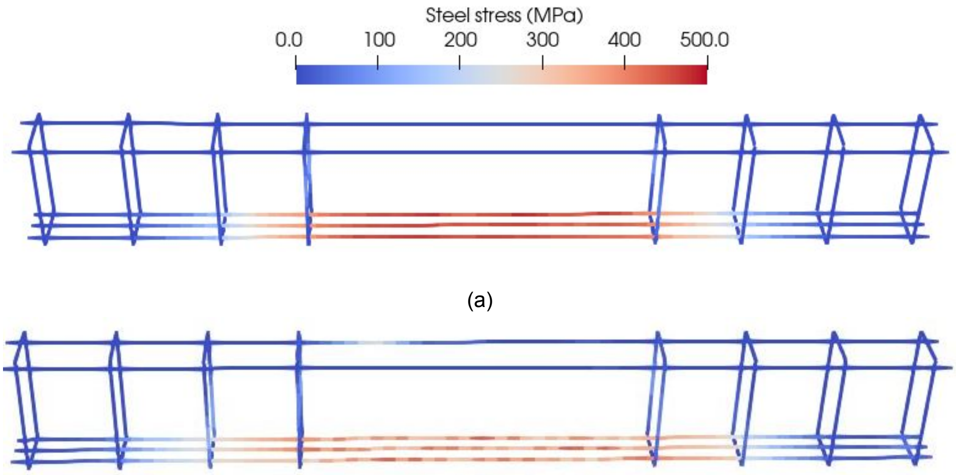

(a)

(b)

Figure 4.42: Steel stress of H300 beam model at a deflection of (a) 4.02 mm (86.67 kN) and (b) 18.38 mm (97.81 kN).

The delamination of the concrete-SHCC interface is determined by cracking of concrete-SHCC interface elements (Figure 4.43). At a deflection of 4.02 mm (86.67 kN), a maximum delamination of 0.33 mm is found. The delamination increases to 1.65 mm, at a deflection of 18.38 mm (97.81 kN).

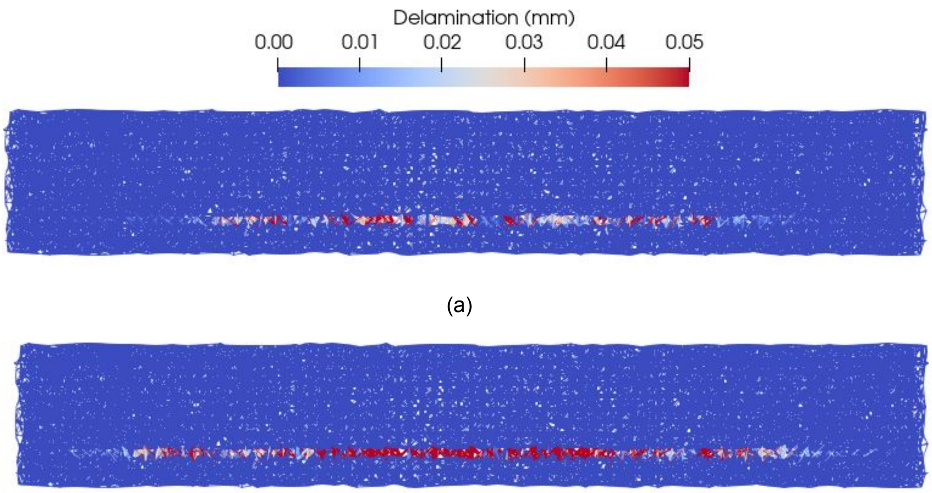

(a)

(b)

Figure 4.43: Delamination of the concrete-SHCC interface at a deflection of (a) 4.02 mm (86.67 kN) and (b) 18.38 mm (97.81 kN).

4.4.6. Hybrid R/SHCC beam of 400 mm height

The 400 mm high hybrid reinforced beam is modelled with an effective span of 2325 mm (Figure 4.44). As the mesh size is 25 mm, the SHCC layer is modelled as a 75 mm high layer, instead of 70 mm as determined in chapter 3.

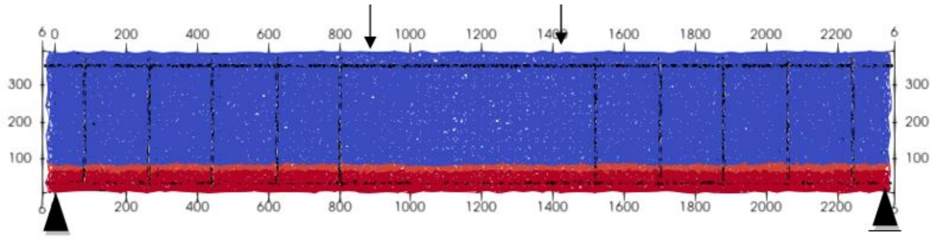

Figure 4.44: Model of 400 mm high hybrid reinforced beam. Red = SHCC elements. Orange = concrete-SHCC interface elements. Black = reinforcement. Blue = concrete elements. Arrow = load application point. Triangle = support point.

A maximum load of 103.70 kN is found with a deformation capacity of 33.63 mm (Figure 4.45). The crack width limit of 0.3 mm is reached at a load of 88.40 kN (Table 4.16). At a deflection of 4.79 mm, the maximum crack width increases suddenly from 0.20 mm to 0.50 mm width. At this deflection, a longitudinal steel element fails, meaning that the steel is yielding.

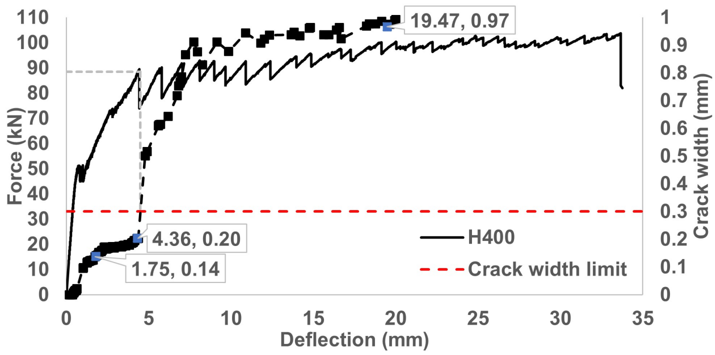

Figure 4.45: Numerical results of H400 beam with load - deflection curve (solid) and maximum crack width - deflection curve (dashed). The maximum crack widths, of the cracking patterns presented in figure 4.46, are labelled.

Table 4.16: Overview of results of the H400 beam model.

Key performance indicators	
Ultimate load	103.70 kN
Maximum deflection	33.63 mm
Number of cracks	20
Average crack spacing	25 mm
Load at 0.3 mm crack width	88.40 kN

The final cracking pattern shows 20 localized cracks in the central 500 mm constant bending region. 2 propagated localized cracks are found in the concrete layer. The cracking pattern develops upon load increments (Figure 4.46). From the development of the cracking pattern it is found that, cracks in the concrete layer are localizing before cracks in SHCC are localizing.

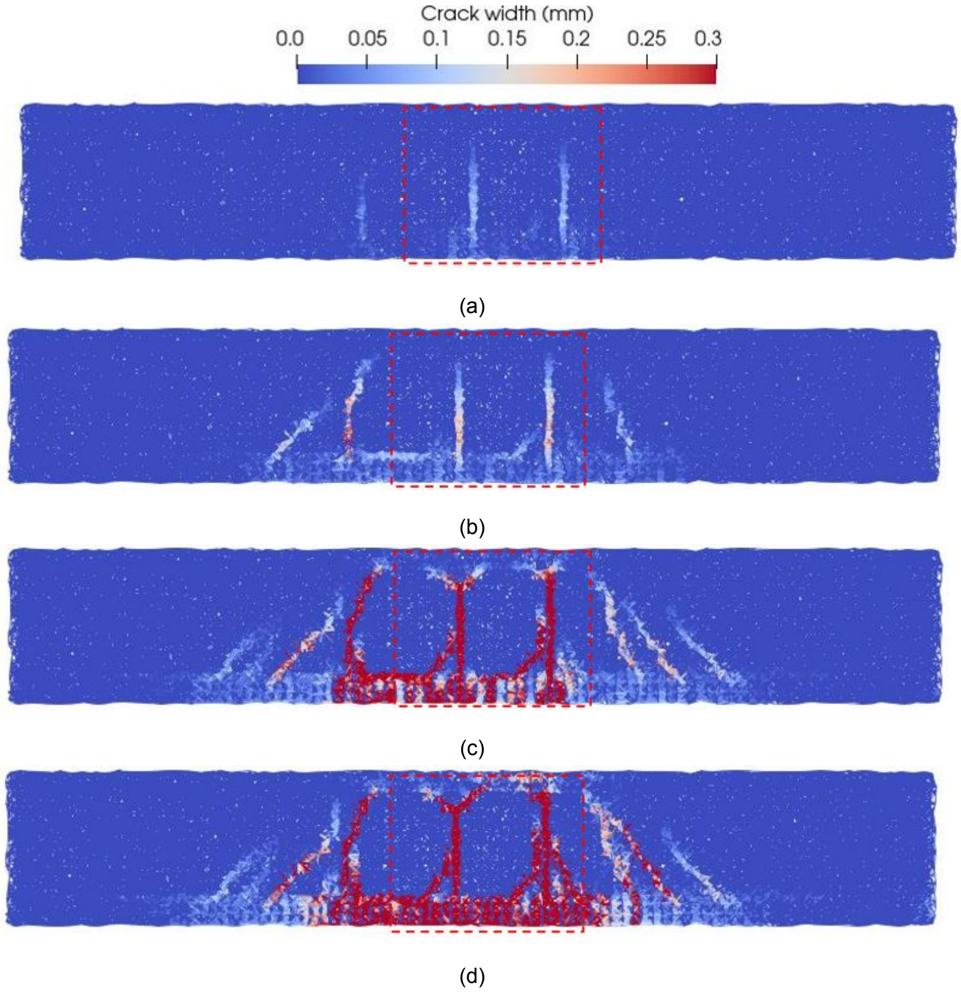

Figure 4.46: Cracking pattern of H400 beam model at a deflection of (a) 1.75 mm (59.50 kN), (b) 4.36 mm (88.52 kN), (c) 19.47 mm (97.52 kN) and (d) 33.57 mm (103.47 kN).

Yielding of the reinforcement is reached at a load of 89.44 kN. The steel stress is found to be 492 MPa at a deflection of 33.57 mm (Figure 4.47). The beam failed by rupture of the reinforcement, as the last element to fail is found to be a steel element. A maximum steel stress of 491 MPa is found at a deflection of 4.36 mm, which is when the 0.3 mm crack width limit is almost reached.

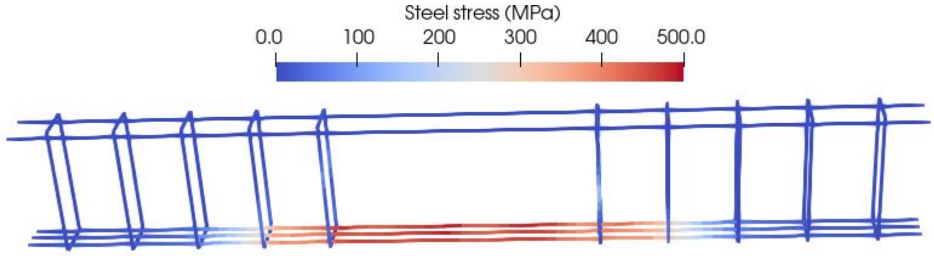

(a)

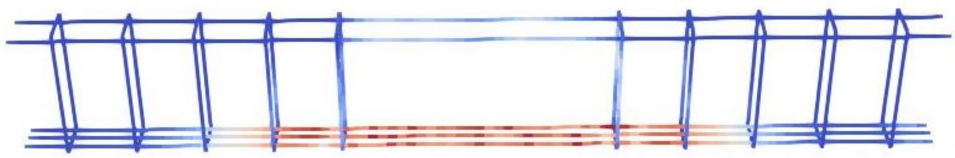

(b)

Figure 4.47: Steel stress of H400 beam model at (a) 4.36 mm deflection (88.52 kN) and (b) 33.57 mm deflection (103.47 kN).

The delamination of the concrete-SHCC interface is determined by cracking of concrete-SHCC interface elements (Figure 4.48). At a deflection of 4.36 mm (88.52 kN), a maximum delamination of 0.31 mm is found. The delamination increases to 4.13 mm, at a deflection of 33.57 mm (103.47 kN).

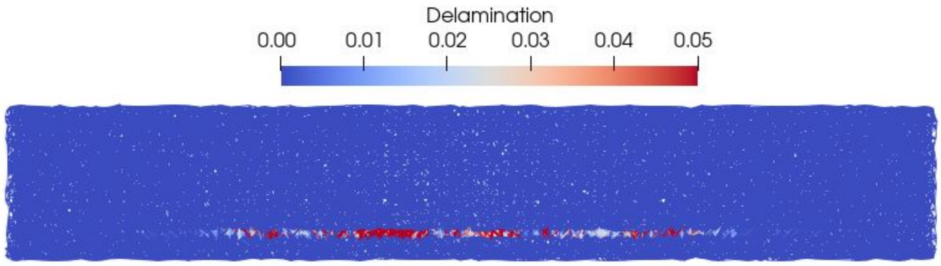

(a)

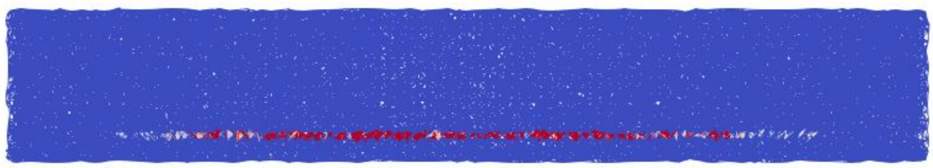

(b)

Figure 4.48: Delamination of the concrete-SHCC interface at a deflection of (a) 4.36 mm (88.52 kN) and (b) 33.57 mm (103.47 kN).

4.4.7. Hybrid R/SHCC beam of 300 mm height with smooth and Vaseline treated longitudinal reinforcement bars

The 300 mm high hybrid reinforced beam with smooth and Vaseline treated reinforcement is modelled with an effective span of 1825 mm (Figure 4.49). As the mesh size is 25 mm, the SHCC layer is modelled as a 75 mm high layer, instead of 70 mm as determined in chapter 3.

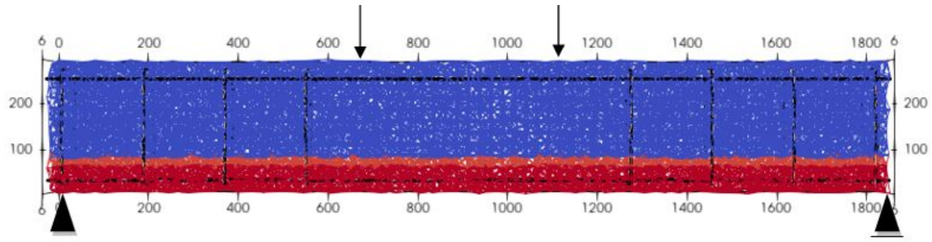

Figure 4.49: Model of 300 mm high hybrid reinforced beam with smooth and Vaseline treated longitudinal reinforcement bars in the tension zone. Red = SHCC elements. Orange = concrete-SHCC interface elements. Black = reinforcement. Blue = concrete elements. Arrow = load application point. Triangle = support point.

A maximum load of 46.38 kN is found with a deformation capacity of 16.40 mm (Figure 4.50). The crack width limit of 0.3 mm is reached at a load of 35.32 kN (Table 4.17).

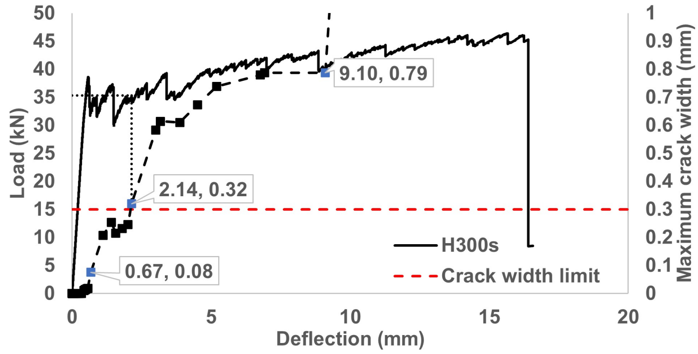

Figure 4.50: Numerical results of H300s beam with load - deflection curve (solid) and maximum crack width - deflection curve (dashed). The maximum crack widths, of the cracking patterns presented in figure 4.51, are labelled.

Table 4.17: Overview of results of the H300s beam model.

Key performance indicators	
Ultimate load	46.38 kN
Maximum deflection	16.40 mm
Number of cracks	8
Average crack spacing	62.50 mm
Load at 0.3 mm crack width	35.32 kN

The final cracking pattern shows 8 localized SHCC cracks in the central 500 mm constant bending region. The cracking pattern develops upon load increments (Figure 4.51). 1 propagated and localized crack is found in the concrete layer.

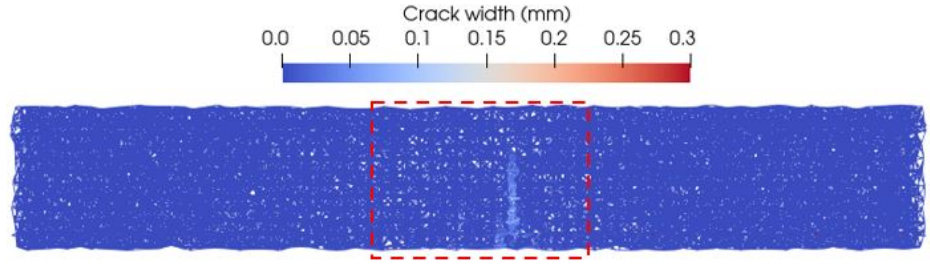

(a)

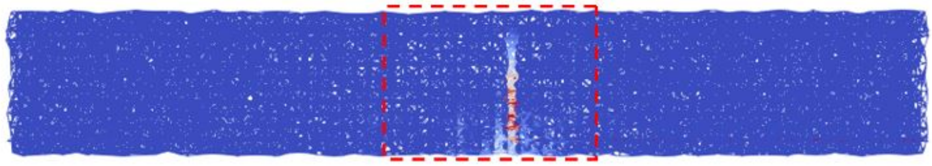

(b)

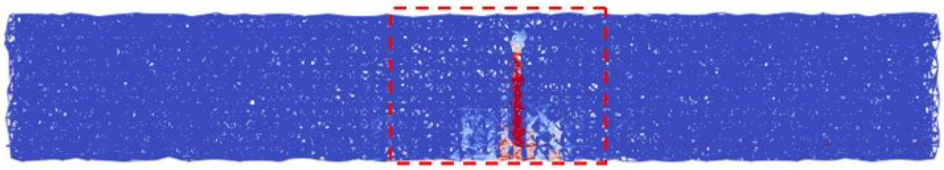

(c)

Figure 4.51: Cracking pattern of H300s beam model at a deflection of (a) 0.67 mm (32.52 kN), (b) 2.00 mm (34.76 kN) and (c) 9.10 mm (40.14 kN).

The maximum steel stress is found to be 16 MPa at a deflection of 9.10 mm (Figure 4.52). Yielding of the reinforcement is not reached. The model fails by propagation of the concrete crack to the compression zone. At a deflection of 2.14 mm, which is when the 0.3 mm crack width limit is reached, the maximum steel stress is 13 MPa.

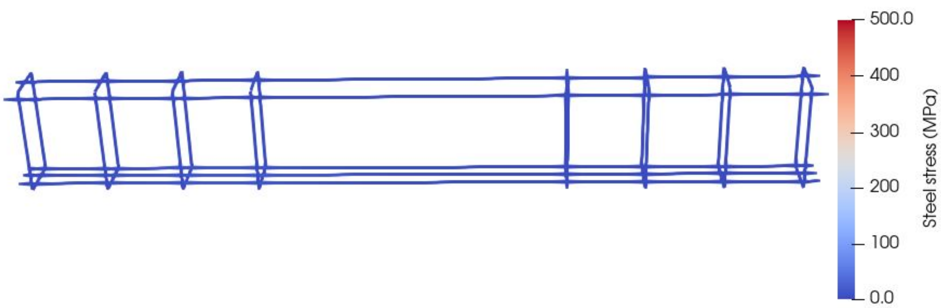

Figure 4.52: Steel stress of H300s beam model at failure load.

The delamination of the concrete-SHCC interface is determined by cracking of concrete-SHCC interface elements (Figure 4.53). At a deflection of 2.00 mm (34.76 kN), a maximum delamination of 0.25 mm is found. The delamination increases to 0.83 mm, at a deflection of 9.10 mm (40.11 kN).

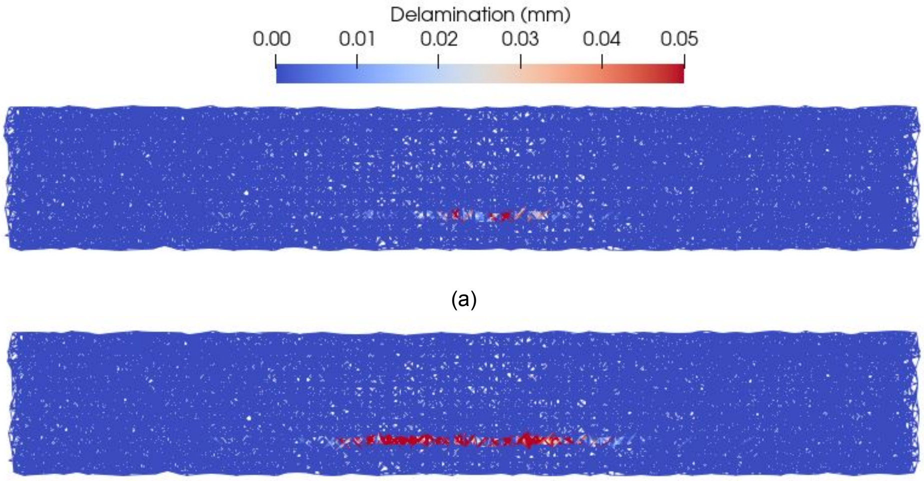

(a)

(b)

Figure 4.53: Delamination of the concrete-SHCC interface at a deflection of (a) 2.00 mm (34.76 kN) and (b) 9.10 mm (40.11 kN).

4.4.8. Comparison of numerical results

In order to see the effect of increasing the height of the beams, the numerical results of the different beams are compared. Beams of different heights are compared with use of moment-deflection curves. The moments (M) are determined with the applied force (F) and length of the shear span (a):

$$M = 0.5Fa \tag{4.25}$$

Comparison of reinforced concrete beams

By comparison of the moment-deflection curves of the reinforced concrete beam models, it is found that, the deformation capacity increases from 27.97 mm (RC200) to 36.75 mm (RC300) and 38.18 mm (RC400). The bearing moment capacity is also found to increase from 16.59 kNm (RC200), to 26.46 kNm (RC300) and 37.02 kNm (RC400). The increase in deformation capacity is large for a height increase from 200 to 300 mm, but smaller between 300 and 400 mm (Figure 4.54). This can be explained by the different failure mechanism that occurred in the beams, as the RC200 beam was the only beam to fail in the compression zone. RC300 and RC400 failed by rupture of the reinforcement. The increase in moment capacity can be explained by the increased internal lever arm of the higher beams. Thereby, internal forces (steel force and compression force) are smaller for the same moment. The maximum crack widths are found to increase, upon increasing the height of the beam. This can be explained by the increased stiffness of the higher beam. As a higher beam is stiffer, the applied moment at a certain deflection is higher, and therefore the maximum crack widths are larger. Due to this difference in stiffness, the moment applied to reach the 0.3 mm crack width limit cannot be compared directly. Therefore, the comparison is made with the moments at which the 0.3 mm crack width limit is reached, relative to the yielding moment of the beams (Table 4.18). The yielding moment is used, as this is besides the crack width limit, the most strict serviceability limit for these beams. From the comparison of the relative moments at which 0.3 mm crack widths are reached, it is found that, no significant differences are present in the ability of controlling crack widths up to 0.3 mm width. However, the cracking pattern is found to be different, as the RC200 beam showed 8 localized cracks of which 7 propagate to the compression region of the beam. For the RC300 beam, only 5 out of the 8 localized cracks propagated. For the RC400 beam, only 4 out of 12 localized cracks propagated. Therefore, the number of propagated cracks decrease upon increasing the height. In addition, the cracking patterns of the RC300 and RC400 show the development of an effective tensile area. This is not observed in the RC200 beam.

Table 4.18: Overview of comparison of reinforced concrete beams.

Key performance indicators	RC200	RC300	RC400
Moment bearing capacity	16.59 kNm	26.46 kNm	37.01 kNm
Maximum deflection	27.97 mm	36.75 mm	38.18 mm
Number of propagated cracks	7	5	4
Moment at 0.3 mm crack width	11.78 kNm	19.36 kNm	26.25 kNm
0.3 mm moment/yield moment	93.18%	92.25%	94.12%

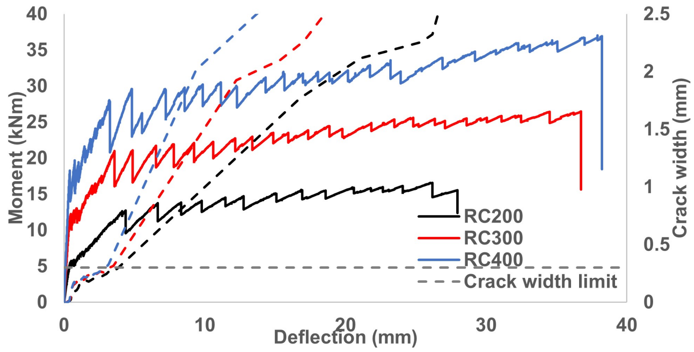

Figure 4.54: Comparison of numerical results for RC200, RC300 and RC400 beam with load - deflection curve (solid) and maximum crack width - deflection curve (dashed).

Comparison of hybrid beams

By comparison of the moment-deflection curves of the hybrid reinforced beam models, it is found that, the deformation capacity is similar between the H200 (20.77 mm) and H300 beam (19.47 mm), but increased for the H400 beam (33.63 mm). It is remarkable that the deformation capacity of H200 and H300 are similar, as the reinforced concrete beams showed an increase in deformation capacity between RC200 and RC300. The limited deformation capacity of H300 can be explained by the final cracking pattern. All the hybrid beams show 20 localized cracks in the SHCC layer. For the H200 beam, the cracks are first localizing in the SHCC, whereas for the H300 and H400 the cracks start localizing in the concrete. In the H400 beam the SHCC cracks localize into multiple concrete cracks. These concrete cracks coalescence into larger cracks concrete cracks, propagating towards the compression zone. The H300 beam does not show this coalescence of multiple concrete cracks into propagated cracks. Therefore, less concrete cracks are present directly above the concrete-SHCC interface in the H300 beam. The coalescence of concrete cracks above the SHCC-concrete interface leads to a bigger release of strain energy, and therefore a higher deformation capacity is obtained. Upon comparison of the bearing moment capacity, it is found that, upon increasing the height from 200 mm, to 300 mm and 400 mm the bearing capacity increases from 20.15 kNm (H200) to 32.83 kNm (H300) and 47.31 kNm (H400). Lastly, the relative moments at which the 0.3 mm crack width limit is reached are compared (Table 4.19). From this comparison, it is found that, upon increasing the height, the relative moment remains similar, as it changes from 99.73% (H200) to 99.21% (H300) and 98.88% (H400). All the hybrid beams are able to control the crack widths up to yielding of the reinforcement. Once the reinforcement yields, the crack widths increase significantly. Upon comparison of the cracking patterns, difference are found between the hybrid beams. The H200 beam developed 7 propagated concrete cracks, whereas the H300 beam developed 4 propagated concrete cracks and the H400 beam developed 2 propagated concrete cracks.

Table 4.19: Overview of comparison of hybrid reinforced beams.

Key performance indicators	H200	H300	H400
Moment bearing capacity	20.15 kNm	32.83 kNm	47.31 kNm
Maximum deflection	20.77 mm	19.47 mm	33.63 mm
Number of propagated cracks	7	4	2
Moment at 0.3 mm crack width	18.30 kNm	29.09 kNm	40.33 kNm
0.3 mm moment/yield moment	99.73%	99.21%	98.88%

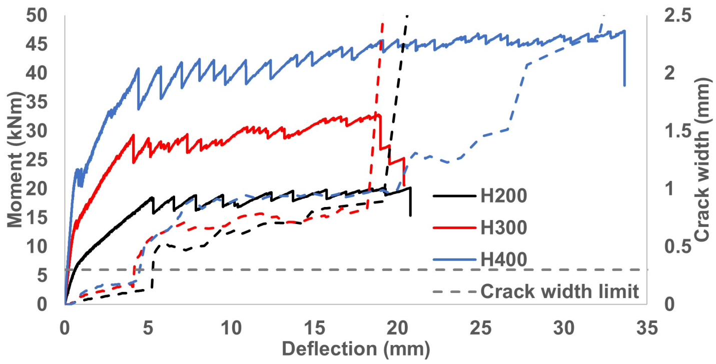

Figure 4.55: Comparison of numerical results for H200, H300 and H400 beam with load - deflection curve (solid) and maximum crack width - deflection curve (dashed).

Comparison of reinforced concrete beams and hybrid beams

Upon comparison of the 200 mm high hybrid beam with the concrete reinforced beam of the same height, it is found that, the bearing capacity increases from 66.36 kN to 80.61 kN (Figure 4.56). This is an increase of 14.25 kN (21%). In addition, the deformation capacity decreases with 7.20 mm (26%) from 27.97 mm (RC200) to 20.77 mm (H200). The load at which the 0.3 mm crack width limit is reached is higher for H200 (73 kN), compared to RC200 (47 kN). The hybrid beam (100%) has a relative higher load at which the 0.3 mm crack width limit is reached, compared to the RC200 beam (93%). The increase in capacity can be explained by the tensile capacity of the SHCC, which shares the tension force with the steel reinforcement. The decrease in ductility can be explained by the hardening properties of SHCC, which are not present in the concrete. From the cracking patterns, it is found that, the H200 beam has a uniform distribution of cracks in the SHCC layer, which localize into 8 concrete cracks. The reinforced concrete beam shows 8 localized cracks in concrete of which 7 propagate to the compression zone. Both beams were found to fail by failure of the compression zone.

Upon comparison of the 300 mm high hybrid beams with the concrete reinforced beam of the same height, it is found that the bearing capacity increases from 79.88 kN (RC300) to 99.12 kN (H300) and 46.38 kN (H300s) (Figure 4.56). This is an increase of 19.24 kN (24%) for the H300 beam and a decrease of 33.50 kN (42%) for the H300s beam. In addition, the deformation capacity decreases with 17.28 mm (47%) from 36.75 mm (RC300) to 19.47 mm (H300) for the H300 beam. For the H300s beam, the deformation capacity decreases with 20.35 mm (55%) from 36.75 mm (RC300) to 16.40 mm (H300s). The load at which the 0.3 mm crack width limit is reached, is 88 kN for the H300 beam and 58 kN for the RC300 beam. Thereby, the hybrid beam improves the crack controlling behavior with 30 kN. Thereby, similar differences are found between the H300 and RC300 beam as are found between the H200 beam and the RC200 beam. For the H300s beam, the crack controlling behavior is compromised, as the 0.3 mm crack width limit is reached at a load of 35.32 kN. This can be explained by the low contribution of the longitudinal reinforcement in the H300s beam, which becomes clear from the low steel stresses found. The final cracking pattern of the RC300 beam shows 8 localized cracks of which 5 propagate to the compression zone, whereas the H300 beam shows a uniform cracking pattern in the SHCC layer and 4 propagated cracks. The H300s beam develops a very limited amount of cracks in the SHCC layer. The concrete layer develops only one propagated crack. The H300 and RC300 beam showed failure by rebar rupture. The H300s beam showed failure by propagation of the crack towards the compression zone.

Upon comparison of the 400 mm high hybrid beam with the concrete reinforced beam of the same height it is found that, the bearing capacity increases from 80.78 kN to 103.70 kN (Figure 4.56). This is an increase of 22.92 kN (28%). In addition, the bearing capacity decreases with 4.55 mm (12%) from 38.18 mm to 33.63 mm. The load at which the 0.3 mm crack width limit is reached is higher for H400 (88 kN) compared to RC400 (58 kN). This is an increase of 30 kN. The hybrid beam (99%) has a relative higher load, at which the 0.3 mm crack width limit is reached compared to the RC400 beam (94%). Both beams were found to fail by failure of the compression zone. From the cracking patterns, it is found that, the hybrid and the concrete reinforced beam show coalescence of concrete cracks. The hybrid beam has a uniform crack distribution in the SHCC layer.

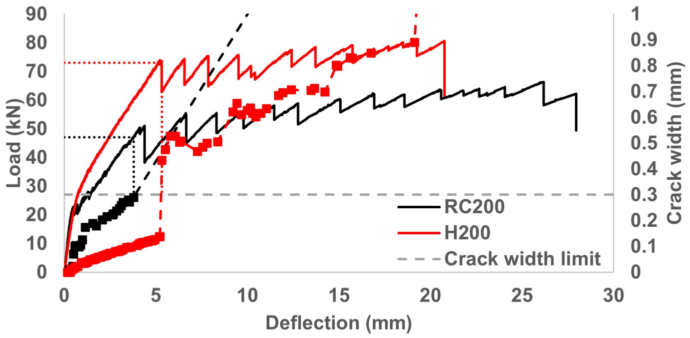

(a)

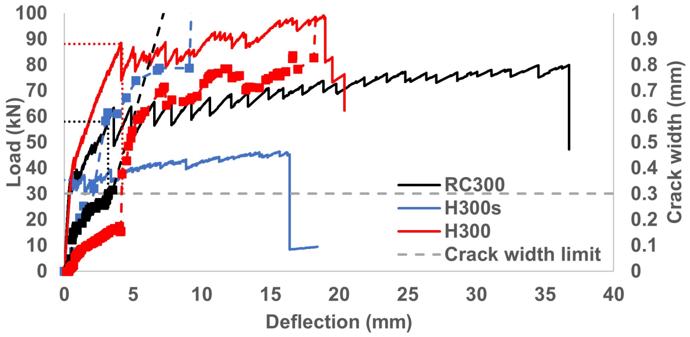

(b)

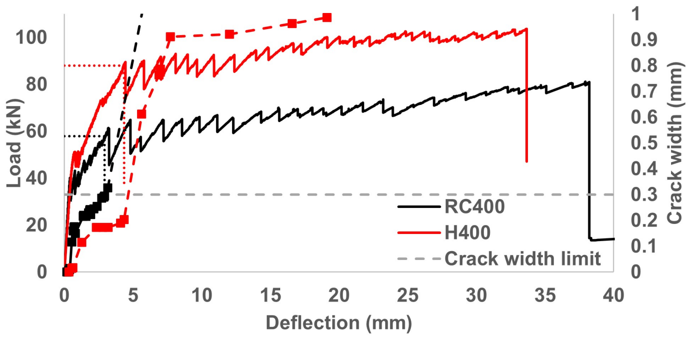

(c)

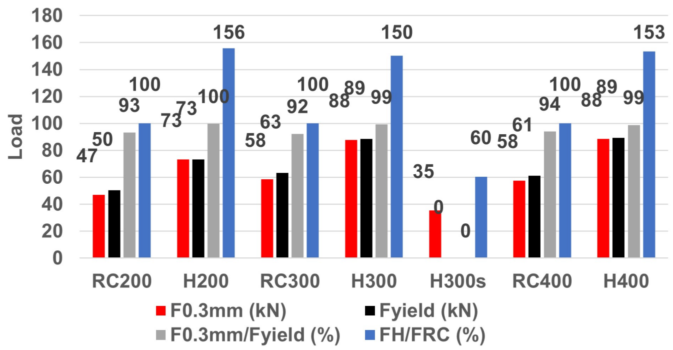

(d)

Figure 4.56: Comparison of numerical results for (a) RC200 and H200 (b) RC300, H300 and H300s, (c) RC400 and H400, and (d) an overview of these results. Solid = load-deflection. Dashed = crack width - deflection. F0.3mm = load when 0.3 mm crack width limit is reached. Fyield = load when yielding of reinforcement is reached. FH = load of hybrid beam when 0.3 mm crack width limit is reached. FRC = load of reinforced concrete beam when 0.3 mm crack width limit is reached.

4.5. Conclusions

Based on the performed numerical study the following can be concluded:

- Calibration of the Delft Lattice model is dependent on the number of elements included in the calibration model. Reducing the number of elements in the model increases the softening branch of the stress-strain curve. The number of elements in the model is both dependent on the sample size and mesh size. Increasing the voxel size from 10 mm to 25 mm was not found to affect the ability of the lattice model to simulate the structural behavior of the 200 mm high reinforced concrete beam as found in the experiments. It should be noted that, a different rebar-concrete material input has been used for the numerical models.

- Increasing the number of segments in the material input for SHCC leads to the ability of modelling the SHCC with larger ductility. As a 3-segmented material input limits the ductility of the prism model to 0.28% ductility, whereas the 7-segmented material input was able to reach a ductility of 2.36%.

- Modelling SHCC with varying elemental radius, for example with Voronoi radius, results in larger local instabilities of the model. The increase in local instabilities is caused by the larger variation of stiffness of the elements and the variation of axial bearing capacity of elements. The cracking pattern, of a prism model with Voronoi radius elements, shows a distribution of cracks over the full height of the prism. As this cracking pattern is considered unrealistic, it is decided to use a constant elemental radius in the beam models.

- Strain-hardening behavior of the prism model is found, when a 7-segmented material input with constant strength over all the segments is used. This is a consequence of the varying elemental lengths. This intrinsic strain-hardening behavior can be overcome by calibration of the segment strength using the so-called output modelling approach.

- The rebar-concrete interface for ribbed rebars can effectively be modelled with the pull-out envelope. This approach eliminates the need for time-consuming calibrations of the beam models.

- The rebar-concrete interface for smooth and Vaseline treated reinforcement bars is modelled, by reducing the clear rib distance and reducing the bond strength in the pull-out envelop approach. By reducing the clear rib distance, the bond becomes more brittle. By reducing the bond strength, the loss of bond by Vaseline is accounted for.

- For the concrete-SHCC interface elements, a simple 1-segmented material input has been used, to model the structural behavior of the hybrid beams. The effect of the chosen input is not investigated in this numerical part. As increasing the height of the hybrid beams, with a constant SHCC thickness, is expected to influence the concrete-SHCC interface, the effect of the interface strength is studied in Chapter 6.

- Upon increasing the height of reinforced concrete beams from 200 to 400 mm, the bearing moment capacity increases from 16.59 kNm (RC200) to 26.25 kNm (RC400). In addition, the deformation capacity increases as a result of the RC300 and RC400 failing by rebar rupture. The RC200 beam failed by failure of the compression zone. The moment at which the 0.3 mm crack widths are reached, relative to the yielding moment, remains similar (92-94%), upon increasing the height of the beams. The cracking pattern changes upon increasing the height, as the RC200 beam showed 7 cracks propagating to the compression zone, whereas this were only 5 and 4 for the RC300 and RC400 beam respectively. In addition, the RC300 and RC400 beam show the development of an effective tensile area.

- Upon increasing the height of the hybrid reinforced beams, the deformation capacity increases the 400 mm high beam, compared to the H200 and H300 beam. The ultimate bearing capacity increased for H300 and H400, compared to H200 from 80.61 kN up to 103.70 kN. The cracking patterns differed among the beams as the H200 beam shows 7 propagated concrete cracks, whereas only 4 and 2 propagated cracks are found for the H300 and H400 beam respectively. The H200, H300 and H400 beams show a uniform crack distribution in the SHCC layer. The moment at which the 0.3 mm crack width is reached, relative to the yielding moment, remains similar for the hybrid beams. The relative moment for the H200 is 99.73%, whereas this is 99.21% (H300) and 98.88% (H400) for the 300 mm and 400 mm high beams. The H200, H300 and H400 beams show a sudden increase in crack width, upon yielding of the reinforcement. In addition, the delamination of the concrete-SHCC interface increases upon increasing the height from 0.62 mm (H200), to 1.65 mm (H300) and 4.13 mm (H400). As it is uncertain if the delamination of the H300 and H400 beam is affecting the crack controlling behavior, it is recommended to study the effect of the concrete-SHCC interface roughness for hybrid beams with a height larger than 200 mm. The effect of a stronger concrete-SHCC interface is numerically studied in chapter 6.

- The H200, H300 and H400 beams showed an increased bearing capacity (21-28%), compared to the concrete reinforced beams of the same height. In addition, the deformation capacity is found to decrease for all the hybrid beams (12-47%), compared to the concrete reinforced beams of the same height. All the hybrid beams show improved crack controlling behavior, by a uniform crack distribution in the SHCC layer, compared to the concrete reinforced beams.

- The simulation of smooth and Vaseline treated reinforcement bars in the 300 mm high hybrid beam decrease the deformation capacity of the hybrid beam from 19.47 mm (H300) to 16.40 mm (H300s). In addition, the bearing capacity is significantly lower for the H300s beam. The steel stress remains low (16 MPa), showing that delamination of the reinforcement occurred. The cracking pattern of the H300s beam shows the formation of a single crack in the concrete layer. This explains the low load at which the 0.3 mm crack width limit is reached (35 kN). Thereby, the crack controlling behavior of the H300s beam is compromised. In addition, the delamination of the H300s beam is almost half the delamination of the H300 beam.

5

Experimental Study

The numerical study showed the presence of height scaling effects. However, the Delft lattice model has limits, especially when SHCC and Hybrid beams are modelled. Therefore, this experimental study is performed. The limitations of the lattice model are treated in detail in Chapter 6, where the experimental results are compared with the numerical results.

5.1. Casting

5.1.1. Preparation

Formwork is made for the beams. Two wooden molds are made (Figure 5.1). The first mold can hold two beams of 2525 mm x 150 mm x 400 mm. The second mold can hold two beams of 2025 mm x 150 mm x 300 mm. This means that, a total of 4 beams can be cast simultaneously. The formwork is cleaned from impurities, by a vacuum cleaner and an air gun. After the molds are cleaned, the molds are oiled and the reinforcement cages, which are made out of steel B500, are placed. Plastic spacers are placed to keep the reinforcement cages in the designed positions. After placement of the cages, wooden strips are placed on top to stiffen the molds (Figure 5.1).

Figure 5.1: 300 mm high wooden mould prepared for casting.

Levelling tools are made to ease the casting of SHCC. As a 70 mm SHCC bottom layer is designed for, two levelling tools of respectively 230 mm and 330 mm long are made (Figure 5.2).

Figure 5.2: Levelling tools of (left) 330 mm long and (right) 230 mm long.

In case the H300s beam is made, the reinforcement cage installed has smooth longitudinal reinforcement bars instead of ribbed steel. The steel quality used is similar, as of the ribbed B500 steel. The smooth rebars are treated with Vaseline over the middle section in between the stirrups (Figure 5.3).

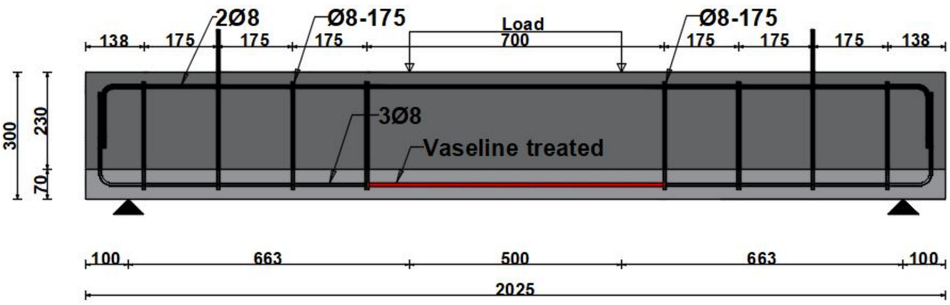

Figure 5.3: Schematic view of part of rebar that is treated with Vaseline.

5.1.2. SHCC layer

The SHCC used is a mixture of cement III/B, limestone powder, PVA fibers, superplasticizer and water (Table 5.1). The mixing procedure of SHCC starts by dry mixing the cement powder, PVA fibers and limestone powders for 1 minute. In the meantime, the water and superplasticizer are mixed with each other.

Table 5.1: (a) Mix design for SHCC and (b) properties of PVA fibers used.

Ingredients	Dry weight (kg/m^3)
CEM III/B 42.5 N	790
Limestone powder	790
PVA fiber	26
Water	411
Superplasticizer	2.13

(a)

Property	
Length (mm)	8
Diameter (mm)	0.04
E (GPa)	40
f_t (MPa)	1600

(b)

After dry mixing, the liquids are added and mixed for 4 minutes. During mixing, the mixer changes its orientation from horizontal to vertical and back. The altering of angle of the mixer is needed, to ensure a uniform mix. Once the mix is uniform, it is cast in the molds. During casting, the levelling tool is used to make the SHCC layer 70 mm high (Figure 5.4). In case one mold is filled with SHCC and the adjacent mold is left empty, wooden spacers are placed in the empty mold. This limits deformation of the separation wall of the molds. After casting, the SHCC is densified by putting the mold on a vibration plate. The mix is vibrated until it looks smooth and air bubbles do no longer appear at the surface. After densifying, the SHCC is cured by closing it off with foil for 14 days.

Figure 5.4: Casted SHCC layer.

5.1.3. Interface treatment

After 14 days the foil is removed and the top surface is steel brushed with a soft steel brush (Figure 5.5). Brushing makes the surface smoother. After steel brushing, the unused mold parts and uncovered reinforcements are cleaned from spilled SHCC, by a scraper and aceton. The top surface is profiled by scanning with the Creaform HandyScan (Figure 5.5).

(a)

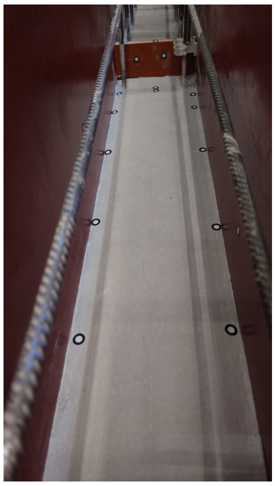

(b)

Figure 5.5: (a) steel brush used for treatment of interface and (b) interface to be scanned.

5.1.4. Concrete

After treating the interface, conventional concrete is made in the mixer. The required volume of conventional concrete is too large for the mixer. Therefore, the mixing of conventional concrete is done in three equal batches of 175L. The concrete is made out of cement I B, aggregates, superplasticizer and water (Table 5.2). A concrete batch is mixed, by first dry mixing the sand and gravel together. After the aggregates are uniformly distributed, cement is added. The dry mixing continues, until a uniform mixture is obtained. The superplasticizer is mixed with the water, after which the water is added to the dry mix. The concrete is mixed until all the liquid is mixed with the dry mix and a uniform consistency is observed. Once the concrete is mixed, it is cast in the molds. The 300 mm high molds are completely filled with one concrete batch. The second and third batch are used to fill the 400 mm high molds. After casting a batch, the concrete is densified with a vibration needle, until the poured concrete appears smooth and popping of entrapped air is no longer observed.

Table 5.2: Mix design for Conventional Concrete.

Ingredients	Dry Weight (kg/m^3)
CEM I B 52.5R	260.00
Sand 0.125-0.25 mm	78.83
Sand 0.25-0.5 mm	256.20
Sand 0.5-1 mm	256.20
Sand 1-2 mm	157.66
Sand 2-4 mm	98.54
Sand 4-8 mm	394.15
Gravel 8-16 mm	729.18
Water	156.00
Superplasticizer	0.26

In case one mold has a SHCC layer and the adjacent mold does not, the empty mold is filled first with concrete up to approximately 70 mm height, after which concrete is poured in both molds at a similar rate. After all the molds are filled with concrete, the molds are sealed with foil for 28 days (Figure 5.6).

Figure 5.6: Sealing of of samples after casting conventional concrete.

5.1.5. Material samples

Besides casting beams, small samples are cast, to verify the material properties. The molds used for this are first cleaned with a cloth, followed by cleaning with the air gun. After the molds are clean, they are oiled. When SHCC is cast for the hybrid beams, cubes of 100 mm x 100 mm x 100 mm, dogbones with a gauge section of 80 mm x 30 mm x 13 mm and a prism of 100 mm x 100 mm x 400 mm are made from the same batch (Figure 5.7). When concrete is cast, 100 mm x 100 mm x 100 mm cubes and a 100 mm x 100 mm x 400 mm prism is made for every batch. All the material samples are vibrated on a vibration table, until escaping of entrapped air is no longer observed. After vibrating the samples, the excess concrete/SHCC is removed and the samples are sealed with foil.

(a)

(b)

Figure 5.7: Casting of SHCC material samples on the vibration table: (a) prism and cubes before removing excess SHCC and (b) dogbones after vibrating and removing excess SHCC.

5.2. Measuring Techniques

In order to measure the structural behavior of the beams, the following measurement techniques are used:

- Digital Image Correlation (DIC)
- Crack-Widths measurements from DIC data
- Linear Variable Data Transformer (LVDT)
- Interface surface profiling
- Surface texture scanning

5.2.1. Digital Image Correlation (DIC)

Digital Image correlation (DIC) is a non-contact optical displacement measuring method. With DIC it is possible to measure a field of displacements and strains, instead of specific predefined points. A software program, in this study GOM correlate, is capable of doing this by comparing a reference image, which is taken before the test starts, with images taken during the test. Comparison is done by overlapping the images. With overlapping, the image is divided in sets of pixels, so-called sub-images (Figure 5.8). Coordinates are assigned to the sub-images. The displacement of a sub-image in an image is found by correlation of the sub-image in the reference image. This correlation is done with the correlation coefficient. The correlation coefficient is the ratio between the amount of grayscale in a sub-image ($\tilde{g}_{ij}$), compared to the reference sub-image (g_{ij}). The correlation coefficient (COF) can be described as (Shih and Sung, 2013):

$$COF = \frac{\sum g_{ij}\tilde{g}_{ij}}{\sqrt{\sum g_{ij}^2 \sum \tilde{g}_{ij}^2}} \tag{5.1}$$

If the sub-image from the deformed image is exactly the same as the sub-image from the reference image, the correlation coefficient is 1. The correlation of sub-images is done by maximizing the correlation factor, which results in a best fit solution. In order to compare a sub-image with sub-images of the reference image, the sample should have a unique pattern, which is recognizable for the software.

Therefore, the pattern should contain enough dots to be created unique sub-images. In addition, the dots should not be too small or too big. Too small dots are not recognized by the correlation software, whereas too large dots lead to loss of data. An image consists of a lot of pixels. To make the computation time feasible, sub-images are created at a predefined interval distance, called point distance. The smaller the point distance, the more sub-images can be made inside the image. If more sub-images are made, the amount of pixels correlated increases, and thereby the accuracy of the measuring is improved. The size of the sub-images, called facet size, influences the measuring accuracy, as a smaller sub-image allows for more sub-images to fit in an image.

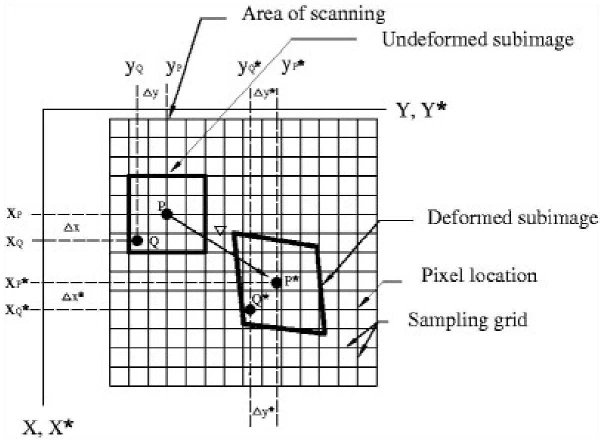

Figure 5.8: Correlation of a sub-image from an undeformed and deformed image Shih and Sung, 2013.

As DIC is an optical measurement method, the accuracy of the data is dependent on the light conditions in the room, but also on the stability of the camera setup. Light conditions are conditioned by using flashes, and with use of limited opening time of the camera lens. In addition, the amount of opening of the camera lens is limited. Stability of the camera is dependent on movements of the surrounding and touching of the camera. Therefore, the camera is controlled remotely and a perimeter is set up.

5.2.2. Crack-Widths measurement from DIC data

From DIC data, displacement fields and strain fields are found. From these displacement and strain fields, cracks are measured over predefined cross sections. As bending cracks are typically conical shaped, the width is largest close to the outer surface. Therefore, a cross section is made 2 mm from the bottom of the beam. In case of hybrid beams, an additional cross section is made at 75 mm from the bottom of the beam. Over the cross section, the Von Mises strain is calculated. A peak in the Von Mises strain is regarded a cracking location. If the strain exceeds a certain threshold, the starting point of the interval of the crack is determined (Figure 5.9). The last point above this threshold is regarded as the endpoint of the interval. The threshold used for the Von Mises strain peaks are 0.3% for SHCC and 0.5% for concrete. A threshold is needed, in order to eliminate noise from the data. A crack is calculated, as the difference in horizontal displacement of the first point of a crack interval and the last point of a crack interval, by:

$$Crackwidth = |dx_1 - dx_2| \tag{5.2}$$

In this formula, dx_1 is the horizontal displacement at the start of the crack interval and dx_2 is the horizontal displacement at the end of the crack interval. Cracks are calculated with a MATLAB script, to automatize the calculations (Appendix A). Cracks can also be calculated manually in GOM correlate, by manually selection of an interval over which the difference in horizontal displacement has to be calculated. This direct calculation from GOM correlate is used to verify the MATLAB script (Figure 5.10).

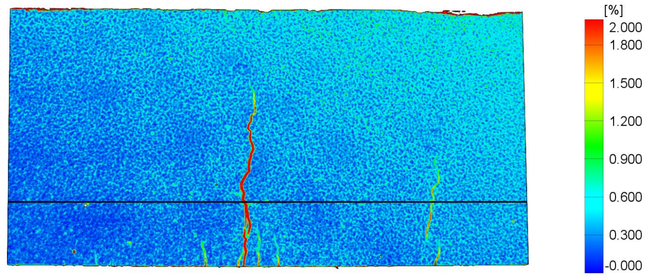

(a)

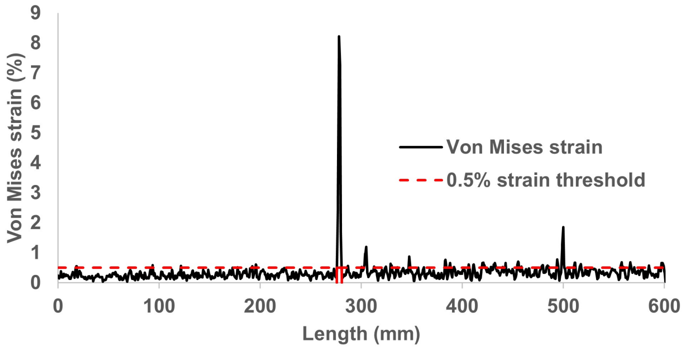

(b)

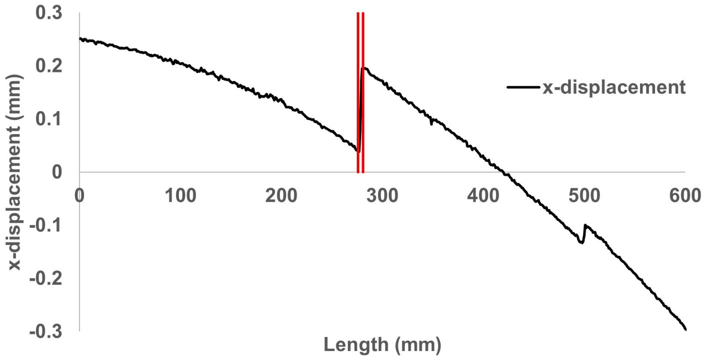

(c)

Figure 5.9: Crack width measurement with (a) Von Mises contour plot and (b) cross section plots of Von Mises strain and (c) horizontal displacement.

The deviations between the MATLAB script and the direct calculation of GOM are used, to determine how good the MATLAB calculations fits the GOM calculations. The deviations used are: the maximum deviation, the mean deviation and residual standard deviation (RMSE). These are determined by:

$$\text{Maximum deviation } = \max(Code(i) - GOM(i)) \tag{5.3}$$

$$\text{Average deviation } = \frac{\sum_{i=1}^{n}(Code(i) - GOM(i))}{n} \tag{5.4}$$

$$RMSE = \sqrt{\frac{\sum_{i=1}^{n}(Code(i) - GOM(i))^2}{n}} \tag{5.5}$$

In these formulas, n is the amount of cracks, $Code$ is the crack widths as determined with the MATLAB code and GOM is the crack widths as determined by GOM correlate. The residual standard deviation is the criteria used to determine if the fit is good. The average deviation and maximum deviation are used to determine how good the fit is, compared to the rest of the data. From figure 5.10 is is found that, the RMSE is below 0.01 mm. This is considered good. As the average and maximum deviations are found to be small, it is decided to use this MATLAB script.

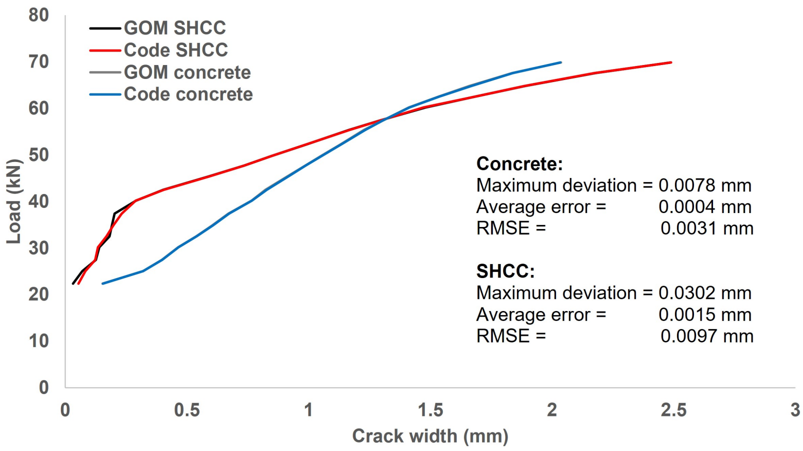

Figure 5.10: Verification of automatized crack width calculation in MATLAB.

5.2.3. Linear Variable Data Transformer (LVDT)

As DIC is sensitive to how it is setup and to the quality of the pattern, it is common to verify the measurements with strain gauges. Linear Variable Data Transformers (LVDTs) are used. LVDTs measure the displacement difference between two predefined locations by compressing a spring or by relaxation of a compressed spring. By displacing the spring, the resistance in the electric circuit is changed, which is measured and converted to the displacement. In order to convert the measured voltage to a displacement, a conversion factor needs to be determined, which is done by calibration of the LVDTs. Calibration of a LVDT is done by applying a known displacement and measuring the occurred voltage.

5.2.4. Interface surface profiling

The hybrid beams have a concrete-SHCC interface. It was found that, the roughness of this interface affects the structural behavior of the hybrid beams (Subsection 2.3.1). Therefore, the interface roughness is determined. The roughness is determined with help of the Creaform HandyScan 3D Black Elite (Creaform, 2022). This is a laser scanner, containing 11 blue light lasers. This scanner is able to measure with a resolution of 0.025 mm. In order to scan, reference points have to be placed every 100 mm in plane of scanning. Additionally, reference points need to be placed on connected planes in order to allow the scanner to orientate the different scanned surfaces. From scanning, a point cloud is generated. By linking the points of the point cloud with each other, edges are formed. By linking the edges, meshes are formed, which leads to the formation of shapes. This forms 3D shapes, which contains the full surface data. In order to determine the surface roughness, predefined cross sections are made. This results in 2D curves, with the height of the points (y-axis) and the length of the cross section (x-axis). The roughness is determined by the arithmetical mean roughness, which is found by:

$$\bar{x} = \frac{\sum x_i}{n_x} \tag{5.6}$$

$$R_a = \frac{\sum x_i - \bar{x}}{n_x} \tag{5.7}$$

In this formula, $\bar{x}$ is the nominal mean and R_a is the arithmetical mean. Besides the arithmetical mean, also the maximum peak (R_p), maximum valley (R_v) and total roughness (R_t) are determined. These are determined by:

$$R_v = max(\sum x_i - \bar{x}) \tag{5.8}$$

$$R_p = min(\sum x_i - \bar{x}) \tag{5.9}$$

$$R_t = R_v + R_p \tag{5.10}$$

5.2.5. Surface texture scanning

Lastly, a surface texture scanner is used. The Artec Leo scanner is used, which has a resolution up to 0.2 mm (Artec3D, 2022). Different from the HandyScan, this scanner is used to capture texture. Texture is captured by varying the flash intensity. The resolution of this scanner is lower than that of the HandyScan, which is needed in order to limit the size of the scanned files. Texture scans are made of the full beam size, in order to capture the deformed shaped after failing of the beam. The scanning starts with placing reference objects. The reference objects, for example a nut, helps the scanner to recognize its orientation, and thereby allows for connecting faces of a different plane. After scanning, the data is processed by registration of the shapes in the global coordinate system. After this, the shapes are fused and empty spaces are filled. The fusion is done without smoothing the data. Once the shapes are fused, texture is painted.

5.3. Series 1

A first series of beams have been cast. The beams cast are presented in table 5.3.

Table 5.3: Beams of Series 1.

Label	Type	Height	Span	Longitudinal reinforcement
H300	Hybrid R/SHCC	300 mm	1825 mm	Ribbed
H300s	Hybrid R/SHCC	300 mm	1825 mm	Plain and Vaseline treated
RC400	Reinforced concrete	400 mm	2325 mm	Ribbed
H400	Hybrid R/SHCC	400 mm	2325 mm	Ribbed

5.3.1. Testing

As soon as the conventional concrete has an age of 28 days, the beams are tested. Before testing, the beams have to be prepared. The preparations include demolding the samples, cleaning of the side faces from leaked conventional concrete, gluing of LVDT holders and preparing for DIC measurements. 5 LVDTs are used as presented in Figure 5.11. One LVDT is used for measuring the deflection at mid span (LVDT 1). The other LVDTs are used to measure the horizontal displacements at the bottom face of the beam. All horizontally placed LVDTs have a measuring range of 200 mm, except for LVDT 5, which has a measuring range of 500 mm.

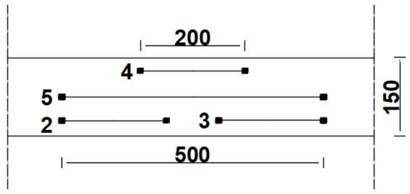

(a)

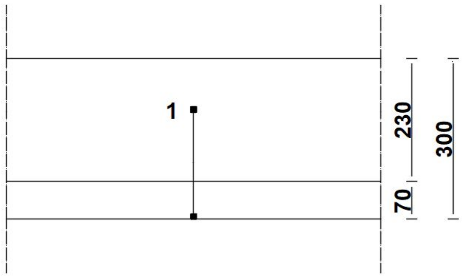

(b)

Figure 5.11: Position of LVDTs on bottom face (a) bottom face and (b) side face.

LVDT 1 is placed on a wooden rod, which is simply support on steel pins glued to the beam. At the center of the span of the beam a steel angle is glued to the bottom face, which allows the LVDT to measure vertically (Figure 5.12).

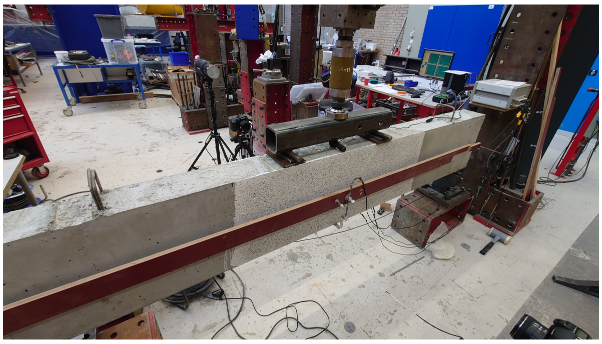

Figure 5.12: Prepared RC400 beam in the setup with the wooden rod and vertical LVDT placed.

DIC measurements are performed on both side faces, over the central 500 mm region of the beams. In order to perform DIC measurements, the side faces white are first painted white. Once the paint is dry, a random black pattern is painted with a paint gun (Figure 5.13). The black-white pattern is chosen for its high contrast, which improves correlation. Once the beams are painted, it is checked if the pattern is recognized in GOM correlate (Figure 5.13). The color green means that the pattern is recognized and strong correlation is present. If yellow or red is observed, it means that the applied pattern is found, but a weak correlation is present. If the the contour plot has white spots, this means that the white spots are uncorrelated and the quality of the pattern is insufficient. In GOM correlate, a facet size of 35 pixels and a point distance of 12 pixels is chosen. If the pattern is of sufficient quality, the beam is placed in the test setup and the DIC cameras are placed. Canon EOS 5DS R cameras with 35 mm fixed lenses are used on both sides. Each camera is connected with a separate flash. The cameras are connected to a trigger box, in order to take pictures simultaneously. The cameras are setup such that they are stable, horizontal and centralized with the center of the beam. The camera setup is checked by a noise analysis (Figure 5.13). A noise analysis is performed by correlation of two successively taken images. The images are taken of the unloaded beam. Upon correlation, the maximum x-displacement is determined. Red areas in the contour plot indicate a relative large x-displacement between the reference image and the successively taken image. By performing this noise analysis, the noise in the measurement setup can be determined. If the maximum found displacement in the second image is below 0.015 mm, the camera setup is accepted.

(a)

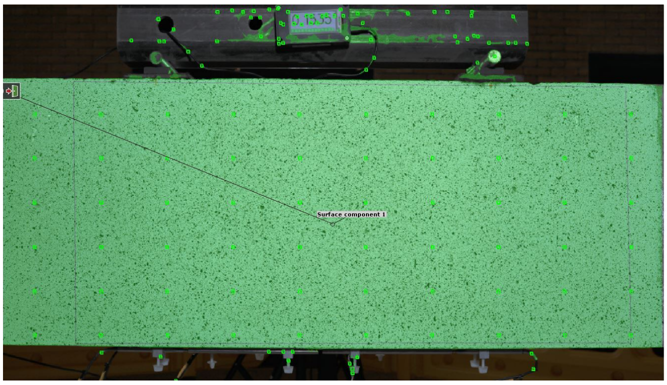

(b)

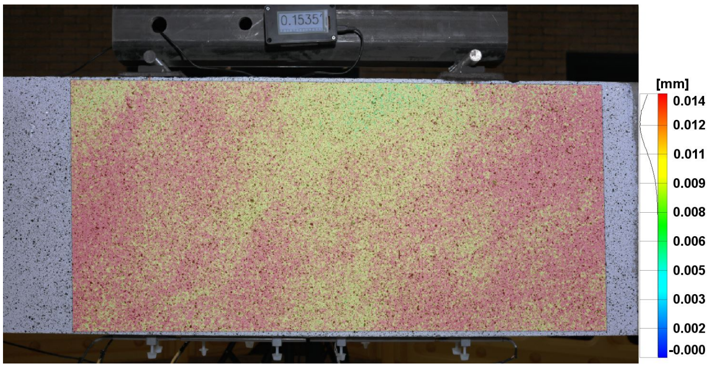

(c)

Figure 5.13: 400 mm high concrete beam with (a) side face prepared for DIC , (b) a quality check of the pattern for DIC in GOM correlate and (c) the noise analysis in GOM correlate.

The setup used is a steel frame made out of HE300B profiles, with a 100 kN hydraulic jack. A steel load spreader, supported on a fixed roller and a free roller, is used to create a four-point bending configuration. In between the sample and the load spreader, felt and 10 mm thick steel plates are placed. The beam is support by 8 mm thick steel support plates, placed on steel rollers. The supports are bolted to steel boxes, which are placed directly on the ground (Figure 5.14).
The test is performed in displacement control with a loading rate of 0.01 mm/sec. A load-display is placed on top of the beam, which allows for the applied load to be displayed inside the images. Images are taken every 5 seconds. After testing, the 3D texture scan are made.

Figure 5.14: Test setup with the load spreader, supports, camera setup and the RC400 beam.

5.3.2. Experimental Results

During the experiments, DIC data is collected from two side faces of the beam and LVDT data is collected from the bottom face of the beam (Figure 5.15).

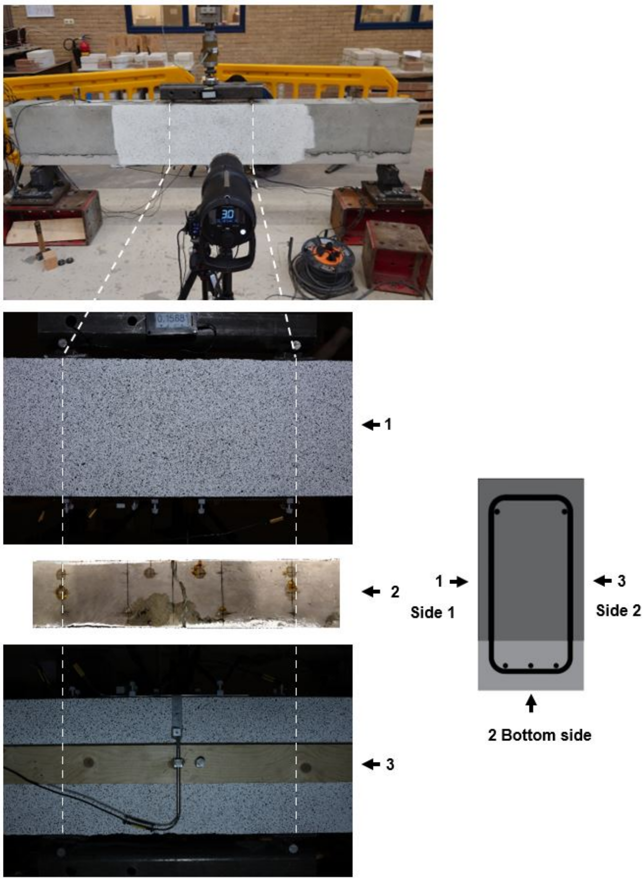

Figure 5.15: Overview of measurement setup with 1. Side 1 DIC, 2. Bottom side of beam with horizontal LVDT measurements and 3. Side 2 DIC with vertical LVDT measurement.

One side face has the wooden rod for vertical LVDT measurements. This side is labelled as side 2. The other side is labelled as side 1.

Hybrid R/SHCC beam of 300 mm height with smooth and Vaseline treated longitudinal reinforcement bars

In figure 5.16 the load-displacement behavior of the H300s beam is presented. In the same figure the maximum crack widths in the SHCC layer are shown. A summary of the key performance indicators of the beam are provided in table 5.4. The beam failed by rupture of the reinforcement. The beam reached yielding of the reinforcement at a load of 68.95 kN.

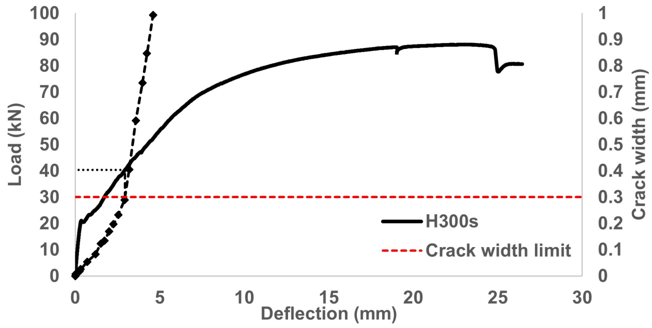

Figure 5.16: Load-deflection (solid) vs. maximum crack width-deflection (dashed) curve.

Table 5.4: Overview of results of experiment of H300s.

Key performance indicators	
Ultimate load	88.09 kN
Maximum deflection	24.85 mm
Number of cracks	24
Average crack spacing	20.83 mm
Load at 0.3 mm crack width	40.37 kN
0.3 mm load/yield load	58.55%

The roughness of the concrete-SHCC interface is determined over the 500 mm constant bending moment region. Both a contour plot and the 3D scanned interface are presented in Figure 5.17. The scale of the contour plot is in millimeters (mm), where red shows the largest peaks and blue the deepest valleys.

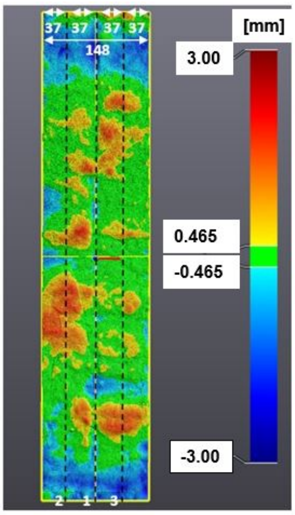

(a)

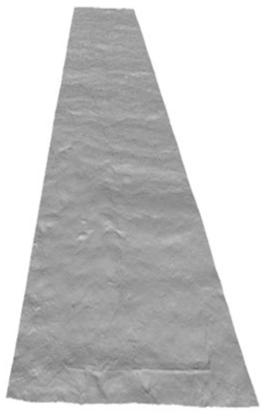

(b)

Figure 5.17: Interface profiling with (a) contour plot and (b) 3D scan.

From the scanned surface, three sections over the length of the interface are made, to determine the roughness. The first section is made at the middle of the width of the interface. Section 2 and 3 are made at 37 mm, respectively left and right of the middle line of the beam. From the sections made, profile graphs are made (Figure 5.18)

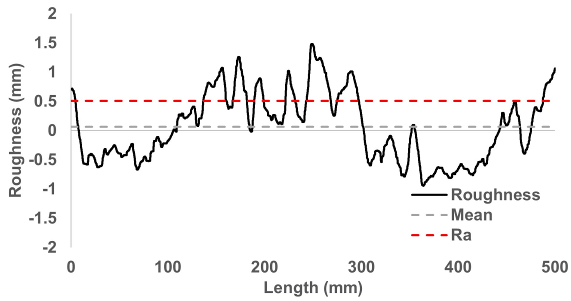

(a)

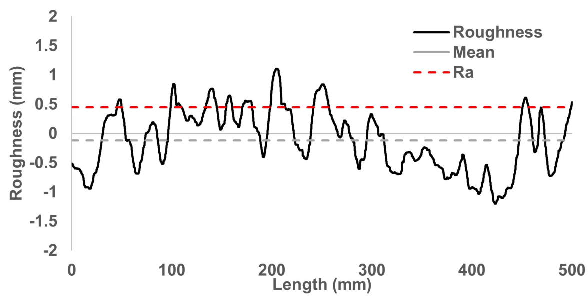

(b)

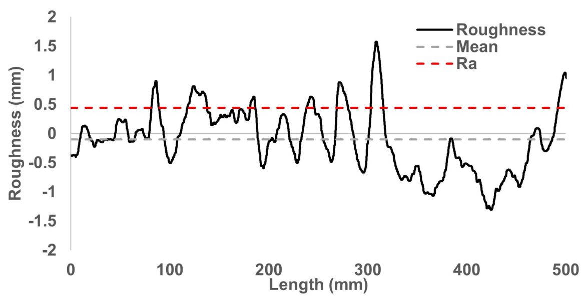

(c)

Figure 5.18: Interface profile graphs at (a) section 1, (b) section 2 and (c) section 3.

An average arithmetical surface roughness of 0.465 mm is found with a maximum peak value of 1.440 mm (Table 5.5). Therefore, the interface is considered smooth.

Table 5.5: Overview of results of interface profiling.

Section	1	2	3	Average
Ra (mm)	0.506	0.448	0.440	**0.465**
Rp (mm)	1.420	1.225	1.675	**1.440**
Rv (mm)	1.009	1.079	1.208	**1.098**
Rt (mm)	2.428	2.304	2.883	**2.538**

Crack widths are measured from two sides with DIC. In order to show the crack development, contour plots of Von Mises strain are made. A green up to red zone indicates strain localization, and thus a crack. SHCC cracks are presented in point cloud graphs. The top graphs belong to side 1, whereas the bottom graphs belong to side 2. The crack widths in concrete are reported inside the contour plots. On side 2, no DIC data is available at the center span, due to the vertical LVDT measurement. SHCC cracks are unknown at this location, whereas concrete cracks are determined over the full length of the region with the missing data. The first crack appears at 10.04 kN (Figure 5.19). Upon increasing the load, more cracks are formed and existing cracks widen (Figure 5.19 to 5.27). Between the two sides, differences in crack widths are found in SHCC and in concrete. The biggest crack is formed at center span of the beam. Upon opening of this crack, adjacent cracks are closed (Figure 5.25). In SHCC the major central crack is branched into smaller ones, however no distributed cracking pattern is found over the full constant bending moment region. Additionally, it is found that the central crack starts in the concrete layer and propagates to the SHCC layer. Therefore, the largest crack widths in the SHCC layer are not found at the bottom of the beam, but directly underneath the concrete-SHCC interface. The reported crack widths are in millimeters (mm).

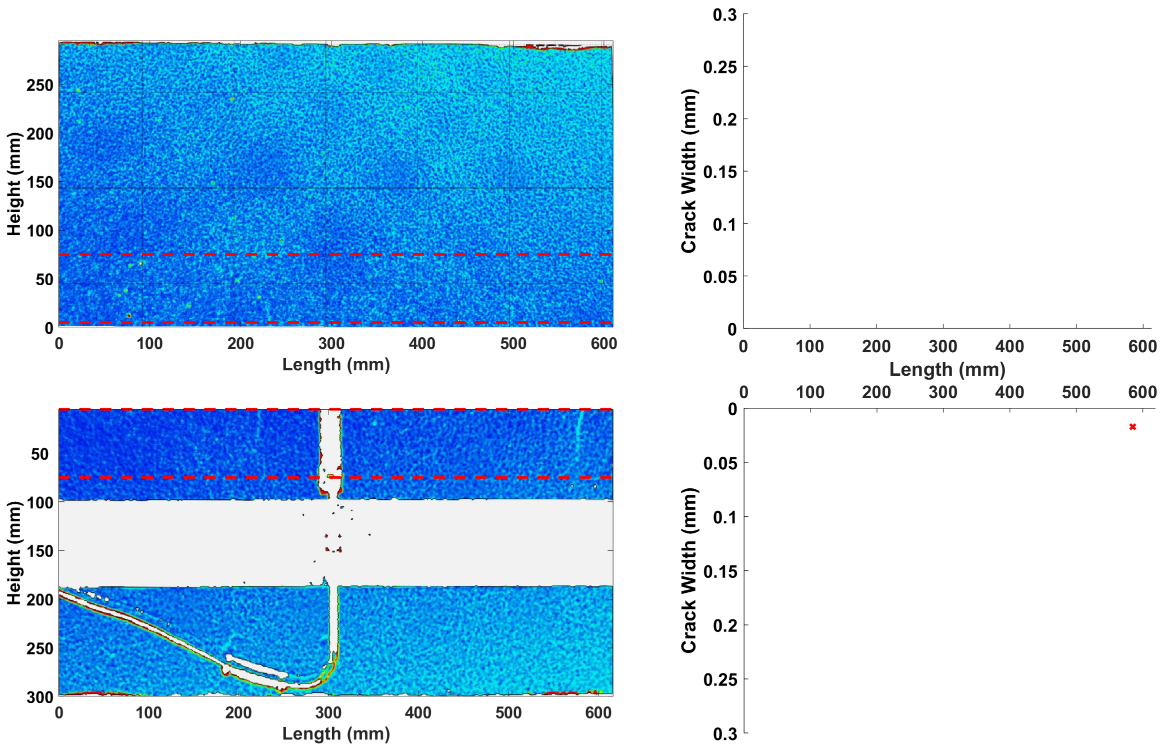

Figure 5.19: Crack widths from DIC data at a load of 10.04 kN.

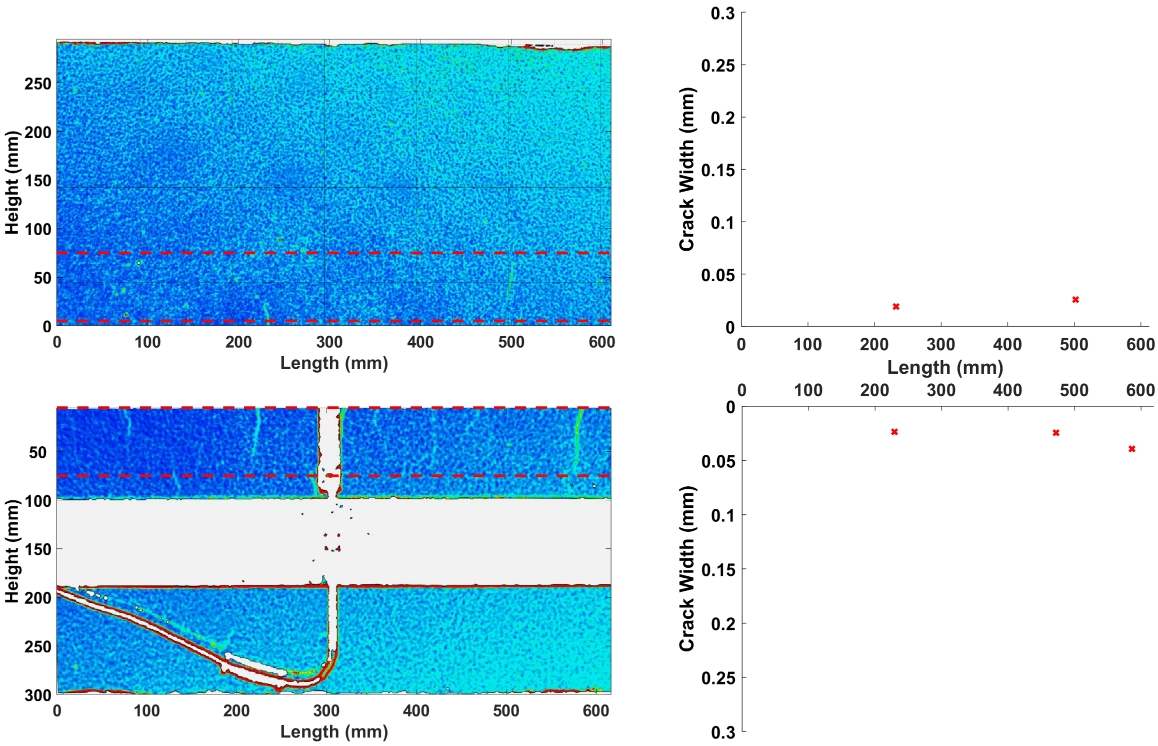

Figure 5.20: Crack widths from DIC data at a load of 20.49 kN.

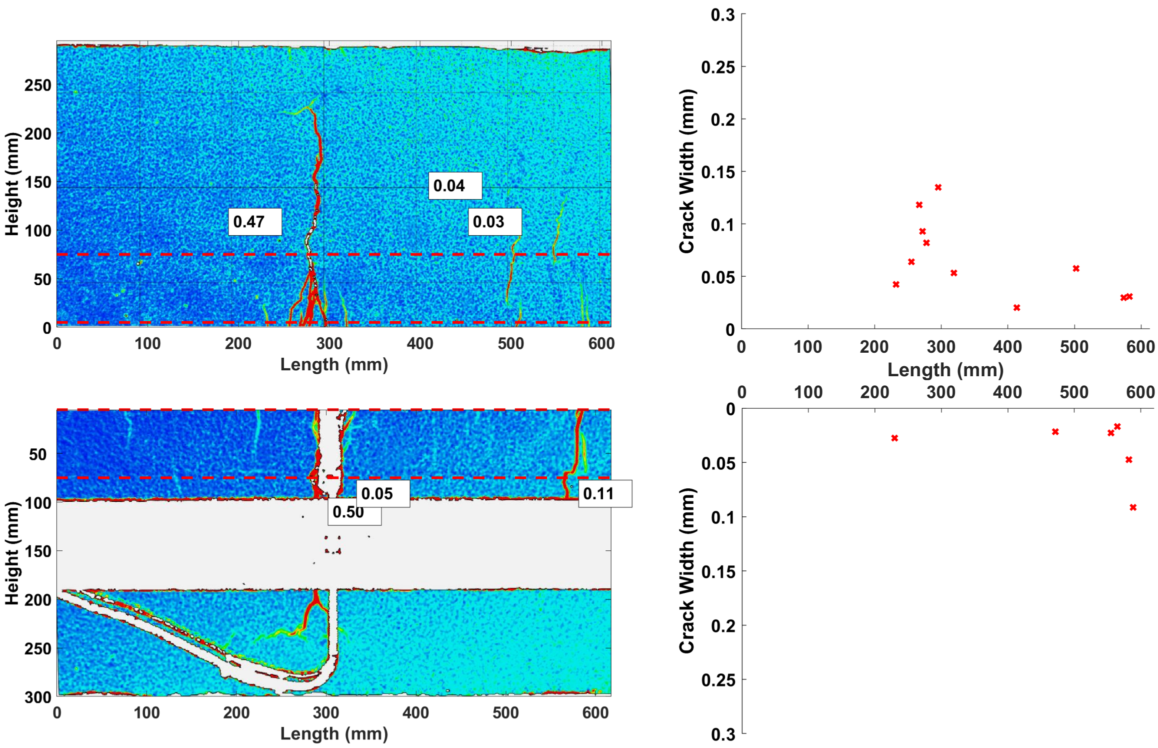

Figure 5.21: Crack widths from DIC data at a load of 30.15 kN.

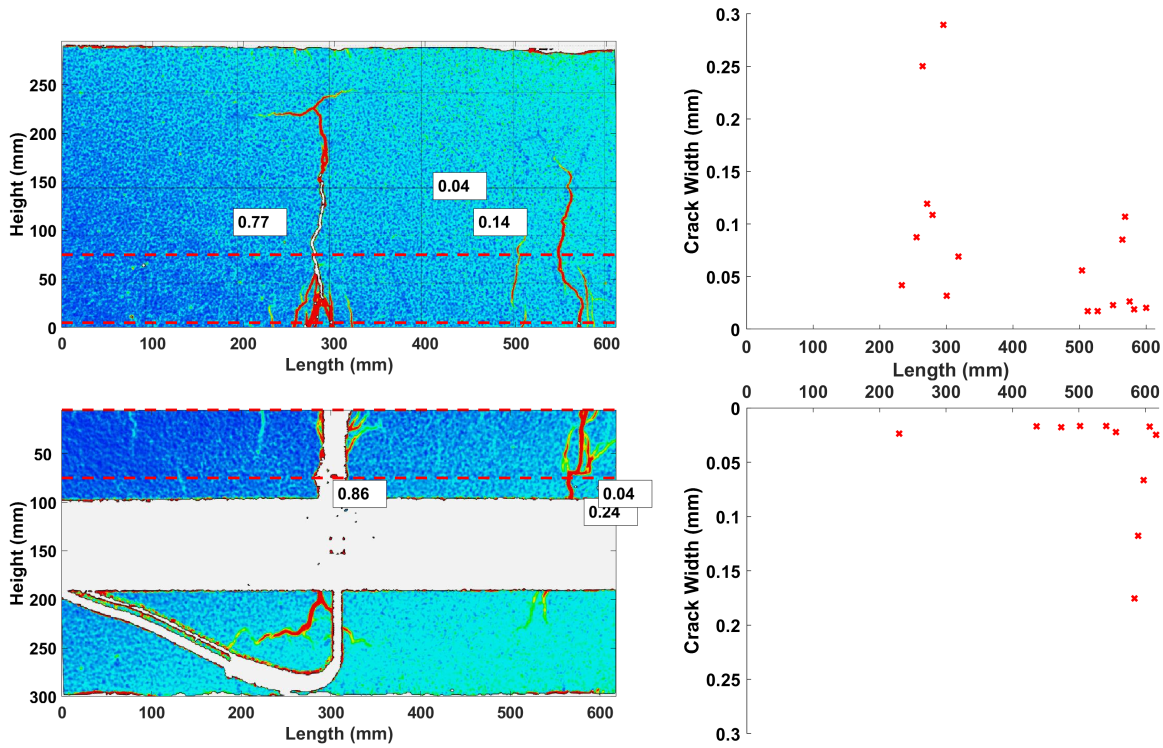

Figure 5.22: Crack widths from DIC data at a load of 40.16 kN.

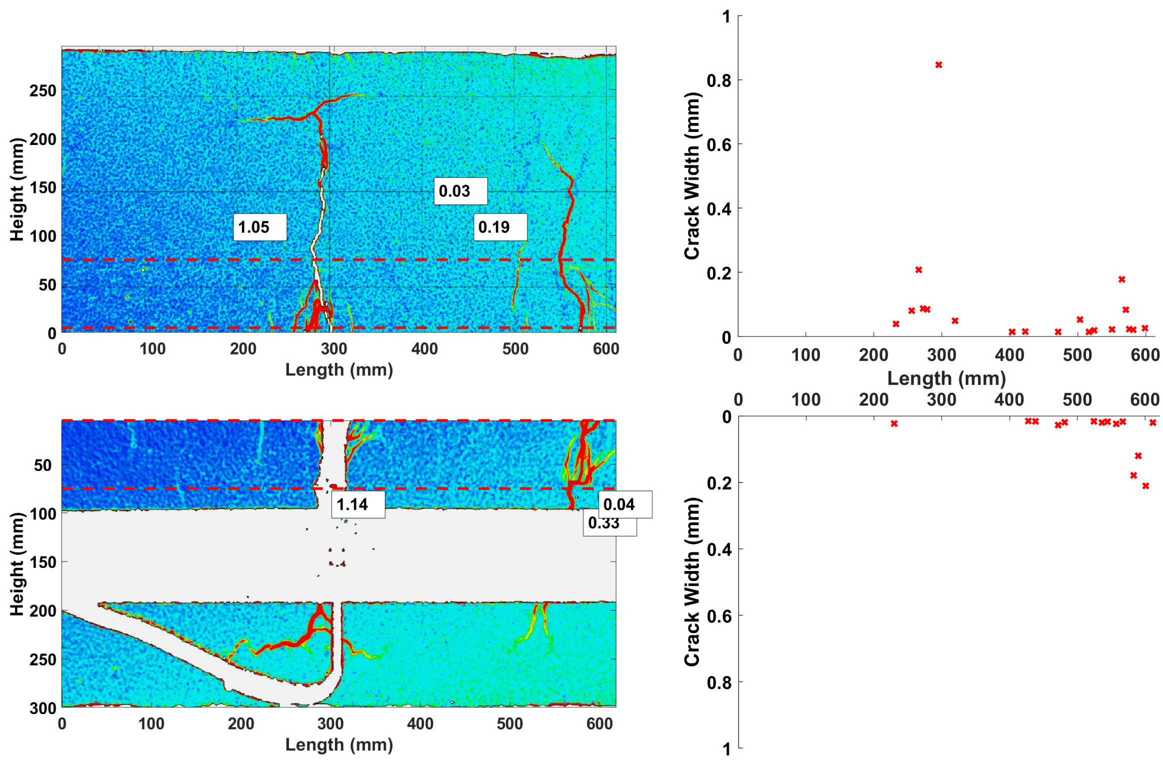

Figure 5.23: Crack widths from DIC data at a load of 49.75 kN.

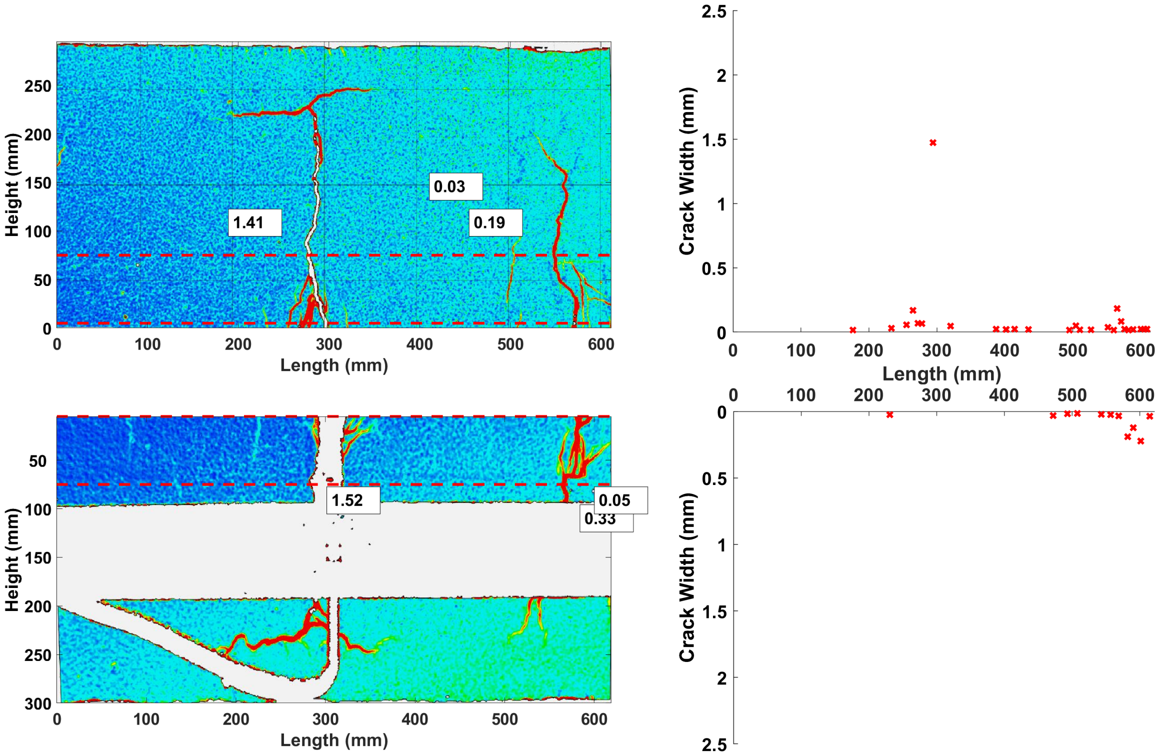

Figure 5.24: Crack widths from DIC data at a load of 60.17 kN.

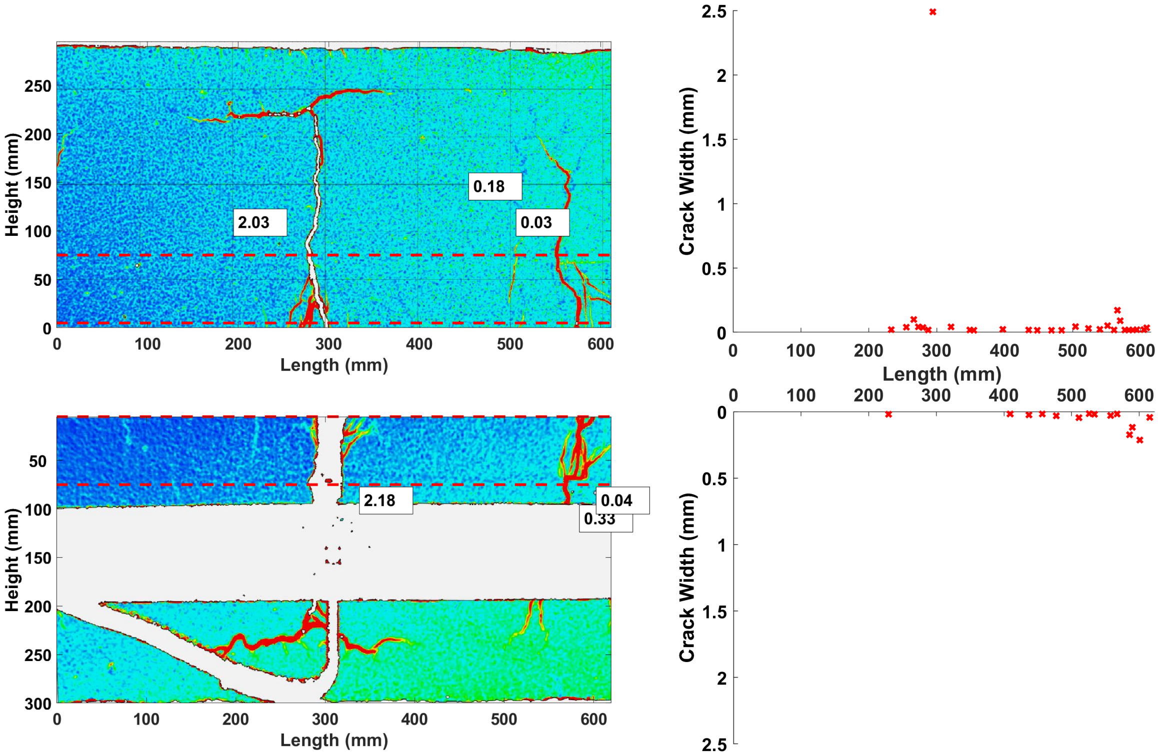

Figure 5.25: Crack widths from DIC data at a load of 69.89 kN.

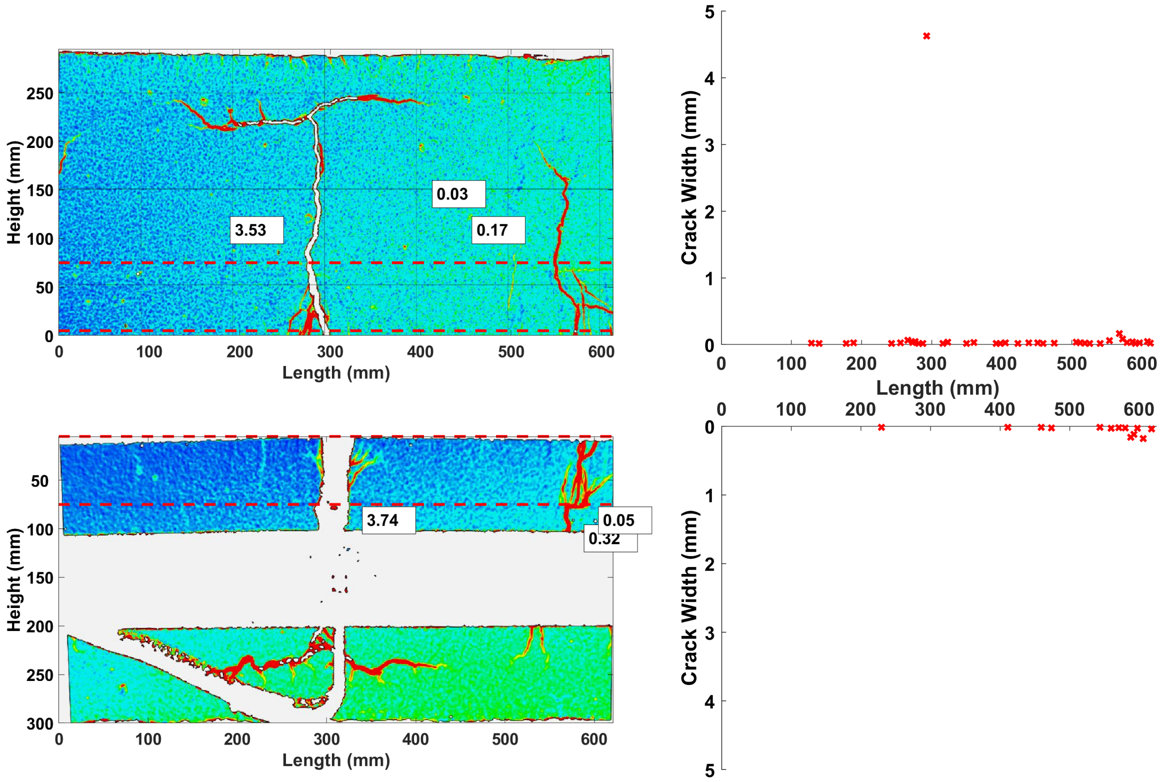

Figure 5.26: Crack widths from DIC data at a load of 80.15 kN.

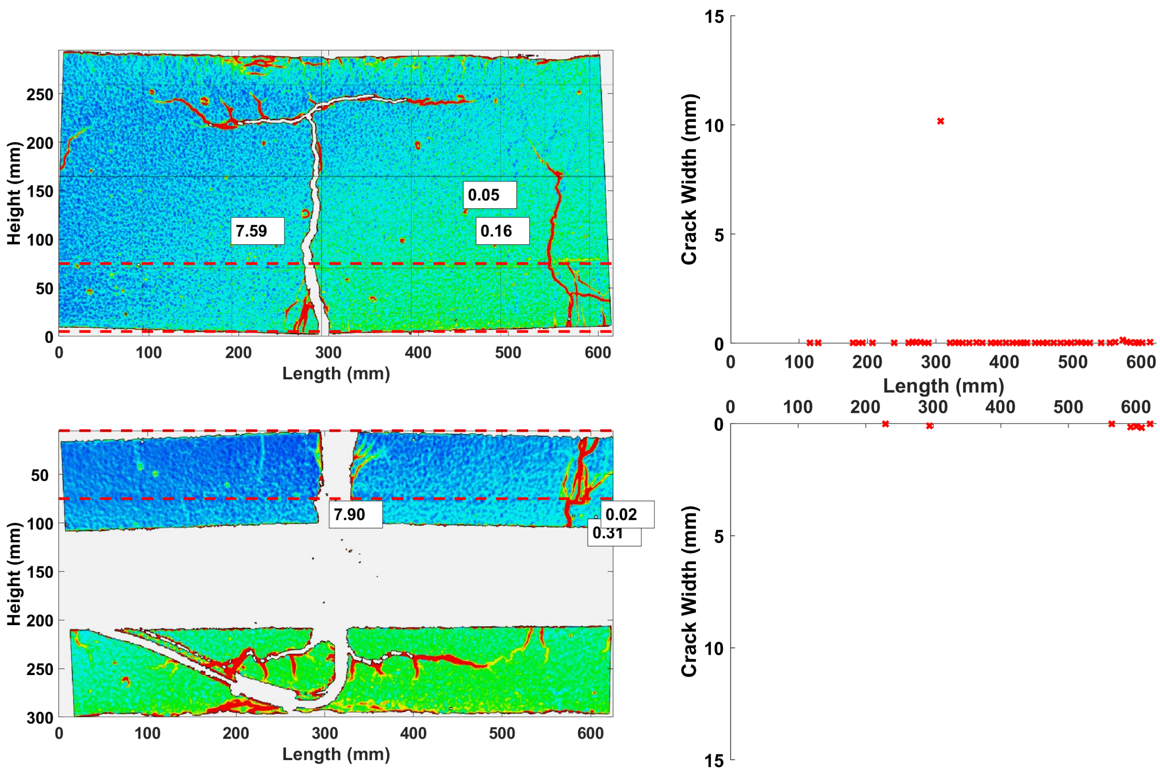

Figure 5.27: Crack widths from DIC data at a load of 88.09 kN.

In addition to the development of the cracking pattern, the behavior of the interface is monitored on side 1 of the beam. The opening (delamination) of the interface and the slip of the interface are measured (Figure 5.28). The slip is measured as the difference in x-displacement, 3 mm below and 3 mm above the interface. Thereby, rigid body motion is ignored. The delamination is measured as the difference in y-displacement, 1 mm above and 1 mm below the interface. Therefore, the slip and the delamination measurements include material strain. These measurements are performed on three predefined locations: center of the constant bending moment region (1), 250 mm on the right of the center span of the beam (2) and 250 mm on the left of the center span of the beam (3). In order to visualize the delamination, contour plots of the vertical strain are presented (Figure 5.28). Delamination is assumed to occur once the slip exceeds 0.05 mm. The delamination is found to start at a load of 30 kN. This load is reached at a deflection of 2.62 mm. It is found that, upon increasing the load, the delamination and slip of the interface increases. The maximum delamination found is 0.09 mm. Therefore, only limited delamination of the concrete-SHCC interface is observed. The maximum slip is 0.5 mm. This slip, relatively large compared to the delamination, can be attributed to the ignored rigid body motion.

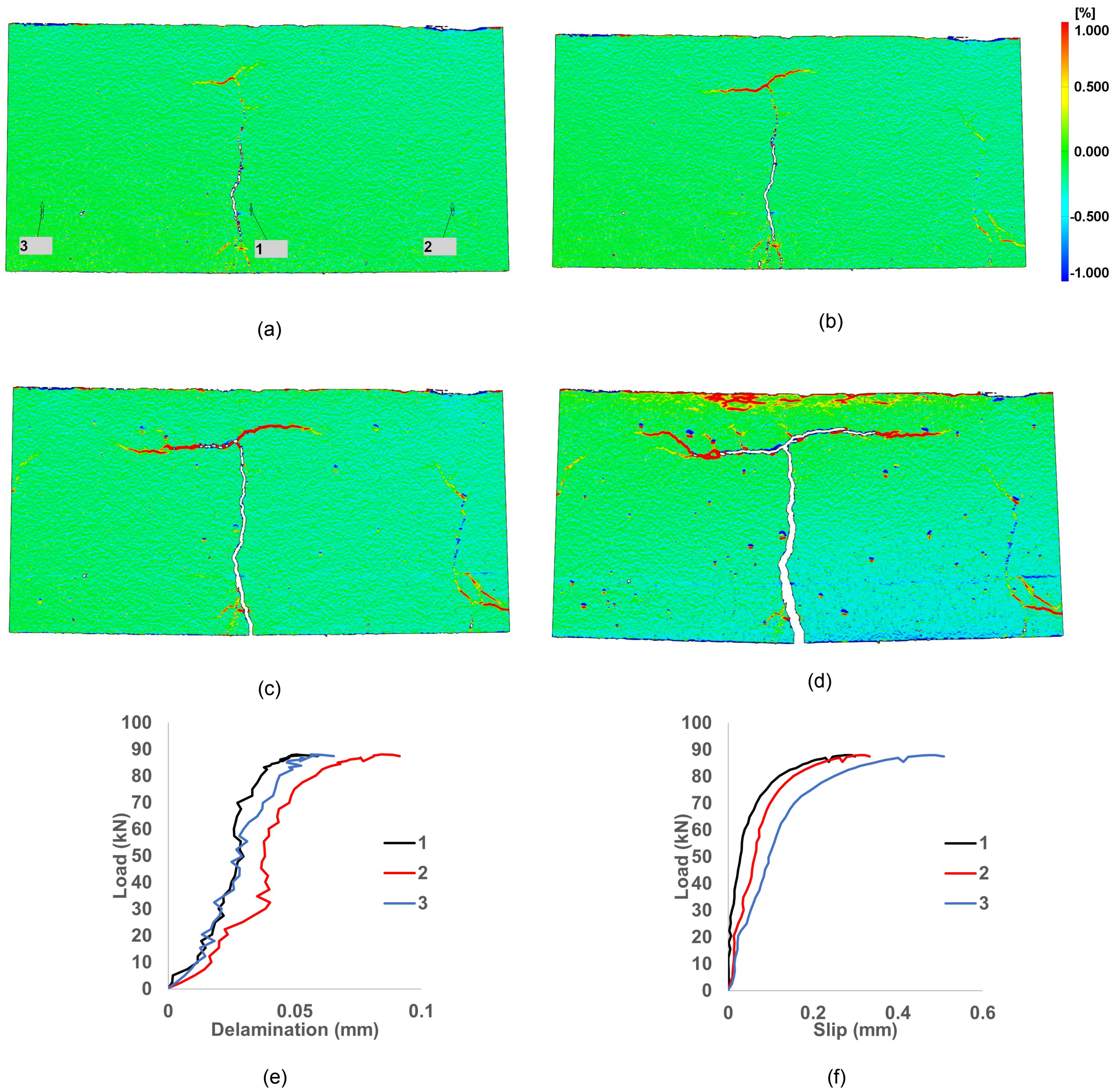

Figure 5.28: Structural behavior of the interface with (a) vertical strain contour plot at 30 kN load, (b) vertical strain contour plot at 40 kN load, (c) vertical strain contour plot at 60 kN load, (d) vertical strain contour plot at 88 kN load, (e) load-delamination curves for the three measuring points and (f) load-slip curves for the three measuring points.

For the crack width measurements, DIC data is used. The DIC data is compared with the LVDT data, to verify the DIC data (Figure 5.29).

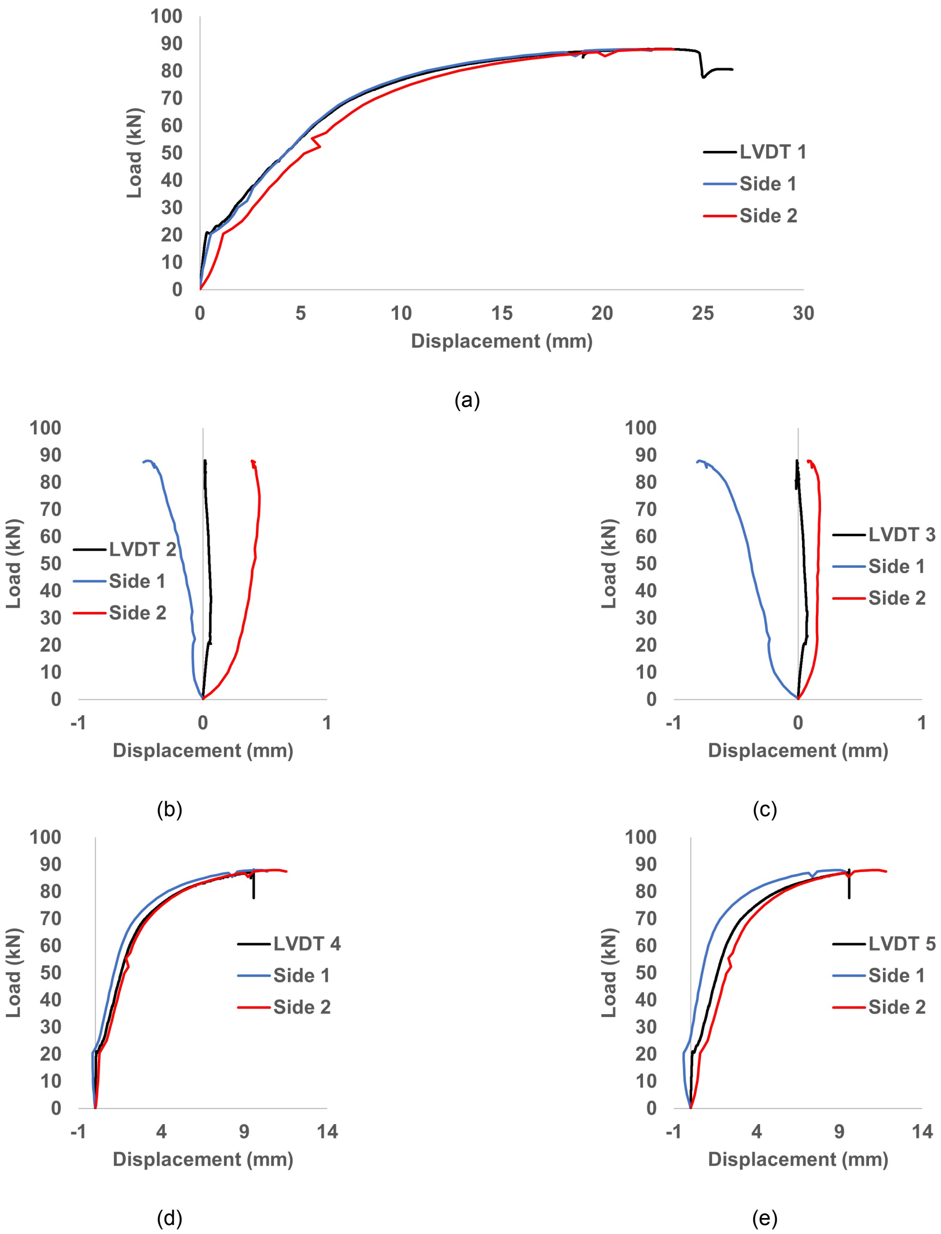

Figure 5.29: Verification of DIC measurements with LVDT data for (a) LVDT 1, (b) LVDT 2, (c) LVDT 3, (d) LVDT4 and (e) LVDT 5. Side 1 refers to DIC measurements on side 1 and side 2 refers to DIC measurements on side 2.

From the comparison of DIC and LVDT data, differences are found. The DIC data from side 2 is showing a larger displacement for all LVDT comparisons. The DIC data from side 1 is showing a smaller displacement for all LVDT comparisons. The largest differences are found in the comparisons of LVDT 2 and 3. These LVDTs recorded relative small displacements, due to localization of the major central crack in the beam, which is outside the measuring range of these LVDTs. From the comparison of LVDT 5 it is found that, the DIC data on side 1 is initially showing negative displacements. As the comparison of the DIC data with the LVDT data shows these differences, further investigation is done to the source of these differences.

Hybrid R/SHCC beam of 300 mm height

Due to the differences found in the comparison of the DIC data and the LVDT data from the previous beam (H300s), the LVDT data and the DIC data of the H300 beam are compared first (Figure 5.30).

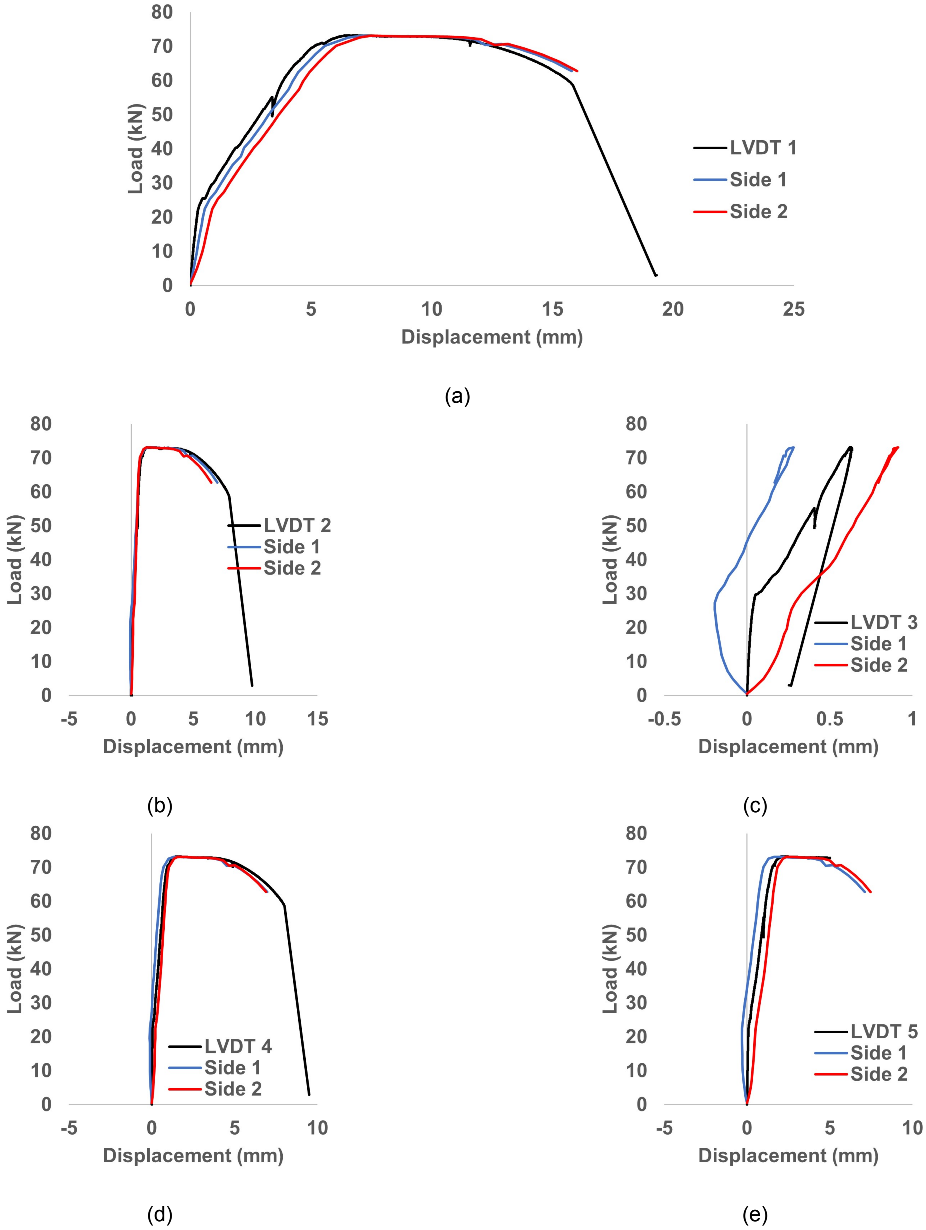

Figure 5.30: Verification of DIC measurements with LVDT data for (a) LVDT 1, (b) LVDT 2, (c) LVDT 3, (d) LVDT4 and (e) LVDT 5. Where Side 1 refers to DIC measurements on side 1 and side 2 refers to DIC measurements on side 2.

Similar as found for the comparison of the LVDT and the DIC data from the H300s beam, differences in the data comparison are found for the H300 beam. Especially, LVDT 3 and 5 show relative large differences for DIC side 1. Side 1 is showing smaller displacements, compared to the LVDT data. The DIC data of side 1 is showing negative displacements. Side 2 is showing the opposite of side 1, by showing too large displacements, compared to LVDT data. As these differences are found once more, further investigation is done before the measured data can be used.

Reinforced concrete beam of 400 mm height
The DIC data is compared with the LVDT data, for the 400 mm high conventional reinforced beam (Figure 5.31).

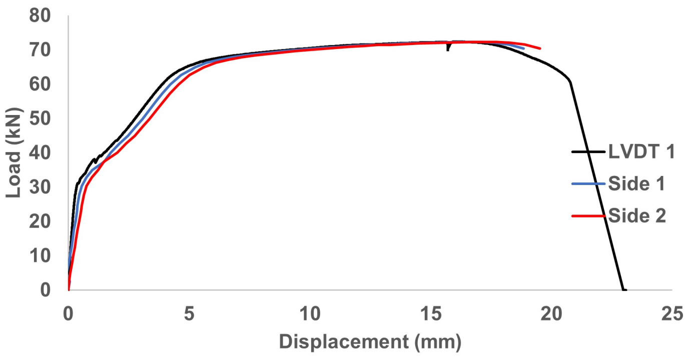

(a)

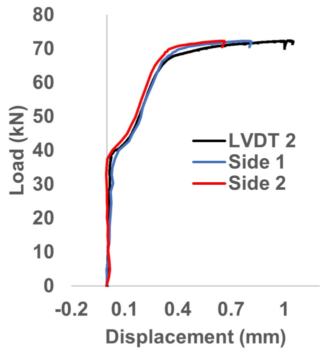

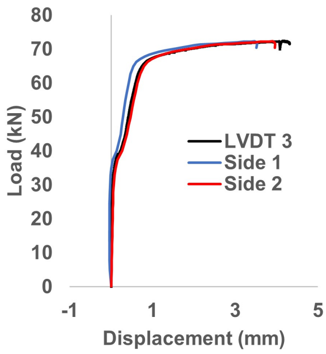

(b) (c)

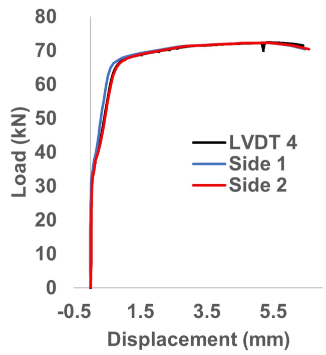

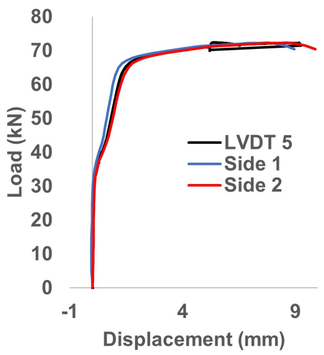

(d) (e)

Figure 5.31: Verification of DIC measurements with LVDT data for (a) LVDT 1, (b) LVDT 2, (c) LVDT 3, (d) LVDT4 and (e) LVDT 5. Where Side 1 refers to DIC measurements on side 1 and side 2 refers to DIC measurements on side 2.

From comparison of the LVDT data with the DIC data of the RC400 beam, similar differences are found, as were found for the H300 and H300s beam. The differences appear for all the LVDTs, but are significantly smaller compared to the differences observed for the previous beams. Nevertheless, negative displacements are found for DIC data of side 1. This becomes most clear from LVDT 3 and 5. Therefore, further investigation is performed.

Hybrid R/SHCC beam of 400 mm height
The DIC data is compared with the LVDT data, for the H400 beam (Figure 5.32)

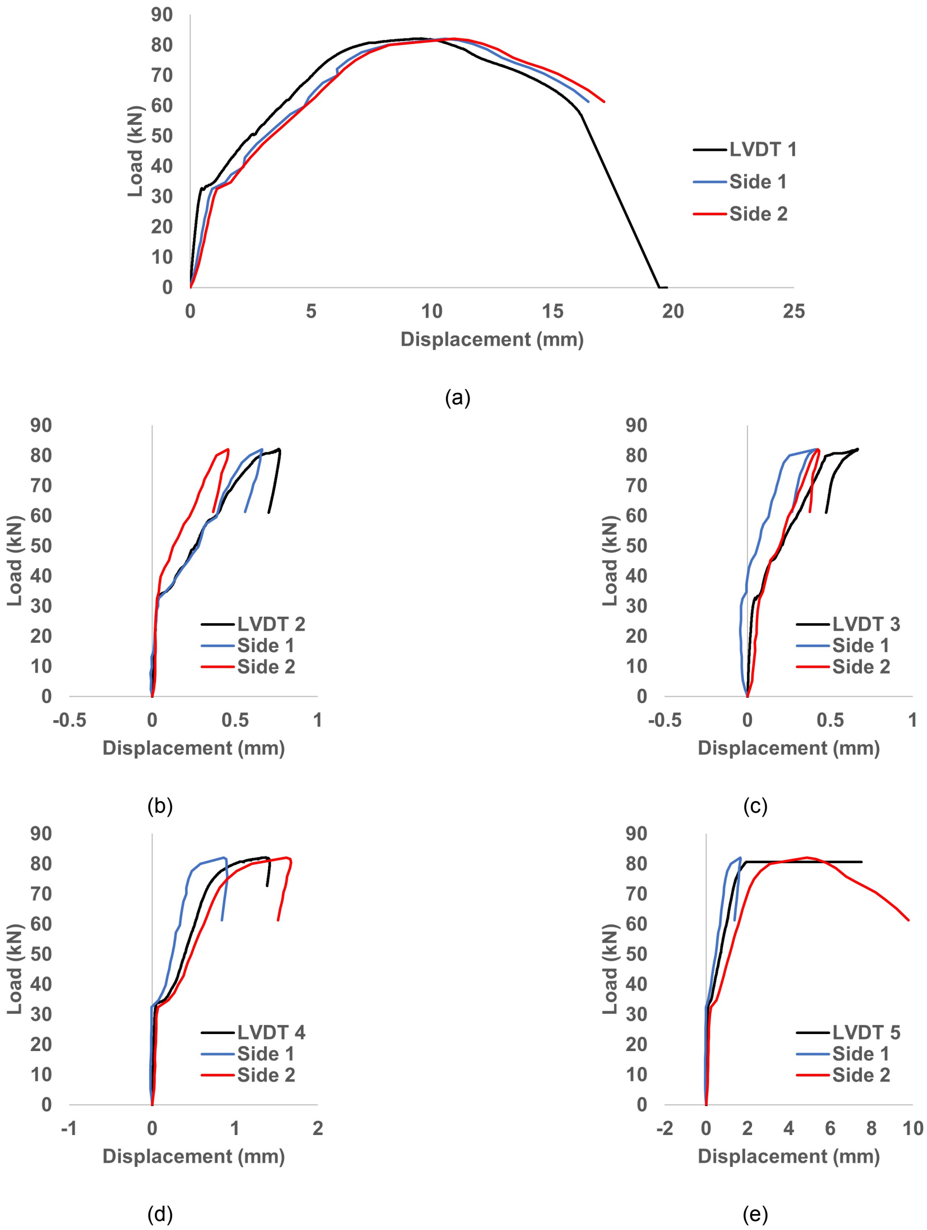

Figure 5.32: Verification of DIC measurements with LVDT data for (a) LVDT 1, (b) LVDT 2, (c) LVDT 3, (d) LVDT4 and (e) LVDT 5. Where Side 1 refers to DIC measurements on side 1 and side 2 refers to DIC measurements on side 2.

Upon comparison of the LVDT data with the DIC data it is found that, similar differences are found as found for the H300, H300s and RC400 beams. The differences are found for all the LVDTs. THe differences found in the data of the H400 beam and are significantly larger, compared to the differences found for the RC400 beam.

5.3.3. Material Tests

Material tests are performed, to investigate the material properties the beams. With differences found between the LVDT data and DIC data, these material tests become of big importance. The material samples for these tests are made from the same batch as the beams.

Testing

Compression strength is tested for both concrete and SHCC. The compression tests are performed on 100 mm x 100 mm x 100 mm cubes with a loading rate of 6 kN/s. The cubes are compressed at the top and bottom surface, whereas all the side faces are free. The compression test is performed by an automatic compression machine with a capacity of 5000 kN (Figure 5.33). The samples are compressed up to failure and the maximum load generated by the jack is recorded. Additionally, the Young's modulus is tested for both concrete and SHCC, with 100 mm x 100 mm x 400 mm prisms. The prisms are loaded in compression up to 30% of their compressive capacity with a loading rate of 1 kN/s. Each prism is loaded three times. Measurements are performed on all four sides by vertical LVDTs with a measuring range of 135 mm (Figure 5.33). Lastly, SHCC dogbones are tested for tensile strength and ductility. The dogbones have a gauge of 80 mm x 30 mm x 13 mm. On the dogbones vertical LVDT measurements are performed over an 80 mm range. In addition, 2D DIC measurements are performed on one side of the dogbone. Steel angles are glued on the ends of the dogbones, to increase the contact area with the setup. In addition, the dogbones are glued in the setup (Figure 5.33). Once the glue is hardenend, the dogbones are axially pulled with a displacement rate of 0.005 mm/s. DIC images are taken every 5 seconds. The dogbones are pulled up to failure.

(a) (b) (c) (d)

Figure 5.33: Testing of material samples for (a) compression, (b) Young's modulus, (c) tensile strength on dogbone with DIC and (d) tensile strength on dogbone with LVDTs.

Results

The material properties of SHCC are tested on 14 days, 28 days and 46 days of age. At 46 days of age, the beams were tested. After 14 days, the SHCC has a compressive strength of 51.45 MPa. Upon ageing of the SHCC, the strength increases to 59.40 MPa on 28 days and 60.21 MPa on 46 days (Table 5.6). The coefficient of variation is found to be below 10% at all the tested ages. This variation in material properties is accepted.

.

Table 5.6: Result of compression test on SHCC at an age of (a) 14 days, (b) 28 days and (c) 46 days.

Sample	Age (days)	Strength (MPa)	Average (MPa)	Std (MPa)	Coeff. of var. (%)
1	14	49.98	51.45	4.55	8.85
2	14	56.55			
3	14	47.81			

(a)

Sample	Age (days)	Strength (MPa)	Average (MPa)	Std (MPa)	Coeff. of var. (%)
1	28	55.53	59.4	5.47	9.21
2	28	63.27			

(b)

Sample	Age (days)	Strength (MPa)	Average (MPa)	Std (MPa)	Coeff. of var. (%)
1	46	62.1	60.21	2.16	3.59
2	46	57.85			
3	46	60.67			

(c)

The Young's modulus is determined by dividing the measured force over the cross sectional area of the prism. In addition, the found LVDT displacements are divided over the measuring range of 135 mm, in order to obtain strains. The strains from the four sides are averaged and the Young's modulus (E) for each loading cycle can be determined by:

$$E = \frac{\sigma_{c30\%} - \sigma_{c10\%}}{\epsilon_{c30\%} - \epsilon_{c10\%}} \tag{5.11}$$

In this formula, (ϵ) is the strain and (σ) is the stress. Stress and strain values of 10% and 30% of ultimate capacity are used. Only the second and third loading cycle are used, as the first loading cycle is used for settling of the specimen in the setup. From the 14 days test, a Young's modulus of 21377 MPa is obtained. Upon ageing, the Young's modulus becomes 21584 MPa at 28 days and 21552 MPa at 46 days of age (Table 5.7).

Table 5.7: Young's modulus of SHCC at an age of (a) 14 days, (b) 28 days and (c) 46 days.

Cycle	Age (days)	E (MPa)	$E_{cm,2,3}$ (MPa)
1	14	21252	21377
2	14	21381	
3	14	21373	

(a)

Cycle	Age (days)	E (MPa)	$E_{cm,2,3}$ (MPa)
1	28	21780	21853
2	28	21863	
3	28	21884	

(b)

Cycle	Age (days)	E (MPa)	$E_{cm,2,3}$ (MPa)
1	46	21572	21552
2	46	21576	
3	46	21527	

(c)

Dogbones are tested at 14 days and 46 days of age (Figure 5.34). At an age of 14 days, an average tensile strength of 4.63 MPa is obtained with an average ductility of 1.86%. At 46 days the strength increases to 5.30 MPa, but the ductility decreases to 1.23% (Table 5.8).

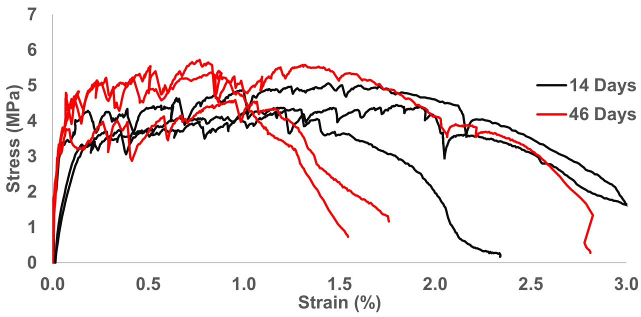

Figure 5.34: Stress-strain curve of tensile tests of SHCC dogbones at 14 days and 46 days of age.

Table 5.8: Overview of results of tensile tests of SHCC dogbones at an age of (a) 14 days and (b) 46 days.

Sample	Age (days)	Strength (MPa)	Ductility (%)
1	14	4.45	2.03
2	14	4.37	1.40
3	14	5.06	2.14
Average		**5.30**	**1.23**
Std (MPa)		0.38	0.40
coeff. of var. (%)		7.12	32.46

(a)

Sample	Age (days)	Strength (MPa)	Ductility (%)
1	46	5.57	1.61
2	46	5.73	1.00
3	46	4.59	1.09
Average		**5.30**	**1.23**
Std (MPa)		0.62	0.33
coeff. of var. (%)		11.65	26.77

(b)

The standard deviation and coefficient of variation are large for the strength and ductility of the dogbones. This is found for all the tested ages. These deviations can partly be explained by imperfections of the samples, which were found to be quite large due to the use of a flexible mold. In addition, the placement of the samples in the setup with glue allow for misalignment. Other influencing factors might be present as well, such as a heterogeneous fiber distribution. This is not investigated.

Concrete is tested for compressive strength at 31 days of age. The beams were tested at the same day. The concrete is found to have a compressive strength of 49.11 MPa, 51.47 MPa and 52.36 MPa for respectively batch 1, batch 2 and batch 3 (Table 5.9). The largest coefficient of variation is 5.01%. This is smaller than the largest coefficient of variation found for the SHCC cubes, which was 9.21%. This is interesting as the SHCC is made with fine particles only, whereas the concrete is made with sand and gravel. Therefore, one would expect to find a larger material spread in the concrete. A possible explanation for the higher coefficient of variation for SHCC could be a heterogeneous fiber distribution. However, this cannot be concluded as the fiber distribution is not measured.

In order to find the characteristic strength of the concrete batches, a correction has to be made for the 100 mm cube size, as the standard is 150 mm cube size. Smaller cubes are generally stronger, compared to larger cubes. Therefore, the characteristic strength of the batches is found by (*Eurocode 2: Design of concrete structures*, 2004):

$$f_{cm,150cube} = 0.91 f_{cm,100cube} \tag{5.12}$$

$$f_{ck} = f_{cm,150cube}(t) - 8 \tag{5.13}$$

This leads to a characteristic strength for batch 1 till 3 of respectively: 36.69 MPa, 38.84 MPa and 39.65 MPa. The mix design was made for C30/37, which has a characteristic compressive cube strength of 37 MPa. This strength is obtained with the concrete batches.

Table 5.9: Concrete compressive strength at 31 days of age for (a) batch 1, (b) batch 2 and (c) batch 3.

Sample	Age (days)	Strength (MPa)	Average (MPa)	Std (MPa)	Coeff. of var. (%)
1	31	50.72	49.11	1.43	2.91
2	31	48.59			
3	31	48.01			

(a)

Sample	Age (days)	Strength (MPa)	Average (MPa)	Std (MPa)	Coeff. of var. (%)
1	31	54.38	51.47	2.58	5.01
2	31	50.58			
3	31	49.46			

(b)

Sample	Age (days)	Strength (MPa)	Average (MPa)	Std (MPa)	Coeff. of var. (%)
1	31	52.73	52.36	2.11	4.04
2	31	50.09			
3	31	54.27			

(c)

The Young's modulus of concrete is tested on 31 days of age for all three batches (Table 5.10). The average Young's modulus is found to be 34546 MPa (Batch 1), 33645 MPa (Batch 2) and 34889 MPa (Batch 3). Concrete clas C30/37 should have an average Young's modulus of 32837 MPa. This is obtained for all the three concrete batches.

Table 5.10: Young's modulus of concrete at 31 days of age for (a) batch 1, (b) batch 2 and (c) batch 3.

Cycle	Age (days)	E (MPa)	$E_{cm,2,3}$ (MPa)
1	31	31934	34546
2	31	34508	
3	31	34584	

(a)

Cycle	Age (days)	E (MPa)	$E_{cm,2,3}$ (MPa)
1	31	30696	33645
2	31	33618	
3	31	33672	

(b)

Cycle	Age (days)	E (MPa)	$E_{cm,2,3}$ (MPa)
1	31	33762	34889
2	31	34831	
3	31	34947	

(c)

5.4. Analysis of Test setup

The material tests showed the desired material properties. Therefore, the differences in the comparisons of LVDT data and DIC data, as found for the tested beams, cannot be explained by the material properties. The high coefficient of variation for SHCC in compression is within the 10% limit. The tensile tests of SHCC dogbones have too many influencing factors, to be able to attribute the large spread in material properties to the fiber dispersion. Even more, the fiber dispersion is not measured. In addition, the RC400 beam showed the same type of differences in the comparison of LVDT data and DIC data. Therefore, the explanation for these differences are not found in material properties. The DIC data is analysed in more detail. A systematic approach is used for this. First, observations from the DIC data are collected. After which, hypotheses are generated of what might have happened during the tests. Next, the hypotheses are tested. Lastly, the findings are reported.

5.4.1. Observations

The DIC data directly retrieved from GOM correlate for the 400 mm high hybrid beam is shown at a load of 18.02 kN (Figure 5.35). Contour plots and cross-sectional graphs of x-displacements are shown for side 1 and side 2 of the beam. In the contour plot of side 1 a histogram is presented, which shows the extent of x-displacement of the image. The origin of the coordinate axis is in the center of the image.

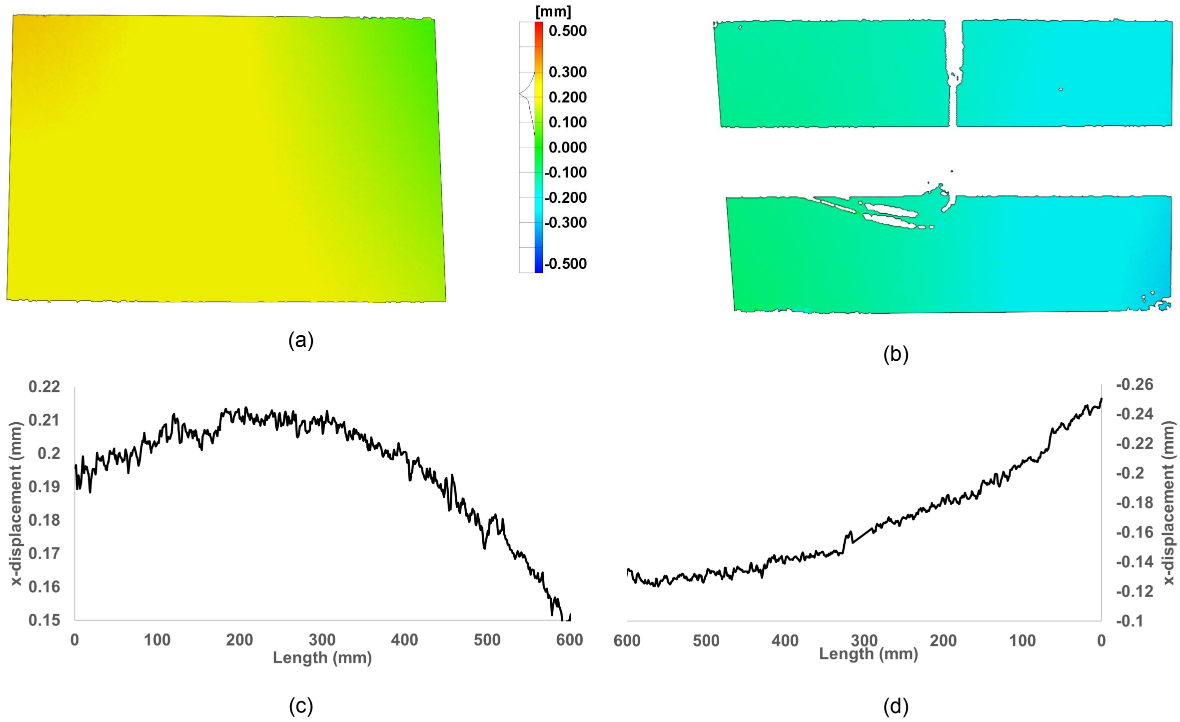

Figure 5.35: DIC data from H400 beam at a load of 18.02 kN with (a) side 1 contour plot of x-displacement, (b) side 2 contour plot of x-displacement, (c) side 1 cross-sectional graph of x-displacement made 2 mm from bottom of the beam and (d) side 2 cross-sectional graph of x-displacement 2 mm from bottom of the beam.

From the DIC data it is found that, side 1 is showing solely positive x-displacements, whereas side 2 is showing solely negative x-displacements. From the histogram it is found that, a uniform x-displacement is present in the image. Lastly, the sectional graphs are parabolic. Similar results are found for the 400 mm high concrete reinforced beam (Appendix B).

The DIC data, directly retrieved from GOM correlate for the 300 mm high hybrid beam with smooth and Vaseline treated reinforcement bars, is shown at a load of 15.47 kN (Figure 5.36). Both contour plots and cross-sectional graphs of x-displacements are shown. The origin of the axis is in the center of the image.

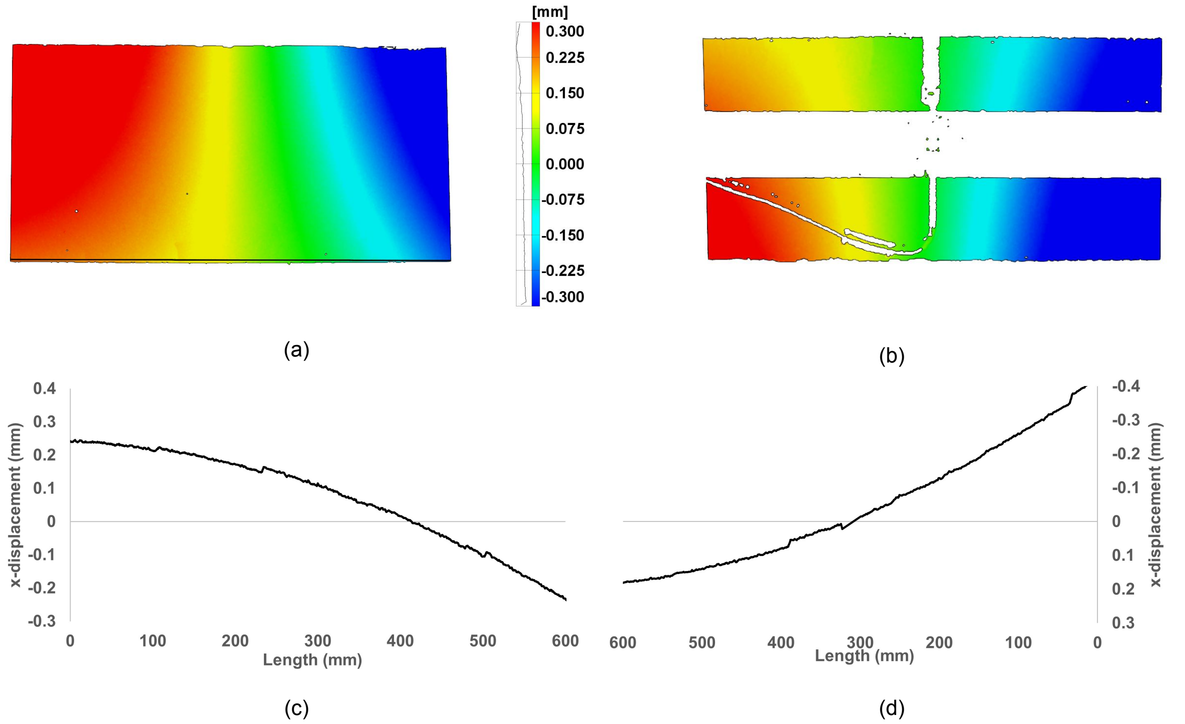

Figure 5.36: DIC data from H300s beam at a load of 15.47 kN with (a) side 1 contour plot of x-displacement, (b) side 2 contour plot of x-displacement, (c) side 1 cross-sectional graph of x-displacement made 2 mm from bottom of the beam and (d) side 2 cross-sectional graph of x-displacement 2 mm from bottom of the beam.

From the DIC data it is found that, side 1 is showing positive x-displacements on the left side of the contour plot and negative x-displacements on the right side of the contour plot. Side 2 is showing the opposite. In addition, the left of the beam is moving in positive x-direction, whereas the right part is moving in the opposite direction. The x-displacements found show little variation over the height of the contour plots. Lastly, the sectional graphs show that the x-displacement at the bottom of the beam changes parabolic over the length of the beam. Similar results are found for the H300 beam (Appendix B).

In addition to the observations made in the DIC data, the used setup is observed. From observations of the setup the following is found:

- The support conditions of the beam allow for both supports to roll. Therefore, horizontal translation of the beam in plane is possible.
- The support boxes are placed directly on the floor, without any connection to the floor. During the placement of the specimens the boxes were pushed in place by hand.
- The support boxes allow for a direct force transfer from the beam to the floor.
- The connection between the load-spreader and the beam does not allow for horizontal translation relative to the beam, as one end of the load-spreader is connected with a fixed hinge and the other end with a sliding hinge.
- The cylinder, which carries the loading cell, has a visual horizontal out of plane alignment directed towards side 2.
- Gluing of the support plates for both the 300 mm high beams was needed, to make the beams fit the setup, without wobbling.
- The 400 mm high beams are tested a day after the 300 mm high beams are tested, which means that the camera setup is changed and the support boxes are moved outwards.

5.4.2. Hypotheses
From the made observations, hypotheses are generated. The list of hypotheses is not exhaustive. The most presumable hypothesis are:

1. The beams moved horizontally in plane, due to both supports having a sliding hinge.
2. The beams moved horizontally out of plane, due to sliding of the support boxes over the floor.
3. The beams moved out of plane, due to misaligned support boxes. This introduces an out of plane component when the beams roll over the rollers.
4. The beams tilt, due to misalignment of the load-spreader.
5. The beams were warped, due to lack of stiffness in the mould.
6. The camera setup is bad, leading to large noises.
7. The beams are bend out of plane, due to the presence of the out of plane alignment of the cylinder.

5.4.3. Hypotheses testing
The most presumable hypotheses are tested by describing what the effect would be if the hypothesis is true, followed by the evaluation of what is observed. In order to test the hypothesis, a better understanding of the effect of out of plane displacements on the 2D DIC data is needed. Out of plane displacements affect the found displacements in the DIC data. If the object moves away from the camera, the real displacement is overestimated. If the object moves towards the camera, the real displacement is underestimated. This effect of out of plane displacement on the DIC data is a result of the scaling of the image (Sutton et al., 2008). The scaling of an image is set with the first image. Therefore, a pixel of an image represents a real dimension. By moving the object away from the camera less pixels in the image capture the object. Therefore, the object appears smaller in the image. As the scaling of the first image is used in all the successively taken images, the smaller appearance of the object results in an increase in the displacement measured (Figure 5.37). The in plane displacement is overestimated.

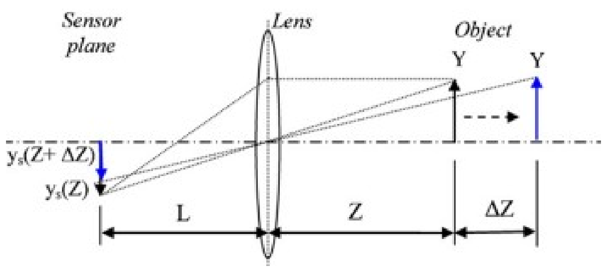

Figure 5.37: Effect of out of plane displacement for an object moving away from the camera (Sutton et al., 2008).

1. The beams moved horizontally in plane, due to both supports having a sliding hinge
If the beams moved horizontally in plane, with the origin of the axis in the center of the beam, the x-displacement contour plot should show a uniform displacement over the length and height of the contour plot. The other side should show the same uniform displacement, however of opposite sign as the movement of the beam appears opposite. This would however not result in differences in the LVDT comparison of the DIC data from the two sides, as the in plane displacements do not change the relative horizontal displacement. Additionally, the cross-sectional graphs should not appear to be parabolic, but should only have a shift in absolute values. From the histogram and x-displacement contour plots, the uniform horizontal displacement is found for the 400 mm high beams. The supporting conditions of the beam allow for this movement. Therefore, this hypothesis is tested to be true for the 400 mm high beams, but it is not likely that this caused the found deviations in LVDT and DIC data.

2. The beams moved horizontally out of plane, due to sliding of the supports boxes over the floor
If the beams moved out of plane with a pure translation, this should lead to overestimation of the real behavior on one side and to underestimation the real behavior on the other side. The cross-sectional graphs should show a linear trend, as a pure translation out of plane moves all parts of the beam equally, resulting in a shift in the found x-displacements in the DIC data. Sliding of the support boxes is a sudden movement at a distinct load step, as sliding occurs under a horizontal force when the sliding resistance is overcome. Therefore, abrupt changes in the DIC data should be observed. As no abrupt changes in the DIC data are observed, this hypothesis is tested to be not true.

3. The beams moved out of plane, due to misaligned support boxes. This introduces an out of plane component when the beams roll over the rollers
If the beams rotated over the z-axis, this should result in differences in out of plane displacement over the length of the beam. As one end of the image would be moving more towards (or away) of the camera compared to the other side of the image. In the cross sectional graph, linear behavior should still be found, as the out of plane displacement (w_{OOP}) is a linear function of:

$$w_{OOP} = l(x)sin(\alpha) \tag{5.14}$$

In this formula, $l(x)$ is the distance from the rotation point to the location in the image and α is the angle, over which the beam rotated. The displacement of the beam over the rollers should be dependent on the elongation and settling of the beam. As no difference in x-displacement within an image is found for the 400 mm high beams, this hypothesis is tested to be not true. For the 300 mm high beams this hypothesis is tested to be true.

4. The beams tilt, due to misalignment of the load-spreader
Tilting of the beams would mean that the top part of the beam is moving closer to one of the cameras, compared to the bottom side of the beam. The opposite happens to the other side of the beam. In the contour plot this should be visible by differences in x-displacements over the height of the beam. The opposite should be observed on the other side of the beam. The cross sectional graphs should be similar to the uniform horizontally out of plane movement, except for the abrupt movement, as tilting can be a slow process. As for none of the tested beams a significant difference is observed in x-displacements over the height of the beam, this hypothesis is tested to be not true.

5. The beams were warped, due to lack of stiffness in the mould
Warping of the beam could occur if the mold of the beam is not stiff enough. Upon loading of the sample, the beam would settle. Therefore, warping should be only present during the start of the test. Warping can be explained as a special type of tilting, where within an image one half of the image width is tilting one way and the other half is tiling in the opposite direction. This would lead to overestimation of the real behavior in one half of the image and underestimation of the real behavior in the other half of the image. In LVDT data this would mean that, the central LVDTs would match the DIC data, whereas LVDT 2 and 3, which were placed left and right of the center, would not match. For the 400 mm high beams, this hypothesis is tested to be not true, as the DIC data did not perform better for LVDT 4 and 5 compared to LVDT 2 and 3. On top of that, insignificant differences in x-displacement over the height of the contour plot are found. For the 300 mm high beams, gluing of the support plates was needed to make the beams stable in the frame. Therefore, the 300 mm high beams were warped. However, as the DIC data does not show a significant difference in x-displacement over the height of the contour plots, the effect of warping on the DIC data is expected to be limited.

6. The camera setup is bad leading to large noises
A bad setup of cameras could result in large noises. Noise in the DIC data could lead to a bad comparison with the LVDT data. For all the tests, side 2 required the camera to be removed in order to move the beams in and out of the setup. On side 1, the camera needed to be setup again, after the 400 mm beams were tested and the 300 mm beams were placed in the setup. Therefore, the tests have been performed with different camera setups. In addition, the noise of the cameras were checked before a test is started by the noise analysis (Subsection 5.3.1). The noise was never found to be larger than 0.015 mm in x-displacement. Therefore, this hypothesis is tested to be not true for all the beams.

7. The beams are bend out of plane, due to the presence of the out of plane alignment of the cylinder

Bending out of plane in 2D DIC data would lead to overestimation of the real behavior on one side of the beam and underestimation of the real behavior on the other side of the beam. On top of that, the real behavior of the beam is no longer a pure bending movement. In DIC data, bending out of plane can be recognised by the x-displacement cross sectional graph being parabolic. Dependent on the curvature of the beam, the out of plane movement can be observed as an out of plane displacement in the contour plots, especially when the load is still small. At higher loads, the contour plots are harder to use as cracks are disturbing the contour plots. The difference with an out of plane translation is the real behavior of double bending. Therefore, in case of double bending, the out of plane displacement increases in correlation with the vertical deflection of a four point bending test, as both are dependent on the force. In order to test if bending out of plane occurred, the out of plane displacement needs to be known. If no out of plane measurements are made during the tests, it is still possible to determine the out of plane displacement, based on the comparison of the LVDT and the DIC data. In order to determine the out of plane displacement, the distance from the camera lens to the object needs to be either known or estimated. This distance can be estimated with the use of the known camera lens angle and the width of the image. The width of the image and angle of view of the camera lens can be used as the full width of the image is recording the beam. This is an important condition to satisfy, to find a good estimate for the distance from the camera to the object. The width of the image is determined by scaling the image, for a known real distance, for example the 500 mm constant bending moment region. The horizontal viewing angle of the camera can be found by the lens specifications. For an EF 35 mm f/2 IS USM Canon camera lens, a horizontal angle of 63 degrees is found (Canon, 2022). The distance from camera to object (d_{object}) can be found by:

$$d_{object} = \frac{\text{Image width}}{2\tan(\frac{\text{horizontal angle}}{2})} \tag{5.15}$$

The distance from the camera to the object (d_{object}) and the deviation in the LVDT and the DIC data (DIC_{Data}) are used, to solve for the out of plane displacement ($d_{OOP,DIC}$):

$$LVDT - DIC_{correction}(d_{OOP,DIC}) = 0 \tag{5.16}$$

$$DIC_{correction}(d_{OOP,DIC}) = DIC_{Data} - LVDT_l(\frac{d_{object}}{d_{object} - d_{OOP,DIC}} - 1) \tag{5.17}$$

In this formula, $LVDT_l$ is the length over which the LVDT is measuring. In addition, this formuale can be used to correct the DIC data. Correction of DIC data for out of plane movement is only use-full, if the out of plane displacement is independent of the force. If the out of plane displacement is dependent on the force, the structural behavior of the beam is affected and the performed test is no longer a pure four point bending test. In order to verify if the occurred out of plane displacement is dependent on the force, the Pearson correlation coefficient is used, between the out of plane displacement and a constant fraction of the vertical displacement. The Pearson correlation (R) is determined with (Pearson, 1896):

$$R = \frac{\sum(x-\bar{x})(y-\bar{y})}{\sqrt{\sum(x-\bar{x})^2(y-\bar{y})^2}} \tag{5.18}$$

In this formula, $\bar{x}$ is the average of variable x and $\bar{y}$ is the average of variable y. If R is close to 1, a high positive correlation is found between variables x and y. If R is close to 0, low correlation is found between variables x and y. If R is close to -1, a high negative correlation between variables x and y is found(Pearson, 1896). Correlation is searched for between the out of plane displacement measured in the DIC data ($d_{OOP,DIC}$) and the theoretical out of plane displacement ($d_{OOP,LVDT}$). The theoretical out of plane displacement is determined as a fraction of the measured deflection with LVDT 1. A fraction of the measured deflection is used as, the in plane stiffness (I_1) differs from the out of plane stiffness (I_2) of the beam and the horizontal force component, causing out of plane bending, is a fraction of the vertical applied force. Therefore, the fraction (n) is determined by:

$$I_1 = \frac{1}{12}bh^3 \tag{5.19}$$

$$I_2 = \frac{1}{12} h b^3 \tag{5.20}$$

$$n = \frac{I_1}{I_2} \tag{5.21}$$

$$d_{OOP,LVDT} = n \sin(\alpha) LVDT_{vertical} \tag{5.22}$$

In these formulas, b is the width of the beam, h is the height of the beam, n is the ratio between the in plane and out of plane stiffness of the beam, α is the angle of the force and $LVDT_{vertical}$ is the deflection of the beam measured with a LVDT.

This method is applied on all the tested beams, including the hybrid S-PVA beam from (Singh, 2019). All theoretical out of plane displacements are determined with an out of plane angle of the force of 1.5 degrees. The out of plane displacements are presented in figure 5.38.

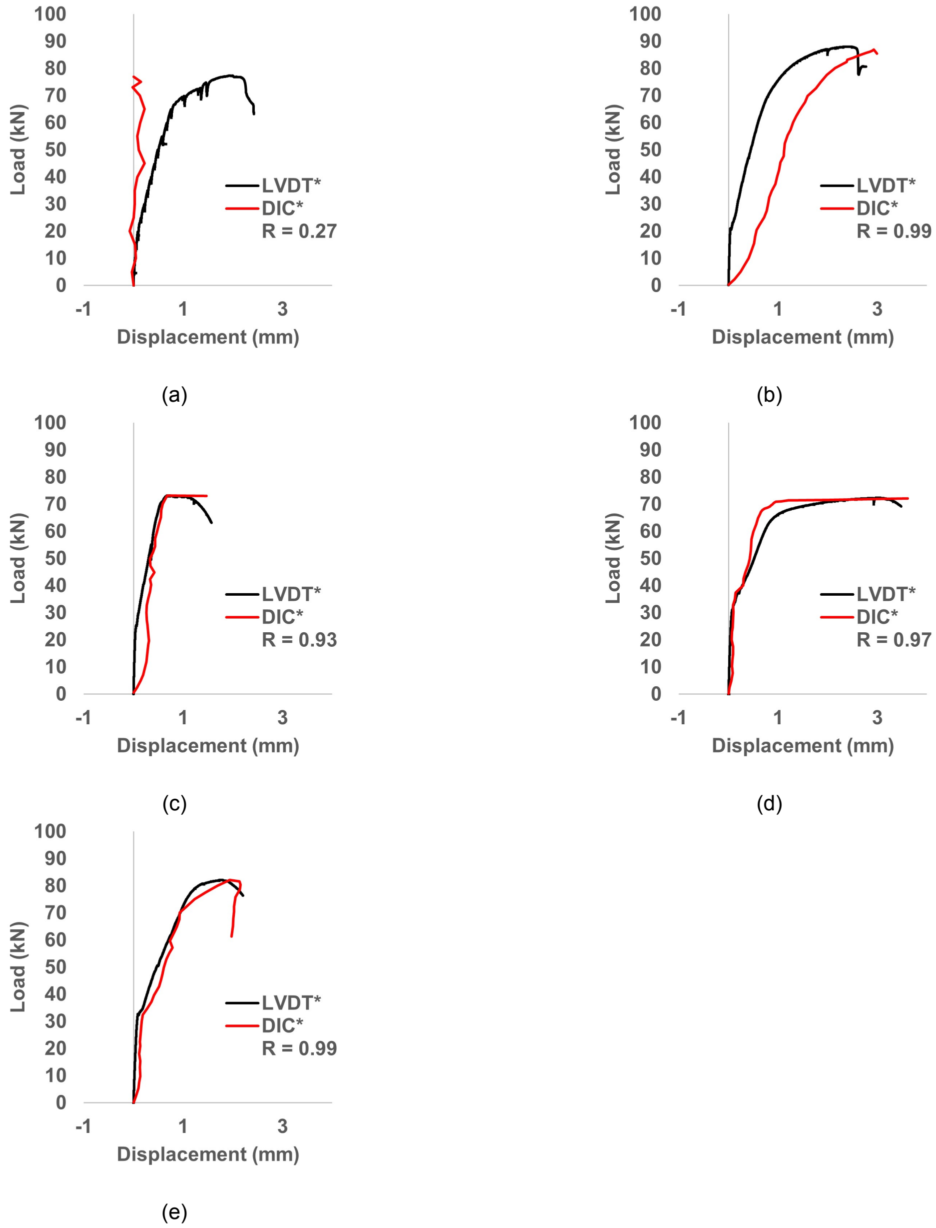

Figure 5.38: Load - Out of plane displacement graphs for theoretical out of plane displacement (LVDT*) and observed out of plane displacement from DIC data (DIC*) for (a) 200 mm high S-PVA beam from (Singh, 2019), (b) H300s, (c) H300, (d) RC400 and (e) H400.

From correlation of the theoretical out of plane displacement and the measured out of plane displacement with DIC is found that, out of plane bending occurred for the tested beams. The correlation is found to be weak for the 200 mm high beam. Therefore, no out of plane bending occurred in the 200 mm high beams. Based on the high correlation found for the beams from testing series 1, this hypothesis is tested true.

5.4.4. Findings

From testing of hypotheses the following is found:

- During the tests of the 400 mm high beams, the beams translated in plane, due to the supporting conditions. Both the supports are two sliding hinges. This in plane translation does affect the DIC data, but does not compromise the experimental results.
- Sliding of the support boxes is found to be unlikely
- Misalignment of support boxes for the 300 mm high beams is found. This does affect the DIC data, however it is not found to compromise the experimental results.
- Tilting of the 300 mm beams could not be excluded from hypothesis testing. The effect of tilting is however believed to be limited, and is not found to compromise the experimental results.
- The 300 mm beams were found to be wobbling in the setup. Therefore, the stiffness of the 300 mm mold is found to be insufficient.
- The used camera setups are found to have acceptable noises. Therefore, it is unlikely that the camera setup caused the observed differences in the DIC data and LVDT data.
- It is very likely that bending out of plane occurred for all the beams. This compromises the test results of series 1.

5.4.5. Adjustments

Based on the findings of the setup analysis, the test setup is improved (Figure 5.39). The following adjustments are made to the setup:

- Placement of bottom horizontal beams, in order to prevent direct force transfer from the supports to the floor.
- Re-alignment of the columns, top beams and bottom beams, in order to make the connections perpendicular.
- Re-alignment of the cylinder.
- Increasing the prestressing force for the column to floor connection
- Increasing the prestressing force for all the bolts in all the steel to steel connections.
- Stiffening the cylinder to top beam connection by placing steel angles.

With these adjustments made, the setup is tested with a steel RHS 100.100.10 (width x height x thickness) beam with a length of 1.4 meter and steel quality S275. During these tests, the out of plane deformation is measured with LVDTs (Figure 5.39).

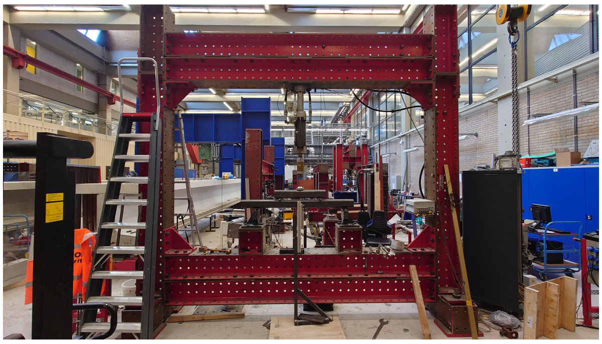

(a)

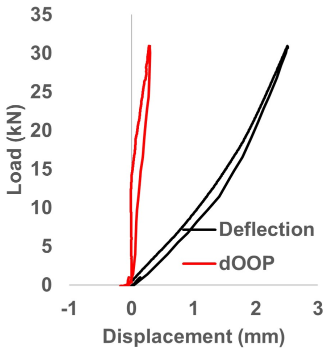

(b)

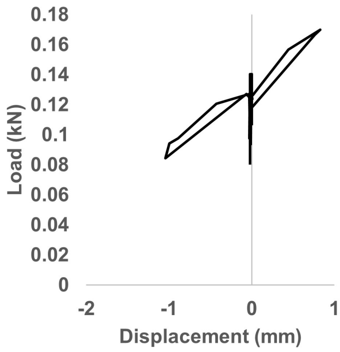

(c)

Figure 5.39: After adjustments with (a) the adjusted setup, (b) force-displacement graph of the steel beam tested for central deflection (deflection) and out of plane displacement of the center of the beam (dOOP) and (c) out of plane movement of the cylinder, due to pushing the cylinder out of plane by hand.

From these performed tests is found that, after the adjustments made 0.30 mm out of plane displacement is present in the center of the steel beam. This out of plane displacement increases with the load. The maximum deflection of the beam is 2.68 mm at a load of 30.78 kN. Thereby, the out of plane displacement remains relative to the vertical deflection large. In addition, the stiffness of the cylinder is checked by applying a horizontal load. The horizontal load is applied by hand. It is found that, the cylinder is able to move 1.04 mm under a small horizontal load. This movement is dependent on the stiffness of the cylinder and the connection of the cylinder to the top beam. As the stiffness of the cylinder is hard to improve in the current setup, the experimental study is continued with another testing setup (Figure 5.40).

Figure 5.40: New setup used for continuation of the experimental study.

5.5. Series 2

This new setup consists of both a stiffer frame and a stiffer cylinder. Therefore, it is expected to solve the out of plane displacement problem of the previous setup. The experimental study is continued with a second series of beams. The beams tested in these second series of experiments are presented in table 5.11.

Table 5.11: Beams tested in Series 2 of experimental study.

Label	Type	Height	Span	Longitudinal reinforcement
RC300	Reinforced concrete	300 mm	1825 mm	Ribbed
H300	Hybrid R/SHCC	300 mm	1825 mm	Ribbed
RC400	Reinforced concrete	400 mm	2325 mm	Ribbed
H400	Hybrid R/SHCC	400 mm	2325 mm	Ribbed

5.5.1. Testing

As soon as the new setup was ready for the tests, the beams are tested. Therefore, the conventional concrete reached an age of 41 days. The preparations for the second testing series are similar to the first testing series. Different from series 1, 6 LVDTs are placed as presented in Figure 5.41. The difference with series 1 is the placement of an additional LVDT (LVDT 6), which measures the horizontal out of plane displacement of a side face at center span of the beam.

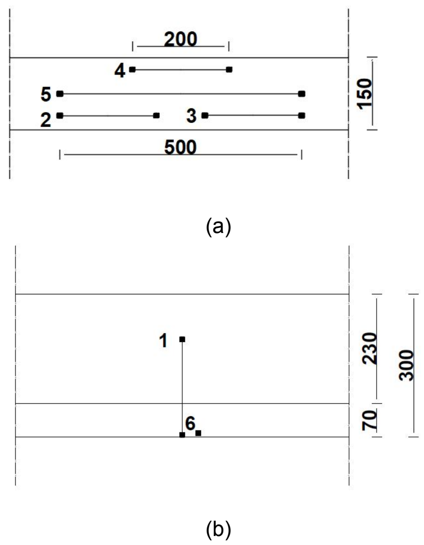

Figure 5.41: Position of LVDTs on bottom face (a) bottom face and (b) side face.

The LVDTs are calibrated and a maximum deviation of 0.021 mm is found. Similar to series 1, 2 sided 2D DIC is prepared for series 2. The performed noise analysis results in a maximum noise of 0.016 mm. The stiffer setup is used with a load cell of 400 kN (Figure 5.42). The supporting conditions of the beam samples are changed. One end of the beam is supported by a sliding hinge. The other end is supported by a fixed hinge. This prevents horizontal in plane movement of the beam. The second series of test are also performed in deformation control with a loading rate of 0.01 mm/s. Pictures are taken every 5 seconds.

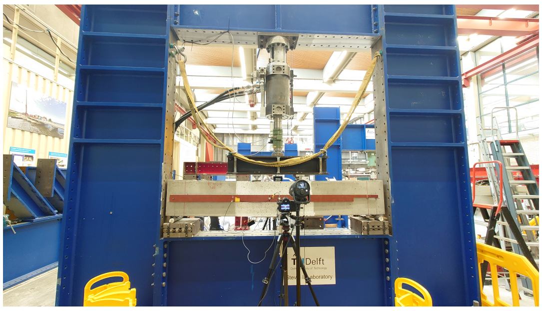

Figure 5.42: Testing of the series 2 beams.

5.5.2. Experimental results

During the experiments DIC data is collected from two side faces of the beam and LVDT data is collected from the bottom face of the beam (Figure 5.43). One side face has a wooden rod for vertical LVDT measurements. This is side is labelled as side 2. The other side is labelled as side 1.

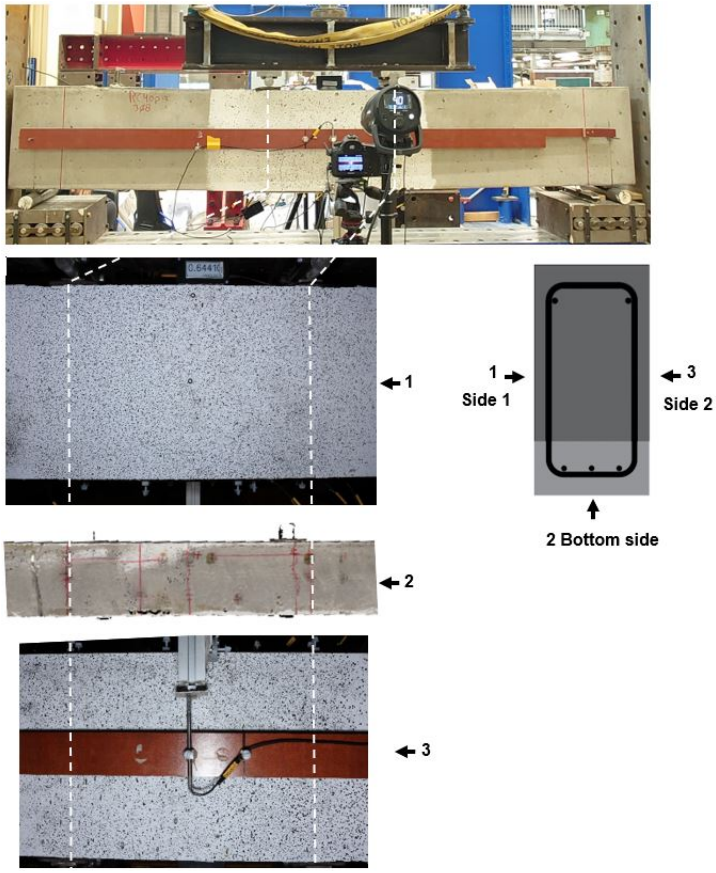

Figure 5.43: Overview of measurement setup with 1. Side 1 DIC, 2. Bottom side of beam with horizontal LVDT measurements and 3. Side 2 DIC with vertical LVDT measurement and out of plane LVDT measurement.

Reinforced concrete beam of 300 mm height

In figure 5.44 the load-displacement behavior of the RC300 beam is presented. In the same figure the maximum crack widths can be found. A summary of the key performance indicators are presented in table 5.12. The beam failed in the compression zone. Yielding of the reinforcement is reached at a load of 67.22 kN.

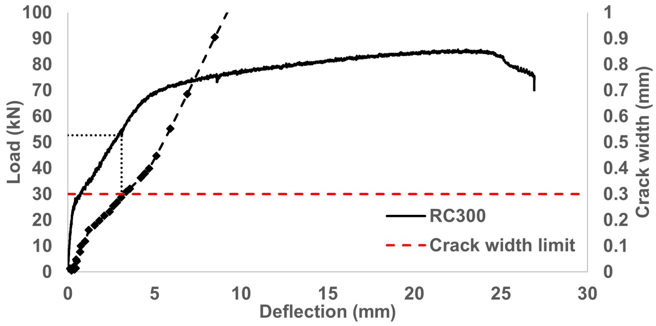

Figure 5.44: Load-deflection (solid) vs. maximum crack width-deflection (dashed) curve.

Table 5.12: Overview of results of experiment of RC300.

Key performance indicators	
Ultimate load	85.76 kN
Maximum deflection	26.93 mm
Number of cracks	7
Average crack spacing	71 mm
Load at 0.3 mm crack width	52.67 kN
0.3 mm load/yield load	78.35%

In order to show the crack development, contour plots of Von Mises strain are made. A green up to red zone indicates strain localization, and thus a crack. The top graphs belong to side 1, whereas the bottom graphs belong to side 2. The crack widths in concrete are reported inside the contour plots. On side 2, no DIC data is available at the center span, due to the vertical LVDT measurement. At this location, concrete cracks are determined over the full length of the region with the missing data. The first crack appears at a load of 18.28 kN (Figure 5.45). Upon increasing the load, more cracks are formed and existing cracks widen (Figure 5.45 to 5.52). Side 1 develops 7 cracks at the bottom, which coalescence into 4 cracks, propagating to the compression zone. Side 2 develops 6 cracks at the bottom, which coalescence into 4 propagated cracks. The crack widths are similar on both sides. The 0.3 mm crack width limit is reached simultaneously on both sides, at a load of 52.67 kN. The reported crack widths are in millimeters (mm).

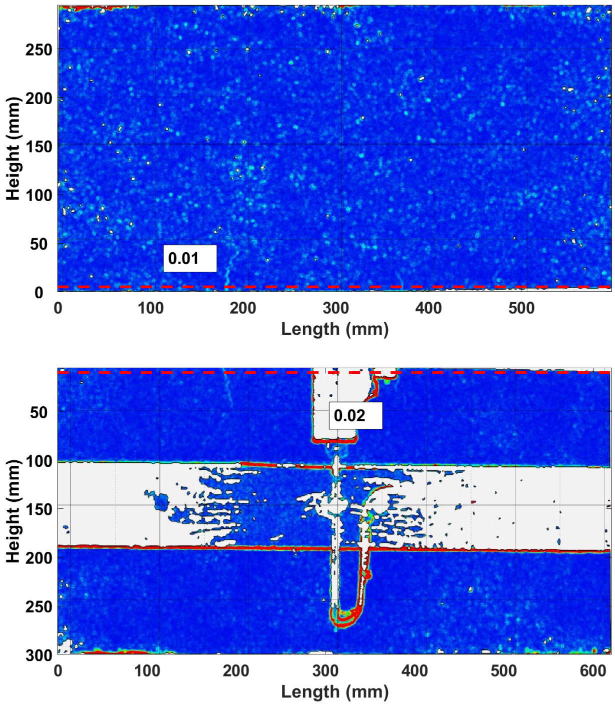

Figure 5.45: Crack widths from DIC data at a load of 18.28 kN.

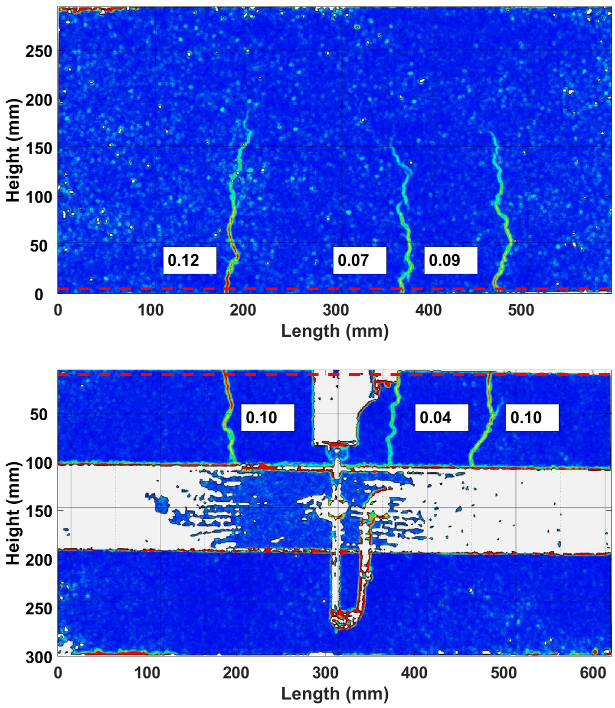

Figure 5.46: Crack widths from DIC data at a load of 29.70 kN.

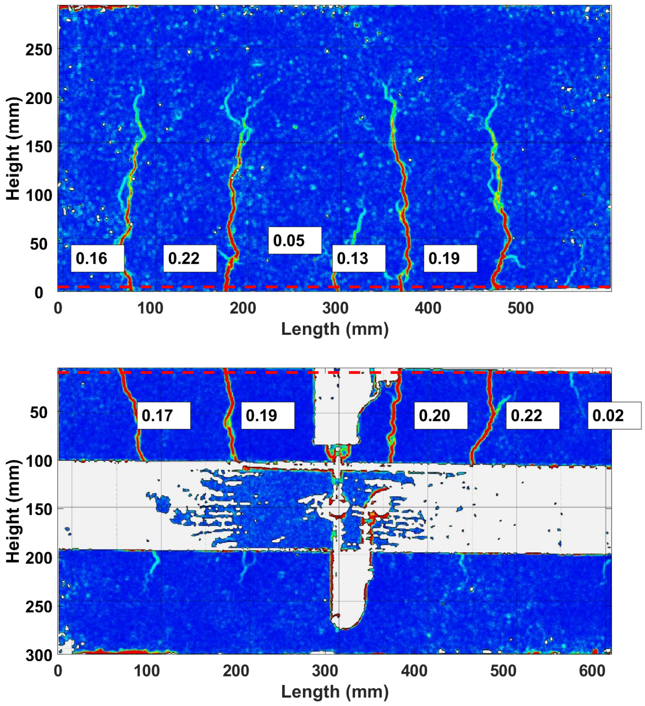

Figure 5.47: Crack widths from DIC data at a load of 40.26 kN.

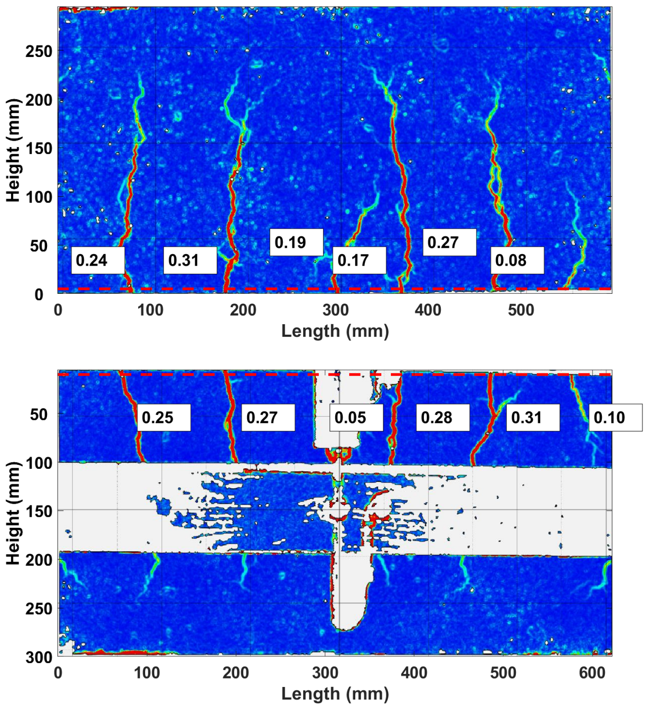

Figure 5.48: Crack widths from DIC data at a load of 52.67 kN.

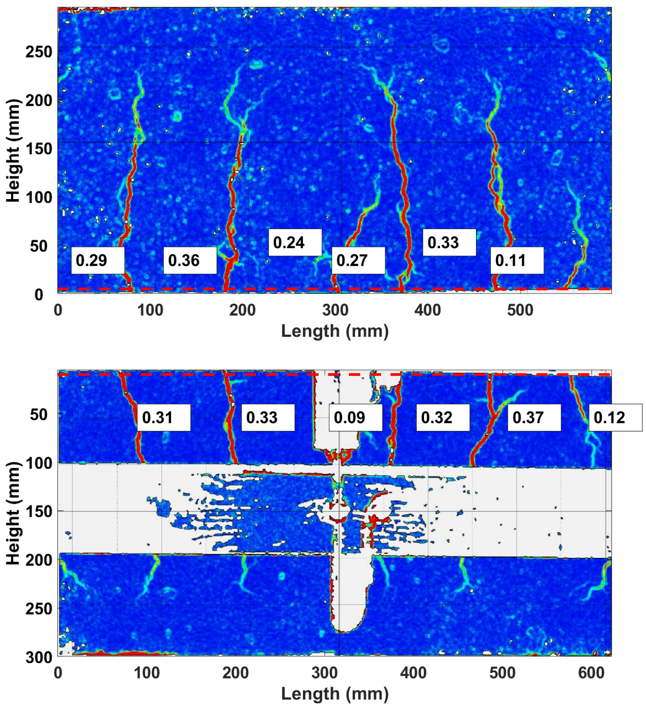

Figure 5.49: Crack widths from DIC data at a load of 61.31 kN.

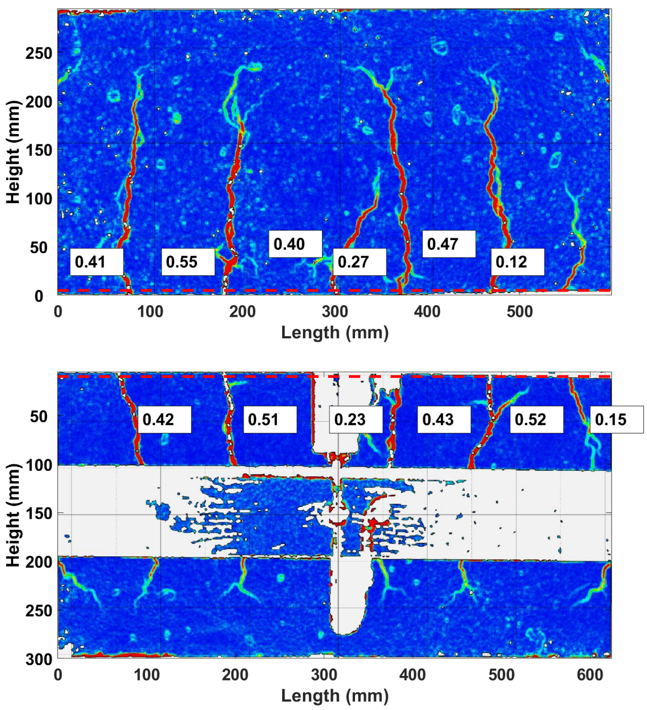

Figure 5.50: Crack widths from DIC data at a load of 70.22 kN.

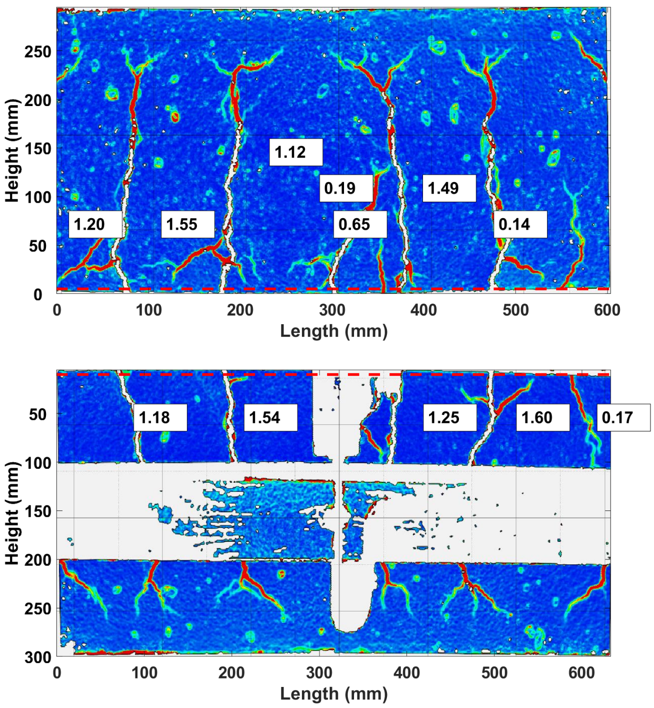

Figure 5.51: Crack widths from DIC data at a load of 80.39 kN.

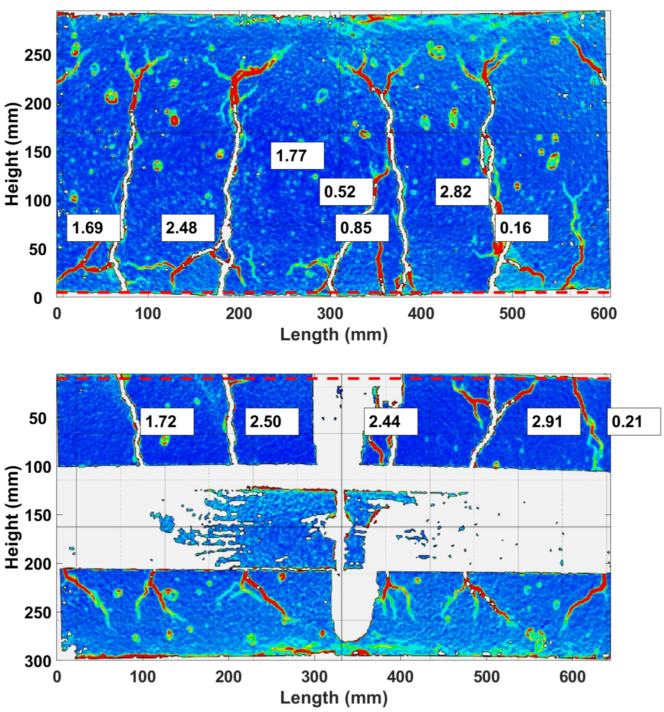

Figure 5.52: Crack widths from DIC data at a load of 85.76 kN.

For the crack width measurements DIC data is used. The DIC data is compared with LVDT data to verify the DIC data (Figure 5.53). Different from series 1, out of plane measurements are performed by LVDT 6. Therefore, direct data of the out of plane displacement is present to verify the extent of out of plane movement. In addition, the out of plane displacement is determined from DIC data, as described in section 5.4. The out of plane displacement measured with DIC data is compared with the LVDT data in Figure 5.53.

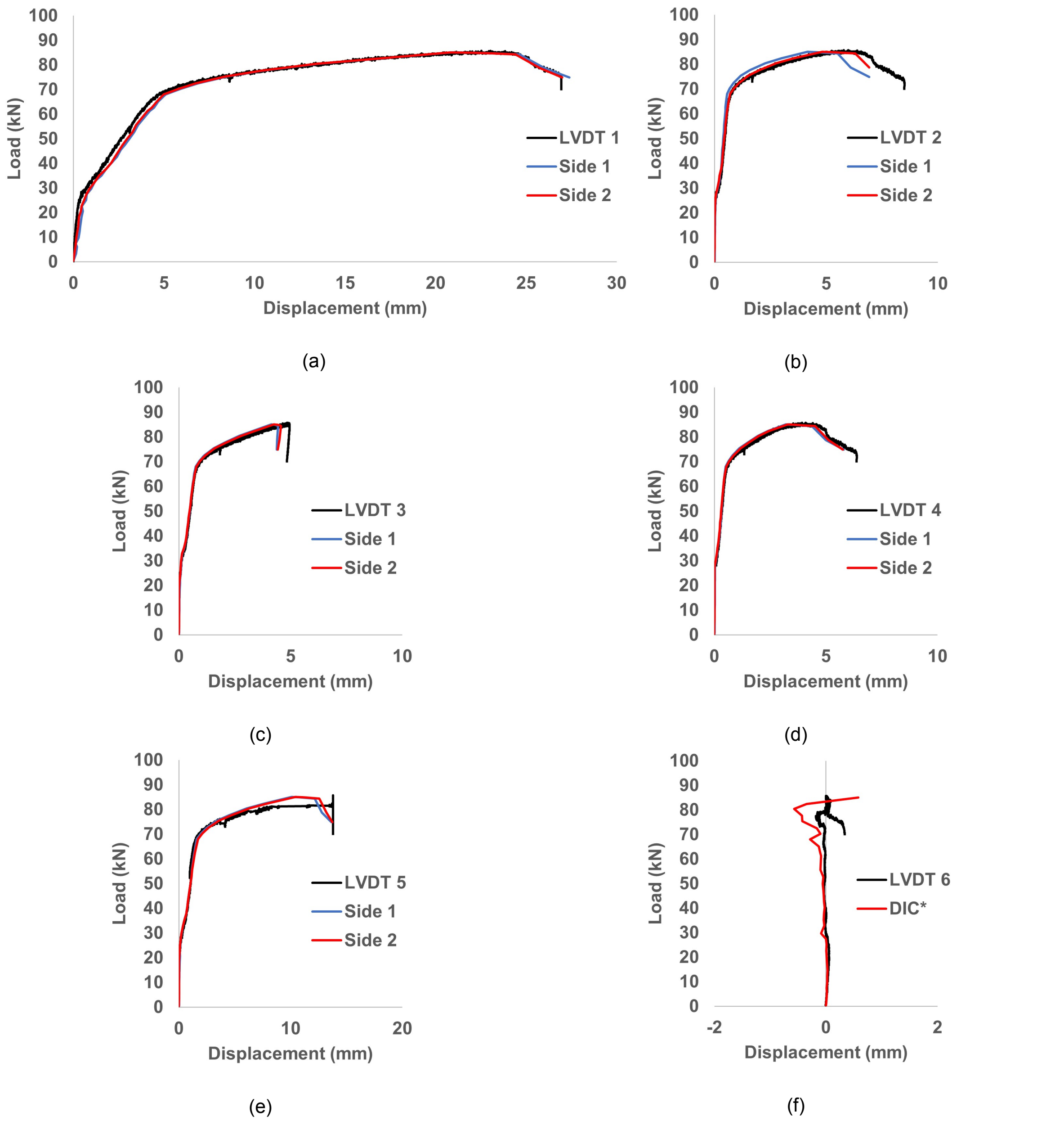

Figure 5.53: Comparison of the DIC data with the LVDT data for (a) LVDT 1, (b) LVDT 2, (c) LVDT 3, (d) LVDT4, (e) LVDT 5 and (f) out of plane displacement by LVDT measurement (LVDT 6) and DIC measurement (DIC*).

Upon comparison of the DIC data and the LVDT data, insignificantly small differences are found. The measured out of plane displacements are found to be very small. Therefore, the DIC data is accepted and the performed test can be considered a pure bending test. In addition, the out of plane displacements measured with the DIC data are similar to the measured out of plane displacement with the LVDT. Therefore, the developed tool to measure out of plane displacements from DIC data is verified.

Hybrid R/SHCC beam of 300 mm height

In figure 5.54 the load-displacement is presented. In the same figure the maximum crack widths in the SHCC layer are shown. A summary of the key performance indicators of the beam are presented in table 5.13. The beam failed by rupture of the reinforcement. Yielding of the reinforcement is reached at a load of 79.11 kN.

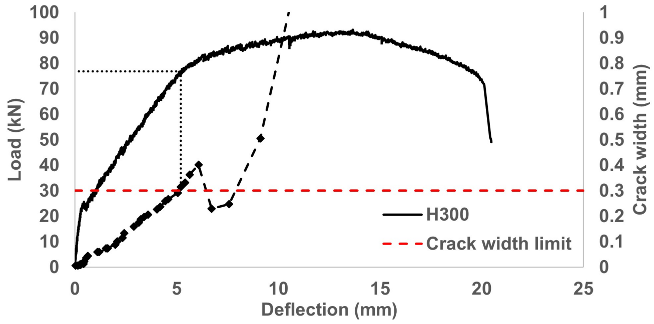

Figure 5.54: Load-deflection (solid) vs. maximum crack width-deflection (dashed) curve.

Table 5.13: Overview of results of experiment of H300.

Key performance indicators	
Ultimate load	93.25 kN
Maximum deflection	20.14 mm
Number of cracks	41
Average crack spacing	12.26 mm
Load at 0.3 mm crack width	76.89 kN
0.3 mm load/yield load	97.19%

The concrete to SHCC interface is profiled over the 500 mm constant bending moment region. Both the contour plot and the 3D scanned interface are presented in figure 5.55.

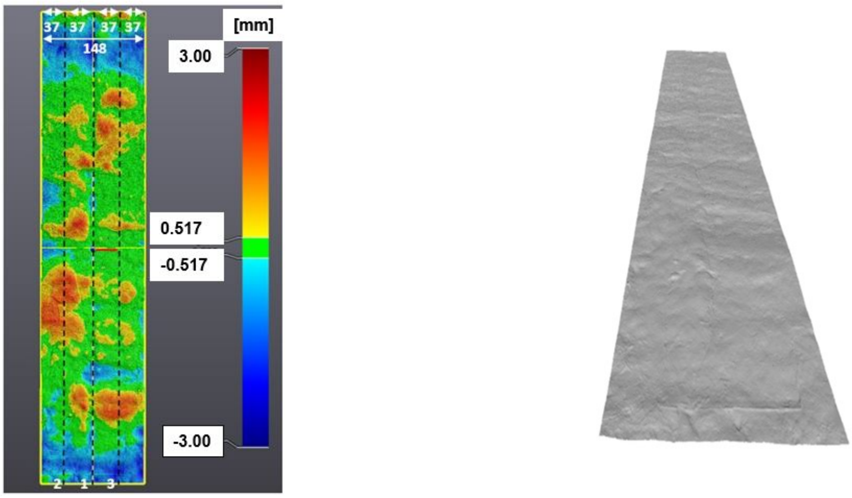

Figure 5.55: Interface profiling with (a) contour plot and (b) 3D scan.

From the scanned surface, three sections over the length of the interface are made to determine the roughness. The first section is made at the middle of the width of the interface. Section 2 and 3 are made at 37 mm respectively left and right of the middle line of the beam. From the sections made, profile graphs are made (Figure 5.56).

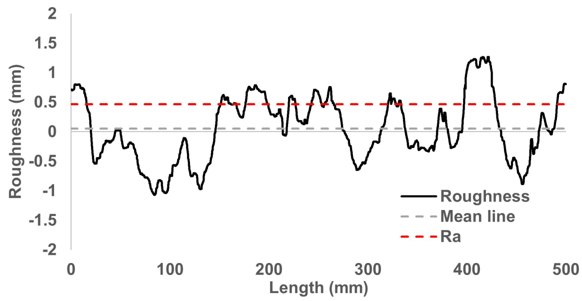

(a)

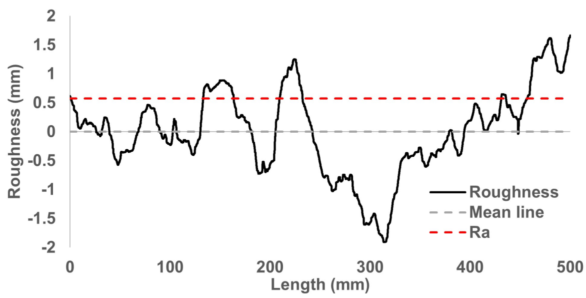

(b)

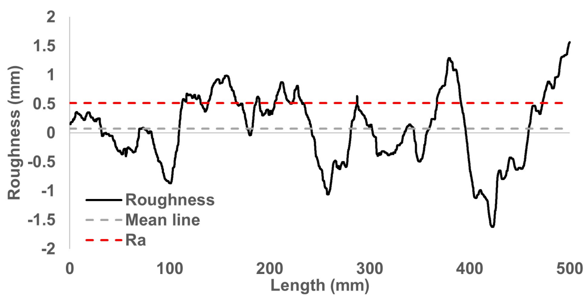

(c)

Figure 5.56: Interface profile graphs at (a) section 1, (b) section 2 and (c) section 3.

An average arithmetical surface roughness of 0.517 mm is found with a maximum peak value of 1.456 mm (Table 5.14). Therefore, the concrete-SHCC interface is considered smooth.

Table 5.14: Overview of results of interface profiling.

Section	1	2	3	Average
Ra (mm)	0.464	0.574	0.514	**0.517**
Rp (mm)	1.213	1.664	1.492	**1.456**
Rv (mm)	1.120	1.906	1.691	**1.572**
Rt (mm)	2.333	3.570	3.183	**3.029**

In order to show the crack development, contour plots of Von Mises strain are made. A green up to red zone indicates strain localization, and thus a crack. SHCC cracks are presented in point cloud graphs. The top graphs belong to side 1, whereas the bottom graphs belong to side 2. The crack widths in concrete are reported inside the contour plots. On side 2, no DIC data is available at the center span, due to the vertical LVDT measurement. SHCC cracks are unknown at this location, whereas concrete cracks are determined over the full length of the region with the missing data. The first crack appears at a load of 18.19 kN (Figure 5.57). Upon increasing the load, more cracks are formed and existing cracks widen (Figure 5.57 to 5.66). A uniform cracking pattern is found in the SHCC layer. The SHCC cracks coalescence into 4 propagating concrete cracks. This cracking pattern is similar for both sides of the beam. The largest crack in SHCC is found on side 1, at the center of the span (Figure 5.63). This is in the region of missing DIC data for side 2. At a load of 82.42 kN, the largest SHCC crack closes, due to opening of an adjacent crack (Figure 5.64). Upon increasing the load this adjacent crack coalescence into the largest crack, leading to a single localization in the final cracking pattern (Figure 5.66). Lastly, the SHCC cracks open up from the bottom of the beam towards the concrete-SHCC interface, but also from the concrete-SHCC face to the bottom of the beam. The reported crack widths are in millimeters (mm).

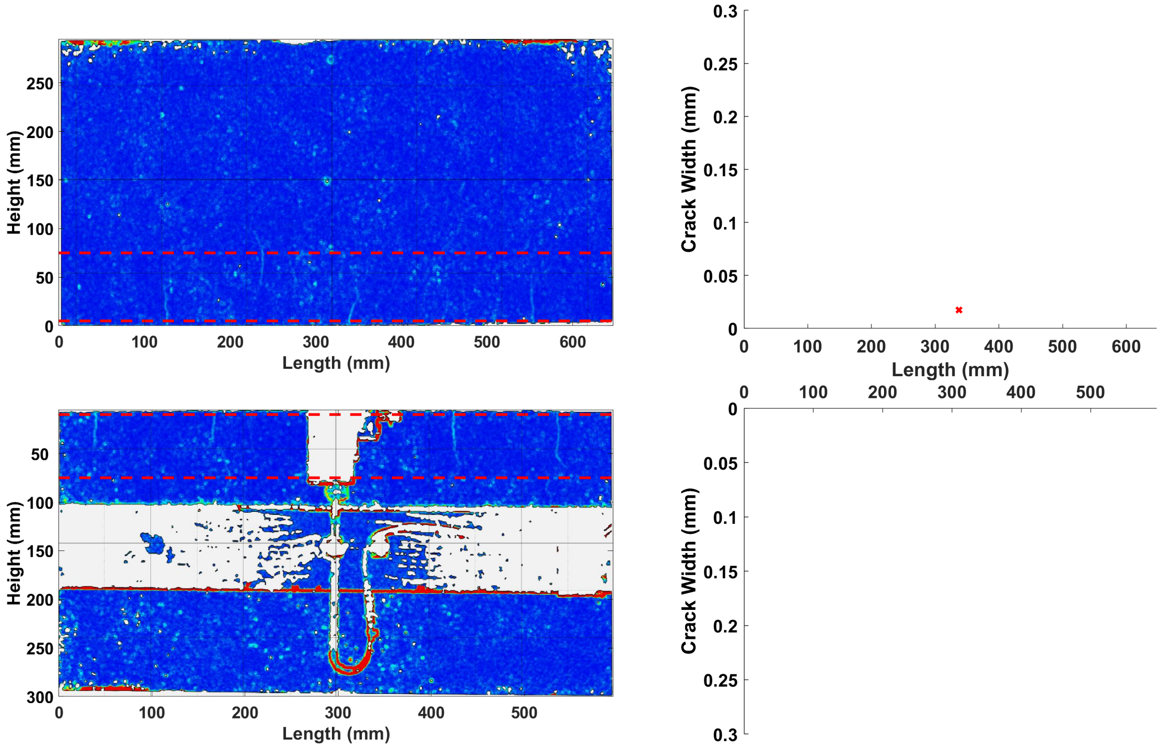

Figure 5.57: Crack widths from DIC data at a load of 18.19 kN.

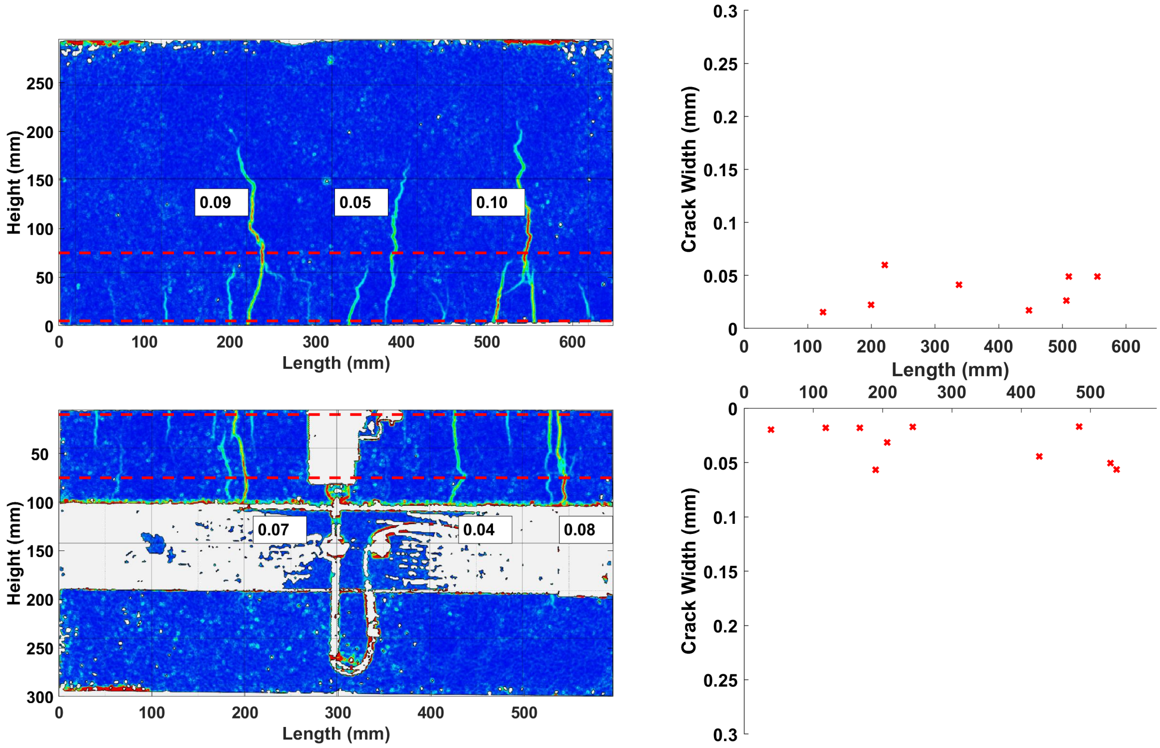

Figure 5.58: Crack widths from DIC data at a load of 29.33 kN.

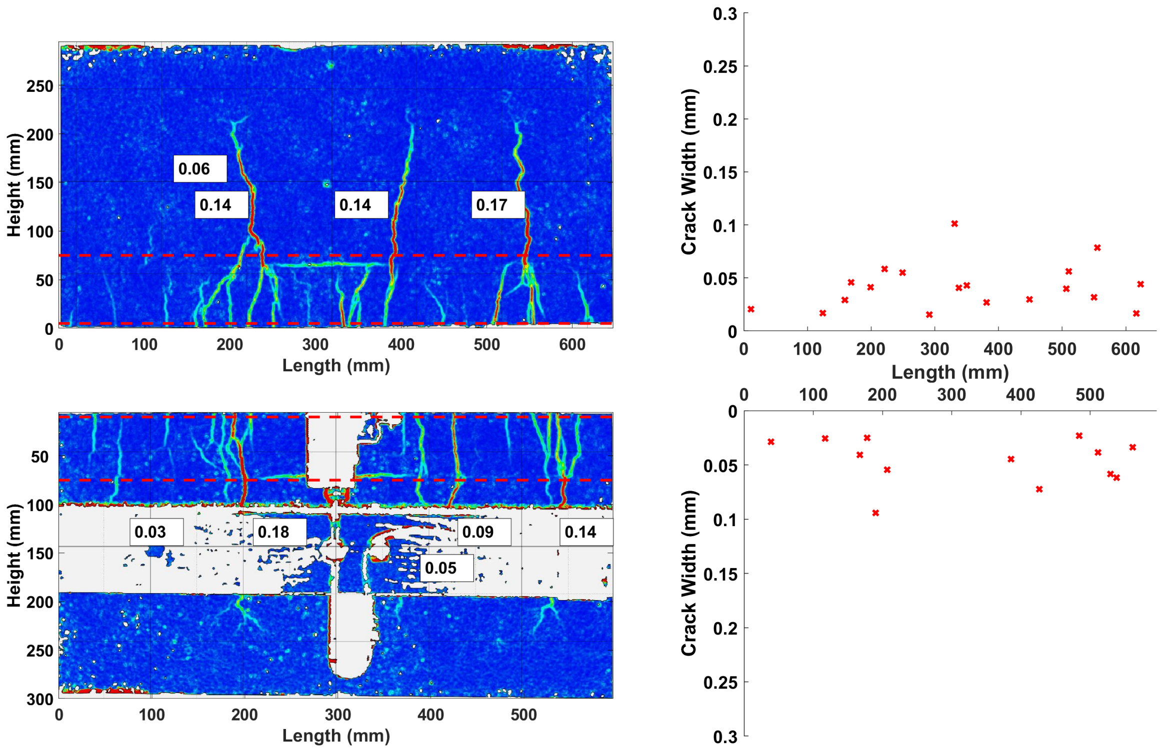

Figure 5.59: Crack widths from DIC data at a load of 41.12 kN.

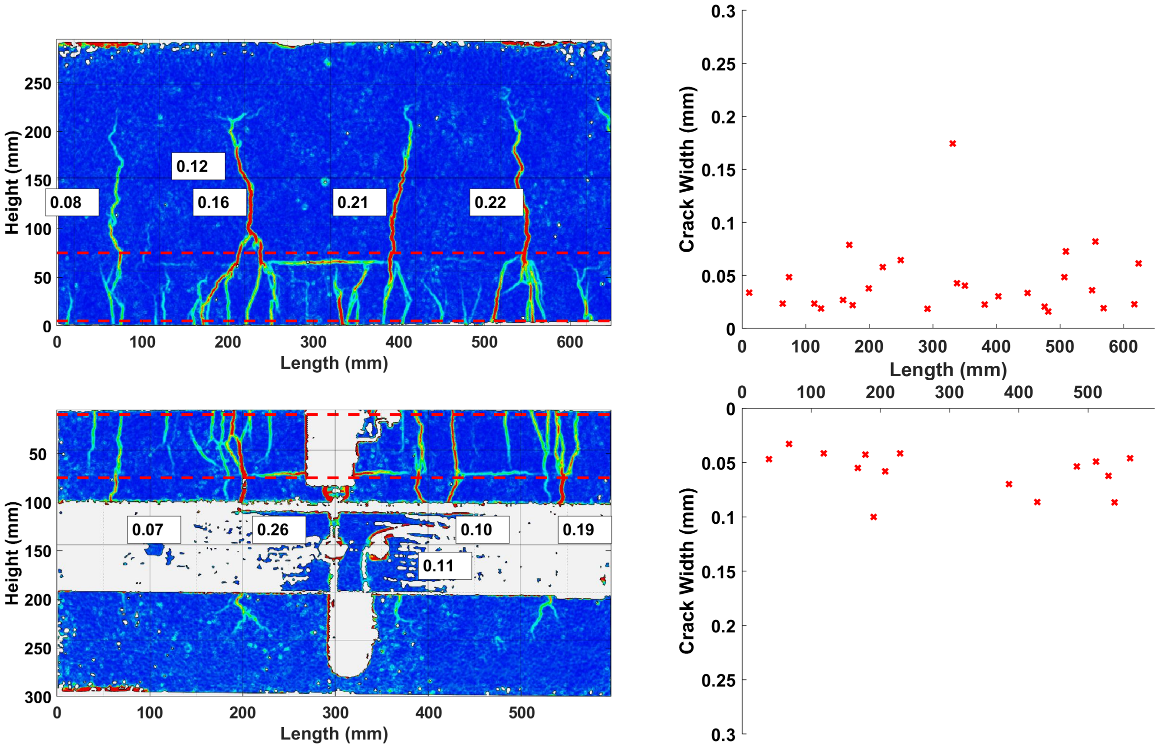

Figure 5.60: Crack widths from DIC data at a load of 50.54 kN.

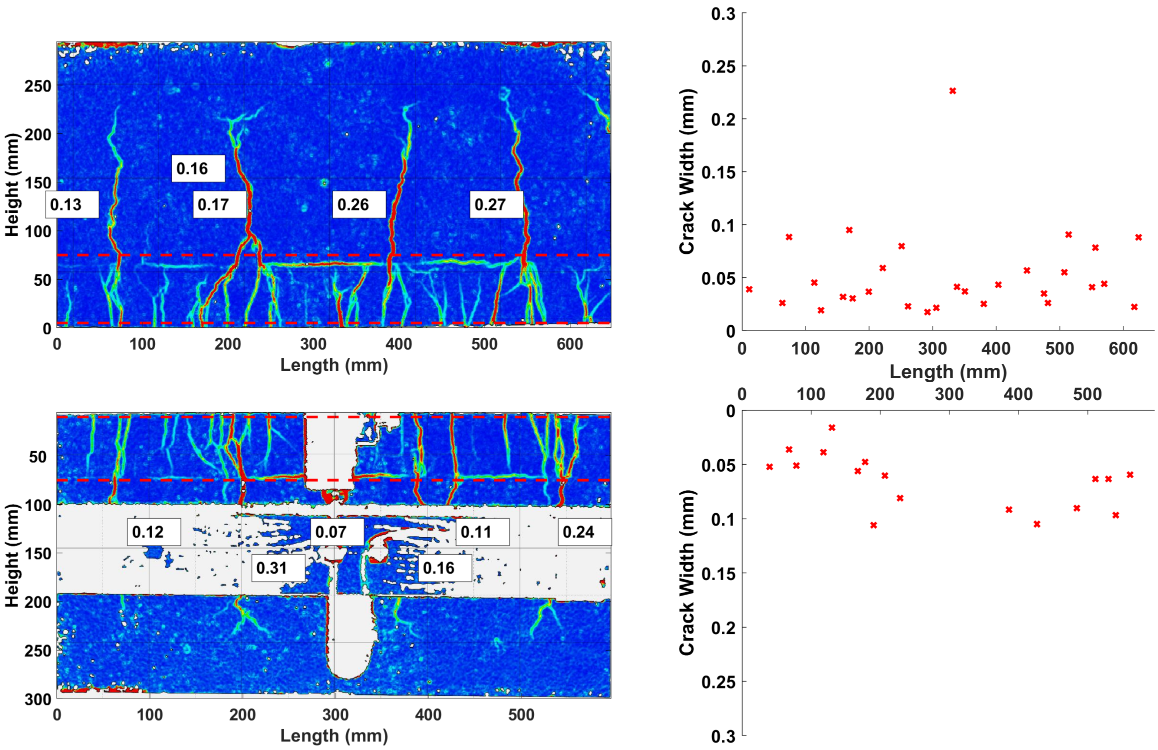

Figure 5.61: Crack widths from DIC data at a load of 60.70 kN.

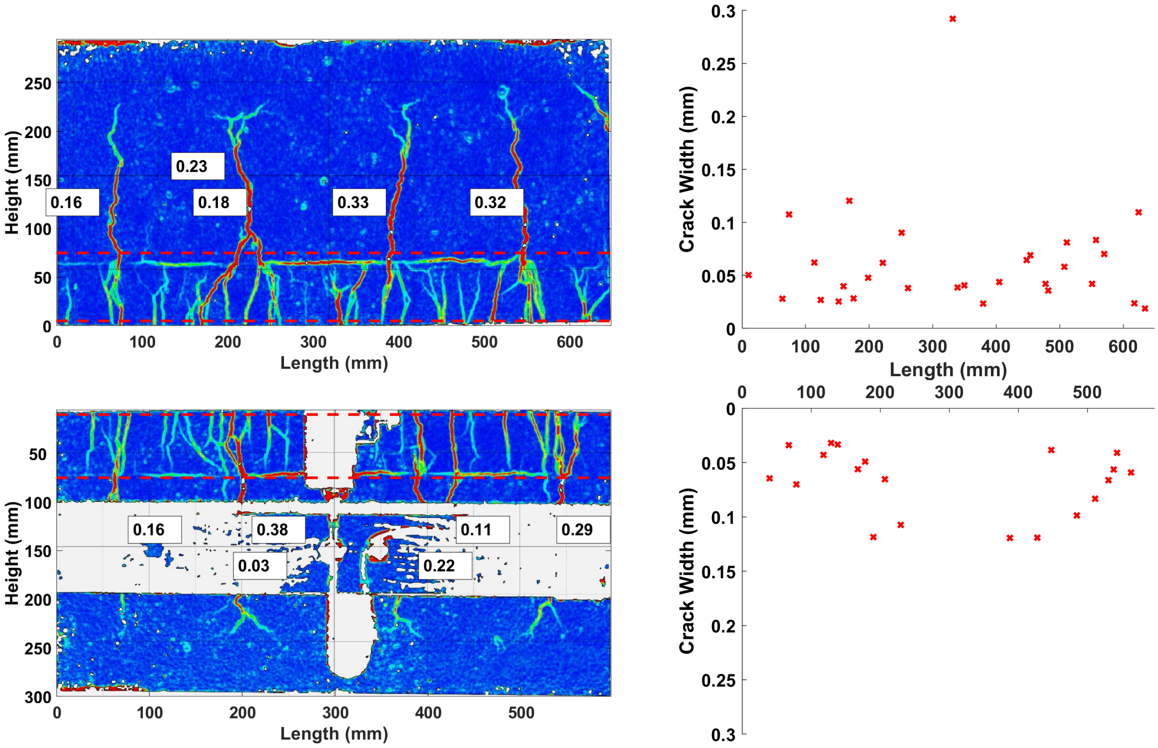

Figure 5.62: Crack widths from DIC data at a load of 75.17 kN.

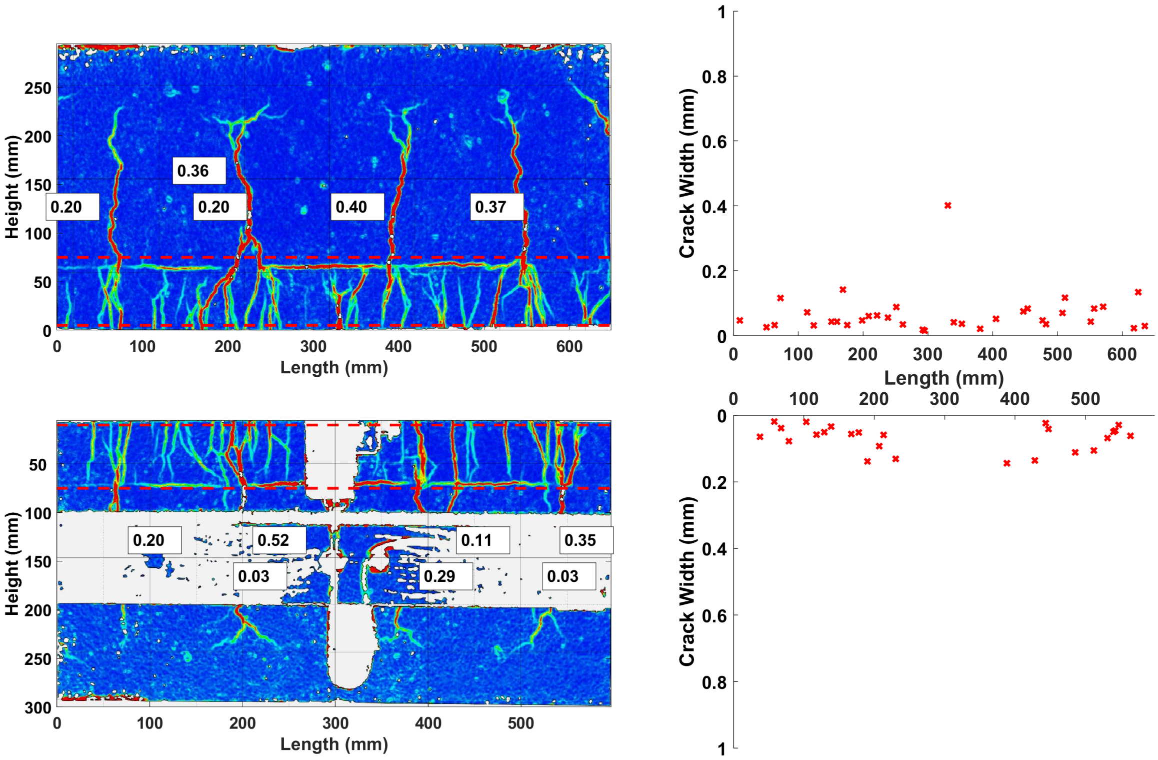

Figure 5.63: Crack widths from DIC data at a load of 80.38 kN.

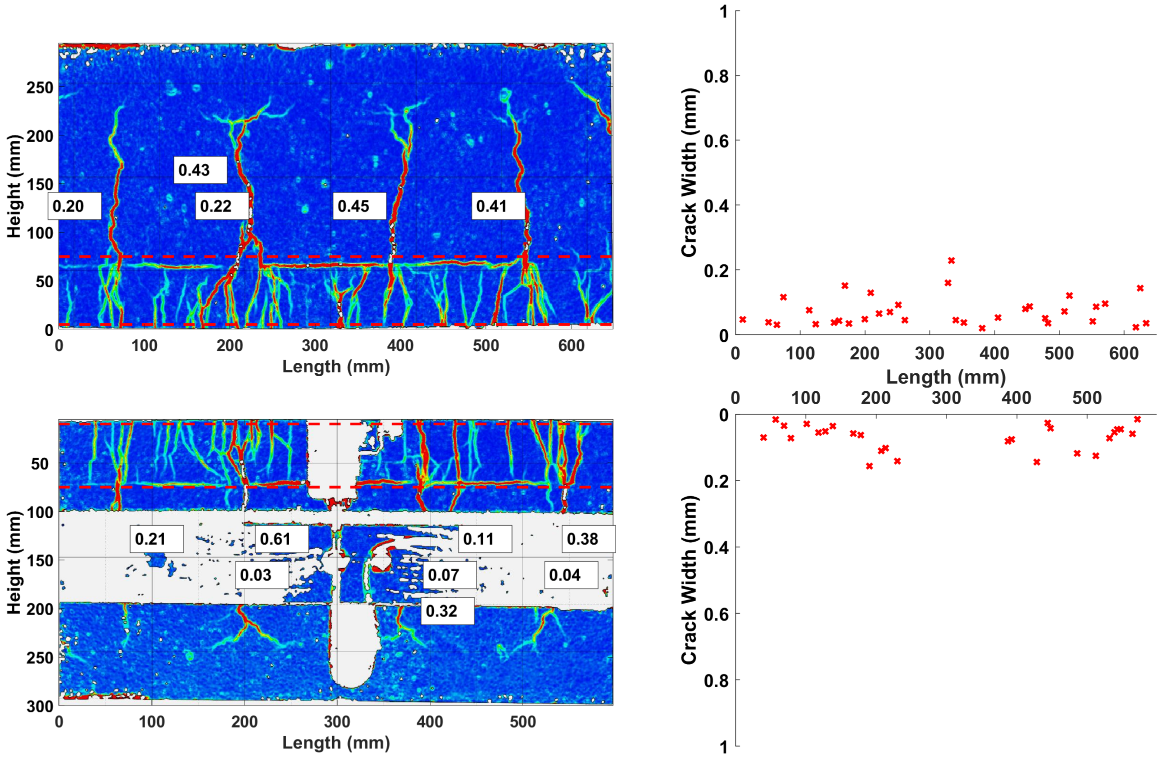

Figure 5.64: Crack widths from DIC data at a load of 82.42 kN.

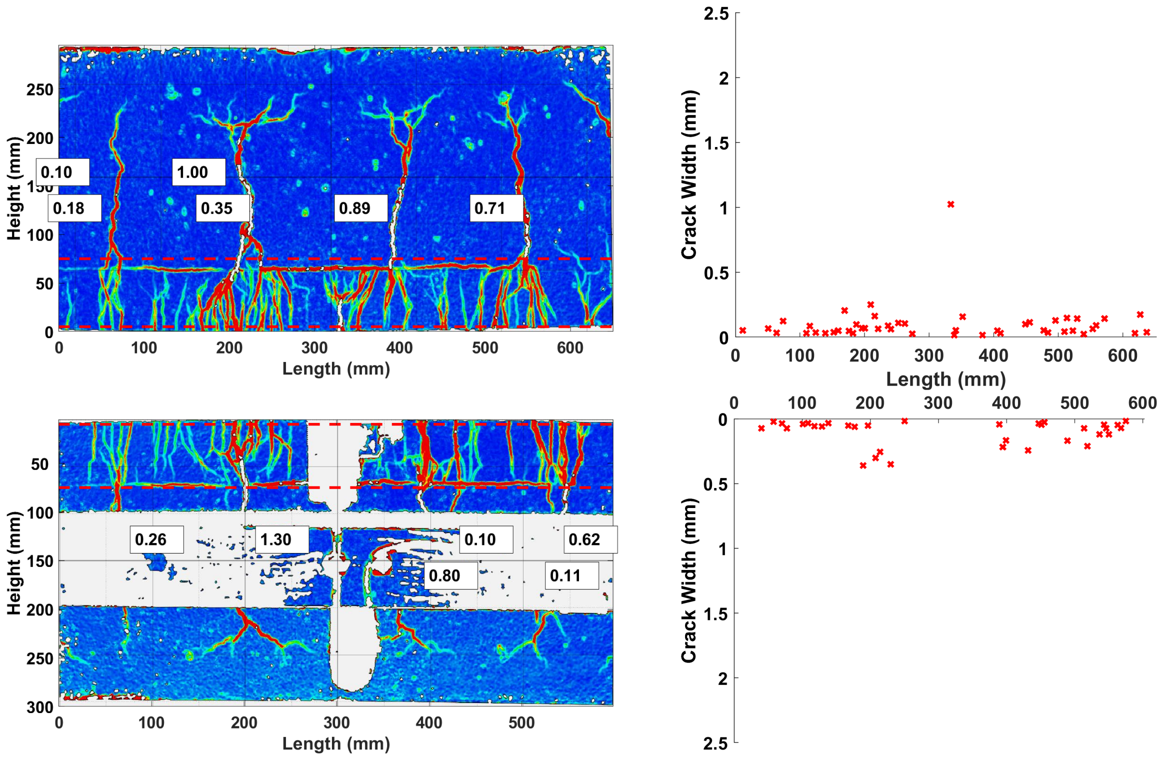

Figure 5.65: Crack widths from DIC data at a load of 90.08 kN.

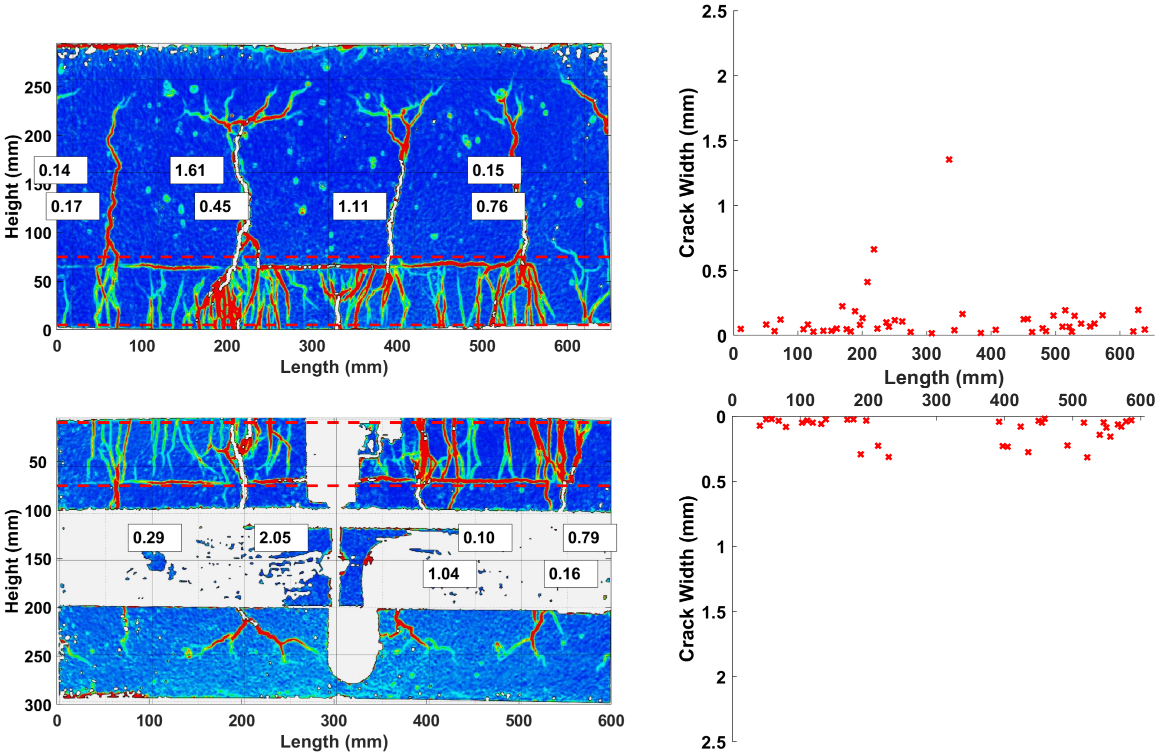

Figure 5.66: Crack widths from DIC data at a load of 93.13 kN.

In addition to the development of the cracking pattern, the behavior of the interface is monitored on side 1 of the beam. The opening (delamination) of the interface and the slip of the interface are measured (Figure 5.67). By measuring the slip, the rigid body motion is ignored. These measurements are performed on three predefined locations: center of the constant bending moment region (1), 250 mm on the right of the center span of the beam (2), and 250 mm on the left of the center span of the beam (3). In order to visualize the delamination, contour plots of the vertical strain are presented (Figure 5.67). It is found that, upon increasing the load the delamination and slip of the interface increase. Delamination is assumed to occur once the slip exceeds 0.05 mm. The delamination is found to start at a load of 67 kN. This load is reached at a deflection of 4.58 mm. In addition, at location 1, where the largest delamination occurs, the slip is small. This can be explained as at the center of the beam the shear stresses of the composite behavior changes sign, and are therefore small. At location 2 and 3 only small delamination is found. The maximum delamination measured is 0.42 mm. This delamination is found at the ultimate load of the beam.

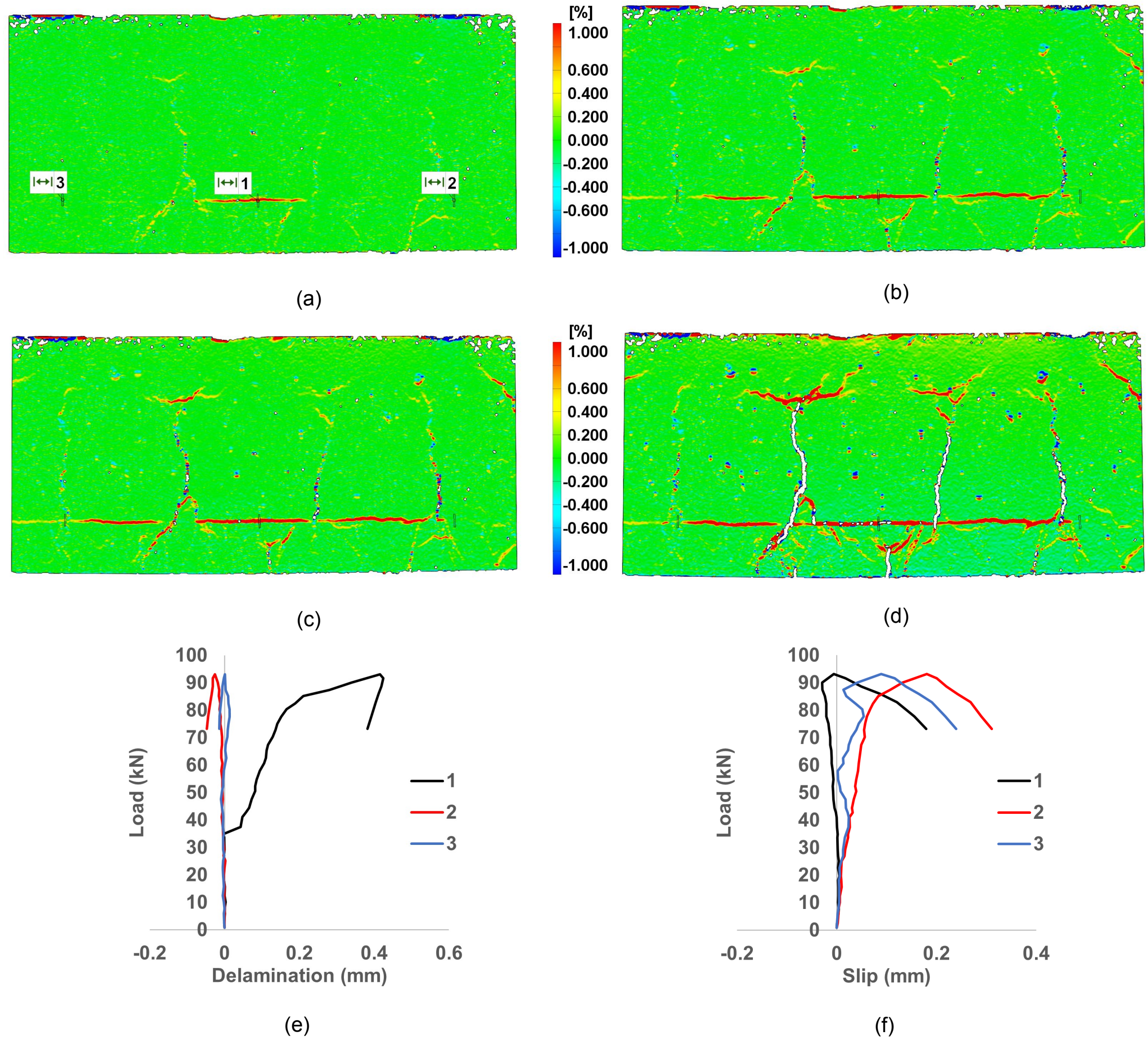

Figure 5.67: Structural behavior of the interface with (a) vertical strain contour plot at 41 kN load, (b) vertical strain contour plot at 67 kN load, (c) vertical strain contour plot at 80 kN load, (d) vertical strain contour plot at 93 kN load, (e) load-delamination curves for the three measuring points and (f) load-slip curves for the three measuring points.

For the crack width measurements DIC data is used. The DIC data is compared with LVDT data to verify the DIC data (Figure 5.68). Different from series 1, out of plane measurements are performed by LVDT 6. Therefore, direct data of the out of plane displacement is present to verify the extent of out of plane movement. In addition, the out of plane displacement is determined from DIC data, as described in section 5.4. The out of plane displacement measured with DIC data is compared with the LVDT data in Figure 5.68.

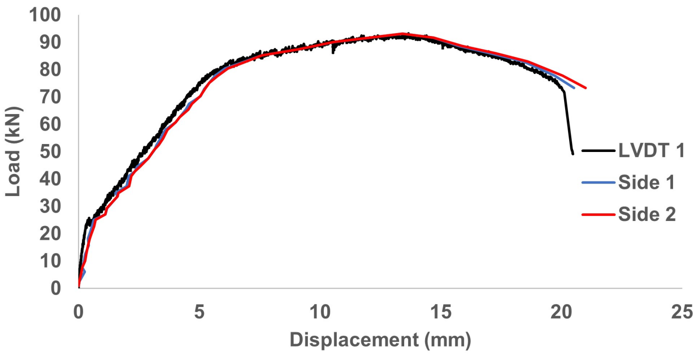

(a)

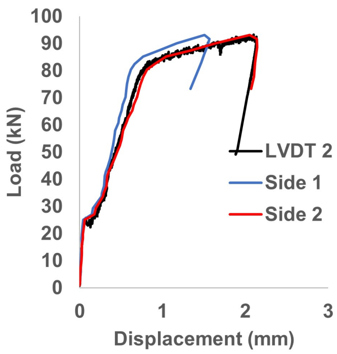

(b)

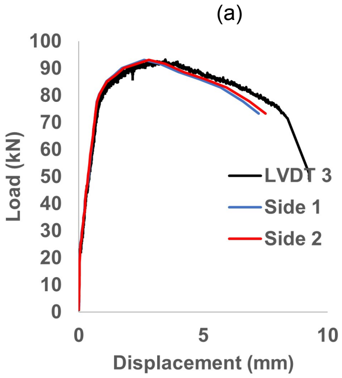

(c)

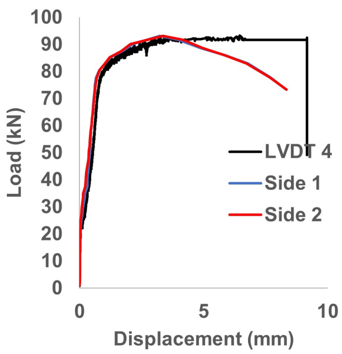

(d)

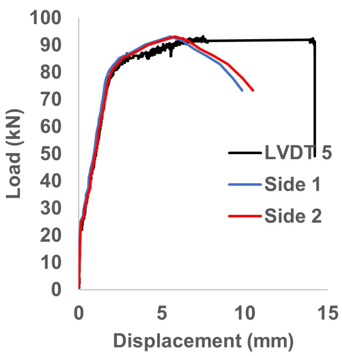

(e)

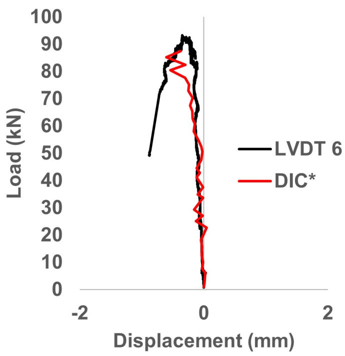

(f)

Figure 5.68: Verification of DIC measurements with LVDT data for (a) LVDT 1, (b) LVDT 2, (c) LVDT 3, (d) LVDT4, (e) LVDT 5 and (f) out of plane displacement by LVDT measurement (LVDT 6) and DIC calculation (DIC*).

Upon the comparison of the DIC and the LVDT data, insignificantly small differences are found. From the out of plane measurements is found that, the beam moves out of plane, upon increasing the load. This out of plane movement is limited to 0.23 mm, at a load of 93.13 kN. At this load, the vertical deflection is 12.41 mm. Upon failing of the beam, the out of plane displacement increases to 0.88 mm. This out of plane movement is not observed in the RC300 beam. A possible explanation for this could be found in the cracking pattern of the hybrid beam, as the number of cracks formed in the SHCC can vary per side. Therefore, the side with more cracks has a lower bending stiffness, compared to the other side. This leads to a path of least resistance, which is oriented partly out of plane. Therefore, upon deforming the beam, the beam moves out of plane. The difference in cracking patterns could be explained by a non uniform fiber dispersion. However, the fiber dispersion is not directly measured. In addition, DIC data is missing on side 2, which makes the counting of cracks inaccurate. The out of plane displacement of this beam is found to have no significant influence on the DIC data. This can be explained by the small out of plane displacement, compared to the vertical deflection. More importantly, the found out of plane displacement is smaller than the out of plane displacement found in the beams of series 1. Lastly, the out of plane displacements found in the DIC data are similar to the out of plane displacements as measured with the LVDT. This verifies the out of plane measuring of DIC data once more.

Reinforced concrete beam of 400 mm height
In figure 5.69 the load-displacement is presented. In the final stage of the experiment the vertical LVDT is out of range (black solid line). In order to present the full load-displacement behavior, the DIC data is used to present the final stage of the load-displacement curve (grey solid line). In the same figure the maximum crack width is presented for every displacement. A summary of the key performance indicators of the beam are shown in table 5.15. The beam failed by rupture of the reinforcement bar. Yielding of the reinforcement is reached at a load of 64.89 kN.

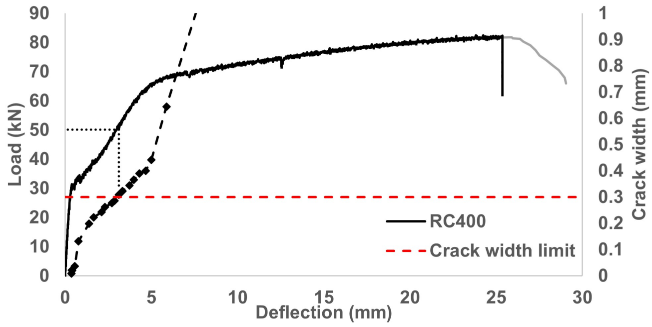

Figure 5.69: Load-deflection (solid) vs. maximum crack width-deflection (dashed) curve.

Table 5.15: Overview of results of experiment of RC400.

Key performance indicators	
Ultimate load	82.47 kN
Maximum deflection	26.98 mm
Number of cracks	7
Average crack spacing	71 mm
Load at 0.3 mm crack width	50.14 kN
0.3 mm load/yield load	77.27%

In order to show the crack development, contour plots of Von Mises strain are made. A green up to red zone indicates strain localization, and thus a crack. The top graphs belong to side 1, whereas the bottom graphs belong to side 2. The crack widths in concrete are reported inside the contour plots. On side 2, no DIC data is available at the center span, due to the vertical LVDT measurement. At this location, concrete cracks are determined over the full length of the region with the missing data. The first crack appears at a load of 22.96 kN (Figure 5.70). Upon increasing the load, more cracks are formed and existing cracks widen (Figure 5.70 to 5.77). Both side faces of the beam develop three propagated cracks, in the 500 mm constant bending moment region. In the final cracking pattern, side 1 forms 6 cracks at the bottom, which coalescence into 3 cracks, propagating to the compression zone. Side 2 forms 7 cracks at the bottom, which coalescence into 3 cracks, propagating to the compression zone. The crack widths are smaller on side 2, compared to side 1. This can be explained by the formation of an additional crack on side 2, at the bottom of the beam. In addition, another crack is found on side 2 just outside the constant bending moment region. These additional cracks are not found on side 1. The 0.3 mm crack width limit is reached at a load of 50.14 kN (Figure 5.73). Thereby, both the crack widths and cracking pattern are similar for both sides. The reported crack widths are in millimeters (mm).

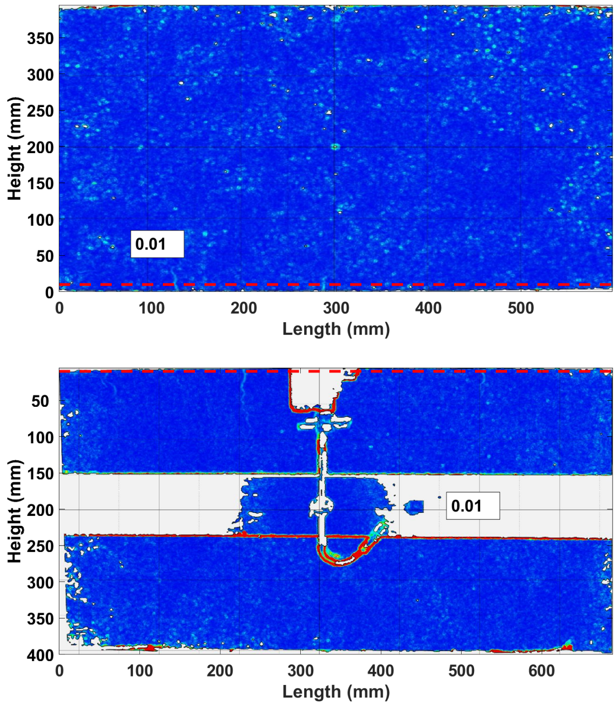

Figure 5.70: Crack widths from DIC data at a load of 22.96 kN.

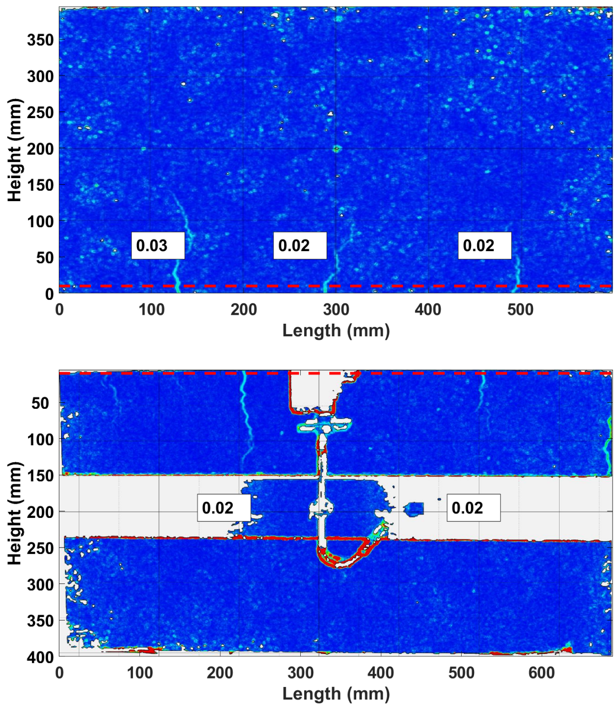

Figure 5.71: Crack widths from DIC data at a load of 30.14 kN.

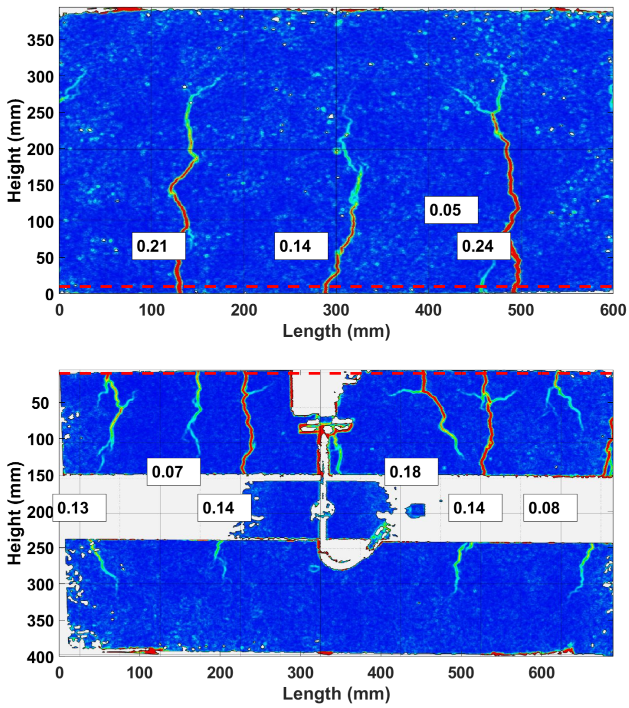

Figure 5.72: Crack widths from DIC data at a load of 40.22 kN.

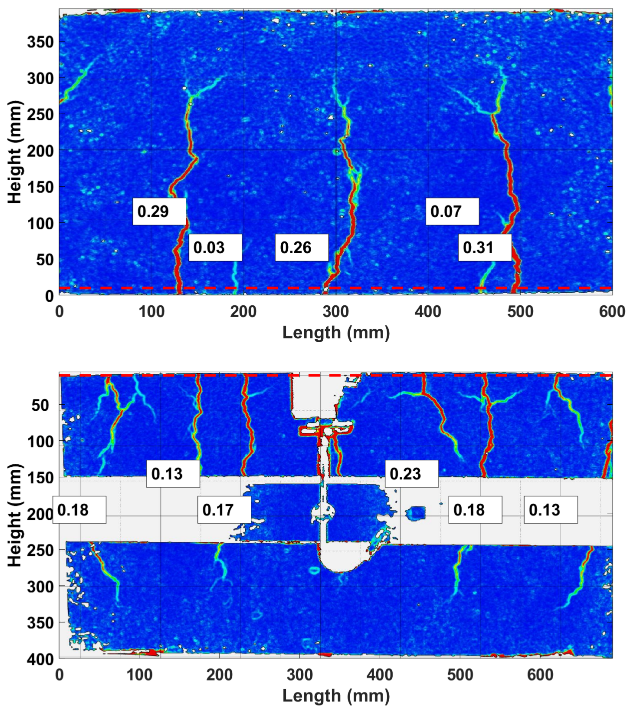

Figure 5.73: Crack widths from DIC data at a load of 50.14 kN.

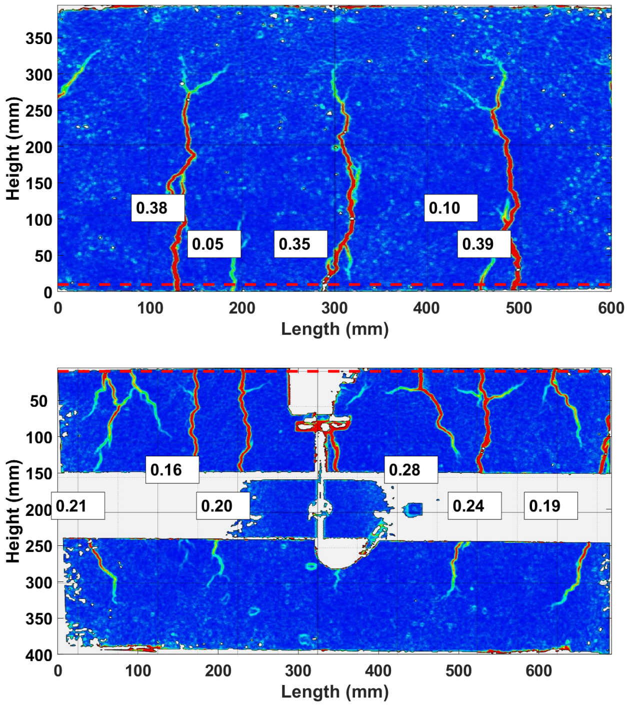

Figure 5.74: Crack widths from DIC data at a load of 60.09 kN.

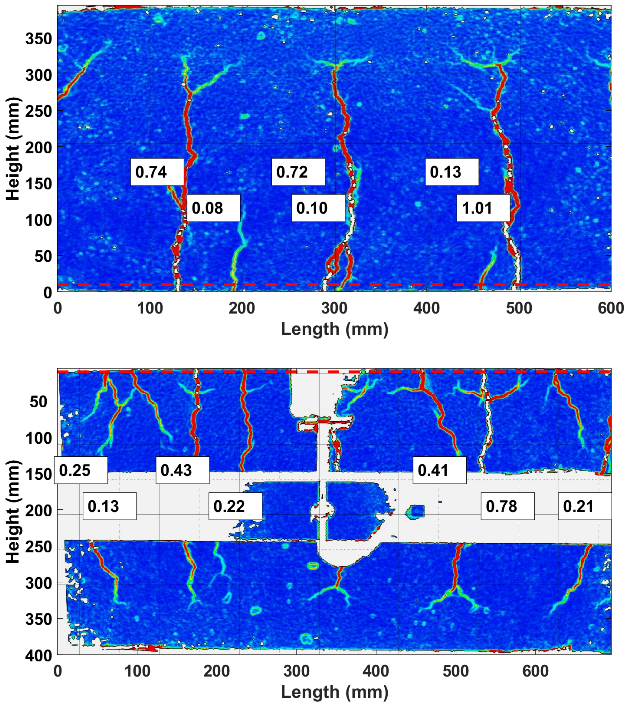

Figure 5.75: Crack widths from DIC data at a load of 70.01 kN.

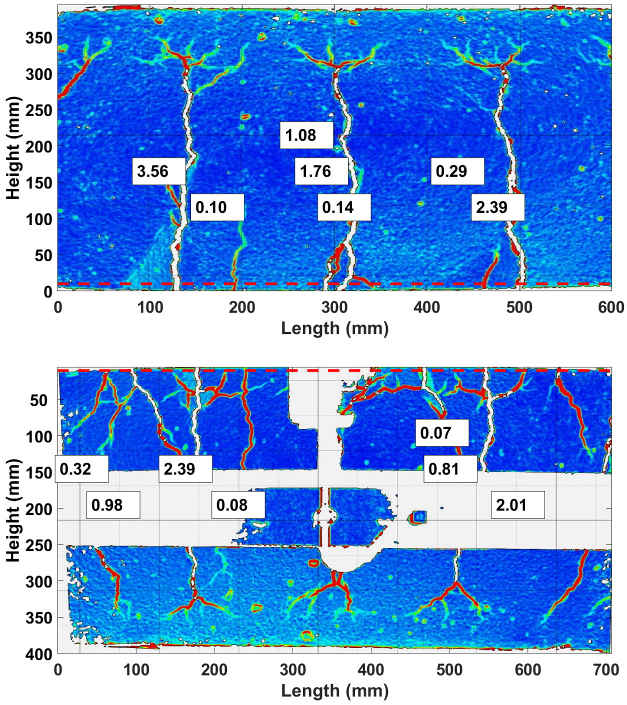

Figure 5.76: Crack widths from DIC data at a load of 80.05 kN.

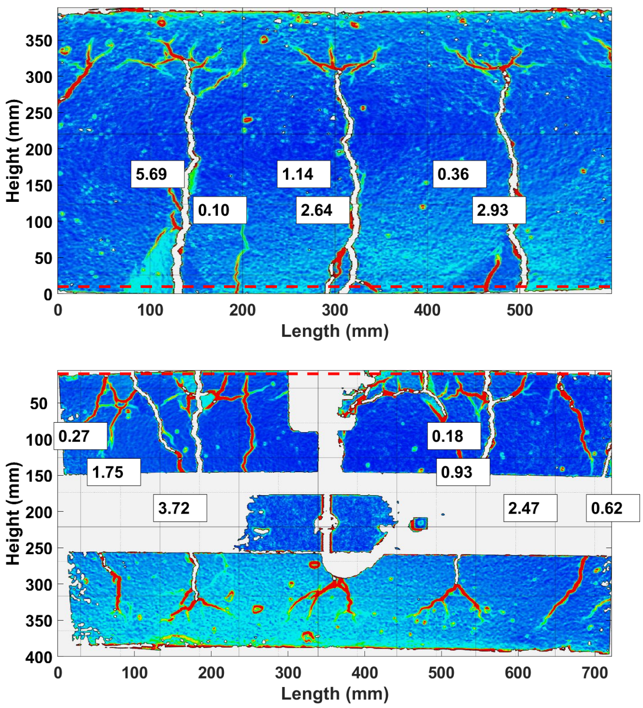

Figure 5.77: Crack widths from DIC data at a load of 81.78 kN.

For the crack width measurements DIC data is used. The DIC data is compared with the LVDT data to verify the DIC data (Figure 5.78).

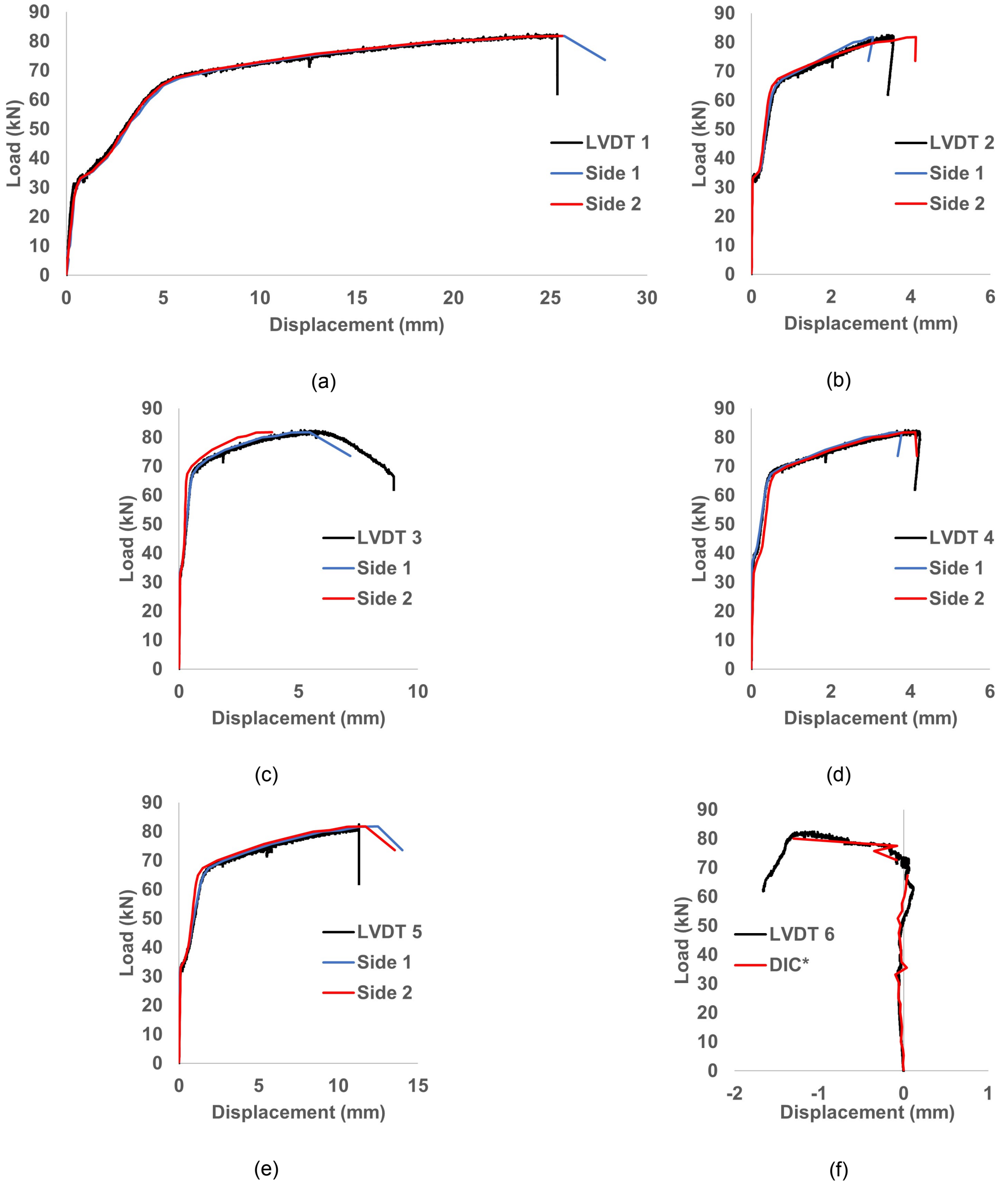

Figure 5.78: Verification of DIC measurements with LVDT data for (a) LVDT 1, (b) LVDT 2, (c) LVDT 3, (d) LVDT4, (e) LVDT 5 and (f) out of plane displacement by LVDT measurement (LVDT 6) and DIC calculation (DIC*).

Upon comparison of DIC and LVDT data, insignificantly small differences are found. LVDT 6 shows limited out of plane displacement (-0.15 mm), up to a load of 76.77 kN. A further increase in the load leads to a relative large increase in out of plane displacement. The out of plane displacement at the ultimate load is -1.31 mm. The negative sign of the out of plane displacement means that the displacement is towards the camera of side 2. This increase in out of plane displacement can be explained by the heterogeneity of concrete. Therefore, the cracking pattern is also heterogeneous. Upon fracturing the beam deforms following the path of least resistance. From the cracking patterns is found that, side 2 has formed more cracks at the bottom of the beam. Therefore, the path of least resistance would be to deform out of plane, towards side 2. Nevertheless, the out of plane displacement of -1.31 mm is still significantly lower, compared to the 3.47 mm out of plane displacement of the RC400 beam from series 1. Lastly, the out of plane displacement determined from the DIC data is corresponding to the measured out of plane displacement from the LVDT.

Hybrid R/SHCC beam of 400 mm height

In figure 5.79 the load-displacement behavior is presented. In the same figure the maximum crack width in the SHCC layer can be found for every displacement. A summary of the key performance indicators of the beam are presented in table 5.16. The beam failed by rupture of the reinforcement. Yielding of the reinforcement is reached at a load of 77.45 kN.

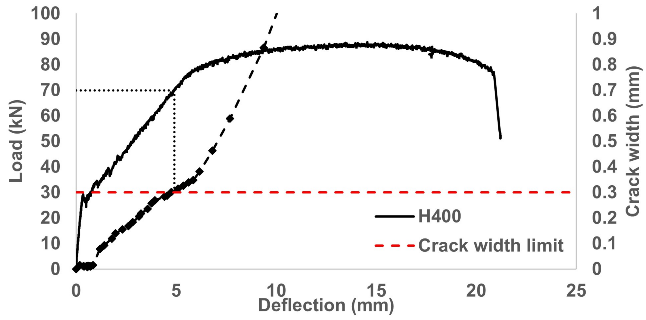

Figure 5.79: Load-deflection (solid) vs. maximum crack width-deflection (dashed) curve.

Table 5.16: Overview of results of experiment of H400.

Key performance indicators	
Ultimate load	88.82 kN
Maximum deflection	20.82 mm
Number of cracks	35
Average crack spacing	14.42 mm
Load at 0.3 mm crack width	69.92 kN
0.3 mm load/yield load	90.28%

The concrete-SHCC interface is profiled over the 500 mm constant bending moment region. Both a contour plot and the 3D scanned interface are presented in figure 5.80. The scale of the contour plot is in millimeters (mm).

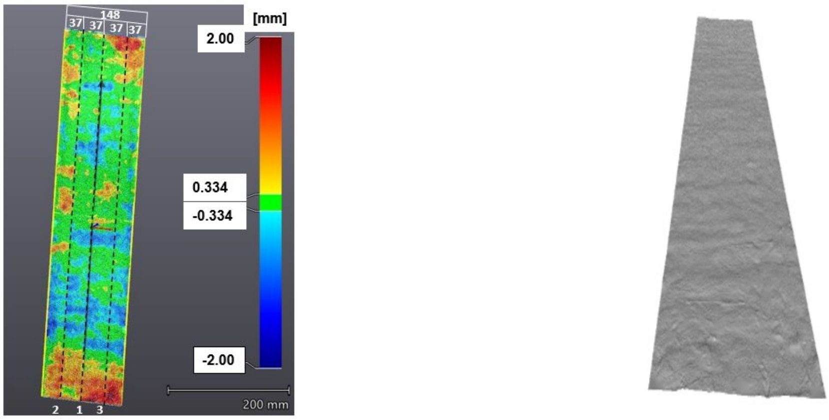

(a)

(b)

Figure 5.80: Interface roughness profiling with (a) contour plot and (b) 3D scan.

From the scanned surface, three sections over the length of the interface are made to determine the roughness. The first section is made at the middle of the width of the interface. Section 2 and 3 are made at 37 mm respectively left and right of the middle line of the beam. From the sections profile graphs are made (Figure 5.81).

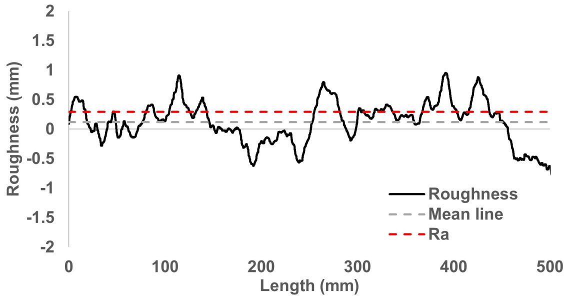

(a)

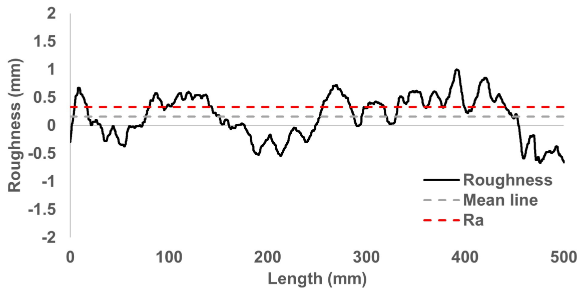

(b)

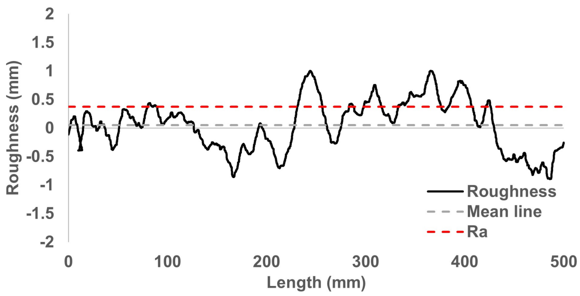

(c)

Figure 5.81: Interface profile graphs at (a) section 1, (b) section 2 and (c) section 3.

An average arithmetical surface roughness of 0.334 mm is found, with a maximum peak value of 0.874 mm (Table 5.17). Therefore, the concrete-SHCC interface is smooth.

Table 5.17: Overview of results of interface profiling.

Section	1	2	3	Average
Ra (mm)	0.294	0.332	0.376	**0.334**
Rp (mm)	0.835	0.837	0.950	**0.874**
Rv (mm)	0.894	0.926	1.158	**0.993**
Rt (mm)	1.729	1.763	2.108	**1.867**

In order to show the crack development, contour plots of Von Mises strain are made. A green up to red zone indicates strain localization, and thus a crack. SHCC cracks are presented in point cloud graphs. The top graphs belong to side 1, whereas the bottom graphs belong to side 2. The crack widths in concrete are reported inside the contour plots. On side 2, no DIC data is available at the center span, due to the vertical LVDT measurement. SHCC cracks are unknown at this location, whereas concrete cracks are determined over the full length of the region with the missing data. The first crack appears at a load of 17.80 kN (Figure 5.82). Upon increasing the load, more cracks are formed and existing cracks widen (Figure 5.82 to 5.89). The 0.3 mm crack width criteria is reached at a load of 69.92 kN. Both sides show 7 concrete cracks, which coalescence into 3 concrete cracks, propagating to the compression zone. The SHCC layer shows a distributed cracking pattern. The biggest crack in SHCC is found outside the constant bending moment region, on the left of side 1. This can be explained, as at this location the applied moment is still large and a weak spot in the material can allow to initiate a crack here. The maximum crack widths in SHCC are larger on side 1, compared to side 2. This difference can be explained by the cracking pattern, as side 2 forms multiple cracks, at the location of the maximum crack width. Therefore, the strain release is more distributed on side 2 compared to side 1. Lastly, it is found that the opening of the concrete cracks leads to the opening of the SHCC cracks. Therefore, the largest width of a crack in SHCC is not always found at the bottom of the beam (Figure 5.84). The reported crack widths are in millimeters (mm).

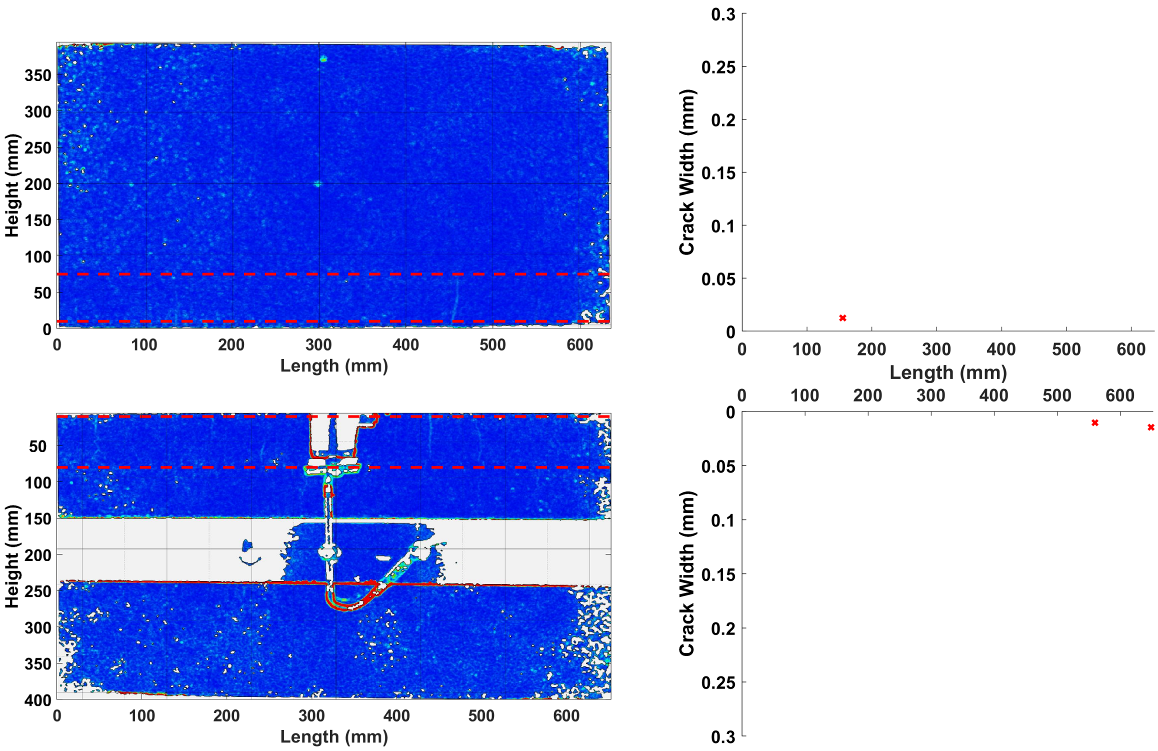

Figure 5.82: Crack widths from DIC data at a load of 17.80 kN.

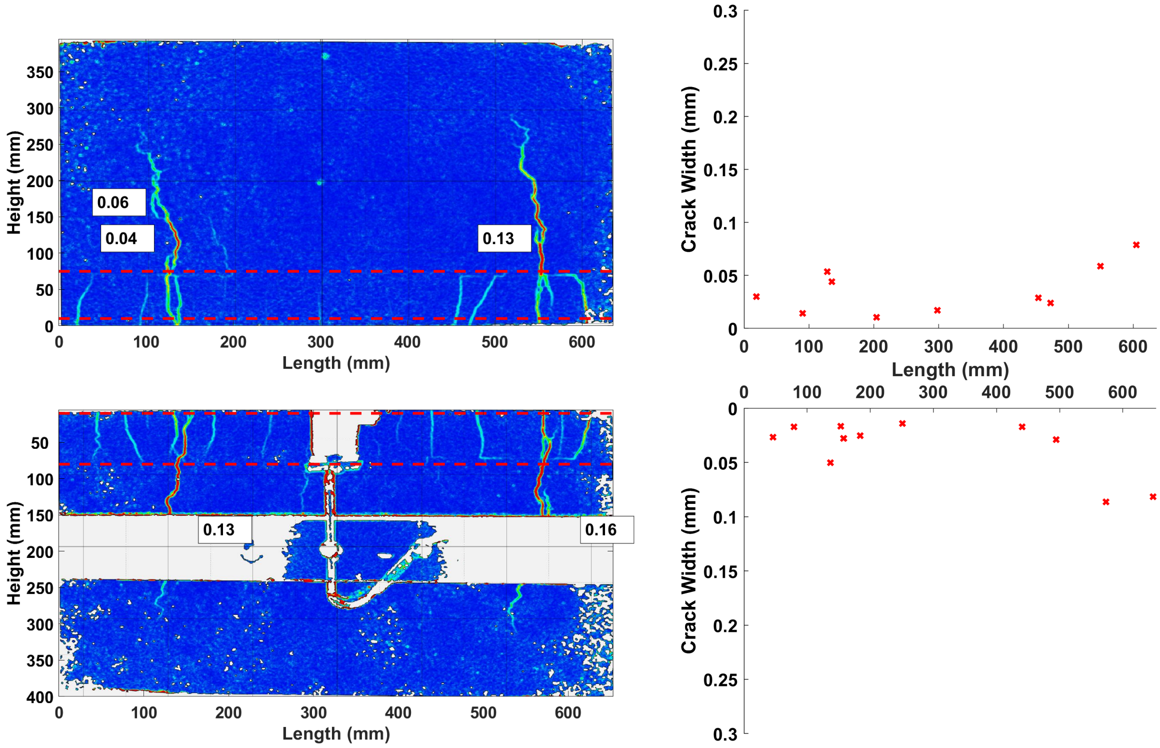

Figure 5.83: Crack widths from DIC data at a load of 29.98 kN.

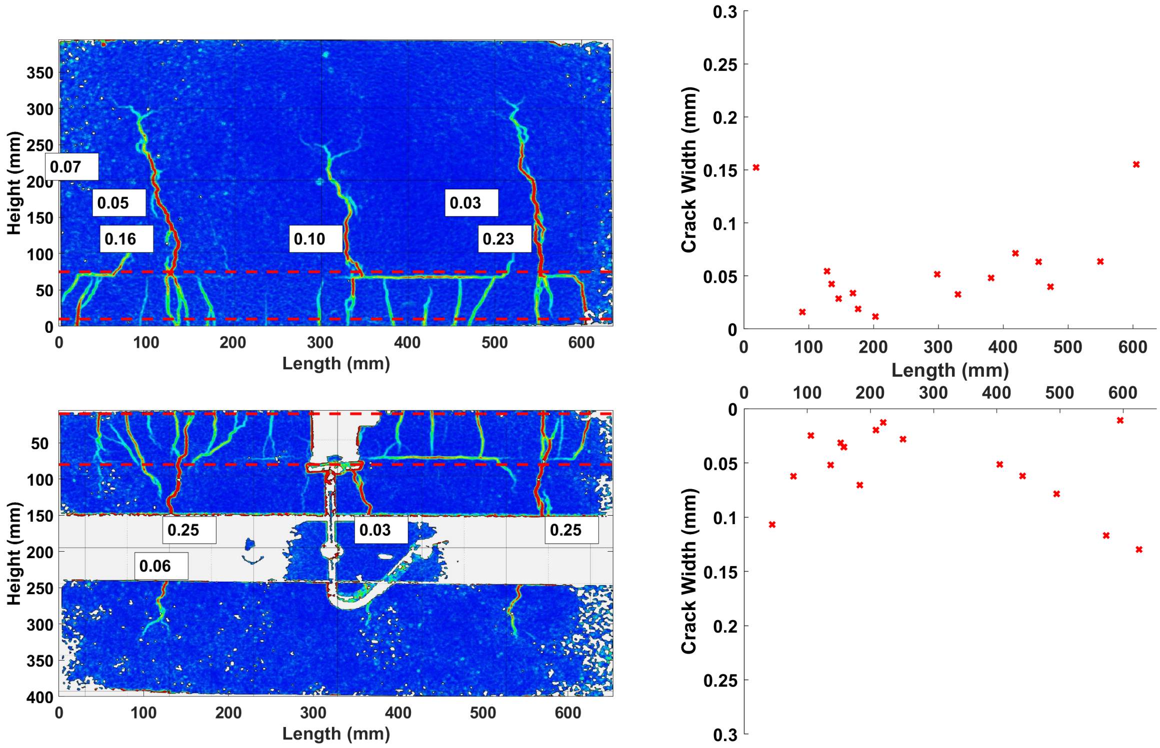

Figure 5.84: Crack widths from DIC data at a load of 40.09 kN.

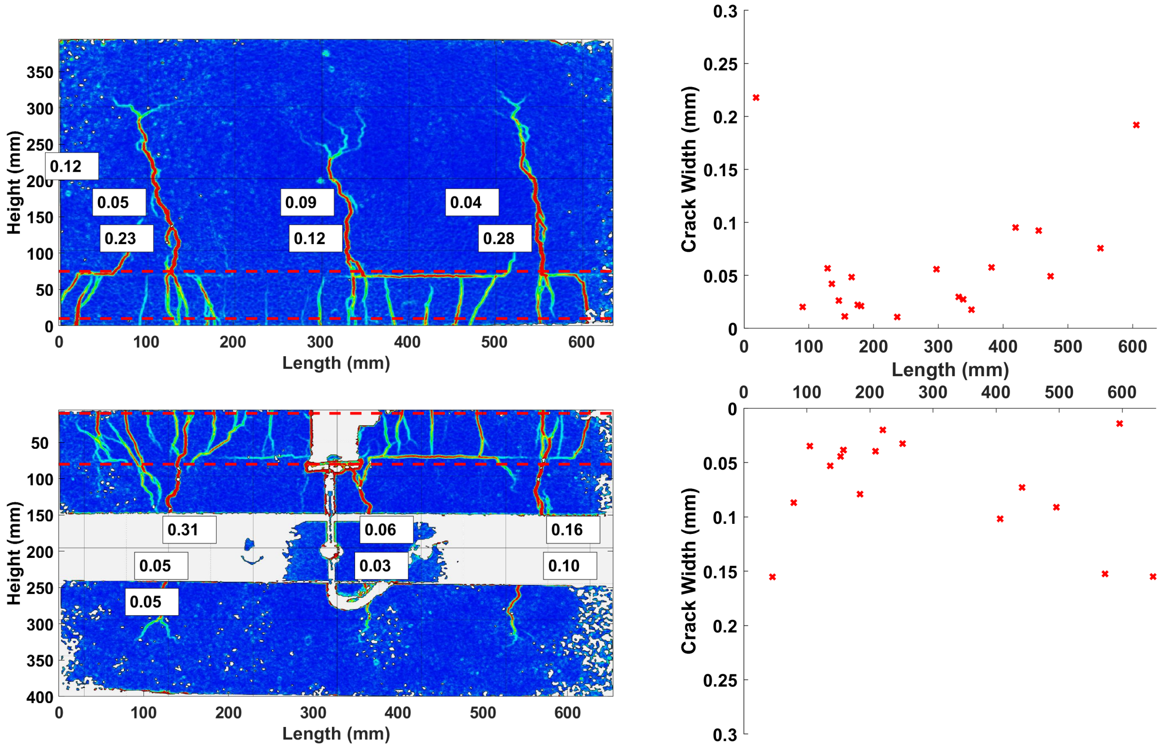

Figure 5.85: Crack widths from DIC data at a load of 50.16 kN.

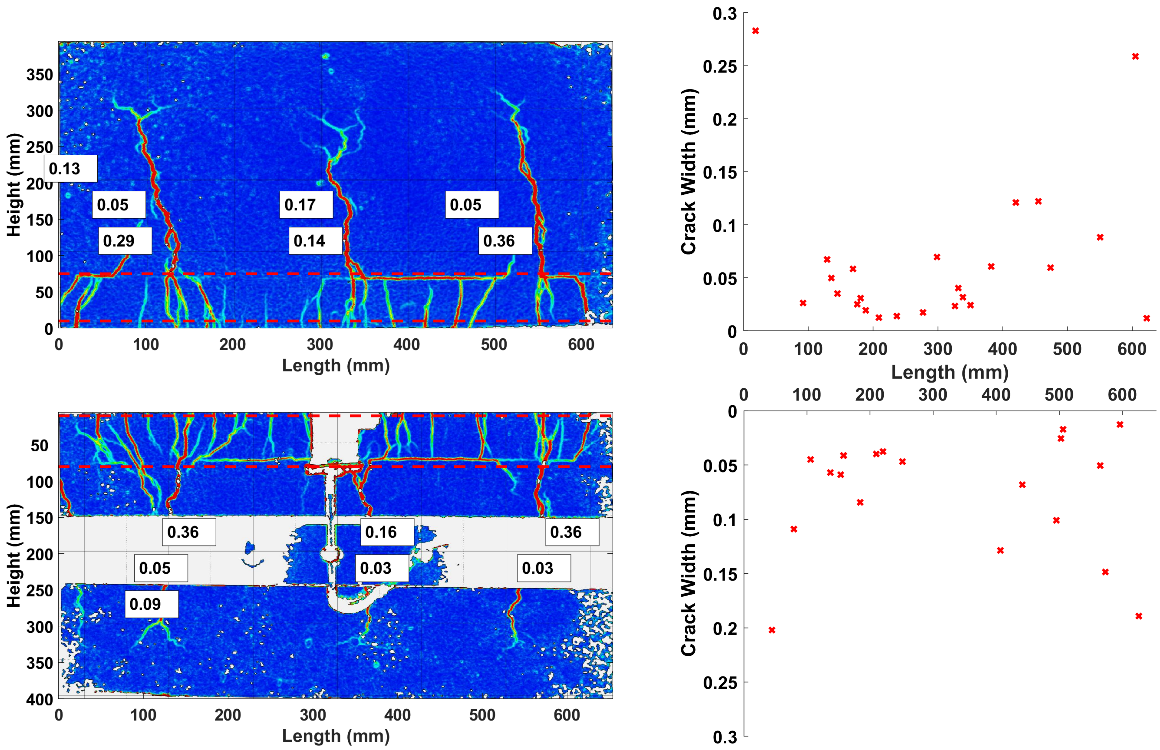

Figure 5.86: Crack widths from DIC data at a load of 60.65 kN.

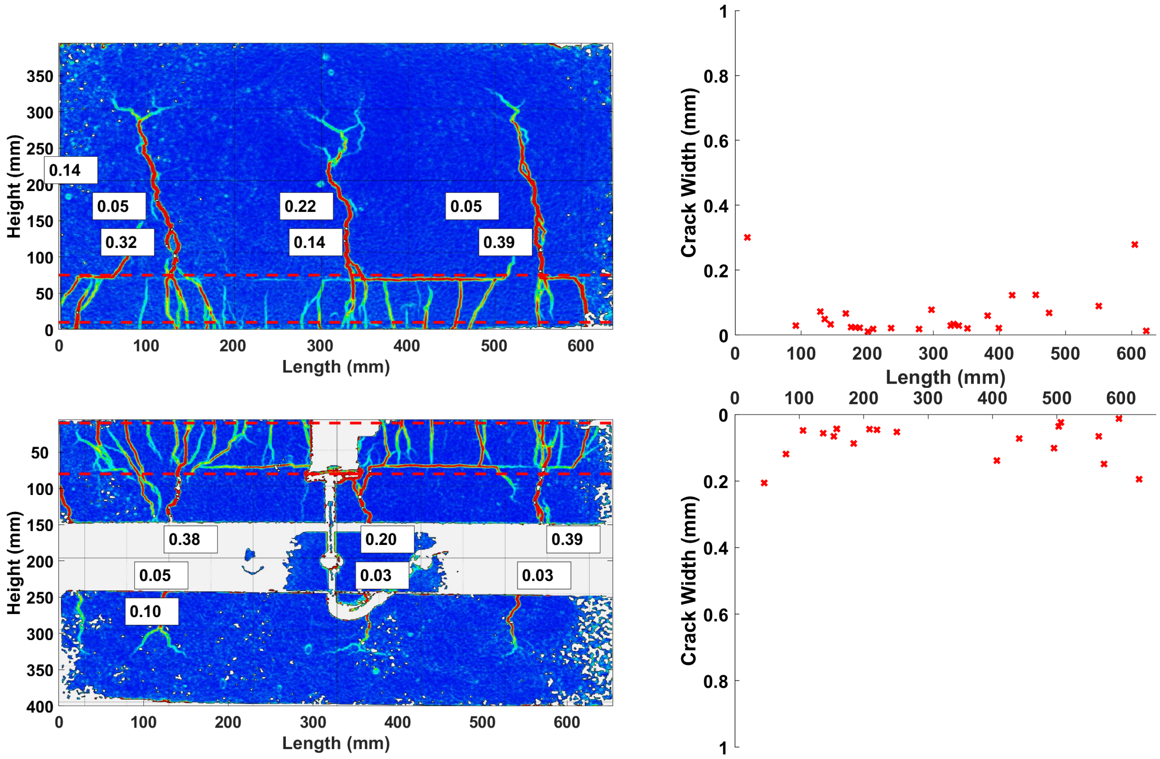

Figure 5.87: Crack widths from DIC data at a load of 70.32 kN.

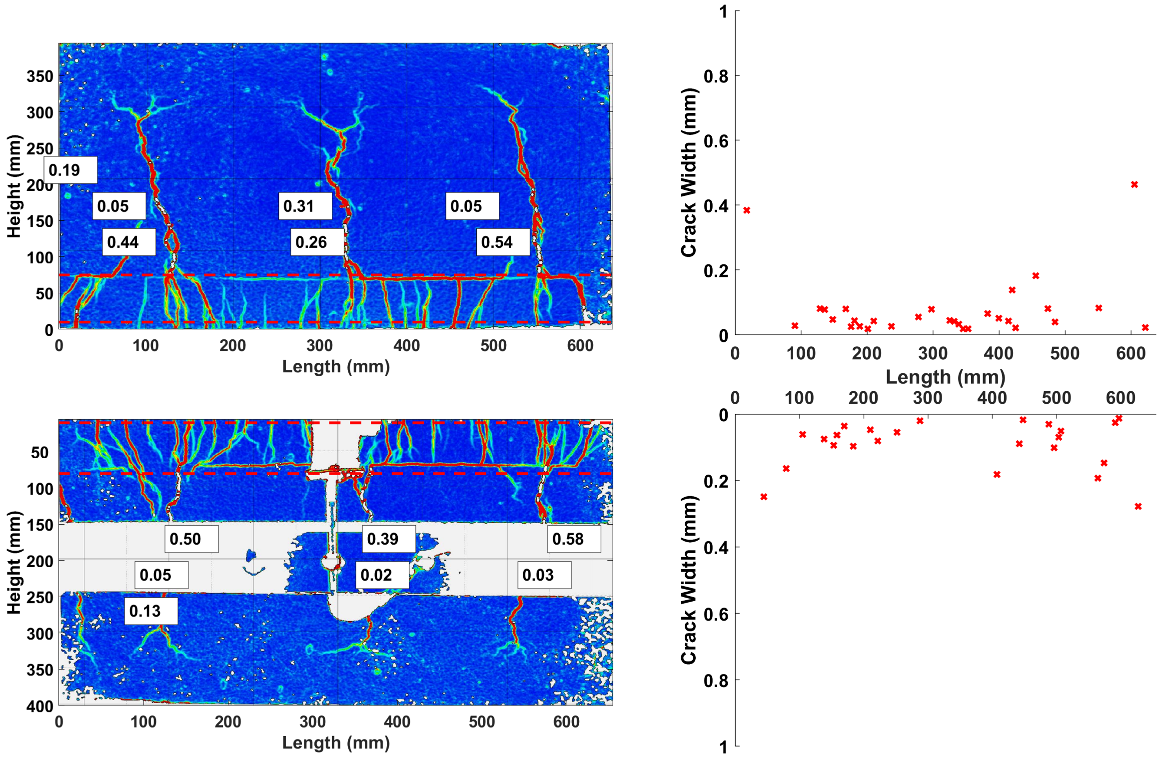

Figure 5.88: Crack widths from DIC data at a load of 79.98 kN.

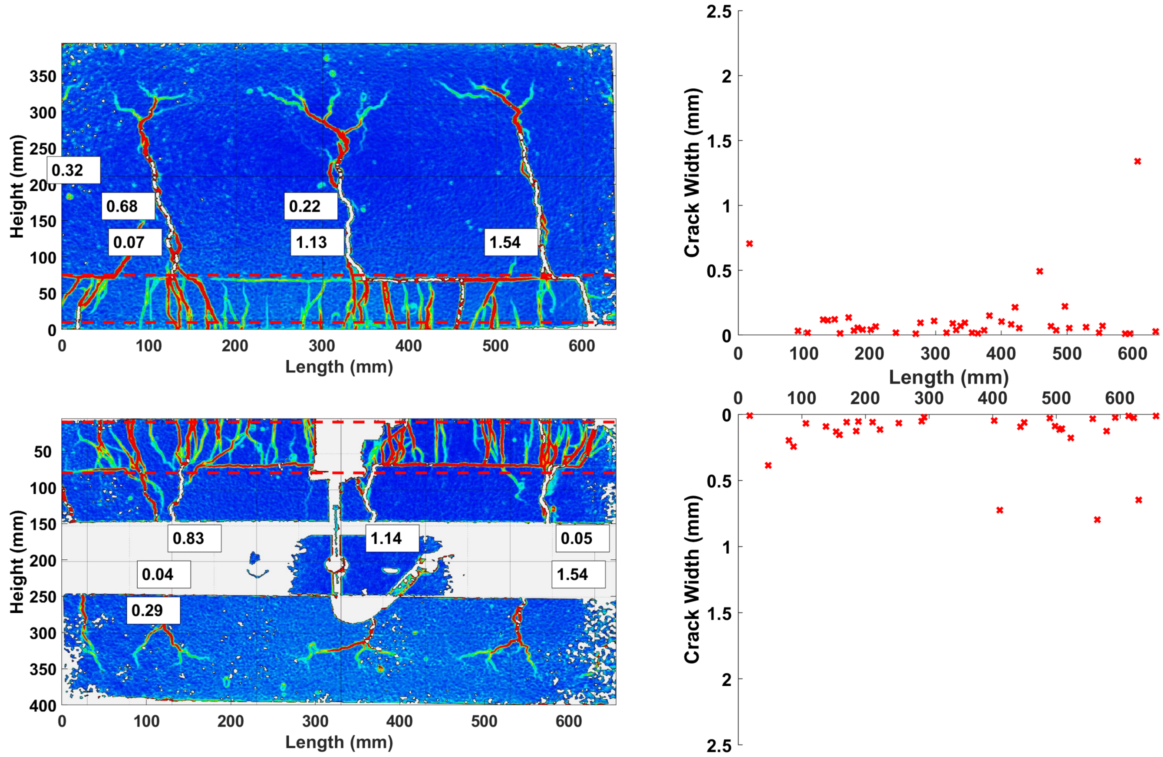

Figure 5.89: Crack widths from DIC data at a load of 87.50 kN.

In addition to the development of the cracking pattern, the behavior of the interface is monitored on side 1 of the beam. The opening (delamination) of the interface and the slip of the interface are measured (Figure 5.90). By measuring the slip, the rigid body motion is ignored. These measurements are performed on three predefined locations: 50 mm on the right of the center of the constant bending moment region (1), 250 mm on the right of the center span of the beam (2), and 250 mm on the left of the center span of the beam (3). In order to visualize the delamination, contour plots of the vertical strain are presented (Figure 5.90). It is found that, upon increasing the load the delamination and slip of the interface increase. Delamination is assumed to occur after the slip exceeds 0.05 mm. Delamination is initiated at a load of 40 kN. The deflection is 2.42 mm at this load. The delaminations are up to the ultimate load similar at the locations measured. After reaching the ultimate load, the delamination and the slip increases at location 2 to respectively 2.04 mm and 4.73 mm. Location 2 is also where the largest SHCC crack is found in the final cracking pattern. From the contour plots is found that, the SHCC cracks do not propagate directly to the concrete layer. The SHCC-concrete interface is contributing to the propagation of the SHCC-cracks. The slip at location 1 is limited, compared to the occurred delamination. This can be explained, as location 1 is close to the center of the span of the beam. Delamination is present over the full constant bending moment region.

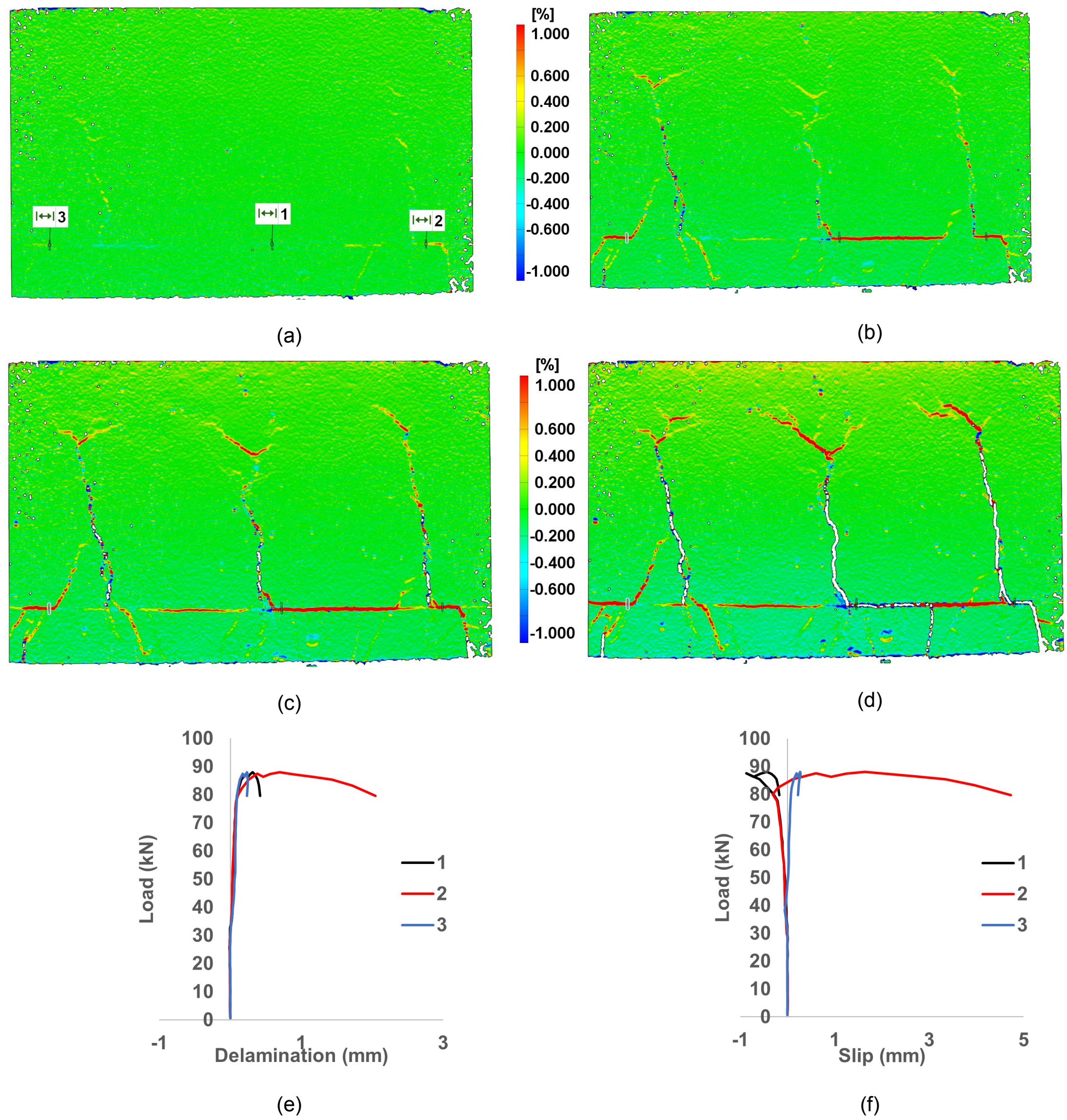

Figure 5.90: Structural behavior of the interface with (a) vertical strain contour plot at 40 kN load, (b) vertical strain contour plot at 70 kN load, (c) vertical strain contour plot at 80 kN load, (d) vertical strain contour plot at 89 kN load, (e) load-delamination curves for the three measuring points and (f) load-slip curves for the three measuring points.

For the crack width measurements DIC data is used. The DIC data is compared with the LVDT data to verify the DIC data (Figure 5.91).

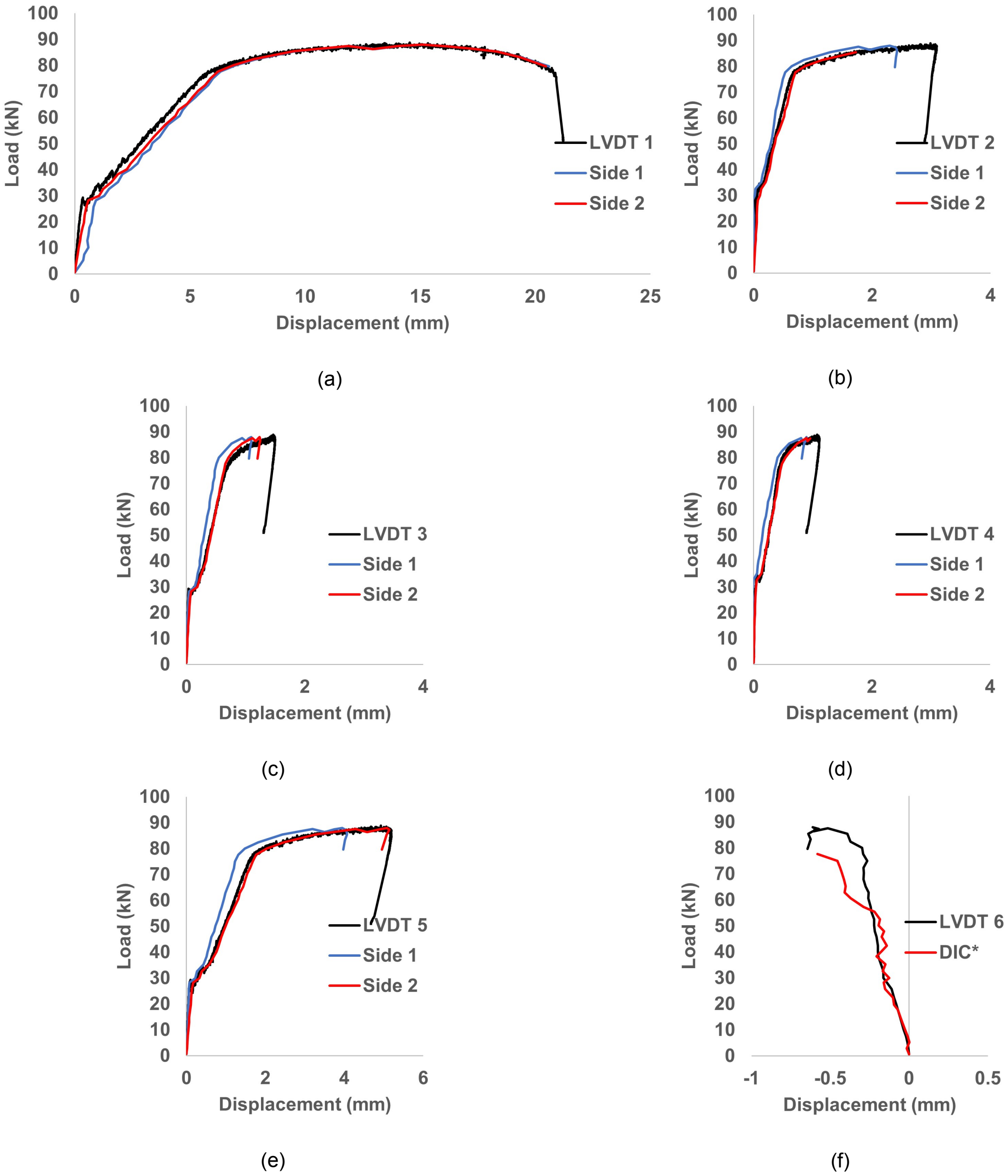

Figure 5.91: Comparison of the DIC measurements with the LVDT data for (a) LVDT 1, (b) LVDT 2, (c) LVDT 3, (d) LVDT4, (e) LVDT 5 and (f) out of plane displacement by LVDT measurement (LVDT 6) and DIC calculation (DIC*).

Upon comparison of DIC and LVDT data, insignificantly small differences are found. From the out of plane measurements is found that, the beam moves out of plane upon increasing the load. At the ultimate load, the out of plane displacement is 0.61 mm, whereas the vertical deflection is 15.19 mm. Therefore, the out of plane displacement is limited to 4% of the vertical deflection. The increase of the out of plane movement upon increasing the load, is not found for the RC300 and RC400 beams, but is found for the H300 beam. The out of plane displacement starts increasing with the load at a load of 8.63 kN. A possible explanation for this behavior can be found in the formation of a path of least resistance, which has an out of plane component. Lastly, the out of plane displacements measured with the LVDT is compared with the out of plane displacements found in the DIC data. Upon comparison similar displacements are found, which means that the out of plane displacement can be found in 2D DIC data.

5.5.3. Material Tests

Testing

The material properties of SHCC and concrete are tested for the series 2 beams. The testing procedure is similar as for series 1 (Subsection 5.3.3).

Results

The material properties of SHCC are tested on 14 days, 28 days and 55 days of age. At 55 days of age of SHCC, the beams were tested. After 14 days, the SHCC has a compressive strength of 52.83 MPa. Upon ageing, the strength increases to 56.21 MPa at 28 days and 67.49 MPa at 55 days (Table 5.18). The coefficient of variation of this testing series is below 10%. Therefore, the results of the compression test are accepted.

.

Table 5.18: Compression strength properties of SHCC at an age of (a) 14 days, (b) 28 days and (c) 55 days.

Sample	Age (days)	Strength (MPa)	Average (MPa)	Std (MPa)	Coeff. of var. (%)
1	14	54.12	52.83	1.86	3.53
2	14	53.67			
3	14	50.69			

(a)

Sample	Age (days)	Strength (MPa)	Average (MPa)	Std (MPa)	Coeff. of var. (%)
1	28	54.47	56.21	2.47	4.40
2	28	59.04			
3	28	55.12			

(b)

Sample	Age (days)	Strength (MPa)	Average (MPa)	Std (MPa)	Coeff. of var. (%)
1	55	66.80	67.49	0.67	0.99
2	55	68.14			
3	55	67.54			

(c)

The Young's modulus is determined, as explained in subsection 5.3.3. From the 14 days test, a Young's modulus of 20202 MPa is obtained. Upon ageing, the Young's modulus changes to 20872 MPa at 28 days and 20074 MPA at 55 days of age (Table 5.19).

Table 5.19: Young's modulus of SHCC at an age of (a) 14 days, (b) 28 days and (c) 55 days.

Cycle	Age (days)	E (MPa)	$E_{cm,2,3}$ (MPa)
1	14	20202	20479
2	14	20457	
3	14	20500	

(a)

Cycle	Age (days)	E (MPa)	$E_{cm,2,3}$ (MPa)
1	28	20746	20872
2	28	20827	
3	28	20916	

(b)

Cycle	Age (days)	E (MPa)	$E_{cm,2,3}$ (MPa)
1	55	19636	20074
2	55	20041	
3	55	20107	

(c)

The dogbones are tested at an age of 14 days, 28 days and 55 days (Figure 5.92). At an age of 14 days, an average tensile strength of 3.93 MPa is obtained with an average ductility of 1.46%. At an age of 28 days, the average strength increases to 4.30 MPa and the ductility increases to 1.69%. At an age of 55 days, the average strength increases to 5.36 MPa, but the ductility decreases to 0.92% (Table 5.20).

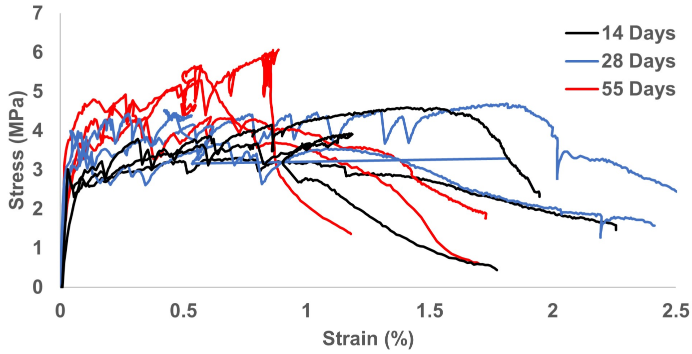

Figure 5.92: Stress-strain curves of tensile tests of SHCC dogbones at an age of 14 days, 28 days and 55 days.

Table 5.20: Overview of results of tensile tests of SHCC dogbones at an age of (a) 14 days, (b) 28 days and (c) 55 days.

Sample	Age (days)	Strength (MPa)	Ductility (%)
1	14	3.30	1.51
2	14	3.92	1.19
3	14	4.59	1.67
Average		**3.93**	**1.46**
Std (MPa)		0.64	0.24
coeff. of var. (%)		16.35	16.74

(a)

Sample	Age (days)	Strength (MPa)	Ductility (%)
1	28	4.67	1.90
2	28	3.7	1.36
3	28	4.52	1.82
Average		**4.30**	**1.69**
Std (MPa)		0.53	0.29
coeff. of var. (%)		12.30	17.21

(b)

Sample	Age (days)	Strength (MPa)	Ductility (%)
1	55	5.66	0.80
2	55	4.35	1.07
3	55	6.07	0.89
Average		**5.36**	**0.92**
Std (MPa)		0.90	0.14
coeff. of var. (%)		16.78	14.94

(c)

The standard deviation and coefficient of variation are both large for the strength and ductility of the dogbones. These deviations can partly be explained by imperfections of the samples, which were found to be large due to a flexible mold used. In addition, the placement of the samples in the setup with glue allowed for misalignment. The crack widths of the 55 days dogbones are investigated with use of DIC measurements. Crack widths are measured over the height of the sample, by creating a section in the middle of the sample's width. The DIC data is verified with the LVDT data (Figure 5.93). After this, the maximum crack widths are presented. The maximum crack width remained below 0.3 mm, before the maximum ductility is reached. Thereby, the material shows its capability of controlling crack widths. In addition, dogbone 3 (S3) shows the smallest maximum crack width and the highest ductility. This can be explained by the ability of sample 3 (S3) to form more cracks, and therefore increase the amount of release of strain energy.

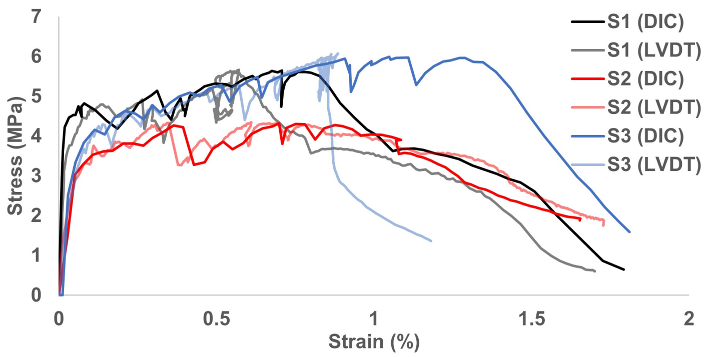

(a)

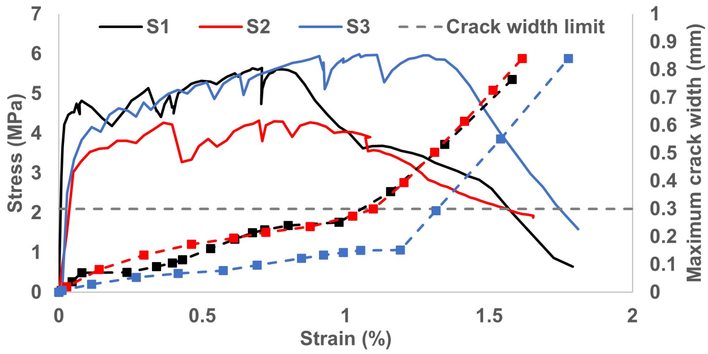

(b)

Figure 5.93: Stress-strain curves (solid) of tensile tests of SHCC dogbones at an age of 55 days, with (a) DIC data (S1 (DIC), S2 (DIC), S3 (DIC)) compared to LVDT data (S1 (LVDT), S2(LVDT), S3(LVDT)) and (b) maximum crack widths-strain curves (dashed).

Concrete is tested for compressive strength at an age of 41 days. At this age, the beams were tested. Compressive strengths of 48.24 MPa (batch 1), 46.00 MPa (batch 2) and 47.62 MPa (batch 3) are found (Table 5.21). The characteristic strength of these batches is determined, as mentioned in subsection 5.3.3. Characteristic strengths of 35.90 MPa (batch 1), 33.86 MPa (batch 2) and 35.33 MPa (batch 3) are found. The mix design was made for C30/37, which has a characteristic compressive cube strength of 37 MPa. Therefore, the designed strength is barely reached. The lower compressive strength of series 2 could be caused by insufficient vibration of the cube samples, as the cubes appeared to be more porous compared to the concrete cubes from series 1. The coefficient of variation is below 10% for all the concrete batches. Therefore, the results of the compression tests are accepted.

Table 5.21: Concrete compressive strength at 41 days of age for (a) batch 1, (b) batch 2 and (c) batch 3.

Sample	Age (days)	Strength (MPa)	Average (MPa)	Std (MPa)	Coeff. of var. (%)
1	44	48.59	48.24	0.31	0.64
2	44	48.01			
3	44	48.12			

(a)

Sample	Age (days)	Strength (MPa)	Average (MPa)	Std (MPa)	Coeff. of var. (%)
1	44	45.46	46.00	1.43	3.12
2	44	44.92			
3	44	47.62			

(b)

Sample	Age (days)	Strength (MPa)	Average (MPa)	Std (MPa)	Coeff. of var. (%)
1	44	50.31	47.62	2.34	4.92
2	44	46.53			
3	44	46.02			

(c)

The Young's modulus of concrete is tested at an age of 41 days (Table 5.22). The average Young's modulus is found to be 35593 MPa (batch 1), 34944 MPa (batch 2) and 35650 MPa (batch 3). Concrete class C30/37 should have an average Young's modulus of 32837 MPa. This Young's modulus is obtained.

Table 5.22: Young's modulus of concrete at an age of 41 days for (a) batch 1, (b) batch 2 and (c) batch 3.

Cycle	Age (days)	E (MPa)	$E_{cm,2,3}$ (MPa)
1	44	33185	35593
2	44	35594	
3	44	35591	

(a)

Cycle	Age (days)	E (MPa)	$E_{cm,2,3}$ (MPa)
1	44	34541	34944
2	44	35077	
3	44	34811	

(b)

Cycle	Age (days)	E (MPa)	$E_{cm,2,3}$ (MPa)
1	44	33430	35650
2	44	35466	
3	44	35834	

(c)

5.5.4. Comparison of experimental results

Comparison of reinforced concrete beams

Upon comparison of the moment-deflection curves of the reinforced concrete beams is found that, increasing the height of the reinforced concrete beam from 200 to 300 mm increases the deformation capacity from 22.12 mm (RC200) to 26.93 mm (RC300) (Figure 5.94). Upon increasing the height from 300 mm to 400 mm, the deformation capacity is not increasing. This can be explained by the failure mechanism that occurred. The RC400 beam failed by rupture of the reinforcement, whereas the RC200 and RC300 beams failed by failure of the compression zone. The ultimate bearing moment is higher for the highest beam. This can be explained by the RC400 beam having the largest internal lever arm. Thereby, the RC400 beam is also the stiffest beam. The moment at which the 0.3 mm crack width is reached, increases upon increasing the height of the beam, as the higher beam is stiffer. Relative to the yielding moment, the moment at which the 0.3 mm crack width is reached, changes insignificantly by increasing the height from 200 mm to 300 mm from 75.51% (RC200) to 78.35% (RC300) and 77.27% (RC400) (Table 5.23). However, the cracking pattern changes upon increasing the height. The RC400 and RC300 beams develops 7 cracks at the bottom. These cracks coalescence into 3 (RC400) and 4

(RC300) propagated cracks. This coalescence of cracks is only limited observed in the R200 beam, where 4 propagated cracks are formed. Therefore, the increase in height of the reinforced concrete beams leads to the development of an effective tensile area in the RC300 and RC400 beam.

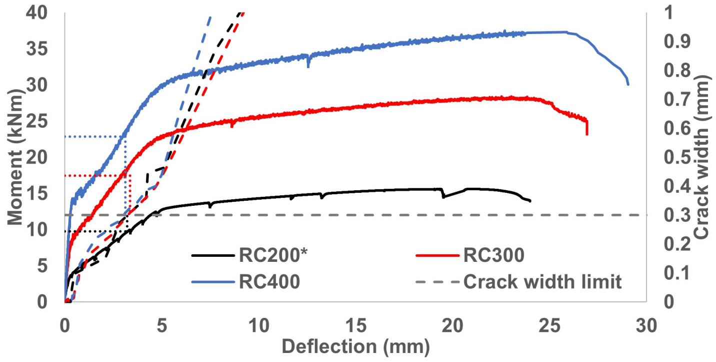

Figure 5.94: Comparison of experimental results for reinforced concrete beams of 200 mm height (RC200), 300 mm height (RC300) and 400 mm height (RC400). *Results retrieved from (Singh, 2019). Solid = load-deflection. Dashed = crack width - deflection.

Table 5.23: Overview of comparison of reinforced concrete beams. *Results retrieved from (Singh, 2019).

Key performance indicators	RC200*	RC300	RC400
Ultimate bearing moment	15.60 kNm	28.41 kNm	37.52 kNm
Maximum deflection	22.12 mm	26.93 mm	26.98 mm
Number of propagated cracks	4	4	3
Moment at 0.3 mm crack width	9.75 kNm	17.45 kNm	22.88 kNm
0.3 mm moment/yield moment	75.51%	78.35%	77.27%

Comparison of hybrid beams

Upon comparison of the moment-deflection curves of the hybrid beams is found that, the bearing moment capacity increases from 19.34 kNm (H200) to 30.89 kNm (H300) and 40.52 kNm (H400). The deformation capacity of the H200 beam is slightly larger, compared to the deformation capacity of the H300 and H400 beam. The H200 beam failed by failure of the compression zone, whereas the H300 and H400 both failed by rebar rupture. The cracking pattern of the hybrid beams differ, which becomes most clear from the number of propagated cracks in concrete. The H200 beam forms 8 propagating cracks in concrete, whereas the H300 forms 4 and the H400 beam forms only 3 propagated concrete cracks (Table 5.24). Also the number of cracks in SHCC decrease, as the H300 beam formed 41 cracks in the SHCC layer, whereas the H400 beam was able to form 35 cracks in the SHCC layer. This difference in cracking pattern leads to a decrease in the moment, at which the 0.3 mm crack width limit is reached relative to the yielding moment. The relative moment at which 0.3 mm crack widths are reached decreases from 109.38% (H200), to 97.19% (H300) and 90.52% (H400). Therefore, the effectiveness of the flexural crack controlling behavior is found to decrease, upon increasing the height of the hybrid beams. In addition, the deflection at which the 0.3 mm crack width limit is reached decreases, upon increasing the height of the hybrid beams (Figure 5.95). Therefore, the H300 and H400 beam reach the crack width limit of 0.3 mm before yielding of the reinforcement occurs. The H200 beam was able to reach the 0.3 mm crack width limit after yielding of the reinforcement. The absolute moment, at which the 0.3 mm crack width limit is reached, increases upon increasing the height of the beam. This is a result of the increased bending stiffness of a beam, upon increasing the height of the beam. Upon comparison of the interface roughness, both the interface of the H300 beam and the H400 beam can be considered as smooth. The interface of H400 (0.334 mm) is smoother compared to the interface of H300 beam (0.517 mm). In addition, the delamination of the concrete-SHCC interface layer showed a delamination of 2.04 mm (H400) and 0.42 mm (H300). Therefore, the delamination of a hybrid beam increases, upon increasing the height from 300 mm to 400 mm. The extent of delamination of the H200 beam has not been reported by (Singh, 2019). Delamination is assumed to occur if the slip exceeds 0.05 mm, as it was found that this slip criteria is the slip limit for a brittle bond (Subsection 2.3.1). The delamination starts at a moment of 18.29 kNm for the H400 beam, whereas the delamination starts at

22.34 kNm for the H300 beam. In addition, the H400 beam has a higher bending stiffness, compared to the H300 beam. The delamination is found to start at a smaller deflection for the H400 beam (2.42 mm), compared to the H300 beam (4.58 mm).

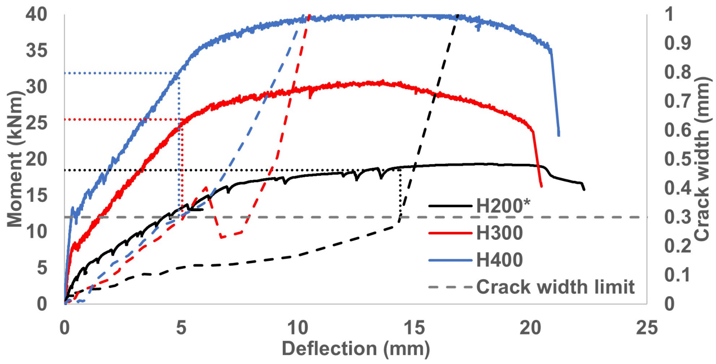

Figure 5.95: Comparison of experimental results of hybrid beams of 200 mm height (H200), 300 mm height (H300) and 400 mm height (H400). *Results retrieved from (Singh, 2019). Solid = load-deflection. Dashed = crack width - deflection.

Table 5.24: Overview of comparison of hybrid beams. *Results retrieved from (Singh, 2019).

Key performance indicators	H200*	H300	H400
Ultimate bearing moment	19.34 kNm	30.89 kNm	40.52 kNm
Maximum deflection	22.30 mm	20.14 mm	20.82 mm
Number of propagated cracks	7	4	3
Moment at 0.3 mm crack width	17.75 kNm	25.47 kNm	31.90 kNm
0.3 mm moment/yield moment	109.38%	97.19%	90.52%

Comparison of reinforced concrete beams and hybrid beams

From comparison of the 200 mm high hybrid beam with the concrete reinforced beam of the same height is found that, the bearing capacity increases from 62.42 kN (RC200) to 77.37 kN (Figure 5.96). This is an increase of 14.95 kN (24%). In addition, the deformation capacity remains similar with 22.12 mm (RC200) and 22.30 mm (H200). The load at which the 0.3 mm crack width limit is reached, is 32 kN higher for the H200 beam (71 kN), compared to the RC200 beam (39 kN). The hybrid beam has a relative higher load at which the 0.3 mm crack width limit is reached (109%), compared to the RC200 beam (76%). The increase in ultimate bearing capacity can be attributed to the tensile capacity of the SHCC. The cracking patterns of the reinforced concrete beam and the hybrid beam differ. The hybrid beam is able to form a uniform distributed cracking pattern in the SHCC layer. Due to this uniform distribution, 8 propagating cracks in the concrete layer are formed. The RC200 beam develops 4 propagating cracks. Therefore, the maximum crack widths in the RC200 beam are larger compared to the H200 beam. Both beams were found to fail by failure of the compression zone.

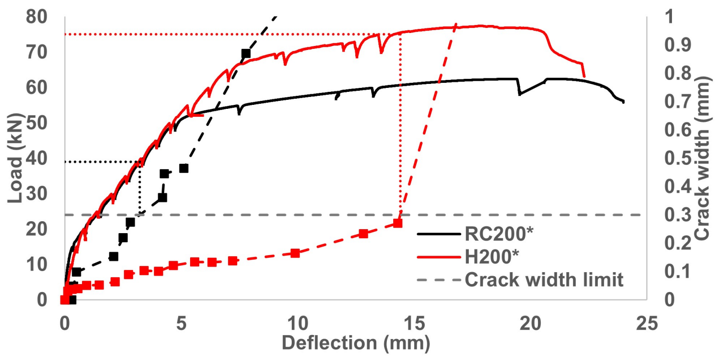

Figure 5.96: Comparison of experimental results of 200 mm high reinforced concrete beam and 200 mm high hybrid beam. *Results retrieved from Singh, 2019). Solid = load-deflection. Dashed = crack width - deflection.

From comparison of the 300 mm high hybrid beams with the concrete reinforced beam of the same height is found that, the bearing capacity increases from 85.87 kN (RC300) to 93.25 kN (H300) and 88.09 kN (H300s) (Figure 5.97). This is an increase of 7.49 kN (8.7%) for the H300 beam and an increase of 2.33 kN (2.7%) for the H300s beam. In addition, the deformation capacity decreases with 6.79 mm (25%) from 26.93 mm (RC300) to 20.14 mm (H300) for the H300 beam. For the H300s beam, the deformation capacity decreases with 2.08 mm (7.7%) from 26.93 mm (RC300) to 24.85 mm (H300s). Therefore, the deformation capacity of the H300s beam is larger, compared to the H300 beam. The H300 beam reaches the 0.3 mm crack width limit at a load of 76.89 kN (97.19% of yielding load), compared to the 52.67 kN (78.35% of yielding load) load of the RC300 beam. This is an increase in load of 24.22 kN. Therefore, the H300 beam shows improved crack controlling behavior by a 24.22 kN load increase, compared to the RC300 beam. The H300s beam reaches the 0.3 mm crack width limit at a load of 40.37 kN (58.55% of yielding load). Thereby, the load at which the crack width limit is reached is decreased by 36.5 kN, compared to the H300 beam. Even more, the load at which the crack width limit is reached is even lower for the H300s, compared to the RC300 beam. Therefore, the crack controlling behavior of the H300s beam is compromised, due to the full delamination of the rebar-SHCC interface. Upon comparison of the cracking patterns is found that, the RC300 beam developed 4 propagated concrete cracks, which is similar to the H300 beam. The H300s beam developed 1 propagated concrete crack. In addition, the H300 beam developed a uniform cracking pattern in the SHCC layer, whereas this is not found for the H300s beam. Upon comparison of the delamination of the hybrid beams is found that, the H300s has a maximum delamination of 0.09 mm, whereas the maximum delamination of the H300 beam is 0.42 mm. This difference in concrete-SHCC interface delamination can be attributed to a lower tensile capacity of the cross section of the H300s beam at central span. The tensile capacity is lower, due to the delamination of the reinforcement in the constant bending moment section. Lastly, the hybrid beams showed failure by rebar rupture, whereas the RC300 beam showed failure in the compression zone.

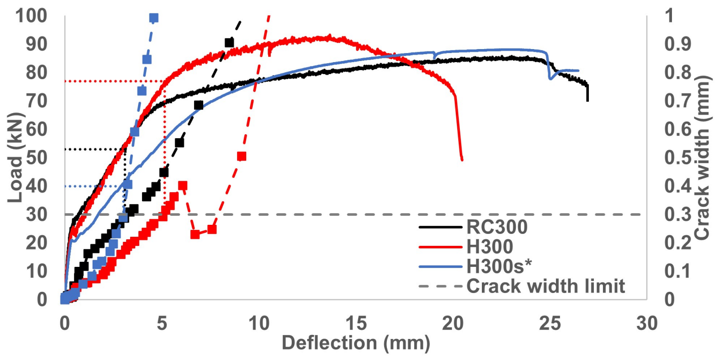

Figure 5.97: Comparison of experimental results of 300 mm high reinforced concrete beam, 300 mm high hybrid beam and 300 mm high hybrid beam with smooth and Vaseline treated reinforcement.*Results retrieved from test series 1. Solid = load-deflection. Dashed = crack width - deflection.

Upon comparison of the 400 mm high hybrid beam with the concrete reinforced beam of the same height is found that, the bearing capacity increases from 82.47 kN to 88.82 kN (Figure 5.98). This is an increase of 6.35 kN (7.7%). In addition, the deformation capacity decreases for the H400 beam with 6.16 mm (23%) from 26.98 mm (RC400) to 20.82 mm (H400). The maximum crack widths are smaller for the hybrid beam, compared to the reinforced concrete beam. The load at which the 0.3 mm crack width limit is reached, is 19.97 kN higher for the H400 beam (69.92 kN) compared to RC400 (50.14 kN). It is found that, the hybrid beam has a relative higher load at which the 0.3 mm crack width limit is reached (91%), compared to the RC400 beam (77%). Both beams were found to fail by failure of the compression zone. Upon comparison of the cracking patterns is found that, the hybrid beam has a uniform distribution of cracks in the SHCC layer with 3 propagated concrete cracks, whereas the reinforced concrete beam developed 3 propagated concrete cracks.

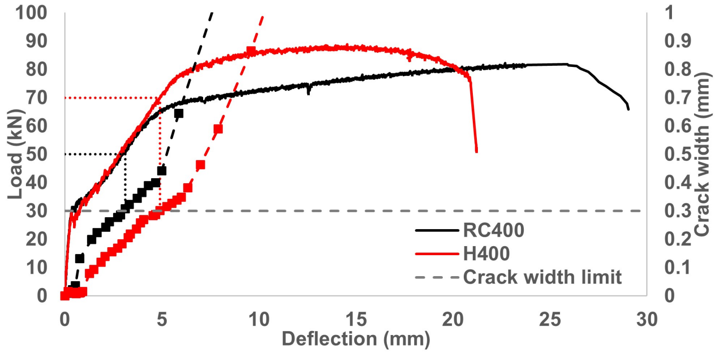

Figure 5.98: Comparison of experimental results of 400 mm high reinforced concrete beam and 400 mm high hybrid beam. Solid = load-deflection. Dashed = crack width - deflection.

An overview of the experimental results is provided (Figure 5.99). A crack width criteria of 0.3 mm is used. This is a common crack width criteria in practise. However, another common crack width criteria is the 0.2 mm crack width limit. This more strict limit is used in environments with a higher risk of corrosion. With use of the 0.2 mm crack width limit, the 200 mm high beams reach the crack width limit at a load of 32 kN (RC200) and 69 kN (H200). This was 39 kN (RC200) and 71 kN (H200) for the 0.3 mm crack width limit. This confirms the crack controlling behavior of the hybrid beam. For the 300 mm high beams, the 0.2 mm crack width limit is reached at a load of 43 kN (RC300), 61 kN (H300) and 37 kN (H300s). Therefore, the H300 beam shows improved crack width controlling behavior, compared to the RC300 beam. The effectiveness of the crack controlling behavior of the SHCC layer decreases for the H300 beam, compared to the H200 beam. For the H300s beam, no improved crack controlling behavior is found compared to the RC300 beam. This was already found with use of the 0.3 mm crack width limit. For the 400 mm high beams the 0.2 mm crack width limit is reached at a load of 37 kN (RC400) and 55 kN (H400). Thereby, the hybrid beam shows improved crack controlling behavior, compared to the reinforced concrete beam, by increasing the load at which the 0.2 mm crack width limit is reached with 18 kN. This is a similar increase as found for the H300 beam. Compared to the H200 beam, this increase in load is smaller, as the H200 beam increases the 0.2 mm crack width load with 37 kN, compared to the RC200 beam.

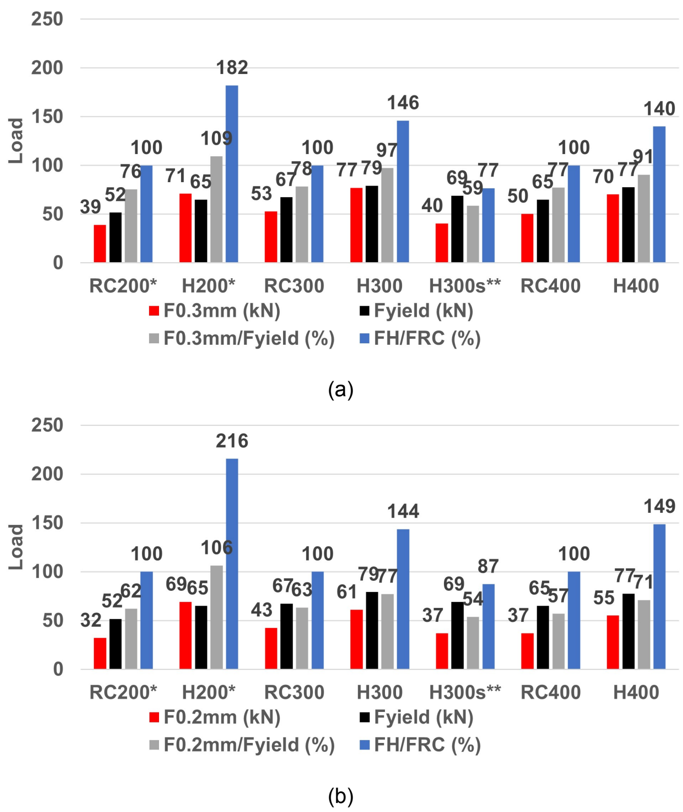

Figure 5.99: Overview of experimental results for (a) 0.3 mm crack width criteria and (b) 0.2 mm crack width criteria. *Results retrieved from Singh, 2019). **Results from test series 1. F0.3mm = load when 0.3 mm crack width limit is reached. F0.2mm = load when 0.2 mm crack width limit is reached. Fyield = load when yielding of reinforcement is reached. FH = load of hybrid beam when reaching crack width limit. FRC = load of reinforced concrete beam when reaching crack width limit.

5.6. Conclusions

Based on the performed experimental study, the following can be concluded:

- From 2D DIC data it was obvious that out of plane displacement occurred in the samples, which could also be quantified. In addition, from the out of plane displacements it is possible to determine if the out of plane displacements are correlated with the force. This method has been verified by out of plane measurements with a LVDT.
- The experiments of series 1 are found to be compromised by out of plane bending. The 2D DIC data is used to determine this. Upon analysing the test setup is found that, the testing setup used in series 1 has too low stiffness. Therefore, a stiffer testing setup is used in test series 2. This reduced the out of plane displacements significantly.
- Out of plane displacements are part of the fracturing process of both reinforced concrete beams and hybrid beams. The out of plane displacements are believed to be caused by deformation of the beams, following the path of least resistance. The out of plane displacement for the reinforced concrete beams is limited, up to reaching the ultimate load. Whereas, the hybrid beams show larger out of plane displacements. This difference between reinforced concrete beams and hybrid beams is believed to be caused by the cracking pattern of the hybrid beams, as the hybrid beams form many cracks reducing the stiffness of the cross section. Further research is needed to confirm the effect of fracturing on out of plane bending. It is important to quantify the out of plane displacement, as it influences the 2D DIC measurements. Therefore, it is recommended to include out of plane displacements in the analysis of experimental results.
- The tension tests for SHCC showed large variations in the results of the tested samples. From the tensile tests is found that, the strain capacity decreases over time, but the material is still able to limit crack widths at 55 days of age close to failure. The high variability in material results for the tensile SHCC tests can be explained by the flexible molds used to cast and the difficulty in placing the samples in the testing setup. In addition, it is suggested that the fiber dispersion of SHCC is also of influence. Further research is needed to confirm this suggestion.
- Upon increasing the height of the reinforced concrete beams from 200 mm to 300 and 400 mm, the ultimate bearing moment increases from 15.60 kNm to 28.41 kNm and 37.52 kNm. The deformation capacity of the 300 mm (26.93 mm) and 400 mm (26.98 mm) high beams were similar, whereas the deformation capacity of the RC200 beam is lower (22.12 mm). The number of propagated cracks decreased from 4 (RC200 & RC300) to 3 (RC400). In addition, the RC300 and RC400 beam developed an effective tensile area, whereas this is not observed for the RC200 beam. The load at which the 0.3 mm crack width limit is reached, relative to the yielding load, is found to not alter significantly, upon increasing the height. This is also found for the 0.2 mm crack width limit. Lastly, it is found that the RC200 and the RC300 beam fail in the compression zone, whereas the RC400 beam failed by rupture of the reinforcement.
- Upon increasing the height of the hybrid beams from 200 mm to 300 and 400 mm, the ultimate bearing moment increases from 19.34 kNm to 30.89 kNm and 40.52 kNm. The deformation capacity of the 300 mm (20.14 mm) and 400 mm (20.82 mm) high beams were similar, whereas the deformation capacity of the H200 beam is larger (22.30 mm). The number of propagated cracks in concrete decreased from 7 (H200) to 4 (H300) and 3 (H400). For the H300 and H400 beam, it is found that, concrete cracks propagate to the SHCC layer, leading to opening of the SHCC cracks. The load at which the 0.3 mm crack width limit is reached, relative to the yielding load, is found to decrease from 109% (H200), to 97% (H300) and 91% (H400). Thereby, only the H200 beam is able to control the cracks up to yielding. The H300 beam is still close to the yielding limit, whereas the H400 beam shows a clear decrease in the crack controlling behavior. The same conclusion can be drawn from the 0.2 mm crack width limit. The delamination of the concrete-SHCC interface is found to increase, upon increasing the height. As it is uncertain if the delamination is affecting the crack controlling behavior of the hybrid beams, it is recommended to study the effect of the concrete-SHCC interface roughness for the H400 beam. The effect of a stronger concrete-SHCC interface is numerically studied in chapter 6. Lastly, the H200 beam is found to fail in the compression zone, whereas the H300 and the H400 beam are found to fail by rupture of the reinforcement.

- Upon comparison of the hybrid beams with the reinforced concrete beams is found that, the hybrid beams show an increased bearing capacity. The increased bearing capacity can be attributed to the tensile capacity of SHCC. The increase in capacity decreases from 14.95 kN (H200), 7.49 kN (H300) to 6.35 kN (H400), upon increasing the height of the beam. This decrease makes sense, as the relative contribution of SHCC decreases, upon increasing the height. In addition, the deformation capacity is similar for the RC200 and H200 beam, whereas the deformation capacity of the H300 (20.14 mm) and H400 (20.82 mm) beam is decreased, compared to the bearing capacity of the RC300 (26.93 mm) and RC400 (26.98 mm) beam. The crack controlling behavior of the hybrid beams is found to decrease, upon increasing the height of the beam. The increase in load, compared to the reinforced concrete beam of the same height, at which the 0.3 mm crack width criteria is reached for the H200 beam is 32 kN (182%). Whereas, this increase in load is 24 kN (146%) for the H300 beam and 20 kN (140%) for the H400 beam. Similarly is found that, the increase in load at which the 0.2 mm crack width limit is reached decreases from 37 kN (H200) to 18 kN (H300) and 18 kN (H400).
- The effect of the delaminated reinforcement bars on the crack controlling behavior of the hybrid beam (H300s) is found to compromise the crack controlling behavior of the SHCC layer. The 0.3 mm crack width limit is reached at a load of 40 kN, whereas the 0.2 mm crack width limit is reached at a load of 37 kN. Thereby, the reinforced concrete beam is found to be able to control the crack widths better. The H300s formed a single propagated crack in concrete and only a limited amount of cracks in the SHCC layer. Only small delamination (0.09 mm) of the concrete-SHCC is found, whereas the H300 beam showed larger delamination (0.42 mm). The ultimate bearing capacity is found to be unaffected by the smooth reinforcement. Lastly, the deformation capacity is found to increase for the H300s beam to 24.85 mm, compared the H300 beam (20.14 mm).

6

Comparison and Discussion

6.1. Comparison of numerical, experimental and analytical results

The numerical models, made in chapter 4, are compared with the experimental results of chapter 5. The differences between the results are discussed. These comparisons of results are made, to study the ability of the Delft Lattice model in simulating the structural behavior of the beams. In addition, the results are compared with analytical calculations from the multi-layer model (Subsection 2.1.8). The material properties used for these calculations are presented in table 6.1.

Table 6.1: Material properties used for analytical calculations.

Property	Concrete		SHCC		Steel	
Segment	1	2	1	2	1	2
f_c (MPa)	-50	-50	-45	-45	-550	-600
ε_c (%)	-0.152	-0.35	-0.243	-0.35	-0.275	-5.00
f_t (MPa)	2.90	-	3.00	5.00	550	600
ε_t (%)	0.00883	-	0.0162	2.50	0.275	5.00
E (MPa)	32837	-	18500	-	200000	-

6.1.1. Reinforced concrete beam of 200 mm height

For the 200 mm high concrete reinforced beam, the experimental results from (Singh, 2019) are used. The comparison of the experimental, numerical and analytical results are presented in figure 6.1. The key-performance indicators are provided in table 6.2.

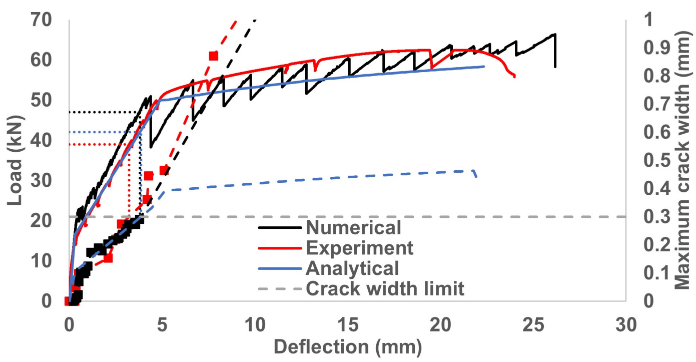

Figure 6.1: Comparison of numerical, experimental and analytical results for the 200 mm high reinforced concrete beam. Experimental results retrieved from (Singh, 2019). Solid = load-deflection. Dashed = crack width - deflection.

Table 6.2: Overview of comparison of results for the RC200 beam. Experimental results retrieved from (Singh, 2019).

Key performance indicators	Experimental	Numerical	Analytical
Ultimate load	62.42 kN	66.36 kN	58.31 kN
Maximum deflection	22.12 mm	27.97 mm	22.32 mm
Number of propagated cracks	4	7	-
Load at 0.3 mm crack width	38.96 kN	47.01 kN	42.49 kN
0.3 mm load/yield load	75.51%	93.18%	85.13%

It is found that, the numerical model is simulating a similar load-deflection curve compared to the experiment. In addition, the maximum crack width - deflection curve is also similar to the experiment. The load at which the 0.3 mm crack width limit is reached is higher for the numerical model, compared to the experiments. The deformation capacity of the numerical model is slightly larger compared to the experiment. The overestimation of the load, at which the 0.3 mm crack width limit is reached, and the overestimation of the deformation capacity can be explained by the cracking pattern. The numerical model is developing 7 concrete cracks, which propagate to the compression zone of the beam. Whereas, in the experiments 4 propagated cracks are observed (Figure 6.2). Therefore, the numerical model is limiting the maximum crack widths, as more cracks are developed. In addition, the numerical model releases more strain energy, as a result of the increased number of formed cracks. This increased release of strain energy leads to a higher deformation capacity, compared to the experiment. The formation of too many cracks in the numerical model can be explained by a too strong concrete-reinforcement bond. A weaker bond results in a longer transferring length of the steel-concrete stress transfer. This leads to larger crack spacing, and therefore less cracks are developed. Lastly, the numerical model failed in the compression zone, which was also found to be the case in the experiment. From the analytical model similar results are obtained, compared to the numerical model. The difference in ultimate bearing capacity of the analytical model, compared to the experiments and numerical model, can be explained by the bi-linear material input of the analytical model and by the simplification of the load-deflection curve into linear segments. The deflection at which the crack width limit is reached in the analytical calculation, is similar to the numerical model. The crack width calculation of the Eurocode is limited to yielding of the reinforcement, as after yielding only small increments in the steel stress occur. Therefore, the crack widths, determined by the analytical calculations, increase insignificantly after reaching the yielding strength of the steel. The analytical model is able to predict the yielding load as found in the experiments. Similarly, the numerical model is also able to simulate the yielding load.

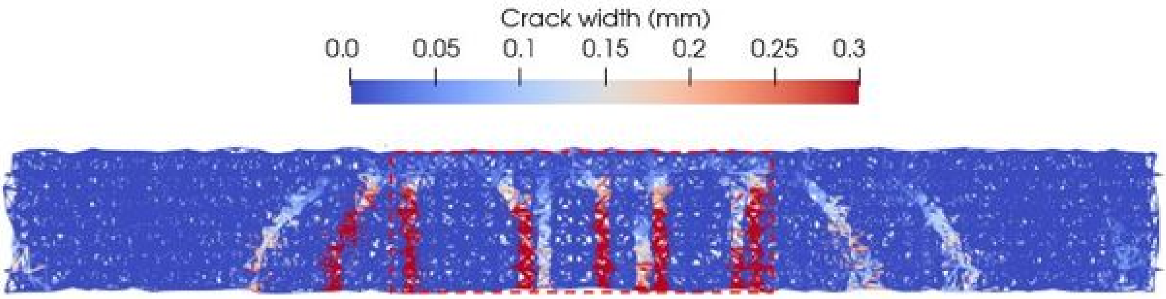

(a)

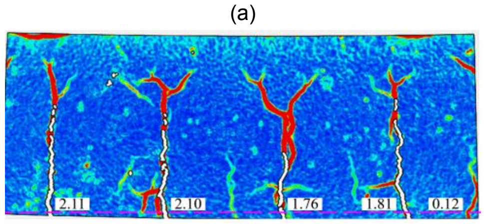

(b)

Figure 6.2: Final cracking pattern of the RC200 beam from (a) numerical study and (b) experimental study. Experimental results retrieved from (Singh, 2019).

6.1.2. Hybrid R/SHCC beam of 200 mm height

For the 200 mm high hybrid beam, the experimental results from (Singh, 2019) are used. The comparison of the experimental, numerical and analytical results are presented in figure 6.3. The analytical calculations are an extension of the reinforced concrete model by providing the SHCC layer a tensile capacity. This extended model contains multiple simplifications, among which the concrete-SHCC interface is considered rigid. The key-performance indicators are provided in table 6.3.

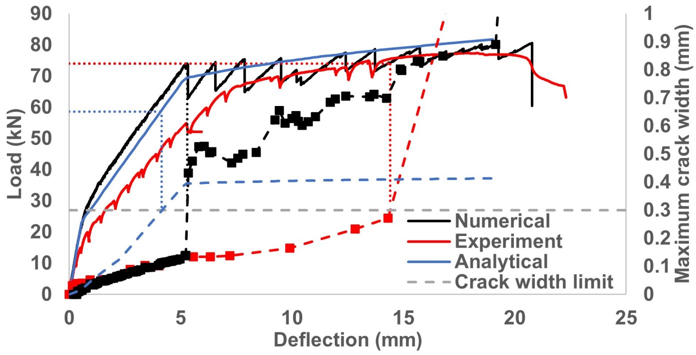

Figure 6.3: Comparison of numerical, experimental and analytical results for the 200 mm high hybrid beam. Experimental results retrieved from (Singh, 2019). Solid = load-deflection. Dashed = crack width - deflection.

Table 6.3: Overview of comparison of results for the H200 beam. Experimental results retrieved from (Singh, 2019).

Key performance indicators	Experimental	Numerical	Analytical
Ultimate load	77.37 kN	80.61 kN	83.25 kN
Maximum deflection	20.56 mm	20.77 mm	21.57 mm
Number of propagated cracks	7	7	-
Load at 0.3 mm crack width	71.24 kN	73.38 kN	58.63 kN
0.3 mm load/yield load	109.38%	99.73%	84.53%

It is found that, the numerical model shows a slightly increased ultimate bearing capacity. Additionally, the deformation capacity of the numerical model is similar as observed in the experiments. The yielding load is significantly overestimated in both the numerical model and the analytical model. This can be explained by the tensile capacity of the SHCC elements, which is overestimated by both the numerical model (2.35%) and the analytical model (2.5%), compared to the experimental results (0.92%). The numerical load-deflection curve is very similar to the analytical calculations. The analytical model is inaccurate in predicting the load at which 0.3 mm crack widths are found. This can be explained by the way the crack widths are calculated. The multi-layer model is including the tensile capacity of SHCC, and thereby the SHCC is able to share the tensile stress with the steel. This effect is only included in the steel stress and not in the average strain difference between steel and SHCC. As SHCC has a much higher ductility compared to conventional concrete, the difference in strain between steel and SHCC can be expected to be smaller. However, the maximum crack spacing, used in the crack width calculation, is not altered, whereas SHCC is able to form a cracking pattern with much smaller crack spacing compared to conventional concrete. Upon comparison of the final cracking patterns of the numerical model and the experimental results, it is found that, the numerical model is able to develop 7 concrete cracks, which is also found in the experiments (Figure 6.4). The numerical model is limited in the ability of forming SHCC cracks, due to the used mesh size. Therefore, the minimum crack spacing is 25 mm, whereas in the experiments a smaller crack spacing is found. In addition, upon yielding of the reinforcement in the numerical model, a sudden jump in the maximum crack width is observed. This can be explained by the failure of a SHCC element in the final material segment upon reloading of the lattice. This leads to removal of SHCC elements from the lattice. Whereas, in reinforced concrete beams, the concrete elements were already removed from the lattice before yielding. Another aspect that should be mentioned is, the numerical model is made with a 75 mm high SHCC layer, whereas in the experiments this was 70 mm. The effect of this higher SHCC layer in the numerical model is found to be insignificant for the ultimate load. Lastly, the numerical model is found to fail in the compression zone, which was also found in the experiments.

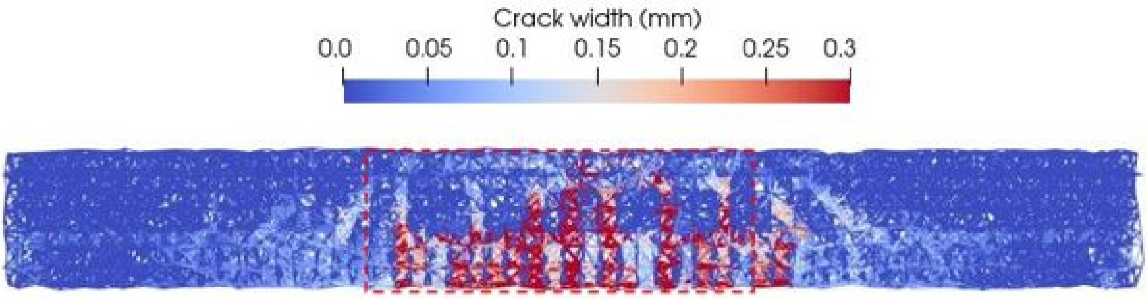

(a)

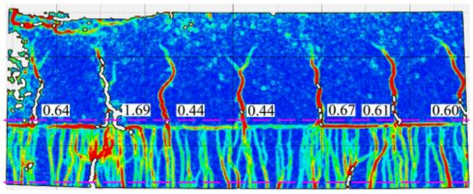

(b)

Figure 6.4: Final cracking pattern of the H200 beam from (a) numerical study and (b) experimental study. Experimental results retrieved from (Singh, 2019).

6.1.3. Reinforced concrete beam of 300 mm height

For the 300 mm high concrete reinforced beam, the experimental results from chapter 5 are used. The numerical results are obtained in chapter 4. The comparison of the experimental, numerical and analytical results are presented in figure 6.5. The key-performance indicators are provided in table 6.4.

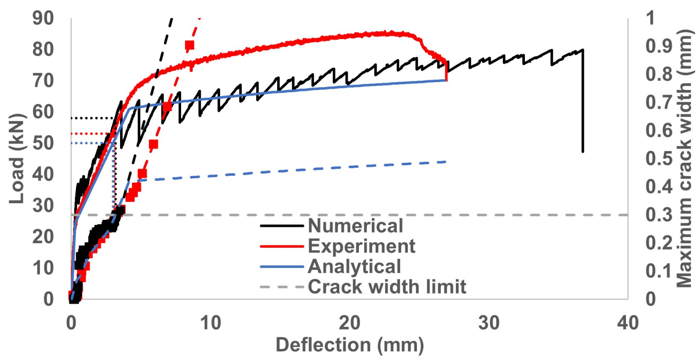

Figure 6.5: Comparison of numerical, experimental and analytical results for the 300 mm high reinforced concrete beam. Solid = load - deflection. Dashed = crack width - deflection.

Table 6.4: Overview of comparison of results for the RC300 beam.

Key performance indicators	**Experimental**	**Numerical**	**Analytical**
Ultimate load	85.76 kN	79.88 kN	70.07 kN
Maximum deflection	26.93 mm	36.75 mm	26.83 mm
Number of propagated cracks	4	5	-
Load at 0.3 mm crack width	52.67 kN	58.45 kN	50.13 kN
0.3 mm load/yield load	78.35%	92.25%	81.93%

Upon comparison of the numerical and experimental results, it is found that, the numerical model has a lower ultimate bearing capacity. The deformation capacity found in the numerical model is significantly larger ,compared to the deformation capacity found in the experiments. These differences can partly be explained by the failure mechanism of the numerical model. As the numerical model is found to fail by rupture of the reinforcement, whereas in the experiments the compression zone failed. This difference in failure can be attributed to the steel properties modelled, as in the numerical model the reinforcement steel is modelled with a bi-linear stress-strain curve, which is a simplification of the reality. In addition, the concrete elements are simplified to elastic-brittle elements, which is a simplification to reality. The ultimate steel strength used in the numerical model is 550 MPa, which can be higher in the experiments. Another reason for the increased deformation capacity is the number of cracks formed in the numerical model. The numerical model developed 8 concrete cracks at the bottom of which 5 propagated. In the experiments, it is found that, the beam develops 7 concrete cracks of which 4 propagate to the compression zone (Figure 6.6). Therefore, the strain release in the numerical model is higher, leading to a higher deformation capacity. This also explains the higher load at which 0.3 mm crack widths are found in the numerical model. Similar as for the RC200 beam, this means that the rebar-concrete interface is assumed too strong in the numerical model. The analytical model predicts a similar yielding load, as found in the numerical model. In addition, the deflection at which the 0.3 mm crack width limit is reached is similar for the analytical calculations, the numerical model and the experimental results.

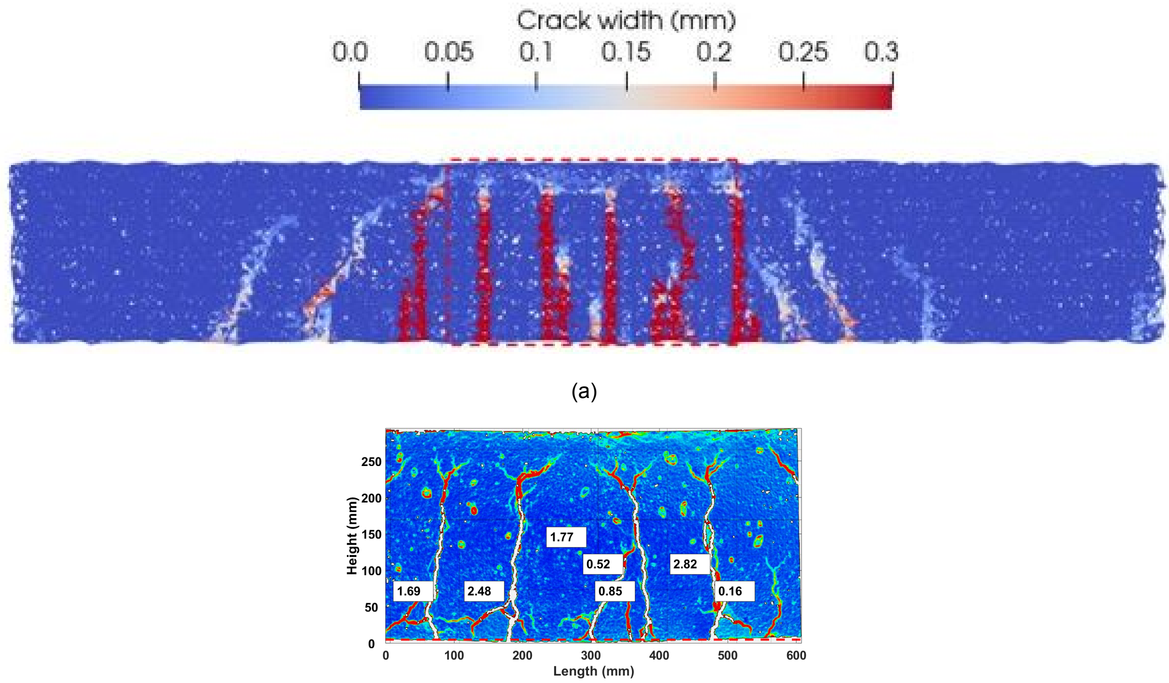

(a)

(b)

Figure 6.6: Final cracking pattern of the RC300 beam from (a) numerical study and (b) experimental results.

6.1.4. Hybrid R/SHCC beam of 300 mm height

For the 300 mm high hybrid beam, the experimental results from chapter 5 are used. The numerical results are obtained in chapter 4. The comparison of the experimental, numerical and analytical results are presented in figure 6.7. The key-performance indicators are provided in table 6.5.

Table 6.5: Overview of comparison of results for the H300 beam.

Key performance indicators	Experimental	Numerical	Analytical
Ultimate load	93.25 kN	99.12 kN	104.96 kN
Maximum deflection	20.14 mm	19.47 mm	22.83 mm
Number of propagated cracks	4	4	-
Load at 0.3 mm crack width	76.89 kN	87.82 kN	71.17 kN
0.3 mm load/yield load	97.19%	99.21%	83.33%

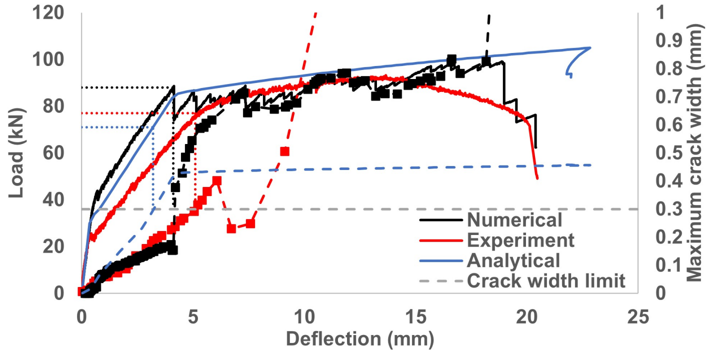

Figure 6.7: Comparison of numerical, experimental and analytical results for the 300 mm high hybrid beam. Solid = load - deflection. Dashed = crack width - deflection.

Upon comparison of the numerical and experimental results, it is found that, the numerical model overestimates the ultimate capacity. The ductility of the numerical model is similar to the found ductility in the experiments. The yielding occurs at a lower deflection in both the analytical model and the numerical model, compared to the experiment. The final cracking pattern of the numerical model shows 4 propagated cracks in concrete, which is similar to the 4 propagated concrete cracks found in the experiments (see figure 6.8). Thereby, the same differences are found between the numerical results and the experimental results, as were found for the H200 beam. The analytical results show a too low load at which 0.3 mm crack width is reached. The ultimate load predicted by the analytical calculations is similar as found in the experiments. Thereby, similar differences between the analytical model and the experimental observations are found, as were found for the H200 beam.

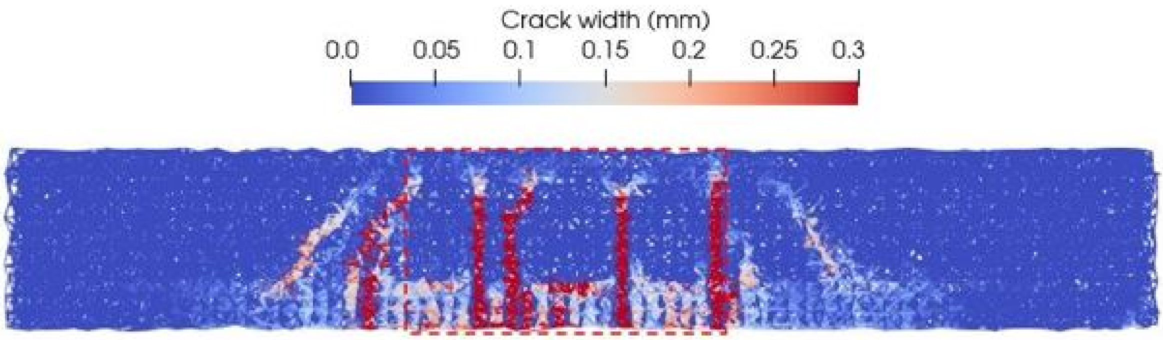

(a)

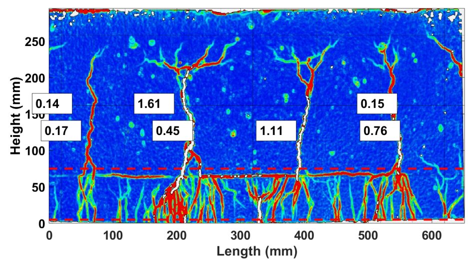

(b)

Figure 6.8: Final cracking pattern of the H300 beam from (a) numerical study and (b) experimental study.

6.1.5. Hybrid R/SHCC beam of 300 mm height with plain and Vaseline treated longitudinal reinforcement bars

For the 300 mm high hybrid beam with smooth and Vaseline treated reinforcement bars, the experimental results from chapter 5 are used. The numerical results are obtained in chapter 4. No analytical results are present, as the analytical model does not consider the rebar-SHCC bond directly. The comparison of the experimental and numerical results are presented in figure 6.9. The key-performance indicators are provided in table 6.6.

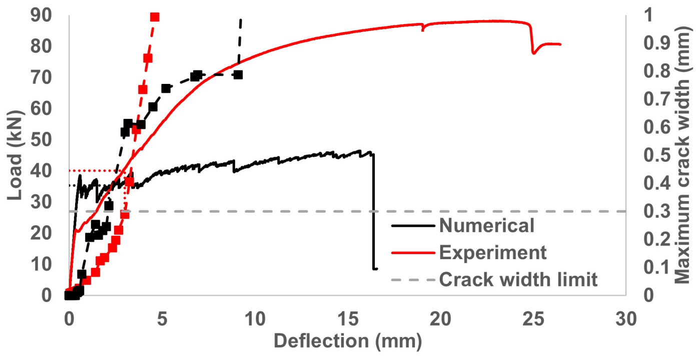

Figure 6.9: Comparison of numerical and experimental results for the 300 mm high hybrid beam with smooth and Vaseline treated reinforcement bars. Solid = load - deflection. Dashed = crack width - deflection.

Table 6.6: Overview of comparison of results for the H300s beam.

Key performance indicators	Experimental	Numerical
Ultimate load	88.09 kN	46.38 kN
Maximum deflection	24.85 mm	16.40 mm
Number of propagated cracks	1	1
Load at 0.3 mm crack width	40.37 kN	35.32 kN
0.3 mm load/yield load	58.55%	-

Upon comparison of the numerical and experimental results, it is found that, the numerical model underestimates the ultimate capacity. The numerical model is slightly underestimating the ductility found in the experiments. The maximum crack widths of the numerical model are overestimating the maximum crack widths found in the experiments. These differences can be explained by the rebar-SHCC bond used as input for the numerical model. As the rebar-SHCC bond is very weak for the full length of the longitudinal reinforcement in the numerical model, whereas in the experiments only the central 700 mm is treated with Vaseline. Therefore, the experiments show the structural behavior of a reinforced element, whereas the structural behavior of the numerical model can be considered unreinforced. The bearing capacity of an unreinforced 300 mm high hybrid beam can be determined analytically by:

$$F_{ult} = \frac{f_{t,SHCC} * b * h_{SHCC} * 0.9 * (h - 0.5h_{SHCC})}{0.5a} \tag{6.1}$$

In this formula, $f_{t,SHCC}$ is the tensile strength of SHCC, b is the width of the beam, h_{SHCC} is the thickness of the SHCC layer, h is the height of the beam and a is length of the shear span. This leads to an analytical bearing capacity of 44.55 kN, which is very similar to the found ultimate capacity found in the numerical model (46.38 kN). Nevertheless, the cracking patterns are found to be similar for the numerical model and the experiment (Figure 6.10). Both cracking patterns show very limited cracks developed in the SHCC layer and only a single crack developed in the concrete layer. Thereby, the numerical model is found to be able to simulate the structural behavior of the smooth and Vaseline treated reinforcement bars. A better match in the load-deflection curves of the experiments and the numerical simulation should be obtained by providing only the central region of the longitudinal reinforcement bar with a weak bond in the numerical model.

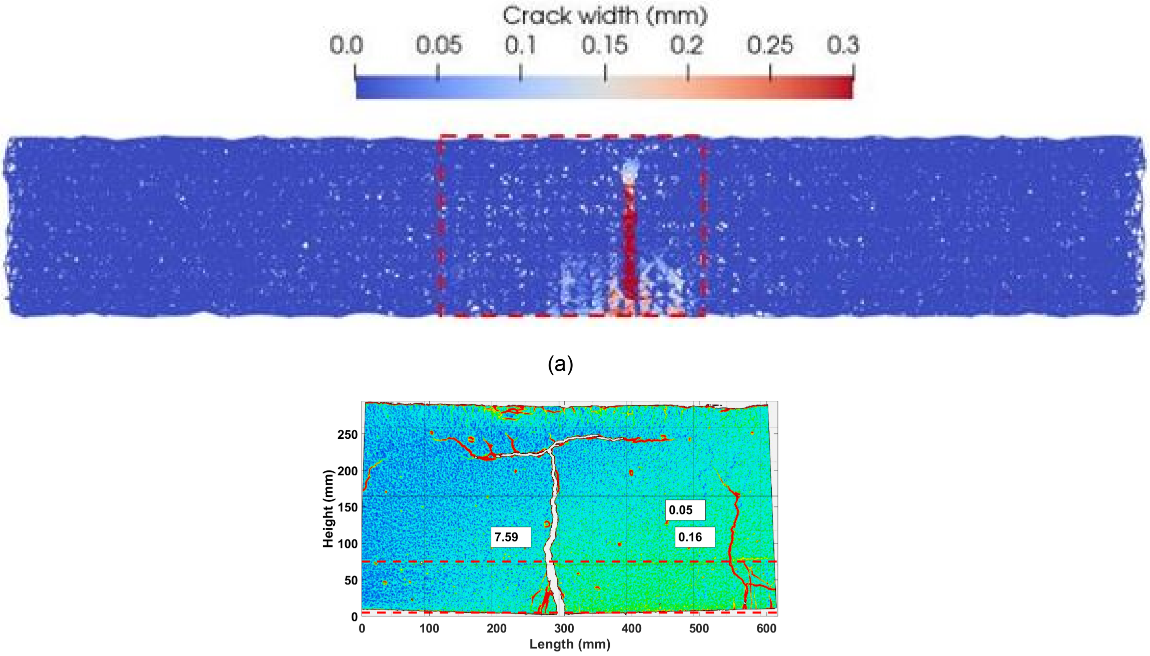

(a)

(b)

Figure 6.10: Final cracking pattern of the H300s beam from (a) numerical study and (b) experimental study.

6.1.6. Reinforced concrete beam of 400 mm height

For the 400 mm high reinforced concrete beam, the experimental results from chapter 5 are used. The numerical results are obtained in chapter 4. The comparison of the experimental, numerical and analytical results are presented in figure 6.11. The key-performance indicators are provided in table 6.7.

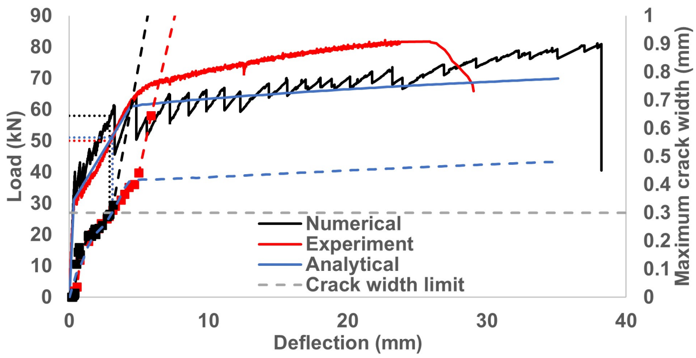

Figure 6.11: Comparison of numerical and experimental results for the 400 mm high reinforced concrete beam. Solid = load - deflection. Dashed = crack width - deflection.

Table 6.7: Overview of comparison of results for the RC400 beam.

Key performance indicators	Experimental	Numerical	Analytical
Ultimate load	82.47 kN	80.78 kN	71.14 kN
Maximum deflection	26.98 mm	38.18 mm	35.12 mm
Number of propagated cracks	3	4	-
Load at 0.3 mm crack width	50.41 kN	57.59 kN	51.20 kN
0.3 mm load/yield load	77.27%	94.12%	83.95%

Upon comparison of the numerical and experimental results, it is found that, the numerical model shows a lower ultimate capacity. The deformation capacity computed in the numerical model is significantly larger compared to the deformation capacity found in the experiment. The cracking pattern of the numerical model shows 2 propagated cracks in the concrete layer, whereas in the experiment, it is found that, the beam develops 3 (Figure 6.12). Thereby, the differences found between the numerical model and the experimental observations are similar as found for the RC200 and RC300 beam. However, it is also found that, the numerical models of the reinforced concrete beams show the same trend in the cracking pattern compared to the experiments, upon increasing the height of the beams. As for the numerical models it is found that upon increasing the height of the numerical model, the number of propagated cracks reduce, while the load, at which the 0.3 mm crack width is reached, relative to the yielding load does not change significantly. Similarly, the analytical calculations show that upon increasing the height the relative load, at which the 0.3 mm crack width limit is reached is not changed.

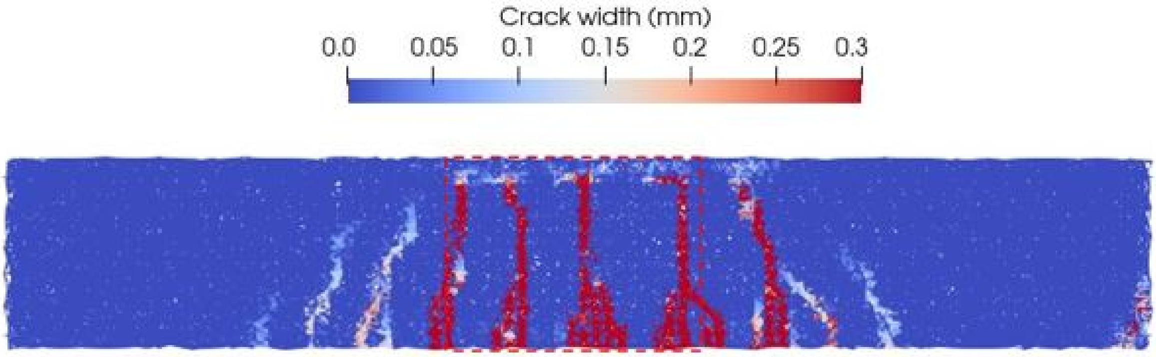

(a)

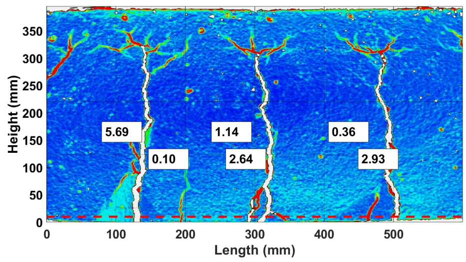

(b)

Figure 6.12: Final cracking pattern of the RC400 beam from (a) numerical study and (b) experimental study.

6.1.7. Hybrid R/SHCC beam of 400 mm height

For the 400 mm high hybrid beam, the experimental results from chapter 5 are used. The numerical results are obtained in chapter 4. The comparison of the experimental, numerical and analytical results are presented in figure 6.13. The key-performance indicators are provided in table 6.8.

Table 6.8: Overview of comparison of results for the H400 beam.

Key performance indicators	Experimental	Numerical	Analytical
Ultimate load	88.82 kN	103.70 kN	104.98 kN
Maximum deflection	20.82 mm	33.63 mm	24.01 mm
Number of propagated cracks	3	2	-
Load at 0.3 mm crack width	70.11 kN	88.40 kN	74.18 kN
0.3 mm load/yield load	90.52%	98.88%	86.37%

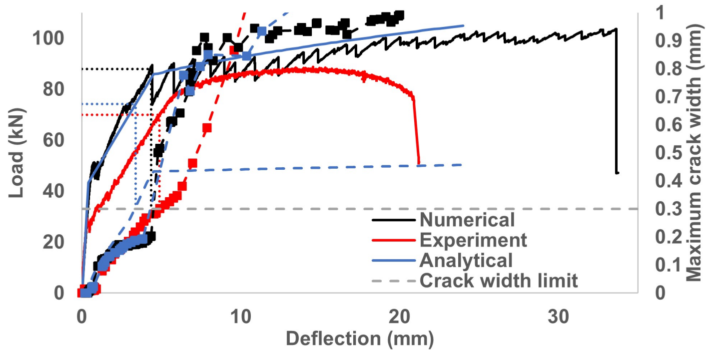

Figure 6.13: Comparison of numerical and experimental results for the 400 mm high hybrid beam. Solid = load - deflection. Dashed = Crack width - deflection.

Upon comparison of the numerical and experimental results, it is found that, the numerical model shows a larger ultimate capacity. The numerical model is also found to model a significantly larger deformation capacity. Additionally, the bending stiffness after crack initiation is higher for the numerical model, compared to what is found in the experiment. The higher deformation capacity of the numerical model can be explained by the number of cracks formed directly above the SHCC-concrete interface. The numerical model shows 5 concrete cracks above the interface, which branch into 2 propagated cracks. Whereas, the experiment shows only 4 concrete cracks with a width larger than 0.3 mm (Figure 6.14). Therefore, the numerical model is able to release more strain energy leading to a higher deformation capacity of the model. The analytical model is overestimating the deformation capacity found in the experiments. Additionally, the ultimate capacity of the analytical model is similar to the numerical model. Thereby, the differences between the experimental results and the numerical and analytical results are similar as found for the H300 beam. The numerical models of the hybrid beams show a decrease in the number of propagated concrete cracks upon increasing the height. This is also found in the experiments. Additionally, the load at which the 0.3 mm crack width limit is reached, relative to the yielding load, reduces in the numerical and analytical models upon increasing the height. This is also found in the experiments. Therefore, it is found that, the numerical models are able to predict the structural trends of the hybrid beams.

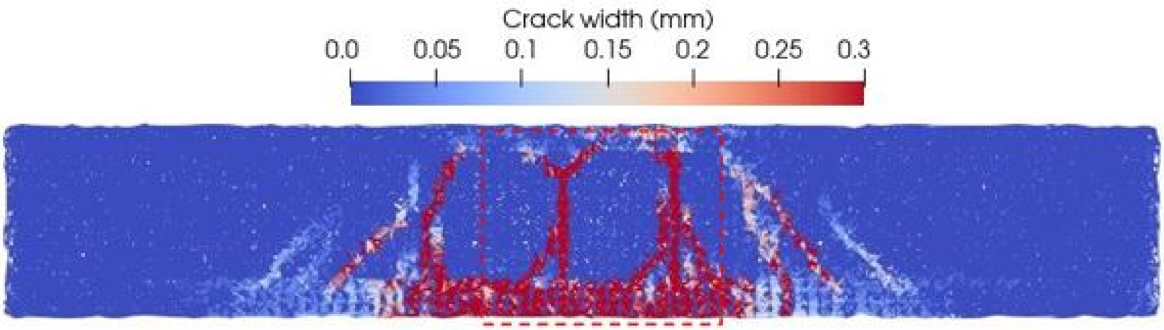

(b)

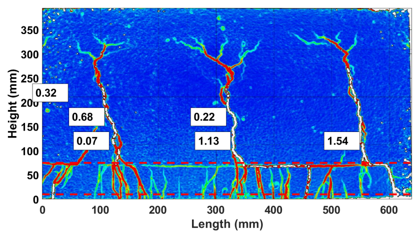

(a)

Figure 6.14: Final cracking pattern of the H400 beam from (a) numerical study and (b) experimental study.

6.2. Comparison of material properties

In order to make the numerical beam models, prism models have been made to calibrate the material properties. In this subsection these modelled material properties are compared with the material properties found from experimental material tests.

6.2.1. Concrete

Firstly, the concrete properties from the experiments are compared with the numerically modelled properties (Table 6.9). A distinction is made between results obtained during this study (Chapter 5) and a previous study (Singh, 2019). This distinction is made as the experimental results of RC200 and H200 are from this previous study. No distinction in the modelling of the material properties has been made for the different experimental studies. Not all properties, used as material input in the numerical model have been tested in the experimental studies. These untested properties are found in the Eurocode and indicated with: *.

Table 6.9: Overview of comparison of numerical and experimental results for concrete properties. *Properties obtained from (*Eurocode 2: Design of concrete structures*, 2004).

Property	Numerical	Experimental Singh	Experimental Series 2
f_{cm} (MPa)	39.83	49.4 (± 5.3)	43.0 (± 1.2)
$f_{t,ult}$ (MPa)	3.00	2.90*	2.90*
E_{cm} (Mpa)	32320	32837*	35396 (± 392)

From comparison of the numerical results and the experimental results, it is found that, the modelled mean compressive concrete strength is lower than found in both experimental studies. The higher compressive strength found in experiments is however not expected to affect the bearing capacity of the RC300 and RC400 beam, as these beams failed by rupture of the reinforcement in the numerical simulations. Young's modulus tests have not been performed by (Singh, 2019), the Young's modulus is taken from Eurocode for C30/37. This results in a similar Young's modulus as modelled. The Young's modulus found in chapter 5 is slightly higher than modelled. This is not found to be of significant influence. Lastly, The experimental studies did not test the tensile strength of concrete. Therefore, the tensile strength for concrete class C30/37 is used from the Eurocode. The tensile strength modelled is similar as found in Eurocode.

6.2.2. SHCC

The properties of SHCC from the experiments are compared with the numerically modelled properties (Table 6.10). Not all properties have been tested in the experimental studies. The untested properties are retrieved from (Mustafa et al., 2022) and are indicated with: *. The experimental results of the SHCC dogbones at 55 days of age (chapter 5 series 2) are also presented (Figure 6.15).

Table 6.10: Overview of comparison of numerical and experimental results for SHCC properties. *Properties obtained from (Mustafa et al., 2022).

Property	Numerical	Experimental Singh	Experimental Series 2
f_{cm} (MPa)	44.58	49.3 (± 5.3)	61.42 (± 0.7)
$f_{t,ult}$ (MPa)	5.02	4.50*	5.36 (± 0.9)
E_{cm} (Mpa)	18332	18500*	20074 (± 47)
Ultimate strain (%)	2.35	-	0.92 (± 0.1)

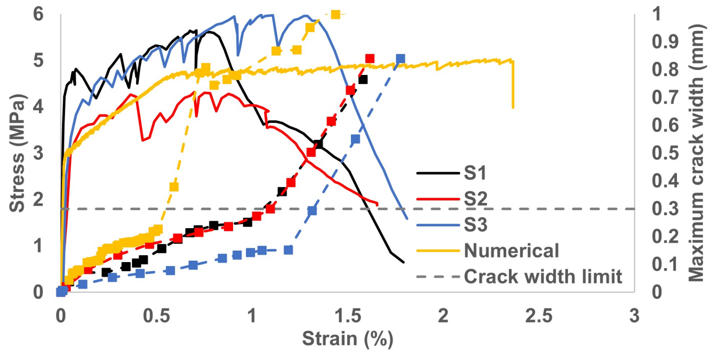

Figure 6.15: Comparison of numerical and experimental (S1, S2 & S3) results of tensile SHCC test. Experimental results are retrieved from Series 2 (chapter 5).

Upon comparison of the numerical and the experimental results, it is found that, the modelled mean compressive strength is lower than found in both experimental studies. The lower compressive strength of the SHCC in the numerical model is of minor influence on the numerical results as SHCC is used in the tension zone. The Young's modulus tests are not performed by (Singh, 2019). Therefore, the Young's modulus is taken from the numerical input from (Mustafa et al., 2022). This Young's modulus is similar to what is numerically modelled. The Young's modulus, found in chapter 5, of SHCC is significantly higher than used in the numerical models. This higher Young's modulus contributes to a higher stiffness for the experimental samples. However, as the numerical models show in general a higher bending stiffness, compared to the experimental results, the underestimation of the Young's modulus in the numerical model is having a minor effect. Lastly, the strain capacity of the SHCC modelled is larger than found in the experiments in chapter 5. This affects the deformation capacity of the beam models, as the SHCC modelled is able to be strained more before the element fails. This high ductility of SHCC is also affecting the cracking pattern, as due to the higher ductility of the modelled SHCC, the SHCC is contributing more in tension and therefore the steel force is lower. This results in a lower force transfer between steel and SHCC, which leads to lower forces in the rebar-SHCC interface elements. Therefore, the overestimation of the ductility of SHCC leads to higher yielding loads, higher 0.3 mm crack width loads and a lower yielding deflection, compared to the experiments. From the crack width development in the numerically modelled SHCC, it is found that, the crack widths are larger, compared to the experiments. At a strain of 0.5%, the crack widths numerically modelled increase suddenly in width. This explains the sudden increase in crack width in the numerical beam models. The sudden increase in crack width in the modelled SHCC could be explained by the reduction in elemental stiffness of the lattice beam elements. Therefore, it is recommended to optimize the numerical material input of SHCC.

6.2.3. Concrete-SHCC interface

Another aspect of the numerical beam models is the concrete-SHCC interface. A simple, 1-segmented, material input has been used for this. This is a simplified approach and a more detailed material input could lead to different structural behavior of the numerical models. Therefore, an additional 400 mm high hybrid beam is modelled with a twice as strong interface bond (H400si). The concrete-SHCC interface is modelled with an 1-segmented material input (Table 6.11).

Table 6.11: Numerical concrete-SHCC interface material input for (a) H400 as used in chapter 4 and (b) H400 with twice as strong interface (H400si).

Property/Segment	1
Radius (mm)	10.5
E (MPa)	33119
G (MPa)	13800
f_c (MPa)	-35
f_t (MPa)	2.00

(a)

Property/Segment	1
Radius (mm)	10.5
E (MPa)	33119
G (MPa)	13800
f_c (MPa)	-70
f_t (MPa)	4.00

(b)

Upon comparison of the numerical results, it is found that, the deformation capacity decreases for the beam with the stronger concrete-SHCC interface (Figure 6.16). Additionally, the load at which the 0.3 mm crack width limit is reached is slightly increased for the beam with a stronger concrete-SHCC interface (Table 6.12). From the Maximum crack width - deflection curves, it is found that, the model with a stronger concrete-SHCC bond (H400si) has a similar development of the maximum crack widths, compared to the model with the weaker concrete-SHCC interface (H400).

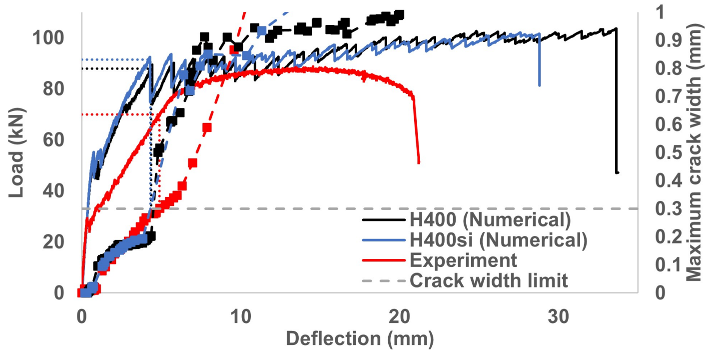

Figure 6.16: Effect of concrete-SHCC interface strength presented by a comparison of numerical results with the concrete-SHCC interface strength used in chapter 4 (H400), numerical results of a twice as strong concrete-SHCC interface (H400si) and experimental results. Solid = load - deflection. Dashed = crack width - deflection.

Table 6.12: Overview of numerical results with the concrete-SHCC interface strength used in chapter 4 (H400), numerical results of a twice as strong concrete-SHCC interface (H400si) and experimental results.

Key performance indicators	Experimental	H400 (Num)	H400si (Num)
Ultimate load	88.82 kN	103.70 kN	102.11 kN
Maximum deflection	20.82 mm	33.63 mm	28.82 mm
Number of propagated cracks	3	2	3
Load at 0.3 mm crack width	70.11 kN	88.40 kN	91.46 kN
0.3 mm load/yield load	90.52%	98.88%	99.41%

Upon comparison of the final cracking patterns, it is found that, the H400si model is developing 3 propagated cracks in the concrete layer (Figure 6.17). This is similar to the experimental cracking pattern. Therefore, the increase of the concrete-SHCC strength in the numerical model improves the simulation of the structural behavior. This means that the used concrete-SHCC interface strength in the numerical models of chapter 4 was too weak. In addition, the strength of the concrete-SHCC interface affects the cracking pattern of the hybrid beam. Therefore, it is recommended to study the concrete-SHCC interface behavior in the Delft Lattice Model to improve the modelling of the structural behavior.

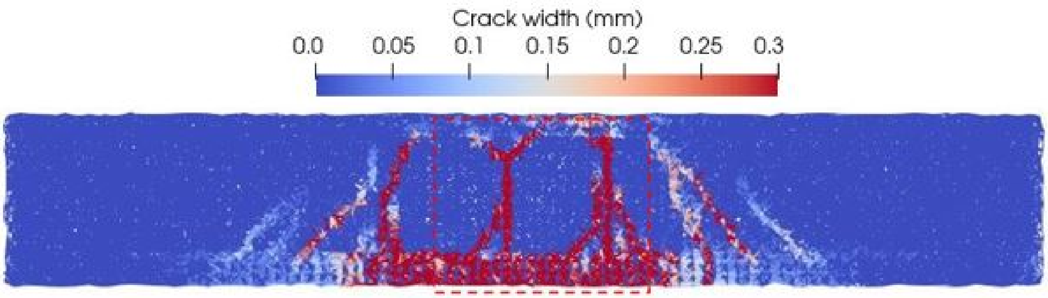

(a)

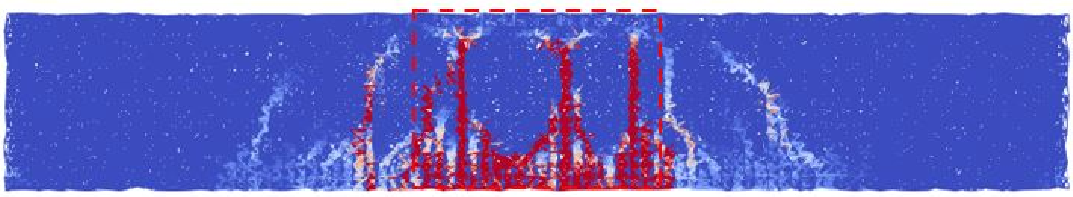

(b)

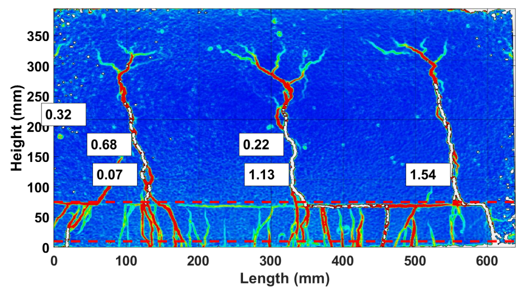

(c)

Figure 6.17: Final cracking pattern of the H400 beam from (a) numerical study (H400) chapter 4, (b) numerical model adjusted with stronger concrete-SHCC interface (H400si) and (c) experimental study.

Upon comparison of the delamination of the concrete-SHCC interfaces, it is found that, the numerical model with a stronger concrete-SHCC interface shows smaller delamination (1.46 mm), compared to the numerical model with a weaker concrete-SHCC interface (4.13 mm) (Figure 6.18). Thereby, the delamination of the numerical model with a stronger interface is more comparable to the maximum delamination found in the experiments (2.04 mm). Therefore, the concrete-SHCC interface strength used in the numerical simulations in chapter 4 is too weak.

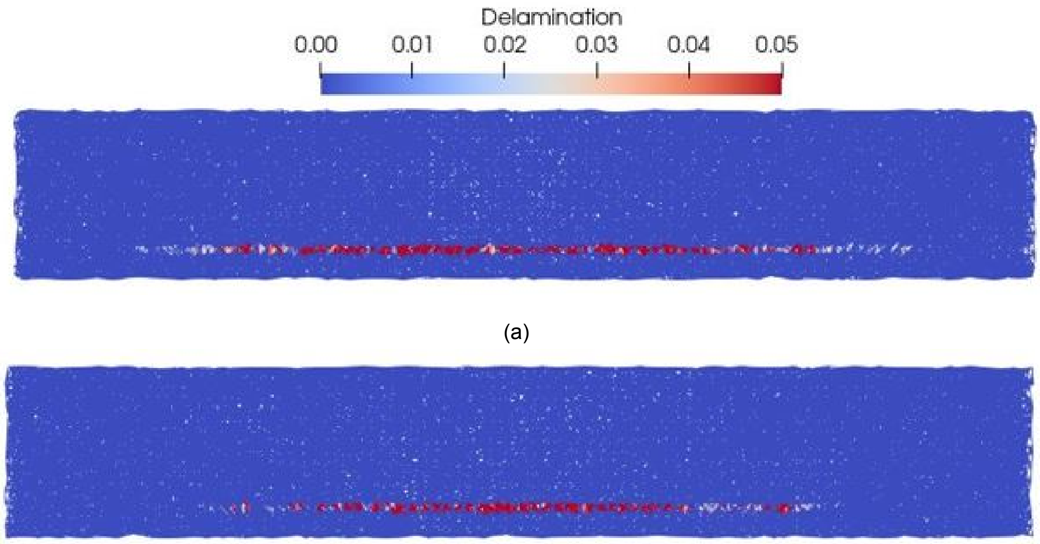

(a)

(b)

Figure 6.18: Comparison of delamination of numerically results of 400 mm high hybrid beam with (a) weak bond (H400) and (b) strong bond (H400si) at ultimate load.

6.2.4. Micro-cracks

Another aspect to mention is the formation of micro-cracks in SHCC. Upon demolding of the hybrid beams, the exposure of the concrete and the SHCC leads to drying shrinkage. As the shrinkage of SHCC is larger than that of concrete, concrete is restraining the shrinkage of SHCC. This leads to the formation of micro-cracks. These micro-cracks are observed in all the hybrid beams of the experimental study. The formation of micro-cracks are not included in the numerical model and the analytical calculations. However, the micro-cracks in SHCC lead to predefined weak spots. In addition, the presence of micro-cracks shows that the SHCC is already stressed due to shrinkage, before the experimental tests is started. These additional stresses are not considered in the numerical model and the analytical calculations. Therefore, neglecting the shrinkage in the numerical model, contributes to the overestimation of the structural behavior in the numerical models.

7

Conclusions and Recommendations

7.1. Conclusions

The main objective of this thesis is to investigate the effect of height scaling on the flexural crack width controlling behavior of hybrid R/SHCC beams. Thereby, the following hypothesis is formulated:

"Upon increasing the height of hybrid R/SHCC beams, the effectiveness of the crack controlling behavior of the SHCC layer decreases."

This hypothesis is tested true, based on the combined experimental study, numerical study and analytical calculations of 200 mm, 300 mm and 400 mm high R/SHCC beams, with a constant 70 mm thick bottom SHCC layer. Reinforced concrete beams of 200 mm, 300 mm and 400 mm height are used as a reference. The findings can be summarized as follows:

- From the performed experiments, it is found that, the load, at which the 0.3 mm crack width limit is reached, relative to the yielding load, decreases from 109% to 97% and 91%, upon increasing the height from 200 mm to 300 mm and 400 mm, respectively (Figure 7.1). Therefore, the 200 mm beam is able to control crack widths below 0.3 mm beyond yielding, which makes the yielding limit the governing serviceability limit state. Whereas, for the 300 mm and 400 mm high hybrid beams, the crack width limit remains the governing serviceability limit state. In comparison, increasing the height of the reinforced concrete beams from 200 mm to 300 mm and 400 mm, this load, at which the crack width limit is reached, relative to the yielding load, is insignificantly affected (76%-78%).
- Upon using a 0.2 mm crack width limit, a similar decrease in the crack controlling behavior of the hybrid R/SHCC beams is found, as the load, at which the crack width limit is reached, relative to the yielding load, decreases in the experiments from 106% (200 mm height), to 77% (300 mm height) and 71% (400 mm height). Using the load difference between the hybrid R/SHCC beam and the reinforced concrete beams of the same height, at which the 0.3 mm crack width limit is reached, a similar decrease in the crack controlling behavior of the hybrid R/SHCC beams is found, upon increasing the height from 200 mm (32 kN), to 300 mm (24 kN) and 400 mm (20 kN). Using a 0.2 mm crack width limit leads to the same conclusions.
- The decrease in the crack controlling behavior can be attributed to a decrease in the number of propagated cracks in the concrete layer from 7 (200 mm), to 4 (300 mm) and 3 (400 mm), upon increasing the height of the hybrid beams from 200 mm, to 300 mm and 400 mm, respectively. The reinforced concrete beams also showed a decrease in the number of propagated cracks, upon increasing the height. Both the hybrid beams and the reinforced concrete beams showed the development of an effective tensile area, upon increasing the height to 300 mm and 400 mm. This trend is also observed in the numerical models. In addition, the experiments and the numerical models both show the cracks in SHCC layer opening up from the bottom of the beam and from the concrete-SHCC interface. This is different from the 200 mm high hybrid beam, which showed solely opening of cracks from the bottom of the beam.

- The delamination of the SHCC-concrete interface is found to increase, upon increasing the height of the hybrid beam. This is both found in the experimental and numerical results. Increasing the strength of the SHCC-concrete interface for the hybrid 400 mm high beam in the numerical model leads to a reduction of the delamination and a decrease in the deformation capacity of the beam. This is different from the experimental results of the interface roughness of the 200 mm high hybrid beams from (Singh, 2019).
- The out of plane measurements, performed in the experiments, provided more insight in the fracturing process of reinforced cementitious beams. It is found that, hybrid beams are more sensitive to out of plane displacements, compared to reinforced concrete beams.
- The numerical simulations showed similar trends in the cracking patterns of the reinforced concrete beams and the hybrid R/SHCC beams, compared to the experiments. The numerical models of the hybrid beams only reached the 0.3 mm crack width limit, upon yielding of the reinforcement. This could be attributed to the overestimation of the ductility of the SHCC and the simplified bi-linear material input for steel. Therefore, the numerical models of the hybrid beams were not able to show a decrease in the effectiveness of the crack controlling behavior, as observed in the experiments (Figure 7.1). For the reinforced concrete beams, the numerical models were able to simulate the same trend, as found in the experiments. With consideration of the limitations of the numerical models, the Delft Lattice Model shows large potential in simulating the structural behavior of reinforced cementitious structures. Even more, the use of a 25 mm voxel size in the reinforced concrete beam model did not compromise the results, compared to the 10 mm voxel size used by (Mustafa et al., 2022). Therefore, the use of a coarse voxel size in the Delft Lattice Model leads to a successful and time-efficient simulation of the structural behavior. The suitability of the Delft Lattice Model is once more confirmed, by the comparison of the load-deflection curves with the analytical calculations, for both the reinforced concrete beams and the hybrid R/SHCC beams.

The secondary objective in this thesis, is to study the effect of delamination of the rebar-SHCC interface on the crack controlling behavior of the hybrid R/SHCC beam. This is studied experimentally and numerically by a 300 mm high hybrid R/SHCC beam with smooth and Vaseline treated longitudinal reinforcement bars. It is found that, full delamination of the rebar-SHCC interface compromises the crack controlling behavior of the 300 mm high hybrid beam. This is both found from the numerical and experimental results. The findings can be summarized as follows:

- From the experiments, it is found that, the load at which, the 0.3 mm crack width limit is reached is 59% (40 kN) of the yielding load (Figure 7.1). This is significantly lower compared to the 97% (77 kN) load, relative to the yielding load, found for the 300 mm high hybrid beam with ribbed reinforcement bars. Even more, the 300 mm high reinforced concrete beam showed better crack width controlling behavior, as the crack width limit is reached at 78% (53 kN) of the yielding load. Similar results are found for applying a 0.2 mm crack width limit.
- The compromised crack controlling behavior can be explained by the cracking pattern of the 300 mm high hybrid beam. The beam with smooth and Vaseline treated longitudinal reinforcement bars showed a single crack propagating in the concrete layer, whereas 4 of these cracks are found in the 300 mm high hybrid beam with ribbed reinforcement bars. Only a limited number of cracks were formed in the SHCC layer in the hybrid beam with smooth and Vaseline treated reinforcement bars, whereas a uniform distribution of cracks is found in the ordinary hybrid beam. This trend in the cracking pattern is also observed in the numerical model. In addition, only small delamination of the concrete-SHCC interface is found for the hybrid beam with smooth and Vaseline treated reinforcement, whereas the 300 mm high hybrid beam with ribbed reinforcement showed significant delamination of the concrete-SHCC interface. This reduction of the delamination of the concrete-SHCC interface is also found in the numerical models.
- The numerical model showed similar cracking patterns for the 300 mm high hybrid beam with smooth and Vaseline treated reinforcement bars, compared to the experiments. The numerical model made has a weak rebar-SHCC bond over the full length of the beam, whereas only the central 700 mm is Vaseline treated in the experiments. Therefore, the numerical model showed

the load-deflection behavior of an unreinforced hybrid beam, whereas the reinforcement contributed to the strength of the hybrid beam in the experiments. With this difference in mind, the Delft Lattice Model shows potential in simulating the structural behavior of a smooth and Vaseline treated reinforcement bar.

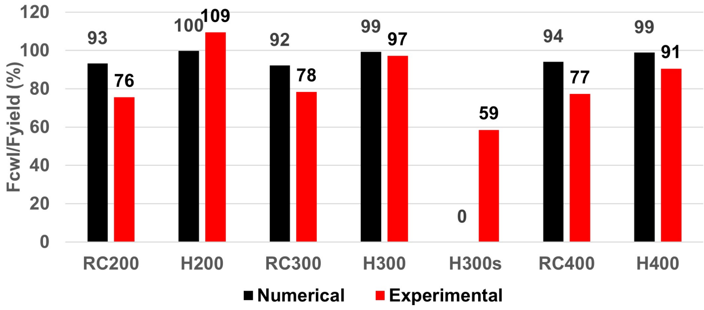

Figure 7.1: Overview of experimental results and numerical results for a 0.3 mm crack width limit. Fcwl = load of beam upon reaching crack width limit. Fyield = load of beam upon reaching yielding of the reinforcement. Experimental results of 200 mm high beams retrieved from (Singh, 2019).

7.2. Recommendations

Based on the conclusions, the following recommendations are made for future studies:

- From the literature study, it is found that, small aggregates in SHCC could be beneficial in dealing with the shrinkage behavior of SHCC. However, the effect on the maximum crack width is unknown. Therefore, it is recommended to study the effect of small aggregates on the crack controlling behavior of hybrid R/SHCC beams.
- It is recommended to study the effect of the SHCC-concrete interface for the hybrid beams scaled in height, as from the numerical analysis, it is found that, the strength of SHCC-concrete affects the cracking pattern, as a stronger interface leads to the formation of an additional propagated crack in the concrete layer. Therefore, the interface roughness could improve the crack controlling behavior of the 400 mm high hybrid beam.
- It is recommended to study the numerical material input of SHCC, to improve the simulation of the structural behavior of the developed beam models. In addition, the material input of the SHCC-concrete interface elements should be studied, to improve the simulation of the structural behavior of the hybrid beams.
- In the experimental study, it is suggested that, the fiber distribution in the SHCC could explain the higher out of plane displacement of hybrid beams, compared to reinforced concrete beams. Additionally, the higher coefficient of variation in the material samples could be attributed to the fiber distribution. Even more, problems with the mixing of SHCC are encountered. Therefore, it is recommended to include measurements of the fiber distribution in future studies to SHCC.
- From the experimental results, it is found that, out of plane displacements are part of the fracturing process of cementitious beams. Especially, the hybrid beams are more sensitive for out of plane displacements. Out of plane displacements influence DIC measurements. Therefore, it is recommended to continue to measure out of plane displacements in future studies to hybrid beams. LVDT measurements showed to be vital for the analysis of out of plane displacements. Therefore, it is recommended to continue to measure with LVDTs, in addition to DIC measurements.

7.3. Reflections for future study

While preparing for the experiments, several difficulties were encountered. In this section, the encountered difficulties are reported and reflected, to provide practical advice for future studies.

7.3.1. Mixing SHCC
The mixing of the SHCC starts by dry-mixing the fibers, cement-powder and limestone power. After dry mixing the water and superplasticizer are added. In the series 1 of the experimental study, 87L of SHCC was made in a single batch. In the series 2 of the experimental study, 70L of SHCC was made. As these volumes are relative large, a mixer of 200L volume is used (Figure 7.2). During the mixing of the SHCC, difficulties are encountered, once the liquids are added. The mixer showed difficulty in mixing the SHCC to a uniform mix, leading to large particles of unhydrated cement. The difficulty of mixing arises from the sticky fluid phase of SHCC. The uniformity of the SHCC mix was improved by rotating the mixer from horizontal to vertical. The uniformity of the SHCC mix is important as unhydrated cement is an impurity reducing the strength of the SHCC. Additionally, the fiber distribution is expected to be better in a uniform SHCC mix.

Figure 7.2: Mixer used for mixing of the SHCC.

7.3.2. Vibrating SHCC
After mixing, the SHCC is cast in the molds and vibrated. As the layer of SHCC is only 70 mm high, vibration with the vibration needle is not possible. Therefore, the molds are placed on a vibration table (Figure 7.3). The vibration table available was too small to vibrate the whole mold in once. Therefore, the molds are placed for only half of their length on the vibration table. After vibrating one half of the beam, the mold is pushed over the table and the other half of the mold is vibrated. The vibration table is most effective in the center of the table. Due to this difficulty in the vibration of the SHCC layer, it is hard to ensure sufficient compaction of the SHCC layer in the beams.

Figure 7.3: Vibration table with beam mold.

7.3.3. Fiber distribution

From the literature study, it was found that, the fiber distribution affects the material properties of SHCC. In the experimental study, it is suggested that, the fiber distribution could cause the out of plane displacement observed in the hybrid beams. Additionally, it is suggested that, the larger spread in material properties in SHCC could be attributed to the fiber distribution. During the experiments, images of the formed cracks are made. These images show a difference in the number of fibers that bridge a crack (Figure 7.4). This supports the suggestion of a heterogeneous fiber distribution in the hybrid beams. However, the fiber distribution is not measured in this thesis. Therefore, the suggestion of a heterogeneous fiber distribution remains inconclusive. It is recommended to include measurements of fiber distribution in future studies to hybrid R/SHCC beams.

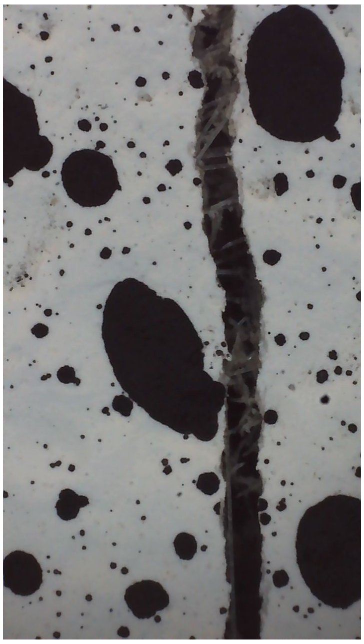

(a)

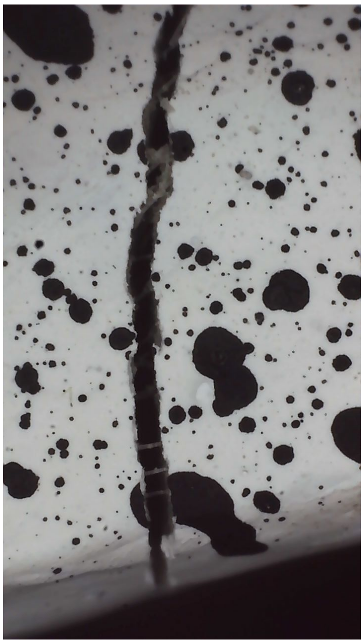

(b)

Figure 7.4: Images of SHCC cracks in hybrid beams made during the experiments with (a) numerous fibers bridging and (b) limited fibers bridging.

7.3.4. Test setup

The experimental study consists of two series of tests. The first testing series is performed with the red setup frame (Figure 7.5). This setup has been used for many years. Therefore, using it for the beams in series 1 seemed like an obvious choice. However, as described in the analysis of this test setup (Chapter 5), multiple aspects of the setup allowed for errors in the performed experiment. Due to the supporting conditions, the beam could be horizontally displaced in plane. Due to unfixed support boxes, the supports could be misaligned under the beam. However, the most important factor is found to be the stiffness of the cylinder. The low stiffness of the cylinder, caused the load to be applied under an angle, leading to out of plane displacements. This compromised the experimental results of series 1. This problem has been overcome by performing the series 2 of the experiments in a stiffer setup with a stiffer cylinder (Figure 7.5). The out of plane displacements found in the reinforced concrete beams in the series 1, becomes insignificantly small in series 2. For the hybrid beams, the out of plane displacements reduced significantly in series 2, compared to series 1. In order to fit the beams of series 2 in the new setup, the top horizontal beam of the frame needed to be lifted and the cylinder needed to be replaced. After adjusting the setup the setup has not been tested, due to the already occurred delays in this project. However, it is recommended to always test the setup, prior to performing the experiments. Testing the setup after adjustments have been made to the setup, allows the setup to settle. Additionally, this reduces the room for errors in a setup.

(a)

(b)

Figure 7.5: Testing setups for (a) series 1 of experiments and (b) series 2 of experiments.

Bibliography

Al Ghazali, A., Schröfl, C., & Mechtcherine, V. (2017). Plastic shrinkage of high-performance strain-hardening cement-based composites (hp-shcc). *Int. Cem. Concr. Technol. Conf. Oman*, 396–408.

Alam, S. Y., Lenormand, T., Loukili, A., & Regoin, J. (2010). Measuring crack width and spacing in reinforced concrete members. *7th International conference on Fracture Mechanics of Concrete and Concrete Structures (FraMCoS-7)*, 377–382.

Artec3D. (2022). Wireless handheld 3d scanner: Artec leo: Best 3d scanning solutions. https://www.artec3d.com/portable-3d-scanners/

Baji, H., & Ronagh, H. (2011). Investigation of ductility of rc beams designed based on as3600.

Bazant, Z. P. (2000). Size effect in compression and tensile quasibrittle fracture. *Journal of the Mechanical Behavior of Materials*, *11*(1-3), 7–12.

Beeby, A. W. (2005). The influence of the parameter ϕ/ρ eff on crack widths. *Structural Concrete*, *6*(4), 155–165.

Bentur, A., & Mindness, S. (2007). *Fibre reinforced cementitious composites* (2nd ed.). Taylor & Francis.

Braam, C. (2019). Crack width control. In C. Vraam (Ed.), *Reinforced concrete*. Technical University of Delft.

Braam, C., & Lagendijk, P. (2008). *Constructieleer gewapend beton*. Cement en Beton Centrum.

Cai, J., Pan, J., Tan, J., & Li, X. (2020). Bond behaviours of deformed steel rebars in engineered cementitious composites (ecc) and concrete. *Construction and Building Materials*, *252*, 119082.

Canon. (2022). Canon ef 35mm f/2 is usm - lenses. https://www.canon.nl/lenses/ef-35mm-f-2-is-usm-lens/

Castel, A., Vidal, T., & François, R. (2006). Effective tension active cross-section of reinforced concrete beams after cracking. *Materials and structures*, *39*(1), 115–126.

Chan, S. H. C. (2012). *Bond and cracking of reinforced concrete* (Doctoral dissertation). Cardiff University.

Chen, Y., Yu, J., Younas, H., & Leung, C. K. (2020). Experimental and numerical investigation on bond between steel rebar and high-strength strain-hardening cementitious composite (shcc) under direct tension. *Cement and Concrete Composites*, *112*, 103666.

Choi, W.-C., & Yun, H.-D. (2013). Effect of expansive admixtures on the shrinkage and mechanical properties of high-performance fiber-reinforced cement composites. *The Scientific World Journal*, *2013*.

Creaform. (2022). Handyscan 3d: Professional portable metrology-grade [3d laser scanner]. https://www.creaform3d.com/en/portable-3d-scanner-handyscan-3d

Deng, M., Pan, J., & Sun, H. (2018). Bond behavior of steel bar embedded in engineered cementitious composites under pullout load. *Construction and Building Materials*, *168*, 705–714.

Eurocode 2: Design of concrete structures. (2004). European Committee of Standardization.

Fischer, G., Stang, H., & Dick-Nielsen, L. (2007). Initiation and development of cracking in ecc materials: Experimental observations and modeling. *3*, 1517–1522.

Gibb, I., & Harrison, T. (2010). Use of control charts in the production of concrete. *ERMCO2010*.

Goszczyńska, B., Trąmpczyński, W., & Tworzewska, J. (2021). Analysis of crack width development in reinforced concrete beams. *Materials*, *14*(11), 3043.

Grzybowski, M., & Shah, S. P. (1990). Shrinkage cracking of fiber reinforced concrete. *Materials journal*, *87*(2), 138–148.

Harajli, M. (2009). Bond stress–slip model for steel bars in unconfined or steel, frc, or frp confined concrete under cyclic loading. *Journal of structural engineering*, *135*(5), 509–518.

Hartsuijker, C. (2016). *Toegepaste mechanica: Spanningen, vervormingen verplaatsingen*. Boom Uitgevers.

Hordijk, D. (1991). *Local approach to fatigue of concrete* (Doctoral dissertation). Technical University of Delft.

Huang, Z. (2017). *Flexural behaviour of reinforced concrete beams with a layer of shcc in the tension zone: Experimental study*. Technical University of Delft. https://repository.tudelft.nl/islandora/object/uuid:6a0cad26-fec1-4329-b408-6e9140573a31

Jang, S.-J., Kim, J.-H., Kim, S.-W., Park, W.-S., & Yun, H.-D. (2019). The effect of shrinkage-compensation on the performance of strain-hardening cement composite (shcc). *Sustainability*, *11*(5), 1453.

Lee, D.-T., & Schachter, B. J. (1980). Two algorithms for constructing a delaunay triangulation. *International Journal of Computer & Information Sciences*, *9*(3), 219–242.

Li, V. C. (2008). Engineered cementitious composites (ecc) material, structural, and durability performance.

Li, V. C., & Stang, H. (2004). Elevating frc material ductility to infrastructure durability.

Li, V. C., Wu, C., Wang, S., Ogawa, A., & Saito, T. (2002). Interface tailoring for strain-hardening polyvinyl alcohol-engineered cementitious composite (pva-ecc). *Materials Journal*, *99*(5), 463–472.

Lukovic, M. (2016). *Influence of interface and strain hardening cementitious composite (shcc) properties on the performance of concrete repairs* (Doctoral dissertation). Delft University of Technology. Delft University of Technology. https://doi.org/10.4233/uuid:28b07d9b-c704-47fa-9ba3-cd9fde10130a

Lukovic, M., Yang, Y., Schlangen, E., & Hordijk, D. (2018). On the potential of lattice type model for predicting shear capacity of reinforced concrete and shcc structures. *High tech concrete: Where technology and engineering meet* (pp. 804–813). Springer.

Magalhães, M., Toledo Filho, R., & Fairbairn, E. (2010). Fracture processes of strain-hardening cement-based composites (shcc) under direct tension and bending loads. *ECF18*.

Mechtcherine, V., Slowik, V., Kabele, P., Mechtcherine, V., Slowik, V., & Kabele, P. (2018). The effect of fiber orientation on the mechanical proprties of shcc. *Strain-hardening cement-based composites: Shcc4* (pp. 46–54). RILEM.

Meddah, M. S., Suzuki, M., & Sato, R. (2011). Influence of a combination of expansive and shrinkage-reducing admixture on autogenous deformation and self-stress of silica fume high-performance concrete. *Construction and Building Materials*, *25*(1), 239–250.

Mohamad, M. E., & Ibrahim, I. S. (2015). Interface shear strength of concrete-to-concrete bond with and without projecting steel reinforcement. *Jurnal Teknologi*, *75*(1).

Mustafa, S., Singh, S., Hordijk, D., Schlangen, E., & Luković, M. (2022). Experimental and numerical investigation on the role of interface for crack-width control of hybrid shcc concrete beams. *Engineering Structures*, *251*, 113378.

Neville, A. M., & Brooks, J. (2010). Concrete technology, 2nd editio. *Edinburgh, England: Pearson Education Limited*.

Pearson, K. (1896). Vii. mathematical contributions to the theory of evolution.—iii. regression, heredity, and panmixia. *Philosophical Transactions of the Royal Society of London. Series A, containing papers of a mathematical or physical character*, (187), 253–318.

Pendyala, R., Mendis, P. et al. (1996). Full-range behavior of high-strength concrete flexural members: Comparison of ductility parameters of high and normal-strength concrete members. *Structural Journal*, *93*(1), 30–35.

Piyasena, R. (2002). *Crack spacing, crack width and tension stiffening effect in reinforced concrete beams and one-way slabs* (Doctoral dissertation).

Randl, N. (1997). Investigations on load transfer between old and new concrete at different surface roughnesses. *Leopold-Franzens-Universität Innsbruck*.

Randl, N. (2013). Design recommendations for interface shear transfer in fib model code 2010. *Structural Concrete*, *14*(3), 230–241.

Schlangen, E., & Garboczi, E. (1997). Fracture simulations of concrete using lattice models: Computational aspects. *Engineering Fracture Mechanics*, *57*(2), 319–332. https://doi.org/https://doi.org/10.1016/S0013-7944(97)00010-6

Schlangen, H. (1993). Experimental and numerical analysis of fracture processes in concrete. http://resolver.tudelft.nl/uuid:8e0d58b0-b5d0-4471-89a3-607ee4d6f7da

Shih, M.-H., & Sung, W.-P. (2013). Application of digital image correlation method for analysing crack variation of reinforced concrete beams. *Sadhana*, *38*(4), 723–741.

Simone, A. (2011). An introduction to the analysis of slender structures - tu delft. https://icozct.tudelft.nl/TUD_CT/CM5/collegestof/files/notes.pdf

Singh, S. (2019). *Influence of interface and type of strain hardening cementitious composite (shcc) on crack control in shcc-concrete hybrid beams*. Technical University of Delft. https://repository.tudelft.nl/islandora/object/uuid3A5d59fd89-6ec4-405e-9fda-b247f1ae8789

Sunaga, D., Namiki, K., & Kanakubo, T. (2020). Crack width evaluation of fiber-reinforced cementitious composite considering interaction between deformed steel rebar. *Construction and Building Materials*, *261*, 119968.

Sutton, M. A., Yan, J. H., Tiwari, V., Schreier, H., & Orteu, J.-J. (2008). The effect of out-of-plane motion on 2d and 3d digital image correlation measurements. *Optics and Lasers in Engineering*, *46*(10), 746–757.

Tai, R. (2015). *Upscaling of strain-hardening cementitious composites*. Technical University of Delft. https://repository.tudelft.nl/islandora/object/uuid:a0d63c1a-dbcf-4141-bb8a-6c7ac1063eed?collection=education

Tekçe, N., Fidan, S., Tuncer, S., Kara, D., & Demirci, M. (2018). The effect of glazing and aging on the surface properties of cad/cam resin blocks. *The journal of advanced prosthodontics*, *10*(1), 50–57.

Tepfers, R. (1973). *A theory of bond applied to overlapped tensile reinforcement splices for deformed bars* (Doctoral dissertation). Chalmers University of Technology.

Toshiyuki, K., Kabele, P., Fukuyama, H., Uchida, Y., Suwada, H., Slowik, V., Rokugo, K., & Kanda, T. (2013). *Strain hardening cement composites: Structural design and performance state-of-the-art report of the rilem technical committee 208-hfc, sc3*. Springer Netherlands.

Ueda, N., & Kawamoto, A. (2017). Influence of coarse aggregate on the mechanical behavior of strain hardening cementitious composites. *International Conference on Strain-Hardening Cement-Based Composites*, 139–146.

Van Mier, J. G. (2012). *Concrete fracture: A multiscale approach*. CRC press.

van Vliet, R. (2018). *A lattice model for prediction of ice failure in interaction with sloping structures* (Doctoral dissertation). Delft University of Technology.

van Zijl, G. P. (2011). Durability under mechanical load–micro-crack formation (ductility). *Durability of strain-hardening fibre-reinforced cement-based composites (shcc)* (pp. 9–39). Springer.

Verschuur, R. (2018). *Effective concrete tension zone: Comparison of the effective concrete tension zone between finite element models using diana and eurocode 2 and jones method*.

Visser, C. R., & Van Zijl, G. (2007). Mechanical characteristics of extruded shcc. *Proc. International RILEM CONFERENCE on High performance fibre reinforced cement composites*, 10–13.

Wu, H.-C., & Li, V. C. (1992). Snubbing and bundling effects on multiple crack spacing of discontinuous random fiber-reinforced brittle matrix composites. *Journal of the American Ceramic Society*, *75*(12), 3487–3489.

Xu, L.-Y., Huang, B.-T., Li, V. C., & Dai, J.-G. (2022). High-strength high-ductility engineered/strain-hardening cementitious composites (ecc/shcc) incorporating geopolymer fine aggregates. *Cement and Concrete Composites*, *125*, 104296.

Yao, J., & Leung, C. K. (2017). Bridging stress of inclined fiber in cementitious composites based on large deflection beam theory. *International Conference on Strain-Hardening Cement-Based Composites*, 37–45.

Yassiri, A. (2020). *Reinforced hybrid concrete beams with a u-shaped shcc mould: Developing the system and extending the multi-layer model to predict its bending behaviour*. Technical University of Delft.

Zhou, J. (2011). Performance of engineered cementitious composites for concrete repairs (phd thesis). *University of technology of TU Delft, Netherlands*.

A

Appendix A: Matlab codes

A.1. Matlab: Image selector

```
clc
clear

Loadstep = 2.5;
Image_Interval = 10;

[v,T,vT]=xlsread('Exp_Data.xlsx', 'Sheet1');
Index = v(:,1);Force= v(:,17);LVDT_5 = v(:,8);
Force_smooth=smoothdata(Force,'movmedian',50);
Total = length(Force_smooth);

A = round(Force_smooth,0);
B = round(A/Loadstep);
C = abs(Force_smooth-(Loadstep*B));

[valleys,loc2] = findpeaks(-C,Index, 'MinPeakProminence',0.1);
valleys = -valleys;

for i=1:length(loc2)
    Selected_Force(i)=Force(loc2(i));
    Selected_LVDT(i)=LVDT_5(loc2(i));
end
Selected_Force=Selected_Force';
Selected_LVDT=Selected_LVDT';
plot(Selected_Force,'ko');

Selected=[Selected_Force Selected_LVDT];
writematrix(Selected,'Selected_Data.xlsx','Sheet',1,'Range','A1')

files = dir('*.JPG');
j=1;
for i=1:Total
    if ismember(Index(i),loc2)
        name1 = files(j).name;
        copyfile (name1, 'Selected')
    end
    if rem(i,Image_Interval)==0
        j=j+1;
```

```
    end
end
```

A.2. Matlab: Crack width calculation

```
clc;
clear;


filenumber = '1';filenumber=convertCharsToStrings(filenumber);
Key='Hybrid_';Key=convertCharsToStrings(Key);
filename=Key+filenumber;
A = 'A'; A=convertCharsToStrings(A);
D = 'D'; D=convertCharsToStrings(D);
sep = ':'; sep=convertCharsToStrings(sep);
Rows = A+filenumber + sep + D+filenumber;

Rows=convertStringsToChars(Rows);

filename=convertStringsToChars(filename);
filenumber=convertStringsToChars(filenumber);
excelname = 'crackwidths.xlsx'
[v,T,vT]=xlsread([filenumber,'.csv'], filenumber) ;
x = v(:,1);Ey = v(:,2);Dy=v(:,3);Ecr=0.30;
x = x(2:end);Ey = Ey(2:end);Dy = Dy(2:end);
length_x = length(x);



% replace with an image of your choice
img_4 = imread([filenumber,'.JPG']);
% set the range of the axes
% The image will be stretched to this.
min_x4 = 0;
max_x4 = max(x);
min_y4 = 0;
max_y4 = 395;

for i = 1:length_x
    if Ey(i) > Ecr && i>1
        ModEy(i) = Ey(i);
    else
        ModEy(i) = 0;
    end
end


[peaks,loc1] = findpeaks(ModEy,x, 'MinPeakProminence',0.1);
[valleys,loc2] = findpeaks(-ModEy,x, 'MinPeakProminence',0.1);
valleys = -valleys;

imagesc(img_4);
xlabel('Raster Column');
ylabel('Raster Row');
colormap(gray);
imagesc([min_x4 max_x4], [min_y4 max_y4], flipud(img_4));
```

```
set(gca,'ydir','normal');
hold on;
ax = gca;
yyaxis left
plot(0,0,'k','linewidth',0.1);
xlim([0 max_x4])
ylim ([0 max_y4])
ax.YColor = [0 0 1];
title('Picture - Strain Overlay', 'FontName', 'Arial')
xlabel ('Distance (mm)', 'FontName', 'Arial')
ylabel ('Distance (mm)', 'FontName', 'Arial')
yyaxis right
E = plot(x,ModEy,'-','Color',[0 0 0],'linewidth',4);
hold on
P = plot(loc1,peaks,'mo','MarkerFaceColor',[1 0 1],'MarkerSize',20);
hold on
V = plot(loc2,valleys,'ks','MarkerFaceColor',[0 0 0],'MarkerSize',20);
ax.YColor = [0 0 0];
ylabel ('Strain in Y (%)', 'FontName', 'Arial')
set(gca,'FontSize',14)
set(gca, 'FontWeight', 'bold')
ylim([0 max(Ey)])
legend([E P V], 'Strain in Y', 'Peaks', 'Valleys','Location','northwest', 'FontName', '


for i = 1:(length_x)
    if ismember(x(i),loc2,'rows')
        CW_Individual(i) = 0;
    elseif ModEy(i) > Ecr && i>1
        CW_Individual(i) = abs(Dy(i) - Dy(i-1));
    else
        CW_Individual(i) = 0;
    end
end

 wrap       = [0, CW_Individual, 0] ;
 temp       = diff( wrap ~= 0 ) ;
 blockStart = find( temp == 1 ) ;
 blockEnd   = find( temp == -1 ) ;
 blocks     = arrayfun( @(bId) wrap(blockStart(bId):blockEnd(bId)), ...
                        1:numel(blockStart), 'UniformOutput', false ) ;
blockCen = floor((blockStart + blockEnd)/2);



if max(blockStart)>length(x)
    blockStart = [blockStart(1:end-1) blockStart(end)-1];
end

if max(blockEnd) >length(x)
    blockEnd = [blockEnd(1:end-1) blockEnd(end)-1];
end

Num_C = length(blockStart);
for i=1:Num_C
    CW{i}=abs(Dy(blockStart(i))-Dy(blockEnd(i)));
```

```

end
CW=cell2mat(CW);
blockCen = [blockCen 0];

j=1;
for i = 1:length_x
    if i == blockCen(j)-1
        CWx(i) = CW(j);
        j=j+1;
    else
        CWx(i) = 0;
    end
end

CWx=CWx';

figure
imagesc(img_4);
xlabel('Raster Column');
ylabel('Raster Row');
colormap(gray);
imagesc([min_x4 max_x4], [min_y4 max_y4], flipud(img_4));
set(gca,'ydir','normal');
hold on;
ax = gca;
yyaxis left
plot(0,0,'k','linewidth',0.1);
xlim([0 max_x4])
ylim ([0 max_y4])
ax.YColor = [0 0 1];
title('Picture - Crack Overlay', 'FontName', 'Arial')
xlabel ('Distance (mm)', 'FontName', 'Arial')
ylabel ('Distance (mm)', 'FontName', 'Arial')
yyaxis right
C = plot(x,CWx,'k','linewidth',4);
ax.YColor = [0 0 0];
ylabel ('Crack Width (mm)', 'FontName', 'Arial')
set(gca,'FontSize',14)
set(gca, 'FontWeight', 'bold')
ylim([0 inf])
legend([C], 'Crack Width','Location','northwest', 'FontName', 'Arial')

n=length(peaks);k=ceil(0.20*n);
Maxk = maxk(CWx,k);MeanMaxk=mean(Maxk);

Max = max(CWx);
ACW = CWx(CWx~=0);
AVG = mean(ACW);

disp (Max);
disp (AVG);
disp(MeanMaxk);
disp(length(Maxk));

figure
```

```
ax = gca;
yyaxis left
plot(0,0,'k','linewidth',0.1);
xlim([0 max_x4])
ylim ([0 max_y4])
ax.YColor = [0 0 1];
title('Picture - Strain Overlay', 'FontName', 'Arial')
xlabel ('Distance (mm)', 'FontName', 'Arial')
ylabel ('Distance (mm)', 'FontName', 'Arial')
yyaxis right
E = plot(x,ModEy,'-','Color',[0 0 0],'linewidth',4);
hold on
P = plot(loc1,peaks,'mo','MarkerFaceColor',[1 0 1],'MarkerSize',20);
hold on
V = plot(loc2,valleys,'ks','MarkerFaceColor',[0 0 0],'MarkerSize',20);
ax.YColor = [0 0 0];
ylabel ('Strain in Y (%)', 'FontName', 'Arial')
set(gca,'FontSize',14)
set(gca, 'FontWeight', 'bold')
ylim([0 max(Ey)])
legend([E P V], 'Strain in Y', 'Peaks', 'Valleys','Location','northwest',
'FontName', 'Arial')

CWx2 = CWx(CWx>0.015); %minimum size for a crack to be plotted
x2 = x((CWx>0.015));
disp(length(CWx2));
A = [max(CWx) mean(CWx(CWx>0.015)) length(CWx(CWx>0.015))];
writematrix(A,excelname,'Sheet',1,'Range',Rows)

C2 = figure
ax = gca;
C = plot(x2,CWx2,'rx','linewidth',2);
ax.YColor = [0 0 0];
ylabel ('Crack Width (mm)', 'FontName', 'Arial')
xlabel ('Length (mm)', 'FontName', 'Arial')
set(gca,'FontSize',14)
set(gca, 'FontWeight', 'bold')
if Max<0.3
    ylim([0 0.3])
end
if Max>0.3 & Max<1
    ylim([0 1])
end
if Max>0.3 & Max>1 & Max<2.5
    ylim([0 2.5])
end
if Max>2.5
    ylim([0 5])
end
xlim([0 max_x4])

exportgraphics(C2,[filename,'.png'],'Resolution',300);
```

A.3. Analyzing tool for out of plane displacements based on 2D in plane DIC data

```
clc
clear

dis_to_obj=1011.17;
LVDT_length=200;

[v,T,vT]=xlsread('Selected_Data.xlsx', 'Sheet1');
Force = v(:,1);LVDT_Exp= v(:,2);LVDT_GOM = v(:,3);

for i=1:length(Force)
    syms x
    func = LVDT_Exp(i)-(dis_to_obj/(dis_to_obj-x)-1)*LVDT_length == 0;
    delta = solve(func,x);
    delta_solved(i)=double(delta);
end

delta_solved=delta_solved';

for i=1:length(Force)
    Corrected_LVDT(i)=(dis_to_obj./(dis_to_obj-delta_solved(i))-1)*LVDT_length;
end

plot(LVDT_Exp,Force)
hold on
plot(LVDT_GOM,Force)
hold on
plot(Corrected_LVDT,Force, 'ko')
```

B

Appendix B: DIC data

B.1. Detailed DIC data

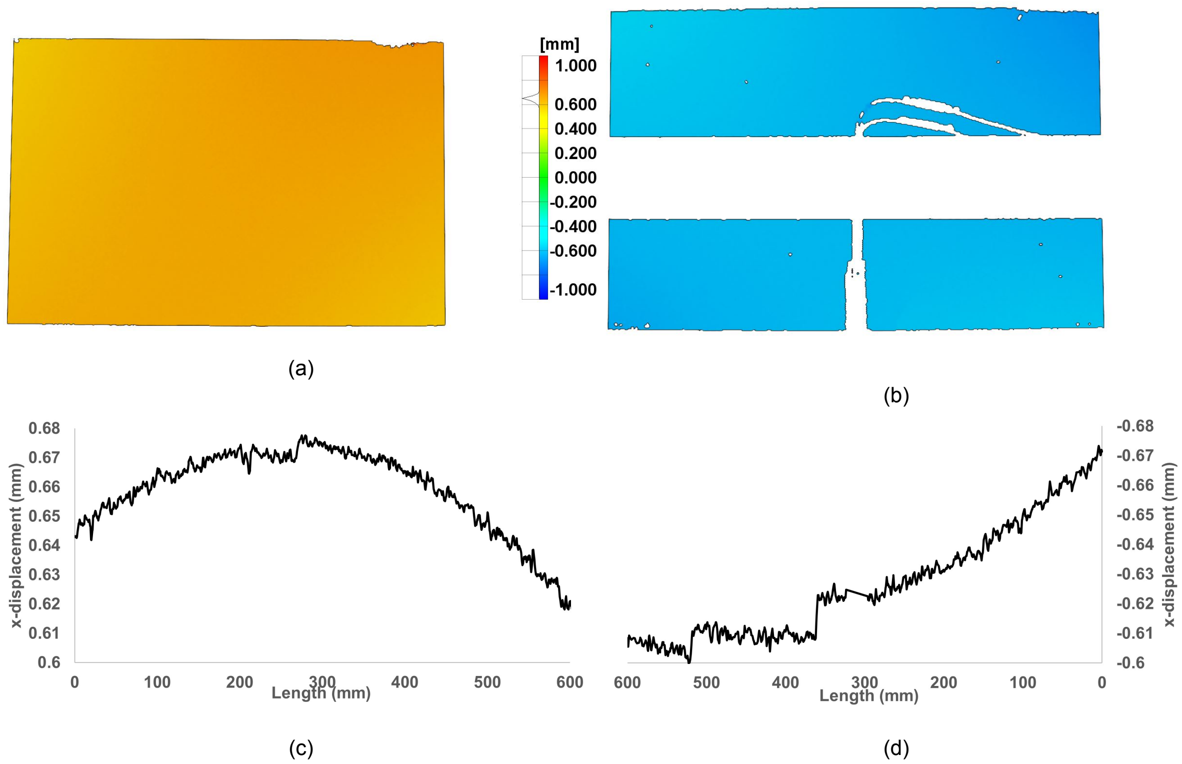

Figure B.1: DIC data from RC400 beam with (a) side 1 contour plot of x-displacement, (b) side 2 contour plot of x-displacement, (c) side 1 cross-sectional graph of x-displacement made 5 mm from bottom of the beam and (d) side 2 cross-sectional graph of x-displacement 5 mm from bottom of the beam.

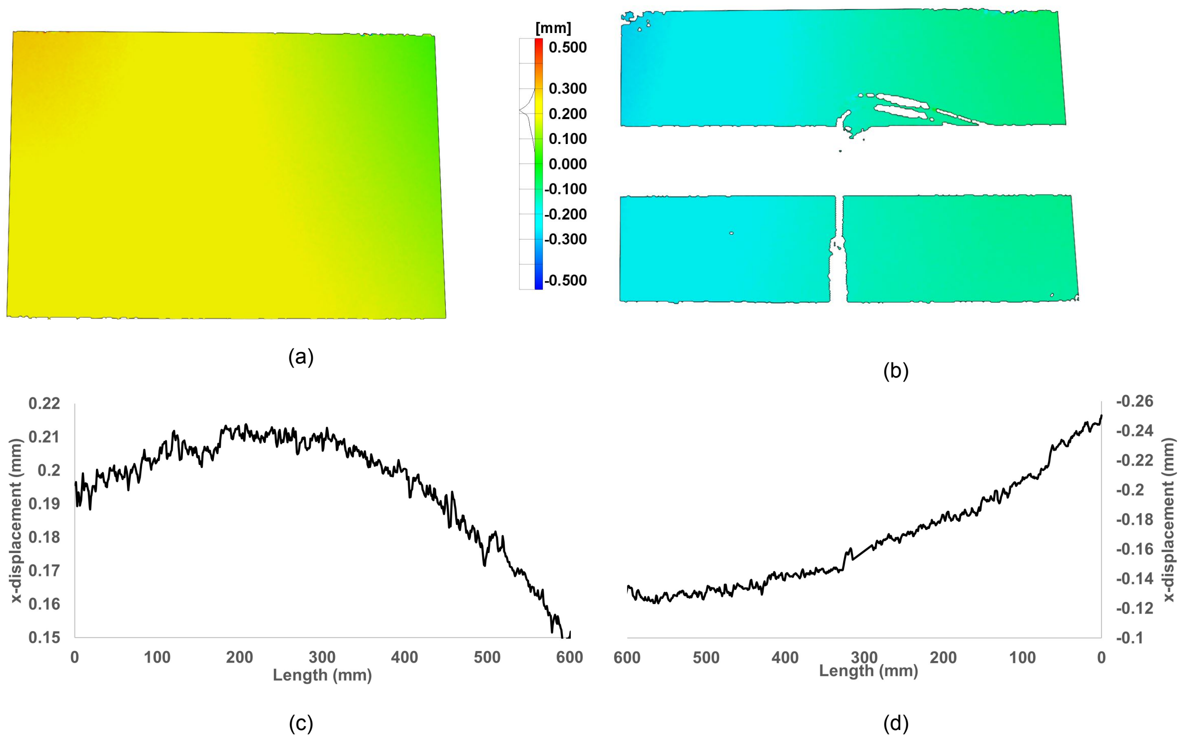

Figure B.2: DIC data from H300 beam with (a) side 1 contour plot of x-displacement, (b) side 2 contour plot of x-displacement, (c) side 1 cross-sectional graph of x-displacement made 5 mm from bottom of the beam and (d) side 2 cross-sectional graph of x-displacement 5 mm from bottom of the beam.